Controlling plasticity in the contour method of residual stress measurement

Thesis

UNRESTRICTED

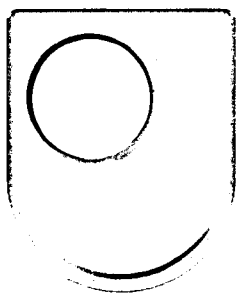

The Open University

Faculty of Mathematics, Computing & Technology

Department of Engineering and Innovation

Materials Engineering Group

CONTROLLING PLASTICITY IN THE CONTOUR METHOD OF RESIDUAL STRESS MEASUREMENT

by

Yéli Traoré

August 2013

A THESIS SUMMITTED TO THE DEPARTMENT OF ENGINEERING AND INNOVATION OF THE OPEN UNIVERSITY FOR THE DEGREE OF DOCTOR OF PHILOSOPHY

Date of Submission: 16 August 2013

Date of Award: 23 October 2013

Abstract

The contour method has emerged as a promising technique for residual stress measurement in relatively large, thick and complex engineering components. The method involves making a cut in the sample of interest, measuring the subsequent relaxed deformation profile of the cut surface and using this profile to back-calculate the original out-of-plane residual stress field by finite element modelling. The method is based on the theory of elasticity in that the stress relaxation during test specimen cutting is assumed to be entirely elastic. However, when measuring residual stresses of magnitude approaching the material yield strength, plasticity can occur which introduces errors in the measured stress profile.

The main aim of this thesis was to develop methods of mitigating and estimating plasticity -induced errors in contour method residual stress measurements.

Based on the principles of fracture mechanics, an analogy was made between the stress relaxation process and a cracked plate to investigate the origin of plasticity in the contour method. It was demonstrated that that the cut tip stress intensity factor (K_I) and the corresponding plastic zone parameters are the most important parameters for characterising plasticity-induced errors in the contour method. Extensive finite element analyses were carried out to understand and control the errors associated with plasticity with a view of improving the accuracy and reliability of the method.

The outcomes of this research provide a valuable insight into how accumulation of plasticity for different restraining conditions affects the performance of the contour method. A novel cutting strategy that aims at mitigating plasticity-induced error by controlling the severity of the cut tip stress concentration (*i.e.* stress intensity factor)

during the cutting process has been developed. Furthermore, procedures (correlations) are developed to estimate the plasticity-induced errors in the results of the contour method. Finally guidelines are proposed and applied to a case study for mitigating the errors associated with plasticity in a contour method residual stress measurement.

Acknowledgement

I would like to deeply express my sincere thanks to all those who taught me so much during this project.

First of all I would like to thank Prof. John Bouchard and Dr. Foroogh Hosseinzadeh for their invaluable guidance, supervision and extremely efficient proof reading. I am also thankful to Dr. John Francis and Prof. Mike Fitzpatrick and Prof. Alain Lodini (at Reims University in France) for their contribution during this project.

This research was funded by Rolls-Royce, Lloyds Register Foundation, the East Midlands Development Agency and their support is greatly acknowledged.

I am also grateful to EDF Energy (formerly British Energy) for provision of test samples, to Dr. Supriyo Ganguly at Cranfield University for manufacturing my test samples. The award of beam time by NRC (Canada), ANSTO (Australia) and ISIS (UK) is also gratefully acknowledged.

I would like to particularly thank Pete Ledgard for his workshop assistance (samples' preparation and wire EDM cutting), and Stan Hiller for kind help when needed in experiments.

A special thanks to Sanjooram Paddea who was always present when I needed and also for neutron diffraction experiments. I also would like to thank Murat Acar, Burak Toparli, Asim Zeybek and David Githinji for their great friendship during this project. I should also thank all my colleagues, post docs (especially Dr. Imran Bhamji) and staff in my department for their helpful discussions and advice.

My deepest and sincere regards to my parents, brothers and sisters in France and Mali for their love and constant encouragement during this project.

I leave my final word of thanks to my wife Kancou and my son Oumar for their continuous support, encouragement and love. This thesis is dedicated to them.

Yéli Traoré

August 2013

Preface

This thesis is submitted for the degree of Doctor of Philosophy of The Open University, United Kingdom. The work described in this thesis was carried out in the Department of the Materials Engineering, Faculty of Mathematics, Computing and Technology, between November 2009 and August 2013 under the supervision of Prof. Peter John Bouchard, Dr. Foroogh Hosseinzadeh, Prof. Michael Edwards Fitzpatrick and Alain Lodini.

Except where clearly referenced, the work is entirely the author's own work. None of this work has been submitted for a degree or qualification at this or other university. Some of the results of this work have been published in an academic journal, conference proceedings and as oral or poster presentations as listed below:

1. **Traoré Y,** Paddea S, Bouchard PJ, Gharghouri MA (2012) Measurement of the Residual Stress Tensor in a Compact Tension Weld Specimen. Experimental Mechanics: 1-14
2. **Traoré Y,** Bouchard PJ, Francis, JA and Hosseinzadeh F (2011) A Novel Cutting Strategy for Reducing Plasticity Induced Errors in Residual Stress Measurements made with the Contour Method, ASME PVP Conference, PVP2011-57509, Baltimore, USA
3. Paddea S, **Traoré Y,** Gharghouri M, Bouchard PJ (2011) Measurement of the Full Residual Stress Tensor in a Welded Compact Tension Test Specimen by Neutron Diffraction, MECA SENS VI, Poster Presentation, Hamburg, Germany
4. **Traoré Y,** Bouchard PJ, Hosseinzadeh F, Fitzpatrick ME, Lodini A (2012) *Steps towards best practice II: Controlling Stress Relaxation*, Contour Method Seminar, Milton Keynes, United Kingdom

List of Notations/Abbreviations

Roman Notations

Symbol	Definition
a	Crack length
d	Lattice spacing for a stressed crystal
d_0	Lattice spacing for an unstressed crystal
Δd	Change in the lattice spacing of a crystal
E	Young's modulus
E'	Generalised Young's modulus
F	External load
$f(a/W)$	Factor of finite width and crack type correction
h	Weight function
$\{hkl\}$	Miller indices defining a family of crystallographic plane
K	Global stiffness matrix
K_I	Mode I stress intensity factor
K_{IC}	Fracture toughness
K_I^i	Mode I stress intensity factor at a the measurement point i
L	Length; cut length
l	final gauge length
l_0	Initial gauge length
Δl	Gauge length variation
n	Integer
n_x	Unit surface normal vector

$\overline{PZD}_{Norm}$	Normalised average plastic zone depth
$\overline{PZS}_{Norm}$	Normalised average plastic zone size
r,θ	Polar coordinate system
r_y	Plastic zone size
T	Specimen thickness
t	Thickness over which the residual stresses are averaged
T_x	Normal traction
T_y	Transverse traction
W	Width
x, y, z	Cartesian coordinate system
Z	Influence function

Greek Notations

Symbol	Definition
$\sigma_x, \sigma_{xx}, \sigma_y, \sigma_{yy}, \sigma_z, \sigma_{zz}$	Normal stress tensors
$\tau_{xy}, \tau_{yz}, \tau_{zx}$	Shear stress tensors
σ_0	Yield strength
σ_{UTS}	Ultimate tensile strength
σ_{Ymax}	Maximum stress at the tip of a blunt cut
σ	Applied stress
ν	Poisson's ratio
λ	Wavelength
δ_{ij}	Chronecker delta
$\Delta\sigma$	Absolute stress error

$\delta\sigma(j)$	Standard deviation stress error for a smoothing spline j
$\sigma(i, j)$	Stress at node i for a smoothing spline j
σ_i	Measured stress at a measurement point i
$\bar{\sigma}_{Error}^{Absolute}$	Average absolute stress error
$\bar{\sigma}_{Error}^{RMS}$	Average RMS stress error
θ	Angle
2θ	Angle between incident and diffracted beam an stressed material
ε	Strain
ε_{ij}	Strain defined by the direction i and j
ρ	Blunt crack radius

Abbreviations

Abbreviation	Definition
2D	Two dimensional
3D	Three dimensional
BC	Boundary condition
CM	Contour method
CMM	Co-ordinate measuring machine
CT	Compact tension
EB	Electron beam
EDM	Electric discharge machining
EPFM	Elastic plastic fracture mechanics
FE	Finite element
FEM	Finite element method

LEFM	Linear elastic fracture mechanics
HAZ	Heat affected zone
MMA	Manual metal arc
ND	Neutron diffraction
PEEQ	Equivalent plastic strain
PZD	Plastic zone depth
PZS	Plastic zone size
RMS	Root mean square
RS	Residual stress
SIF	Stress intensity factor
TOF	Time of flight

Table of Contents

List of Figures

List of Tables

Chapter I: Introduction

Residual stresses are stresses that are self-equilibrated and present within material free from any external load, constraint and temperature gradient. Residual stresses are introduced through different manufacturing processes such as casting, welding, machining, cold expansion, heat treatment or forging. When uncontrolled, these stresses can have negative effects on materials' properties (*e.g.* fatigue life, creep and corrosion resistance) and in some cases can lead to catastrophic failures [1-3]. Reliable knowledge of residual stresses is required for accurate assessment of the engineering significance of residual stresses that remain in structures [4,5], for example where public safety, component life or economic viability is jeopardised. Moreover, control of residual stresses is of increasing importance in advanced manufacturing processes such as high energy narrow gap welding [6] and "near net shape" technologies [7].

Residual stresses can be determined from different sources including analytical and numerical predictions [8-11]. However, for safety critical applications, analytical and numerical predictions need to be experimentally validated.

The current techniques of residual stress measurement fall under two major groups: non-destructive and destructive methods. The non-destructive techniques include diffraction methods, ultrasonic methods, piezo-electric technique, magnetic methods and Raman spectroscopy [12]. The most frequently used destructive techniques include surface centre hole-drilling, deep hole-drilling, the ring core method, the Sachs method [13], the slitting method, the sectioning method [14] and the curvature method [12]. Details of some of these methods are given in Chapter 2.

A relatively recent destructive technique for residual stress measurement, the contour method, has been invented by Prime [15]. The method involves sectioning the body containing residual stress into two halves by wire electro-discharge machining (Wire EDM), which causes components of the residual stress tensor originally in the body in the vicinity of the cut to relax. The distorted shapes (the contours) of the newly cut faces are measured and then the displacement data applied as a boundary condition in a finite element mechanical analysis of one of the cut halves in order to back-calculate the component of residual stress normal to the cut surface that was originally present.

The new destructive technique has emerged as an effective tool for generating two-dimensional maps of residual stresses normal to the cut plane in relatively thick components using a direct calculation, while most destructive methods such as hole drilling and deep hole-drilling require elastic inversion calculations to determine the residual stresses and only one-dimensional stress profiles are obtained. Furthermore the contour method has been recently extended to measure multiple stress tensor components [16,17].

Other measurement techniques enabling multiple stress component measurement and two-dimensional mapping of residual stresses (*e.g.* neutron and synchrotron diffraction) have several limitations. Radiation sources with sufficient flux to penetrate engineering metallic components are based at national or international facilities; these usually have to be accessed on a research basis via peer review mechanisms as commercial purchase of beamtime can be prohibitively expensive. The thickness of metallic components that can be probed by neutrons or synchrotrons is limited to a few centimetres. Diffraction experiments are also very sensitive to microstructure gradients, which are always present at weldments. In contrast the contour method is relatively simple, cheap, can be

conducted with widely available equipment and is not affected by microstructure gradients, which makes it ideally suited for measurements of residual stress in welded components.

Although the contour method has all of the above-mentioned advantages, it still needs further investigation to overcome some potential sources of error and uncertainties.

This is due to the fact that the theory of the contour method, like most measurement techniques, involves some assumptions which are not strictly accurate in practice. For example, it assumes that the stress relaxation process during test specimen cutting is purely elastic, that is no plasticity occurs. If any plasticity is introduced during the stress relaxation process then this can compromise the accuracy of contour method measurements. This thesis focuses on understanding and controlling plasticity related errors in contour residual stress measurements with a view to improving the accuracy and reliability of the method.

1.1. Research aims

The contour method, like most mechanical strain relief residual stress measurement techniques, is prone to errors due to plasticity. This is especially the case when dealing with the measurement of residual stresses having a magnitude of the same order of the material yield stress.

A limited number of studies have been conducted on this subject using the finite element method [18-20], where it has been reported that "secure clamping" close to the cut line can reduce the effects of plasticity. However, "secure clamping" (rigid restraint in a finite

element model) is not achievable in practice, and therefore the issue of plasticity remains a concern in contour method measurement of residual stress.

The main objectives of this research are as follows:

- ✓ Investigate and understand the origins of plasticity in contour method residual stress measurements;
- ✓ Investigate the effect of restraint on plasticity-induced errors in the contour method;
- ✓ Develop strategies that mitigate the occurrence of plasticity during stress relaxation associated with cutting the test specimen;
- ✓ Develop approaches to estimate the level of error in residual stress measurement that can be introduced by plasticity;
- ✓ Develop a procedure (good practice guidelines) for mitigating plasticity induced errors in residual stress measurements made with the contour method.

1.2. Research methodology

To investigate the effect of plasticity-induced errors in residual stress measurements made with the contour method, the basic theory of plasticity is first reviewed to understand the conditions leading to non-linear material behaviour. Then, an analogy is made between the stress relaxation during the cutting process in the contour method and a cracked plate subjected to an internal stress distribution acting on the crack surfaces. The nature of the crack tip stress distribution in linear elastic fracture mechanics and associated small scale plastic zone (size and shape) is examined in detail.

Methodologies are developed to simulate by the finite element method the entire contour method process (cutting and stress back calculation). This allows the stress error

introduced to be quantified and the effects of test component restraint in contour method measurements to be assessed. Different cutting/restraining configurations based on the control of the cut tip stress concentration (characterised by the mode I stress intensity factor) are analysed in order to mitigate plasticity-induced errors in the residual stress measurements made with the contour method. Correlations for estimating the plasticity-induced errors are developed using both finite element analysis and linear elastic fracture mechanics. Finally a procedure (good practice guidelines) for mitigating the plasticity-induced errors in the results of the contour method is proposed.

The research is supported by diverse residual stress measurements on the following components:

- ✓ A composite electron beam weld compact tension (CT) specimen for investigating the plasticity-induced errors associated with an unrestrained contour cut;
- ✓ Specially designed laser heated (autogenously welded) plates used to introduce controlled levels of plasticity during contour measurements and thereby validate correlations developed in the thesis for estimating plasticity-induced errors.
- ✓ An AISI Type 316L austenitic steel flat plate containing a three-pass finite length part-thickness slot weld which is used to study plasticity-induced errors in contour method and strategies for mitigating such errors.

1.3. Layout of the Thesis

The thesis presents research carried out on the investigation, minimisation and estimation of plasticity-induced errors in residual stress measurements made with the contour method. The layout of the thesis is as follows:

Chapter 2 reviews current literature available on general aspects of residual stress and focuses on the contour method of residual stress measurement. In the second part of the chapter, a brief introduction to the theory of plasticity is presented followed by a review of plasticity-induced error assessment approaches for some mechanical strain relief techniques, with particular emphasis on the contour method. As the cutting process associated with the contour method can be represented by a moving (blunt) crack, basics of linear elastic fracture mechanics and finite element method concepts are introduced. Furthermore, the different techniques used in previous published work to assess contour method plasticity by simulating the cutting process are reviewed.

The early part of Chapter 3 presents residual stress measurements carried out by the contour method on a welded CT specimen using unrestrained boundary conditions required for a slitting measurement. The results are compared with those obtained by neutron diffraction and slitting in order to assess the different types of error potentially present in the contour method results. In the latter part of the chapter, two-dimensional finite element analysis is carried to assess plasticity-induced errors associated with restrained and unrestrained boundary conditions.

In Chapter 4, an analogy is made between relaxation of residual stress in a body during cutting and a cracked plate where normal tractions are applied to the crack surfaces. This superposition fracture mechanics analogy is used to assess the merits of different cutting/restraining strategies with respect to mitigating plasticity-induced errors in contour measurements. In particular a novel cutting strategy starting inside the body (i.e. creating an embedded cut) is developed and assessed.

Chapter 5 deals with finite element simulation of the contour cutting process which can be sensitive to the mesh type/size cut width and cut tip shape. The second part of the chapter concentrates on the development of correlations for estimating plasticity–induced errors in the contour method based on fracture mechanics and the finite element method.

Chapter 6 presents experimental validation of the proposed correlations for estimating plasticity-induced errors in contour method measurements using specially designed laser heated (autogenously welded) test plates.

Chapter 7 provides guidelines for optimising the cutting strategy and restraint (specimen holding) conditions in order to minimise or entirely mitigate plasticity-induced errors in contour method measurements. A case study, where the different steps of the guidelines are applied, is presented in the latter part of the chapter.

Finally in Chapter 8, overall conclusions are drawn together and suggestions made for future work.

1.4. References

1. Bouchard PJ (2001) Residual stresses in lifing and structural integrity assessment. In: Buschow KHJ (ed) Encyclopaedia of Materials Science and Technology Pergamon, Oxford,

2. Bouchard PJ (2007) Validated residual stress profiles for fracture assessments of stainless steel pipe girth welds. International Journal of Pressure Vessels and Piping 84 (4):195-222

3. Withers PJ (2007) Residual stress and its role in failure. Reports on Progress in Physics 70 (12):2211

4. British Standard - BS 7910 (2005) Guide to methods for assessing the acceptability of flaws in metallic structures.

5. Central Electricity Generating Board (1982) Assessment of the Integrity of Structures Containing Defects: Validation. Supplement 1. CEGB Research Division,

6. Jonsson M, Josefson BL, Näsström M (1993) Experimentally Determined Deformations and Stresses in Narrow-Gap and Single-U Multi-Pass Butt-Welded Pipes. Journal of Offshore Mechanics and Arctic Engineering 115 (2):116-122

7. Fogarassy P, Manescu A, Markocsan N, Rustichelli A (2004) Residual Stress Analysis in Near Net-shape Formed Specimens Obtained by Thermal Spraying. Physica B: Physics of Condensed Matter 350 (1):E537-E539

8. EDF Energy (2013) R-Code.V4.4. http://www.r-desk.co.uk/software. Accessed 24 February 2013

9. ABAQUS (2010) ABAQUS/Standard Documentation Version 6.10.2. ABAQUS, Inc

10. Ogawa K, Chidwick LO, Kingston EJ, Dennis R, Bray D, Yanagida N (2008) The Measurement and Modelling of Residual Stresses in a Stainless Steel Pipe Girth Weld / PVP2008-61542. Paper presented at the ASME Pressure Vessels and Piping Division Conference, Chicago, USA,

11. Free JA, Porter Goff RFD (1989) Predicting residual stresses in multi-pass weldments with the finite element method. Computers & Structures 32 (2):365-378

12. Withers P, Bhadeshia H (2001) Overview Residual Stress Part 1 - Measurement Techniques. Materials Sci Technol 17:355

13. Procter E, Beaney EM (1987) The trepan or ring core method, centre-hole method, Sach's method, blind hole methods, deep hole technique. Adv Surf Treat 4:166-198

14. Tebedge N, Alpsten G, Tall L (1973) Residual-stress measurement by the sectioning method. Experimental Mechanics 13 (2):88-96

15. Prime MB (2001) Cross-sectional mapping of residual stresses by measuring the surface contour after a cut, vol 123. American Society of Mechanical Engineers, New York, NY, ETATS-UNIS

16. DeWald A, Hill M (2006) Multi-Axial Contour Method for Mapping Residual Stresses in Continuously Processed Bodies. Experimental Mechanics 46 (4):473-490

17. Pagliaro P, Prime M, Swenson H, Zuccarello B (2009) Measuring Multiple Residual-Stress Components using the Contour Method and Multiple Cuts. Experimental Mechanics 50 (2):187-194

18. Shin S (2005) FEM analysis of plasticity-induced error on measurement of welding residual stress by the contour method. Journal of Mechanical Science and Technology 19 (10):1885-1890

19. Dennis RJ, Leggatt NA, Kutarski EA (2009) Investigation of the Performance of the Contour Residual Stress Measurement Method When Applied to Welded Pipe Structures / PVP2009-77470. Paper presented at the ASME Pressure Vessels and Piping Division Conference, Prague, Czech Republic,

20. Dennis RJ, Bray DP, Leggatt NA, Turski M (2008) Assessment of the Influence of Plasticity and Constraint on Measured Residual Stresses Using the Contour Method / PVP2008-61490. Paper presented at the ASME Pressure Vessels and Piping Division Conference, Chicago, USA,

Chapter 2: Literature review

The main objectives of this research are to investigate and understand the origins of plasticity in contour measurements, to estimate the level of error in residual stress measurement that can be introduced by plasticity and to develop plasticity mitigation strategies.

Residual stresses are inevitably introduced during the manufacturing of engineering structures, and they are believed to have a significant impact on the performance and life of structures. Therefore, accurate knowledge of residual stresses is essential for reliable integrity assessment of engineering structures [1-3].

The early part of this chapter concentrates on residual stresses, including their general aspects, origin, types and some measurement techniques. The theory and experimental implementation of the contour method of residual stress measurement is covered in detail as it is the primary focus of this thesis. Different sources of error in contour method measurement are discussed. Elements of the theory of plasticity along with a review of plasticity-induced errors in the contour method and some other mechanical strain relief techniques are also covered.

The latter part of the chapter reviews different techniques that can be used to simulate the contour method cutting process and assess errors in the results introduced by plasticity associated with the cutting. As the cutting process associated with the contour method can be represented by a moving (blunt) crack, basic linear elastic fracture mechanics and finite element method concepts are introduced.

2.1. General aspects of residual stresses

In general, failure in engineering structures is avoided by careful design and by applying inspection processes. Structural design and safe-life assessment [4] are mainly based on conventional strength of materials (Figure 2-1-a) and fracture mechanics approaches respectively (Figure 2-1-b).

For both approaches the loading conditions and materials properties are undoubtedly the most critical factors. When in service, materials experience different types of loading conditions including external loads (*e.g.* pressure) and heat gradients. Such loads can be easily determined by measurement, or more usually from predictions. However, for safe-life assessment, residual stresses must be taken into account as they can be detrimental to structural integrity [1-3].

Residual stresses can increase or decrease the loading conditions of a structure or structural components in-service; depending on the magnitude and sign of residual stresses (*i.e.* compressive or tensile stresses). Therefore, residual stresses are either beneficial or detrimental to the performance of a material or the life of a component [5]. For example, tensile residual stresses, often unintentionally introduced by welding processes, superimposed with tensile loading can lead to unexpected or premature failure of a material; while compressive residual stress combined with structural loads improve its service life.

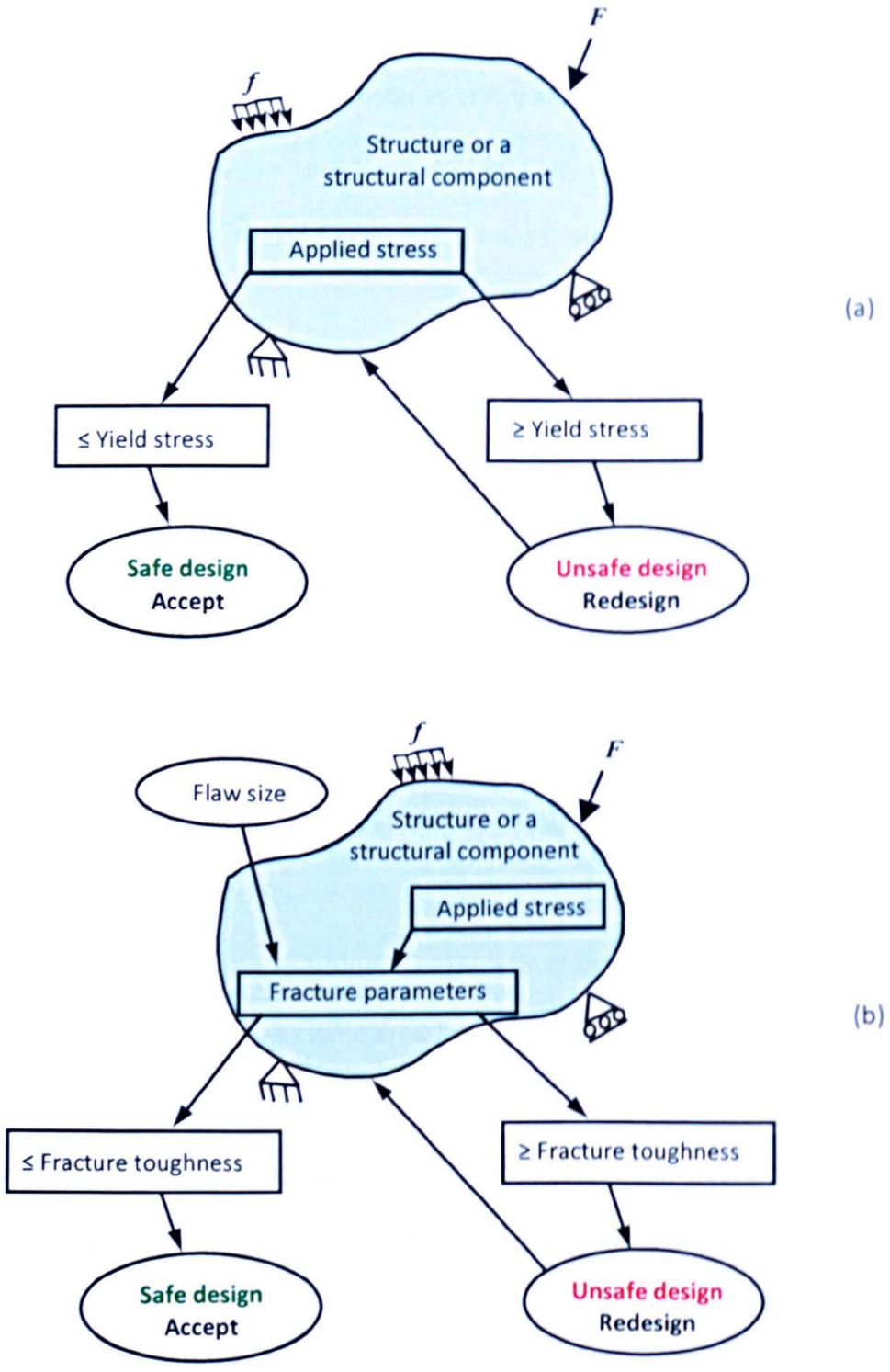

Figure 2-1: Schematic diagram showing structure design based on the strength of materials (a) and safe-life assessment based on linear elastic fracture mechanics (b) approaches (excluding consideration of margins of safety).

Residual stresses within components can be determined in different ways including from measurement data, analytical solutions [6-8] and numerical methods [9-11]. However, in contrast to external loads, residual stresses are difficult to predict. Therefore, for safety critical applications, reliable measurement techniques are required for determining or confirming these stresses. In the following section the origin and types of residual stress are described followed by a review of residual stress measurement techniques with a particular focus on the contour method.

2.2. Origin and types of residual stresses

Residual stresses are usually caused by a 'misfit' in materials [12,13]. Plastic deformations that the material experiences during manufacturing or when in service are the most common sources of this 'misfit' [14]. Figure 2-2 illustrates different 'misfits' and corresponding residual stresses that are introduced by different processes.

The processes that generate residual stresses can be divided into three major groups:

- ✓ Mechanical processes: machining, drawing, extruding, shot peening, forging, and bending;
- ✓ Thermal processes: casting, welding, heat treatment;
- ✓ Chemical processes: nitriding and carbonitriding of steels.

In this thesis, residual stresses generated by different welding processes (manual metal arc, electron beam and laser welding) are studied.

In general residual stresses are classified according to the length over which they self-equilibrate [15]. On this basis, three different types of residual stresses are noticeable: first-order, second-order and third-order stresses (Figure 2-3).

First-order stresses, known as macro-stresses, can be introduced from machining and secondary processing such as welding and heat treatment. These stresses equilibrate over the length-scale of the sample geometry. Second-order stresses arise as a consequence of inhomogeneity in the microstructure of material [16]. They are balanced over dimensions corresponding to only a few grains. Third-order stresses exist over atomic dimensions and are equilibrated within a grain. Dislocations and other crystalline defects are essentially the cause of this order of stress [16]. Second and third-order stresses are often referred to as micro-stresses.

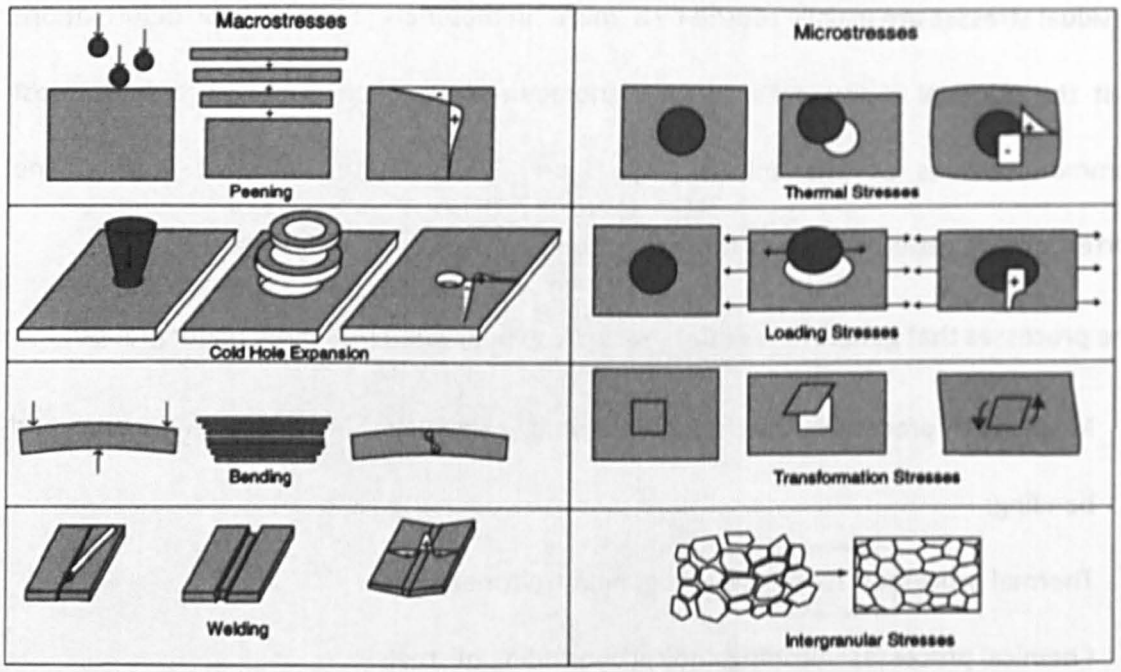

Figure 2-2: Misfits that cause macro and micro scale residual stresses. For each case the process that causes the residual stresses (on the left), the misfit (in the centre) and the resulting stress (on the right) are shown [14].

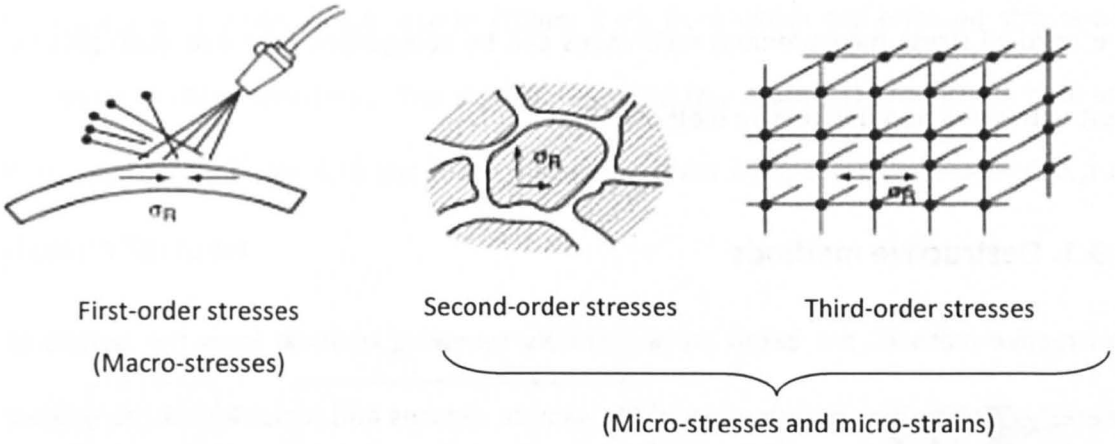

Figure 2-3: The three types of residual stresses: first-order stresses (equilibrate over the specimen), the second-order stresses (equilibrate over a few grains), and the third-order stresses (equilibrate over a single grain) [17].

Relaxation methods, like the contour method, measure the total stress. In principle, that is the sum of first, second and third-order stresses. However, the contour method is generally applied to macro-scale samples, containing many grains, causing the measured stresses to be averaged over large areas or volumes. Second and third-order stresses therefore average to zero over those length scales [18], and only first order stresses are in fact measured. Since this project is mainly focused on the contour method, throughout this report any discussion on residual stress refers to first-order macro-stresses.

2.3. Current techniques of measuring residual stresses

There is a wide range of methods available to measure residual stresses in engineering components [12,19]. Current measurement techniques of residual stresses can be classified based on the depth probed, the spatial resolution, the cost, the number of stress components they can measure and the state of the sample after measurement. In the present thesis the state of the sample after measurement is considered. On this basis

the residual stress measurement techniques can be categorised into two main groups: destructive and non-destructive methods [12,16,20].

2.3.1. Destructive methods

Destructive methods are based on deliberately removing material from the sample of interest. The resulting deformation of the sample reduces and redistributes the original residual stresses in the sample. The distortion of the component is monitored and used to reconstruct the original state of residual stresses using either numerical or analytical methods [19]. All destructive techniques are based on the assumption that the removal of material results in entirely elastic redistribution of the internal stresses [19]. As the categorisation name implies, the test sample can be either semi or fully destroyed and in some cases no further residual stress measurement can be undertaken.

In the remainder of this section the destructive methods commonly used for residual stress measurement are presented including surface centre hole-drilling, deep hole-drilling and slitting methods. Since the slitting method is used for residual stress measurement in Chapter 3 more details are given about its experimental and data analysis procedures. The contour method, a relatively new destructive technique, is described in detail in section 2-4.

Incremental centre hole-drilling

The incremental centre hole-drilling method [21] is perhaps the most commonly used material removal residual stress measurement technique. The measurement procedure is relatively simple and has been standardised in ASTM Standard Test Method E837 [22]. Its general principle comprises drilling incrementally a small hole within the component at

the centre of a strain gauge rosette (Figure 2-4), from which the released strains are measured in three directions. The strains measured (ε_1, ε_2 and ε_3) around the hole are then used to back-calculate the bi-axial residual stress components (σ_x, σ_y and σ_{xy}) as shown in Figure 2-4.

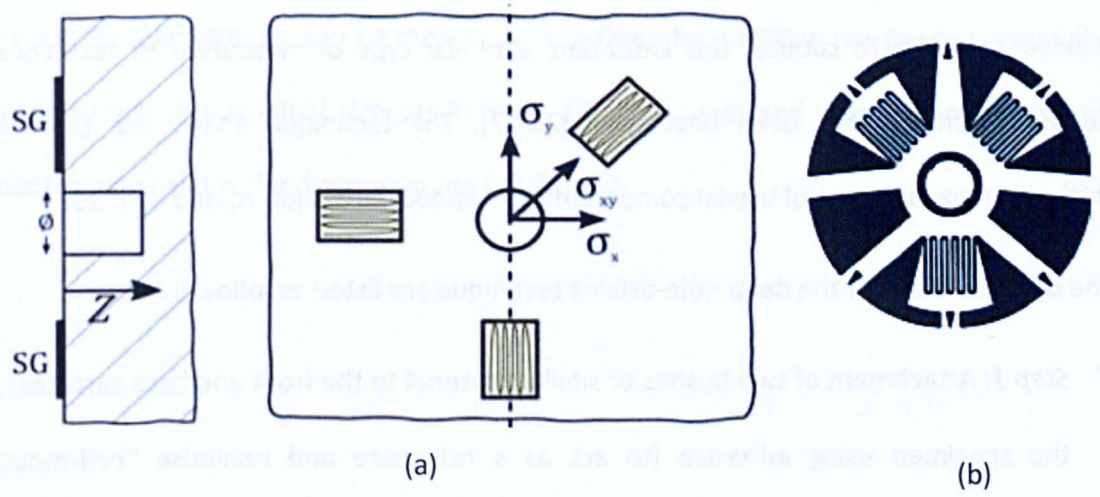

Figure 2-4: Schematic representation of the hole-drilling technique (a) [23] and typical strain gauge (SG) rosette used in hole drilling (b) [24].

One of the advantages of the incremental surface hole-drilling method is its versatility as it can be used for laboratory or 'on-site' residual stress measurements. Furthermore, the hole-drilling method can be applied to a wide range of materials, including metallic and non-metallic materials, to measure bi-axial stress components and is not affected by the material microstructure (*i.e.* grain structure and texture) [23].

Despite all these advantages, the hole-drilling method is still limited for residual stress measurement in complex shapes and in terms of measurement depth [12]. Like most mechanical strain relief techniques for residual stress measurements, the hole-drilling

method is also affected by plasticity when measuring residual stresses close to the material yield stress [25].

Deep hole-drilling

As mentioned above the centre hole-drilling is only capable of measuring near surface residual stresses. To counter this limitation, a similar type of measurement technique, deep hole-drilling, has been developed [26,27]. The technique allows the through-thickness measurement of biaxial components of residual stress (σ_x, σ_y and σ_{xy}) [23].

The different steps of the deep hole-drilling technique are listed as follows:

- ✓ *Step 1:* Attachment of two bushes of similar material to the front and back surfaces of the specimen using adhesive (to act as a reference and minimise "bell-mouth effects").
- ✓ *Step 2:* Drilling a high fidelity reference hole through the bushes and the component using a gun drill.
- ✓ *Step 3:* Measurement of the diameter of the reference hole at various angles through the thickness using an air probe;
- ✓ *Step 4:* Removing by trepanning a core of material, coaxial to the reference hole using electro-discharge machining. The front and back bushes are not trepanned;
- ✓ *Step 5:* Re-measurement of the diameter of the reference hole after trepanning. The changes in reference hole diameter are used to calculate the residual stresses in the plane normal to the reference hole axis using simple models based on the theory of elasticity.

Figure 2-5 shows a schematic of the different steps of the deep hole-drilling residual stress measurement technique. As for the centre hole-drilling method, deep hole-drilling can be used for residual stress measurements within a wide range of metallic and non-metallic materials and the technique is not sensitive to material microstructure. However, deep-hole drilling is limited in terms of the minimum thickness of components in which residual stresses can be measured [27]. Deep hole-drilling has been successfully applied to measure residual stresses in many different types and shapes of components including pipes and welded components [28,29].

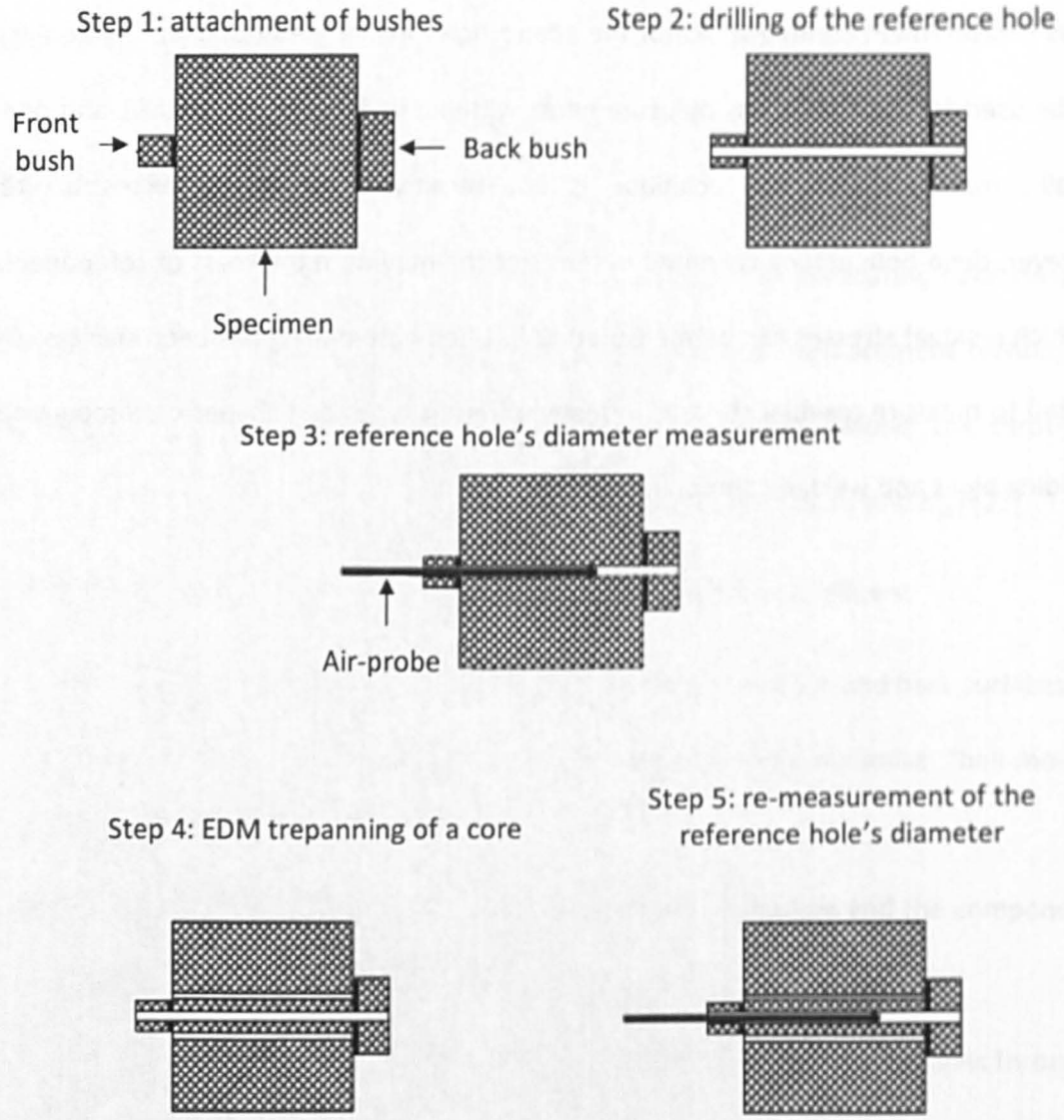

Figure 2-5: Schematic of the different steps of deep hole-drilling [26].

Slitting method

The slitting method [30,31] consists of introducing incrementally a narrow slot into a body that relaxes residual stresses at the cut surfaces and redistributes the residual stress field within the entire body. The cutting process is conducted using wire EDM. The change in strain induced by the release of residual stresses over the entire thickness is measured as a function of the cut depth at carefully chosen locations using strain gauges attached on

top and bottom surfaces (Figure 2-6). The top face strain gauges are only used for near surface stress measurements (first few increments). The strains recorded from the back strain gauges are more important. That is because they enable residual stress determination in the bulk of the test specimen.

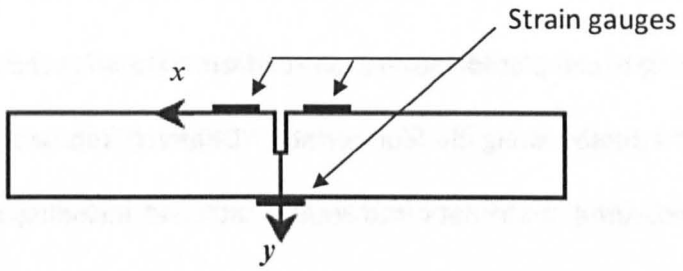

Figure 2-6: Slitting method: The slot is incrementally cut, the top strains gauges are placed close to the slot and the centre of the back strain gauge is located at the centre-line of the slot.

Experimental procedure

The slitting method experimental procedure [23,32,33] consists of carefully attaching strain gauges on the front and back faces of the sample and conducting incremental wire EDM cutting. As illustrated in Figure 2-6, two strain gauges (or one) can be glued on the top surface and one on the back face after cleaning the corresponding gauge locations. The centre of the back strain gauge is positioned at the centre-line of the slot. The top face strain gauges are placed close to the slot. The strain gauges are connected to the strain reader through lead wires. Since the entire test specimen is submerged into water during the wire EDM process, waterproof strain gauge systems are required.

Following strain gauge attachment, a series of increment cuts are made. For each cut increment the wire EDM is stopped and strains are read from the different strain gauges before completing the next cut increment.

Data analysis

Once the cutting is completed the measured strain data are used to back calculate the distribution of stresses along the cut surface. Different approaches can be applied to convert the measured strain data into residual stresses including series expansion [34], truncated Legendre series, regularised Legendre series [35], regularised unit pulsed [35] and the fracture mechanics approach [20,33,34,36]. Since the latter approach is more relevant to this project, details are given.

Residual stress back calculation in the slitting method using the fracture mechanics approach consists of three different steps: influence function determination, residual stress intensity factor calculation and corresponding residual stresses determination [37]. The influence function [36] defines the sensitivity of the strain measurement point with regard to the stress released at the cut plane. It depends on the geometry of the test specimen studied and strain measurement location. Determination of the influence function is crucial and may require significant computational and analytical effort. However, for a given geometry and measurement location, the function needs to be determined once only. The influence function is calculated from Equation 2-1.

$$K_I = \frac{E'}{Z(a)} \frac{d\varepsilon}{da} \qquad \text{Eq. 2-1}$$

where E' is the material generalised elastic modulus ($E' = E$ for plane stress and $E' = E/(1-\nu^2)$ for plane strain), ε is the measured strain at the cut depth a, and Z is the influence function.

As it can be seen from Equation 2-1, in addition to the material elastic constants, the stress intensity factor and strain data for different cut increments are required to calculate the influence function. Two different approaches can be used to obtain the influence function: linear finite element analysis [32,38] or solutions from published literature [36]. However, published influence function solutions can only be applied for a limited range of test specimen designs, as they have to correspond to the particular sample geometry that is being studied. Conversely finite element analysis can be used to determine the exact influence function for a wide range of test specimen geometries.

In this thesis linear finite element analysis is used to calculate the stress intensity factor and strain data for different cut increments, which are then used for the influence function calculation. To determine the stress intensity factor and strain data for a given geometry and measurement location, the slitting incremental cut is simulated using a simple 2D finite element model of the test specimen. Only one half of the model representative of the specimen geometry is created by defining symmetry boundary conditions in the y-direction on the cut line (see Figure 2-7-b). As shown in Figure 2-7 nodal constraint in the x-direction is applied to avoid free movement of the model. The test specimen of interest is meshed with either plane stress or plane strain elements (depending on the test specimen geometry). Material elastic constants (Young's modulus and Poisson's ratio) are defined. Finally the slit extension is simulated by incrementally releasing the symmetry boundary conditions and simultaneously loading the model with a uniform tensile stress on the free edge parallel to the cut line as shown in Figure 2-7-c.

The magnitude of the applied tensile stress does not affect the determined influence function [36]. For each cut increment, stress intensity factor and nodal displacements in the y-direction (corresponding to the different gauges' locations) are extracted from a linear elastic mechanical finite element (FE) simulation. The nodal displacements are then used to manually calculate the strain for each cut increment using the conventional strain calculation expression (see Equation 2-2). Finally, the determined strains and stress intensity factor data are used to calculate the influence function by an elastic inversion process of Equation 2-1.

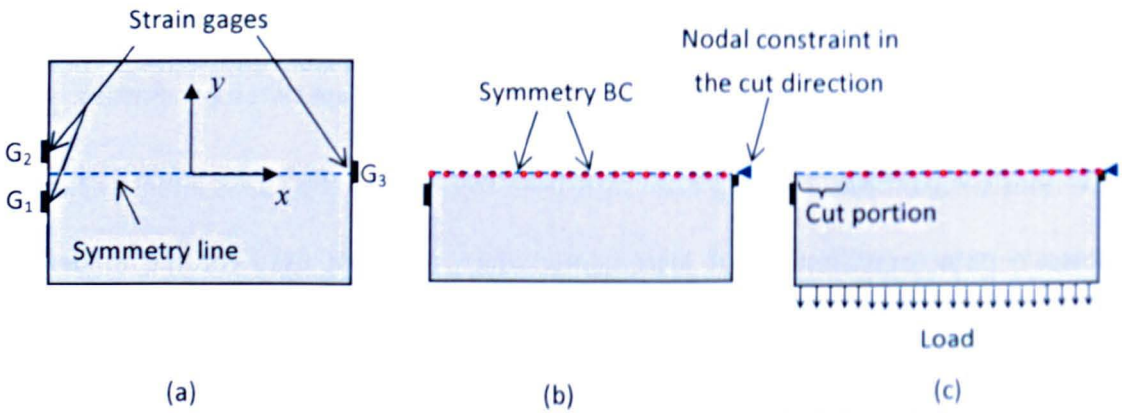

Figure 2-7: Schematic of the test sample used in FE analysis for stress intensity factor and strain gauges (G_1, G_2 and G_3) displacement calculations. The schematic shows the symmetry line (a), the symmetry boundary conditions (BC) and nodal constraint (b) and the cut portion and the load applied on the free edge parallel to the cut line (c).

$$\varepsilon = \frac{l - l_0}{l_0} \qquad \text{Eq. 2-2}$$

where l_0 is the strain gauge initial length and l is the deformed strain gauge length.

The next step is to calculate the stress intensity factor distribution using the determined influence function, the measured strain data from the different gauges and Equation 2-1. Note that Equation 2-1 is applied twice; first for determining the influence function (using strain and SIF data obtained from FE) and secondly for calculating the stress intensity factor distribution (using the determined influence function and measured strain data).

The calculated stress intensity factor data are then used for determining the residual stress distribution using an elastic inversion process, Equation 2-3.

$$K\ a\ =\ \int_0^a h\ x\ a\ \sigma_{rx}\ dx \qquad \textbf{Eq. 2-3}$$

where $h(x, a)$ is the weight function and σ_{rx} is the residual stress to be determined.

As indicated a weight function, $h(x, a)$, is required for residual stress calculation; for common shapes this function is available from the open literature [39]. Equation 2-4 gives the weight function for a single edge crack within a finite width rectangular plate.

$$h(x,a)=\sqrt{\frac{2}{\pi a}}\cdot\frac{1}{\sqrt{1-x/a}}\left(1+\frac{1}{(1-a/W)^{1.5}}\sum_{\eta,\lambda}A_{\eta,\lambda}(a/W)^{\lambda}\times(1-x/a)^{\lambda+1}\right) \qquad \textbf{Eq. 2-4}$$

Advantages and disadvantages of slitting method

One of the advantages of the slitting method is that it measures the stress intensity factor distribution directly and then uses well-known linear elastic fracture mechanics expressions to back calculate the residual stress distribution.

However, the slitting method allows determination of only one stress component perpendicular to the cut face. Furthermore, the strains recorded from the different

gauges are due to the release of residual stresses across the entire thickness. Therefore, any stress gradient over the sample thickness is not captured. Finally, as most mechanical strain relief techniques, the level of uncertainty in the measurements can increase with the residual stress magnitude because of plasticity effects [25].

2.3.2. Non-destructive methods

Non-destructive techniques rely on the fact that some properties of the material are related to stress. They use different forms of probe such as X-rays, neutrons, synchrotron X-rays (diffraction methods), ultrasonic waves (ultrasonic methods), or magnetism (magnetic methods) for residual stress measurement [19]. In this thesis only the neutron diffraction method is described as it is used for residual stress measurement for validating the different findings throughout this project.

Neutron diffraction

Diffraction techniques, including neutron diffraction [14,40], are based upon Bragg's law (Equation 2-5, Figure 2-8) [14,19], which relates the atomic lattice spacing for crystallographic planes (lattice parameter, d_{hkl}) to a particular angle (Bragg scattering angle, θ_{hkl}), at which the peaks from these planes are observed.

The letters h, k, and l are Miller's indices and define the crystallographic planes [14,41]. For instance for the {311} crystallographic planes, Miller's indices are $h=3$, $k=1$ and $l=1$.

$$2d_{hkl}\sin\theta_{hkl} = n\lambda \qquad \textbf{Eq. 2-5}$$

where θ_{hkl} is the Bragg scattering angle, d_{hkl} is the atomic lattice spacing, λ is the radiation wavelength and n is an integer.

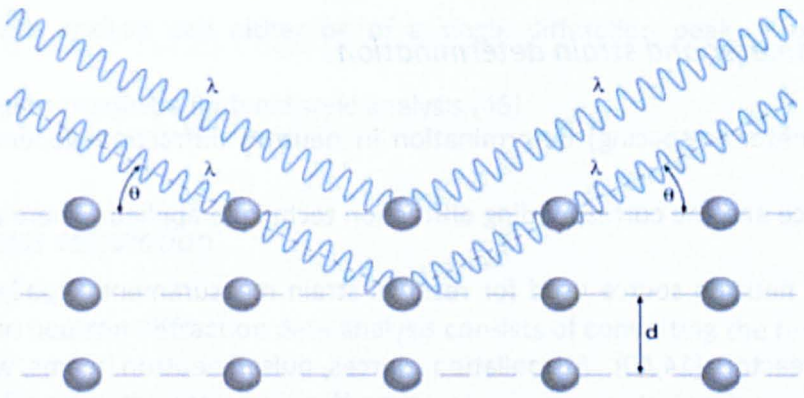

Figure 2-8: Illustration of Bragg's law for diffraction techniques [42].

Residual stress measurement by the neutron diffraction technique consists of the following steps: lattice parameter measurement for both stressed and stress free material and data analysis (diffraction peak fitting, strain and stress calculation).

Stress-free lattice parameter measurement

The stress-free lattice parameter, d_0, is one of the most important parameters in neutron diffraction residual strain measurement. A small change in the d_0 value can result in significant errors in measurements. Changes in material composition and inter-granular strains are examples of different factors which can affect the stress-free lattice parameter [43]. Therefore particular care should be taken for its determination.

Different techniques can be applied for obtaining an estimate of the stress-free lattice parameter [43,44] such as far-field (stress free) measurements, measurement on a stress free powder or fillings, cutting stress free-cubes or combs from the test specimen studied or by applying a force/moment balance approach. In this work "stress–free" cubes and far-field measurement are used for determining the stress-free lattice parameter.

Lattice parameter and strain determination

Lattice parameter (*d*-spacing) determination in neutron diffraction depends upon the neutron source and the corresponding diffraction technique applied. There are currently two types of neutron source used for residual strain measurements: spallation sources and nuclear reactors [14,40]. At spallation sources, pulsed neutron beams, with different wavelengths (*i.e.* energy) are produced for residual strain measurements while a continuous monochromatic beam (*i.e.* single wavelength) is generated by fission at reactor sources to conduct residual strain measurements [14,41].

Two diffraction techniques are currently applied at different neutron diffraction facilities: monochromatic 2θ strain scanning and the time of flight technique [14]. Monochromatic 2θ strain scanning is usually employed at reactor sources. Residual stress in a sample causes a shift in the diffraction peak (in terms of diffraction angle) from a particular plane relative to that in a stress free sample. Residual stresses in the sample are therefore determined by analysing these shifts in diffraction peaks. Since the wavelength is constant (monochromatic beam), Equation 2-5 can be differentiated to Equation 2-6. This latter expression is then applied for strain calculation.

$$\varepsilon = \frac{\Delta d}{d_0} \qquad \text{Eq. 2-6}$$

where Δd is the change in lattice spacing and d_0 is the stress free lattice spacing.

When pulsed neutrons are used for residual strain measurement, the time of flight approach [14,45] is applied for the strains calculation. The measurement principle at a time-of-flight (TOF) source is fundamentally similar to that at a reactor, except that at a time-of-flight source, an entire diffraction spectrum is obtained in each measurement,

and hence data analysis can either be of a single diffraction peak or of the entire diffraction spectrum using a Rietveld style analysis [46].

Residual stress calculation

The last step in neutron diffraction data analysis consists of converting the residual strains into stresses by using the material's diffraction elastic constants (analogous to the bulk Young's modulus and Poisson ratio of isotropic materials) and by applying the classical Hooke's law (See Equation 2-7).

When single crystal elastic constants for the material are known, the crystallographic diffraction elastic constants can be determined, for example by applying the Kroner model [47] or by using the open source DECcalc software [48]. This open source is utilised in Chapter 3 and Chapter 6 to calculate the crystallographic elastic constants for neutron diffraction measurements carried out on a stainless steel compact tension specimen blank and on ferritic laser heated plates, respectively.

$$\sigma_{xx} = \frac{E}{(1+\nu)(1-2\nu)}[(1-\nu)\varepsilon_{xx} + \nu(\varepsilon_{yy} + \varepsilon_{zz})]$$

$$\sigma_{yy} = \frac{E}{(1+\nu)(1-2\nu)}[(1-\nu)\varepsilon_{yy} + \nu(\varepsilon_{xx} + \varepsilon_{zz})] \qquad \textbf{Eq. 2-7}$$

$$\sigma_{zz} = \frac{E}{(1+\nu)(1-2\nu)}[(1-\nu)\varepsilon_{zz} + \nu(\varepsilon_{xx} + \varepsilon_{yy})]$$

where σ_{xx} is the relevant stress direction and E and ν are the crystallographic Young's modulus and Poisson's ratio, respectively.

For pulsed sources, where several diffraction peaks from different crystallographic planes are used to calculate the lattice parameters, bulk values of Young's modulus and Poisson's ratio are utilised to calculate the residual stresses. In Chapter 6, bulk elastic constants are used for residual stress calculation in the laser heated plates.

Strengths and weaknesses of neutron diffraction

Neutron diffraction can measure elastic strains within relatively thick stressed samples (~ 50mm of steel) [49] allowing the complete stress tensor [38,50] to be determined. The method is attractive in that the test sample is not destroyed. Furthermore, the technique can be applied to a wide range of materials and to specimens with complex shapes.

However, it is sometimes difficult to gain access to facilities where neutron diffraction experiments can be conducted. It is also expensive to conduct experiments at neutron facilities relative to certain other residual stress measurement techniques. In addition, the stress free lattice parameters must be determined very carefully.

2.3.3. Summary of residual stress measurement techniques

There is a variety of techniques for measuring residual stress in engineering components. The choice of the technique depends on:

- ✓ Whether the sample can be destroyed or not;
- ✓ The required components of the residual stress tensor;
- ✓ The required spatial resolution;
- ✓ The availability of the technique;
- ✓ The depth of penetration;
- ✓ The clients' budget.

Overall, there is no one technique which can be applied to any specimen. Very often some of the requirements for a particular sample have to be compromised. All in all, development of new techniques, such as the contour method, that could unlock more information about the state of residual stress in a component is desirable.

2.4. The contour method

The contour method is a destructive technique for residual stress measurement that was invented in 2001 [51]. It is a powerful strain relief technique that can measure through-thickness residual stresses in engineering structures. In particular it is attractive in that it provides a 2D map of residual stress over a plane of interest.

The contour method has been successfully validated using well-known residual stress measurement techniques such as neutron diffraction [52,53], synchrotron X-ray diffraction [53,54], hole drilling [55], crack compliance [56] and sectioning [57].

In the following sections the theory of the contour method, the experimental procedure and the data analysis required are described in detail.

2.4.1. Theory of the contour method

The contour method is based on Buckner's elastic superposition principle which tells us that *"If a cracked body subject to external loading or prescribed displacements at the boundary has forces applied to the crack surfaces to close the crack together, these forces must be equivalent to the stress distribution in an uncracked body of the same geometry subject to the same external loading"* [58].

Illustration "A" in Figure 2-9 shows the original residual stress state in a stressed body. In step "B" the part is cut into two halves along a plane of interest, and this causes the cut faces to deform due to the stress relaxation. The resulting deformations normal to the cut faces are measured over each entire surface. The virtual stresses that would be required to force back the deformed surface to its uncut position are calculated in step "C", using linear elastic finite element calculations. This is achieved by applying the measured deformations in step "B" as boundary conditions to the linear finite element model. Because the deformations are small compared to the geometry of engineering components and the analysis is elastic, an undeformed finite element model of the cut part is built in the stress back-calculation step. The original residual stress distribution in step "A" is the superposition of the stress state in steps "B" and "C".

From Figure 2-9 it can be seen that the deformations in step "B" are not only due to the relaxation of stresses normal to the cut surfaces (σ_x). The in-plane shear stresses (τ_{xy} and τ_{xz}) also contribute to the deformation of the cut surface. Apart from these three stress components (σ_x, τ_{xy} and τ_{xz}), the remaining stress components on the cut plane, *i.e.* transverse stresses (σ_y, σ_z and τ_{yz}) will not affect the cut face deformations in the cut part [51,58].

The three stress components of the cut surface (*i.e.* σ_x, τ_{xy} and τ_{xz}) could be determined if the deformation in the corresponding directions are measured. However, in practice only the deformations normal to the cutting plane (*x* direction) can be measured; hence, only stresses acting normal to the plane of the cut (σ_{xx}) are measured by the contour method. The shear stress contributions (τ_{xy} and τ_{xz}) are removed by implementing an average of the displacements of the two cut faces. This process can be explained from the surface tractions equivalent notion as illustrated in Figure 2-10.

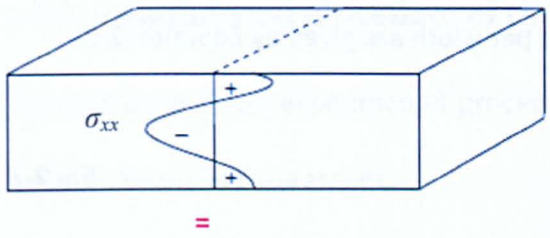

Step A: Original stresses to be measured (σ_{xx})

=

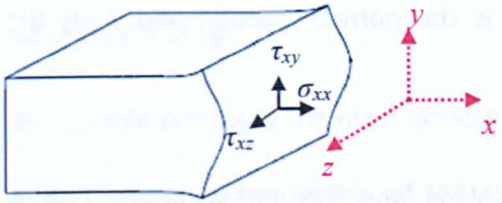

Step B: Part cut into 2 halves where the cut faces are deformed because of residual stress relaxation ($\sigma_{xx} = \tau_{xy} = \tau_{xz} = 0$).

+

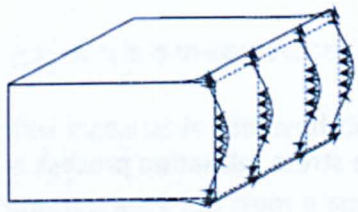

Step C: Cut faces forced back to the step A for residual stress calculation (σ_{xx})

σ_{xx} (A) = σ_{xx} (C), τ_{xz} (A) = τ_{xz} (C), τ_{xz} (A) = τ_{xz} (C)

Figure 2-9: Elastic superposition principle to calculate residual stress from the measured surface contours of cut faces [59].

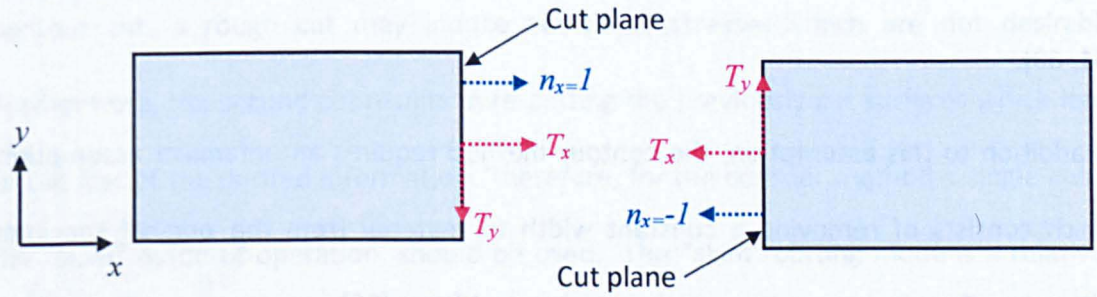

Figure 2-10: Surface tractions equivalent for releasing residual stress on the cut surface. T_x (for negative σ_{xx}) is symmetric about the cut plane and T_y (positive τ_{xy}) is anti-symmetric about the cut plane [51].

On the cut face the equivalent surface tractions per width are given by Equation 2-8.

$$T_x = -n_x\sigma_x; \quad T_y = -n_x\tau_{xy} \qquad \textbf{Eq. 2-8}$$

where n_x is the unit surface normal vector, T_x is the normal traction and T_y is the transverse traction.

It can be seen that T_x is symmetric about the cut plane, and T_y is anti-symmetric, which explains how the shear stresses contribution are cancelled out by averaging the data of the two cut faces.

The above-described superposition principle assumes that the stress relaxation process is purely elastic and that no additional stresses are introduced by the cutting process [51]. These assumptions are common to all stress relaxation methods [19].

Therefore, for the contour method a single cut, in the "skim" mode of operation, should be used. The "skim" cutting mode is a relatively low energy regime, which provides a low roughness surface finish, minimises the EDM affected layer and cutting induced stresses [51, 60].

In addition to this assumption, the contour method requires an unfamiliar assumption, which consists of removing a constant width of material from the original specimen without performing a re-cutting on the previous cut faces [59].

Any deviation from these two assumptions of the contour method results in errors in the measured stresses. Section 2-5 and 2-6 review the different sources of error that can arise during the cutting process of the contour method.

2.4.2. Experimental procedure of the contour method

The contour method experimental procedure consists of two steps: sample cutting and surface contour measurement.

Sample cutting

The sample cutting is the most critical step in the contour method as all the subsequent steps depend on the quality of the cut faces. Wire electric discharge machining (Wire EDM) is a cutting technique which best fulfils the requirements of contour method cut [51]. It is a non-contact technique that uses a fine, moving, and electrically charged wire. The material is removed due to the energy contained in discharge sparks. The wire is continuously fed from a spool held between upper and lower guides moving in the *X-Z* plane (Figure 2-11). The sample to be cut is submerged in deionised water, which minimises thermal effects and helps with flushing away cutting debris.

In conventional wire EDM, at least two cuts are usually performed to obtain the best surface finish: a rough cut followed by one or more skim cuts. However, when making a contour cut, a rough cut may induce additional stresses which are not desirable. Furthermore, the second cut results in re-cutting the previously cut surfaces which leads to the loss of the desired information. Therefore, for the contour method a single cut, in the "skim" mode of operation, should be used. The "skim" cutting mode is a relatively low energy regime, which provides a low roughness surface finish and also provides low stresses induced by the cutting process.

An additional requirement of the contour cutting process is to securely, and if possible, symmetrically clamp the sample [51]. Conversely in conventional wire EDM only one side

of the sample being cut is usually restrained. The aim of symmetric clamping is to prevent any movements of the sample during cutting and provide a constant cut width. Furthermore, it is advisable to clamp the sample on both sides as close as possible to the cutting plane [61].

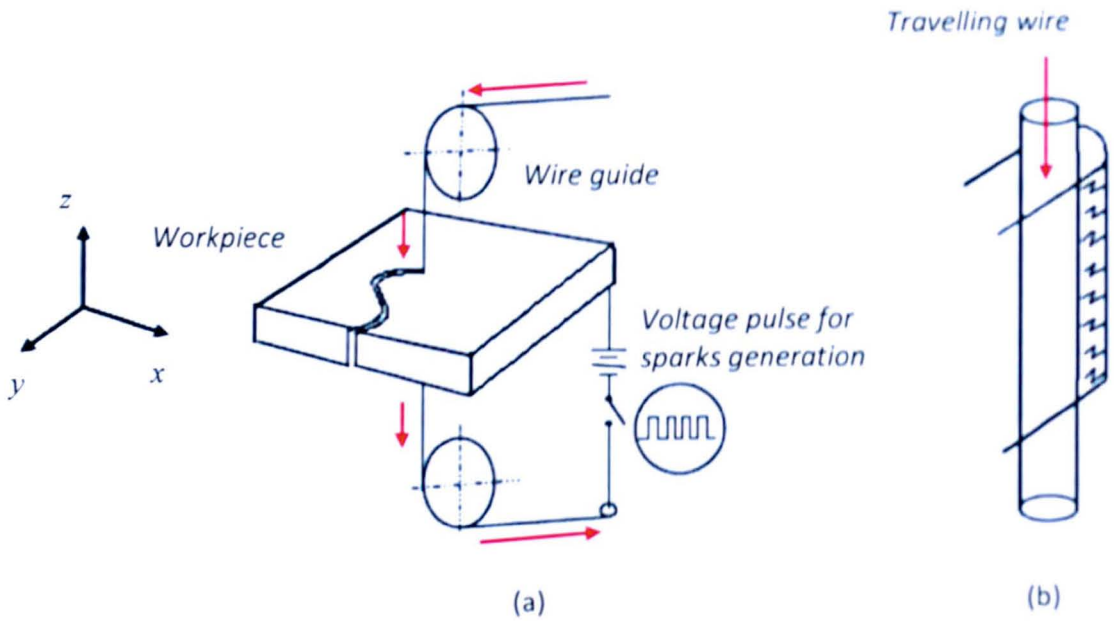

Figure 2-11: Schematic of wire electro-discharge machining process [62].

The contour measurement

Following sample cutting, the deformation contours of the newly cut faces are measured. The coordinate measuring machine (CMM) (Figure 2-12) is probably the most widely used system for measuring the cut face deformations in the contour method.

The CMM is a mechanical system designed for measuring a physical geometry. It comprises a workspace, where the two halves of the test sample are placed, a probing system used as a sensor for detecting the specimen surface, a movement mechanism to lead the probing system around the workspace, and a computer system and software to

program the machine and extract the required information. Other systems, for example based on laser probes [63], can also be used to measure surface deformation contours.

Figure 2-12: The Mitutoyo Crysta Plus 574 coordinate measurement machine [64]

There is a wide range of probing systems that can be integrated with a coordinate measuring machine (or to the mechanical structure used) such as touch trigger probes [65], scanning probes [66], triangular optical probes [63] and confocal sensors [63]. In this thesis the touch trigger system is used and therefore this system only is reviewed here.

Touch trigger probing system

The touch trigger probing system comprises the tip, the stem and the probe body (see Figure 2-13).

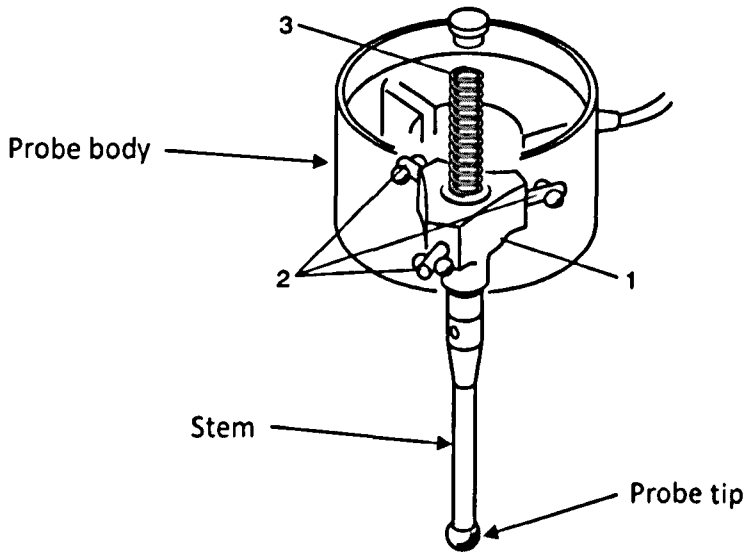

Figure 2-13: Kinematic location of Renishaw touch trigger probe showing the probe tip, the stem, the probe body, the pivotal plate (1), the three bearing points (2) and the helical spring (3) [67].

The probe tip is the component of the probing system that is in contact with the sample during the measurement. It is a sphere usually made of very hard material such as ruby, silicon nitride, zirconia, ceramic or tungsten carbide [68].

The stem is the long part that links the probe tip to the probe body. It can be made with a wide range of materials including steel, tungsten carbide, ceramic, carbon fibre, aluminium and titanium. The probe tip mounted on the stem is often referred to collectively as the stylus.

The probe body is the most complex part of the touch trigger system. Figure 2-13 shows the kinematic location of a Renishaw touch trigger probing system. The probe body consists of three bearing points supporting a pivotal plate which is maintained by a helical compression spring. The stylus is mounted on the pivotal plate. When the stylus is in contact with the workpiece, the helical spring goes into compression. After the contact is released, the stylus returns to its initial position.

Contour measurement

Before undertaking contour measurements, the cut parts are left in the CMM laboratory to attain thermal equilibrium. The thermal equilibrium during measurement is maintained by a thermal compensation system always in contact with the part being measured. A calibration process of the probing system is performed prior to measurement of the sample and if a collision occurs during the measurement. This is achieved by using the manufacturer's calibration master ball.

Surface deformation measurement for the contour method consists of three different steps: local coordinate system definition, contour perimeter measurement and surface deformation measurement.

The first step is manually achieved by the user and the other two (*i.e.* contour perimeter and surface deformation measurements) are automatically accomplished by the CMM.

The most important parameters for the contour perimeter and surface deformation measurements are the measurement spacings in the orthogonal directions across the surface.

During contour perimeter measurements, lateral intermittent contacts are made between the probe tip and the sample side faces (see Figure 2-14-b); while for the cut surface normal direction deformation measurement, intermittent contacts (by pushing the stylus up) are made between the cut face and the probe tip (see Figure 2-14-a). On completion of the measurement programme, a list of (x, y, z) coordinates is generated for the contour perimeter and surface deformation of each half of the cut component.

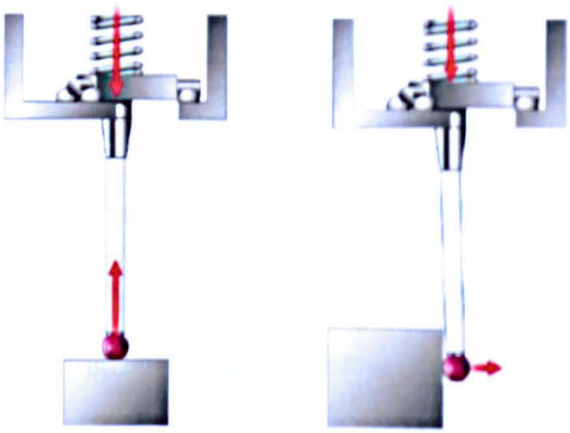

(a) (b)

Figure 2-14: The two different types of contact during the surface deformation (a) and contour perimeter (b) measurements [69].

2.4.3. The measured contour data analysis

The presence of noise and outliers is inevitable within the measured raw data. These might be due to cutting artefacts, surface roughness or errors associated with the

measurement system. The noise and outliers can result in significant errors in the calculated stresses. Hence, the raw data has to be processed prior to being applied as displacement boundary conditions in the linear elastic finite element model. In addition, the raw data may not be on a regular grid and not necessarily at the same locations as the nodes of the linear elastic finite element model used to back-calculate the stresses.

There are four different steps in the contour method data processing: alignment of the two data sets, averaging of the two data sets, outlier removal and data smoothing.

Data alignment

As mentioned earlier, the contour perimeter and the surface deformations of each cut half are measured in their own coordinate system. Therefore, before averaging the two data sets, their alignment in the same coordinate system is required.

To perform the alignment, data from one cut face are arbitrary assumed as a reference and the other cut face data are considered as floating. The first step of the alignment process consists of mirroring the 'floating' outline and data onto the 'reference' outline and data. The mirroring process is performed about the *y*-axis. After mirroring, the 'floating' data sets are rotated and translated to lie coincident with the 'reference' data sets. Figure 2-15 illustrates the different steps of the data alignment process.

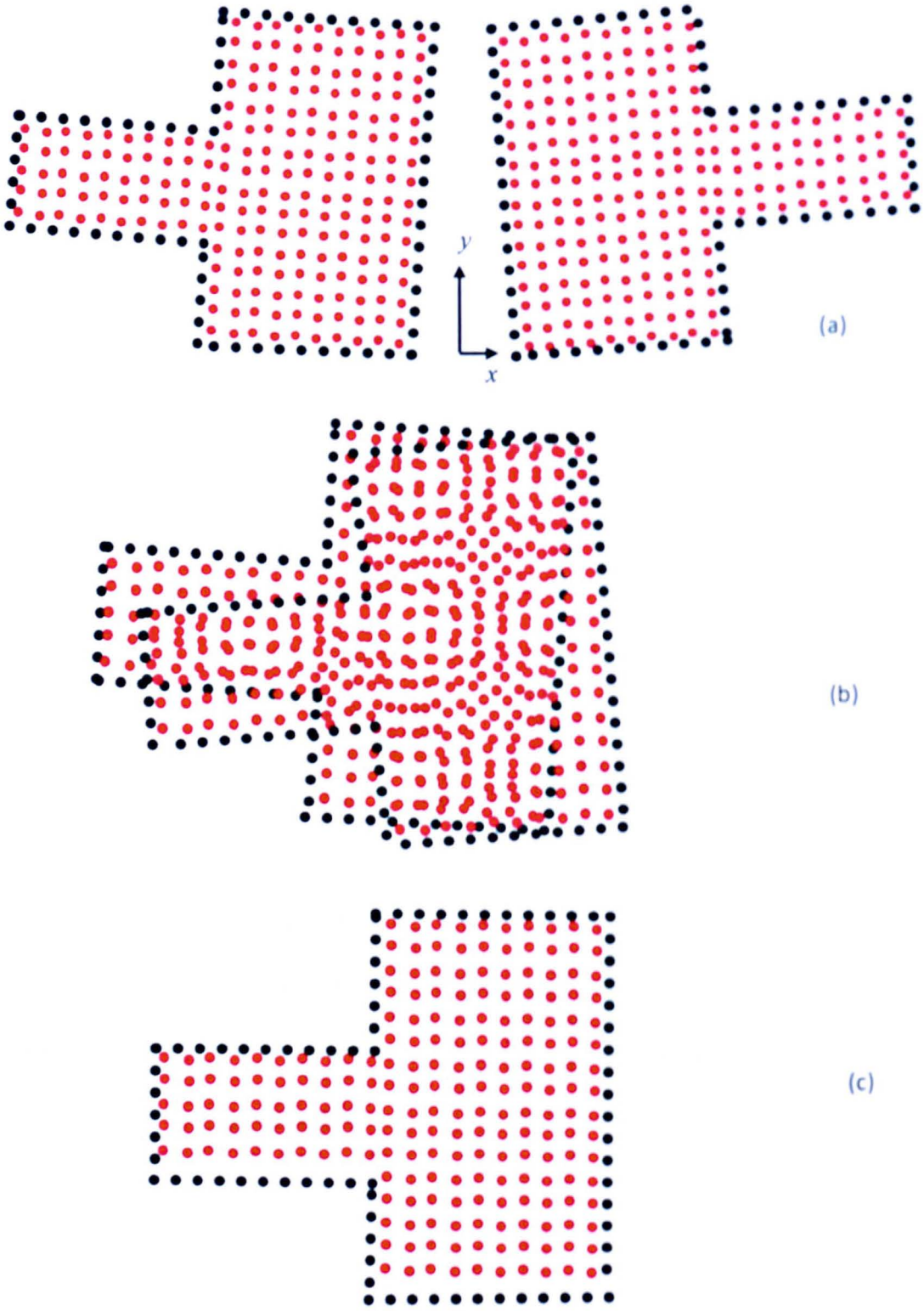

Figure 2-15: Schematic showing the two sets of data as measured (a), mirrored about *y*-axis (b) translated and rotated (c) for alignment. The black dots represent the contour perimeter data and the red dots represent the cut surface deformation data.

Data averaging and outlier removal

On completion of the data alignment, the two data sets are interpolated into a uniform common grid using linear Delaunay triangulation [63]. The density of the gridded data is approximately identical to the initial one. If necessary, the gridded data are extrapolated up to perimeter boundaries to fill in any missing regions. Finally, the common and uniform gridded data are averaged into single data sets. The averaging of the two data sets cancels out the shear stress effect and other sources of errors (see section 2.5).

Although averaging the two data sets removes a majority of outliers, sometimes a manual cleaning operation is necessary to remove errors introduced by local cutting irregularities such as wire breakage and overburning artefacts. The corresponding regions are filled in by an interpolation process. This step of the data analysis is very subjective and needs to be conducted very carefully as rough cleaning of data might lead to a loss of information.

Data smoothing

To minimise noise in the results, the averaged data have to be smoothed. Different methods of data fitting can be found in the open literature such as the polynomial approach, Fourier surface technique and bivariate spline fitting [63,66]. In early contour method work, Fourier surfaces [70] were used for the data smoothing [63]. However, according to Prime, this approach was unable to capture all features of the surface contour that can now be resolved [63]. Polynomial smoothing can also be applied for data treatment. Currently a new polynomial approach based on previous work of Viera *et al* [71] is under development at The Open University. It is an iterative method which consists of locally fitting and updating the position of each measurement point. The approach is applied to smooth the contour data in Chapter 3.

The third and probably most used smoothing technique in the contour method is bivariate spline fitting [32,72,73]. A bivariate spline consists of piecewise polynomials joined at given locations called "knots" which define the domain of each polynomial. The fitting process is achieved by minimising the error between the data points and the fit. The density of knots and order of polynomial can affect the resulting smoothed fit to the data. A larger knot density may result in over smoothing of the measured data, while lower knot spacing may result in under smoothing.

To determine the optimum fit, different approaches can be applied. The most straightforward approach consists of comparing the fitted data to raw measurements [74]. In Chapter 3, this approach is applied to determine the optimum knot spacing. In the second approach for determining the optimum knot spacing, a series of finite element analyses is undertaken to back-calculate (see next section) residual stresses [63]. The approach consists of finding the optimum spline fit corresponding to the minimum stress error for different fitting parameters. This is achieved by incrementally increasing the knot spacing and determining the average stress error for each increment. The approach is applied in Chapter 6 and Chapter 7 of this thesis.

The different steps of data analysis have been facilitated by using advanced scripts within MatLab [75], which were developed through collaboration between The Open University and the University of Manchester [63,66,76].

2.4.4. The stress back-calculation

The contour method residual stress back-calculation is conducted using linear finite element analysis. A 3D model of one of the cut parts is created using a standard FE code (*e.g.* ABAQUS) based on the measured perimeter of the part. Because the deformations

are small compared to the geometry of the component being measured and the analysis is elastic, an undeformed finite element model of the cut part is built and meshed.

The mesh usually consists of brick elements which can be either continuum linear hexahedral 8-node elements or continuum quadratic hexahedral 20-node elements, both preferably with reduced integration. The coordinates of all nodes (especially on the cut faces) are recorded, for instance in a text file.

The signs of the smoothed deformation data are then reversed and applied as displacements to the mesh grid of the cut surface for FE analysis. To avoid rigid body motion during the analysis, three additional nodal displacements are applied to the FE mesh as shown in Figure 2-16 [77]. Because of the contour method elastic superposition principle, the material behaviour is elastic and generally assumed to have isotropic properties (defined by Young's modulus and Poisson's ratio). When applying the contour method to a multi-materials test component (e.g. weld components), appropriate elastic properties must be defined for each material of the component being studied. For an anisotropic material, directional elastic constants must be used for the stress back calculation.

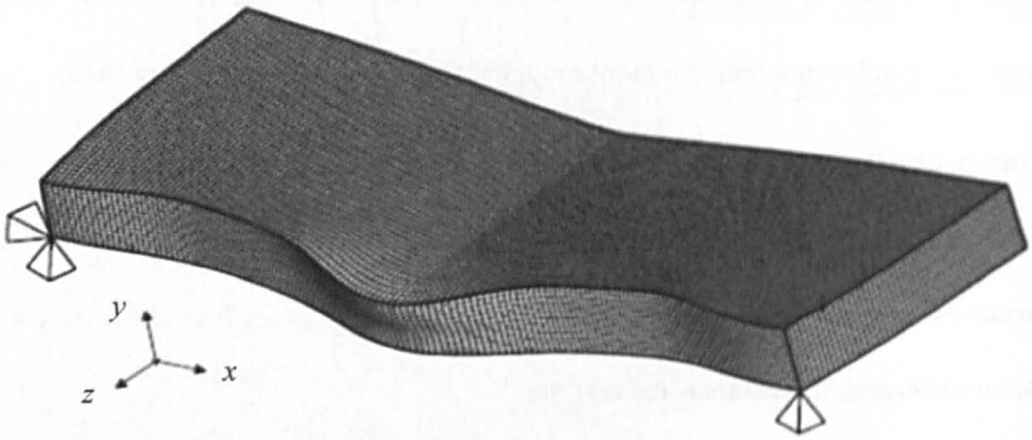

Figure 2-16: A deformed 3D linear FE model showing the additional constraints applied to avoid rigid body motion [77].

2.4.5. Contour method *vs.* common measurement techniques

As stated previously, the contour method has emerged as a valuable technique for residual stress measurements in recent years. The technique is relatively simple and uses widely available 'off the shelf' equipment. One of the unique strengths of the contour method over most destructive techniques such as hole-drilling, deep-hole drilling or slitting method is that it provides a two-dimensional residual stress map.

Although diffraction techniques (*e.g.* neutron and synchrotron diffraction) can provide similar 2D stress maps, they are limited in terms of measurement depth and material micro-structural gradients can make the extraction of stress free specimens difficult. Furthermore, these techniques are expensive and sometimes not very accessible.

Converse to most mechanical strain relief techniques for residual stress measurement, the contour method does not require application of an elastic inversion process for data analysis.

One of the limitations of the contour method compared to some residual stress measurement techniques has been that it only allows measurement of one component of the stress tensor. However, the contour method has been extended recently to allow measurement of multiple stress components by carrying out more than one cut or by applying multiple methods, for example X-ray diffraction [78,79].

The contour method is a fairly new process and therefore less well developed relative to other techniques. Its implementation, most significantly sample cutting, can also result in measurement errors. The following sections review several different sources of error in the contour method.

2.5. Cutting errors in the contour method

This section describes the different types of error which can arise during sample cutting for contour method residual stress measurements with particular emphasis on errors introduced by inelastic behaviour (that is plasticity).

Symmetric and anti-symmetric errors

Consider a stressed body that has different stress components along the measurement plane (e.g. normal and shear stresses). When the body is cut into two halves an asymmetric surface contour, due to the relaxation of both normal and shear stresses, is obtained. Referring to the equivalent surface traction notion previously described in section 2-4-1, the equivalent surface traction due to the release of normal stresses is symmetric while the equivalent surface traction for releasing the shear stresses is anti-symmetric. Therefore, the deformation from the stress relaxation along the entire cut faces can be divided into a symmetric portion generated by the normal stresses and an

anti-asymmetric portion caused by the shear stresses (see Figure 2-17). Hence, two groups of cutting errors in the contour method [59,80] can be considered: errors arising from the anti-symmetric portion and from the symmetric portion [59].

The former group of errors (anti-symmetric) is usually removed by averaging the two contour deformation data sets in the data analysis step. Contrary to the anti-symmetric errors, the symmetric errors are not averaged out. Symmetric errors can be divided into two sub-groups: those independent and those dependent on the stress magnitude.

Symmetric errors independent of stress magnitude can be caused by wire breakages, overburning or wire vibration. Change in the cut width is another type of symmetric error independent of stress magnitude. The change in the cut width is usually caused by material inhomogeneity or sometimes the variation of the sample thickness in the cutting direction. Symmetric errors independent of stress magnitude can be removed in the data analysis step or avoided by using good Wire EDM settings [59]. Most of these errors (*e.g.* wire vibration and overburning errors) can be detected and corrected by undertaking a stress free test cut [59]. This is achieved by removing a thin layer (usually about 1 mm) from one of the newly cut faces. Since, the thin layer is stress free, no deformation will occur, and only the effect of the irregularities will be observed. Thus, they can be corrected by subtracting the error from the measured contour data.

There are two types of symmetric error that depend on the stress magnitude: elastic bulging and plasticity related. Each of these two errors will be explained in detail. In order to explain the origin of plasticity-induced errors, the basic theory of plasticity is first introduced followed by a review of published work concerning such errors in the contour method and some other mechanical strain relief techniques.

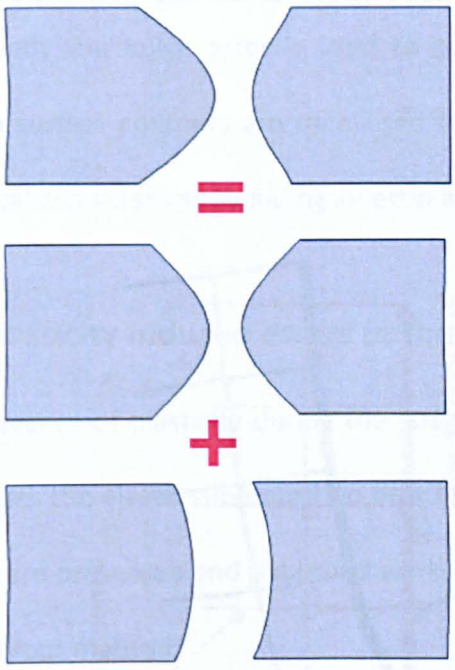

Figure 2-17: Asymmetric contour separated into symmetric and anti-symmetric contours [59].

Bulging error

Bulging errors occur when the cut width varies along the cut depth during the wire EDM process (Figure 2-18) [59]. When cutting through a field of tensile residual stress the material at the cut tip is stretched elastically. However, the physical cut width is determined by the wire diameter and EDM conditions that remain notionally constant. Therefore, less material is removed compared with the initial state of the cutting process, which results in a non-uniform cut width along the cut. Thus, the apparent deformed contour of cut faces will contain a contribution from variable material removal. This violates the assumption of the contour method that a constant cut width is removed during wire EDM [59] and invalidates the superposition principle. Errors in contour stress measurements can be introduced by this mechanism. Bulging can result in different types

of errors such as shift in the location of peak stress or change in the peak stress magnitude.

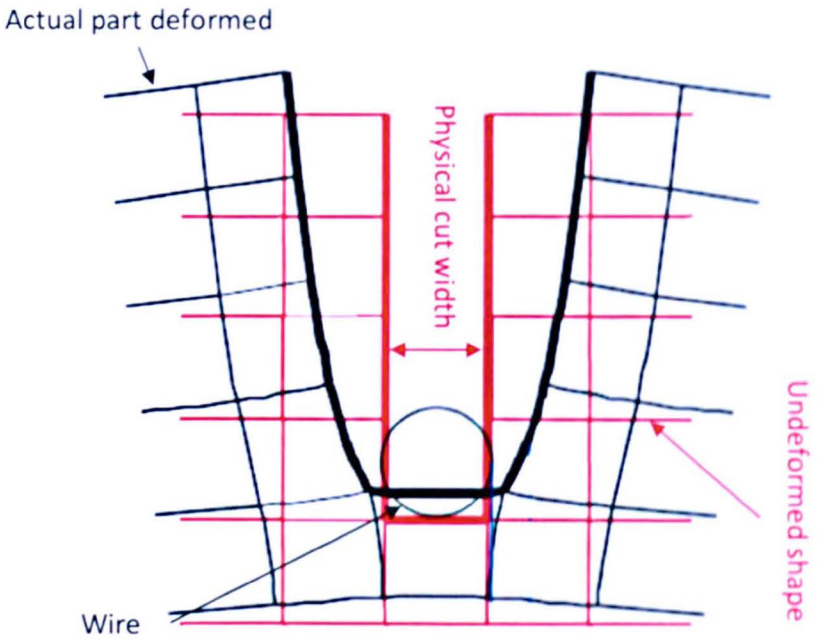

Figure 2-18: Illustration of the bulging effect during the cutting process as stresses relax [66]. The bulging effect shown here assumes tensile stress relaxation.

The component restraining regime during the cut plays a significant role in generating/mitigating this type of error. The level of the induced-error obviously depends on the state and magnitude of the cut tip stresses. To correct for the bulging effect Prime *et al.* have developed an iterative approach using the finite element method [59] and applied it to experimental data obtained from residual stress measurements in a bent steel beam.

In the iterative approach the measured contour residual stress profile (affected by elastic bulging) is used as an initial guess and is mapped into a finite element model of the component being measured as an initial residual stress field. Then the contour cutting

process is simulated for determining bulging error in terms of displacements [59]. Subsequently the bulge error is used to correct the measured surface contours. The corrected surface contours are then used to calculate stresses. This process is iterated until the calculated stress including an estimated bulge error converges [59].

2.6. Plasticity induced errors in the contour method

The occurrence of plasticity during the stress relaxation process in the contour method also violates the elastic superposition principle. In this section, elements of the theory of plasticity are presented and published work reviewed relating to plasticity-induced errors in the contour method.

2.6.1. Elements of the theory of plasticity

The theory of plasticity [81-84] is a branch of mechanics that describes the non-linear stress-strain behaviour of material when loaded beyond the yield stress. Contrary to elasticity, the material deformations in plasticity are permanent. To help understand the theory of plasticity, an analysis of the stress-strain curve for a typical ductile material is helpful (Figure 2-19). Here, a ductile material refers to any material that has the ability to yield before failure.

Uniaxial stress-strain curve

In materials science, a uniaxial tensile test is one of the simplest tests that can be conducted to determine material mechanical properties. The test consists of pulling a sample with a monotonic load and recording the displacement. The obtained data can be plotted as load *vs.* displacement or stress *vs.* strain.

A uniaxial stress-strain curve (see Figure 2-19) provides many basic material mechanical properties including the material elastic modulus (E), the yield stress (σ_0), the ultimate tensile strength (σ_{UTS}) and ductility. The material is usually assumed to be homogeneous with isotropic elastic constants (*i.e.* properties are the same in all directions).

A typical stress-strain curve for a ductile material consists of two main regions: reversible elastic behaviour and non-linear plastic regions. The former region is characterised by the material elastic modulus. The yield stress is the transition point from elastic to plastic region. The plastic region can be divided into two sub-regions: a strain hardening region and necking. In the strain hardening region the material is able to support higher load values despite the cross-section reduction. The limit of this sub-region is defined by the material ultimate tensile strength. During necking, the material strain hardening rate drops till it keeps pace with the cross-section reduction rate. The necking leads to fracture of the material.

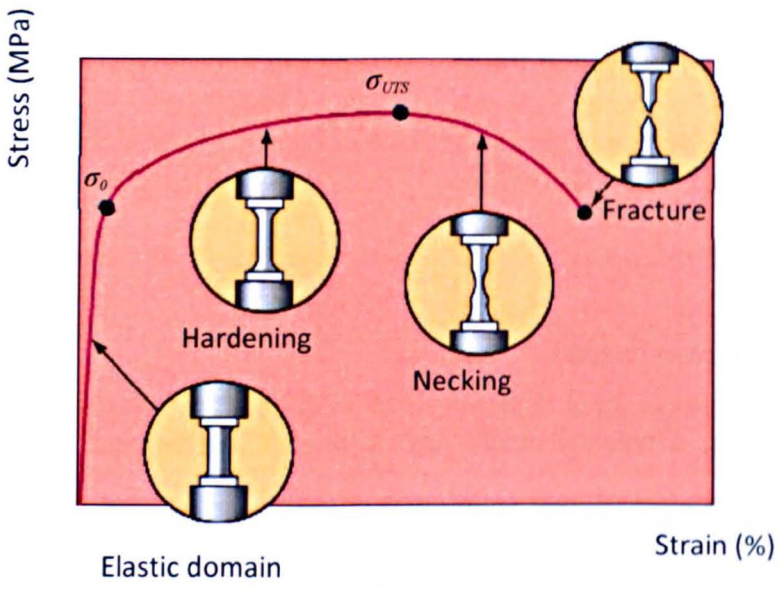

Figure 2-19: Stress-strain curve for a typical ductile material [85].

Mathematical description of plasticity

A mathematical description of material plasticity [83,86] can sometimes be complex. Because of this, idealised stress-strain curves are sometimes assumed in engineering science as shown in Figure 2-20. When compared to real material behaviour, the elastic region and the hardening region are not present in idealised rigid-plastic behaviour. The strain hardening effect is ignored in elastic-perfectly plastic behaviour. Ramberg-Osgood and other elastic-plastic models can provide a reasonable representation of the behaviour of most ductile materials.

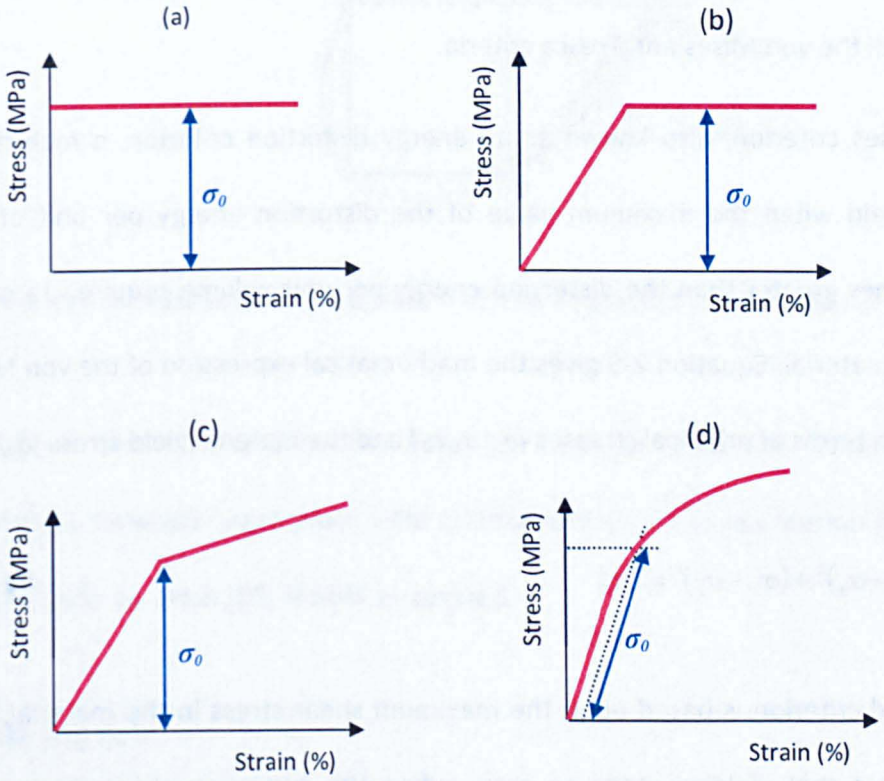

Figure 2-20: Idealised bilinear stress-strain curves: rigid ideal plastic (a), elastic perfectly plastic (b), elastic plastic material with strain hardening (c) and Ramberg-Osgood (d) where σ_0 is the material yield stress.

Three equations are generally used to describe plasticity behaviour in materials engineering: the yield criteria, the hardening rule and the flow rule.

Yield criteria

The stress-strain curves illustrated above have been assumed for materials subjected to a uniaxial loading. However, during service, engineering components can experience complex loading conditions which result in a multi-axial (*e.g.* biaxial and triaxial) stress state in the material.

Two well-known yield criteria for predicting the onset of yielding in isotropic materials are commonly used: the von Mises and Tresca criteria.

In the von Mises criterion, also known as an energy distortion criterion, a material is expected to yield when the maximum value of the distortion energy per unit of the material becomes greater than the distortion energy per unit volume required to cause yielding in the material. Equation 2-9 gives the mathematical expression of the von Mises yield criterion in terms of principal stresses (σ_1, σ_2, σ_3) and the material yield stress (σ_0).

$$(\sigma_1-\sigma_2)^2+(\sigma_2-\sigma_3)^2+(\sigma_3-\sigma_2)^2=2\sigma_0^2 \qquad \textbf{Eq. 2-9}$$

The Tresca yield criterion is based upon the maximum shear stress in the material. The criterion assumes that yielding starts to occur when the maximum shear stress goes beyond the material yield stress (σ_0). The mathematical expression for the criterion is given by the Equation 2-10.

$$Max\ (|\sigma_1-\sigma_2|,\ |\sigma_2-\sigma_3|,\ |\sigma_3-\sigma_1|)=\sigma_0 \qquad \textbf{Eq. 2-10}$$

The von Mises and Tresca yield criterion can be graphically represented in two or three-dimensional space, depending on the stress state in the materials studied (*e.g.* biaxial and triaxial stress state) and using the principal stresses. The graphic representation of the two yield criterion is the so-called yield surface. Figure 2-21 illustrates the yield surface in two-dimensional space for von Mises and Tresca criterion.

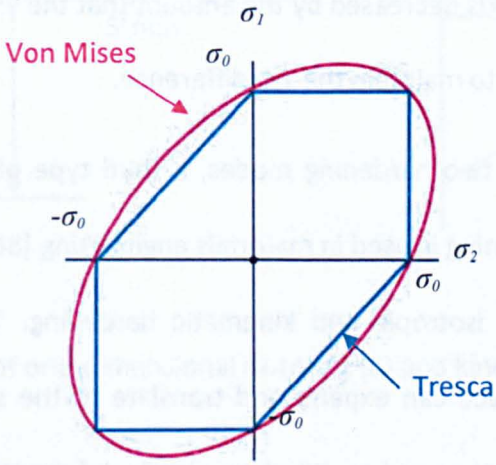

Figure 2-21: Two-dimensional illustration of Von Mises and Tresca yield surface.

The above two criteria are only valid for isotropic materials. When dealing with anisotropic materials appropriate yield criteria such as Hill yield criterion [86] and Logan-Hosford yield criterion [55] should be applied.

Hardening rule

The hardening rule defines the evolution of the yield surface. The hardening rules can be categorised into three types: isotropic, kinematic and mixed hardening [86].

In isotropic hardening (Figure 2-22-a), the yield surface dilates when the initial yield point is exceeded without changing of the shape while in the kinematic hardening (Figure 2-22-

b) the yield surface translates with material yielding. As illustrates in Figure 2-22-b the shape and the size remained unchanged in kinematic hardening.

Isotropic and kinematic hardening can also be illustrated under reverse loading (Figure 2-23). The yield stress in compression for isotropic hardening is equal to the maximum equivalent stress reached in tensile loading for uniaxial cycling loading while in kinematic hardening; this parameter is decreased by the amount that the yield stress is increased in the tensile phase in order to maintain the $2\sigma_0$ difference.

In addition to the above two hardening modes, a third type of hardening often called mixed or combined hardening is used in materials engineering [86]. As its name implies, it is a combination of the isotropic and kinematic hardening. Therefore, in combined hardening, the yield surface can expand and translate at the same time. This type of hardening rule is sometimes used to simulate plastic deformations during the welding process [87].

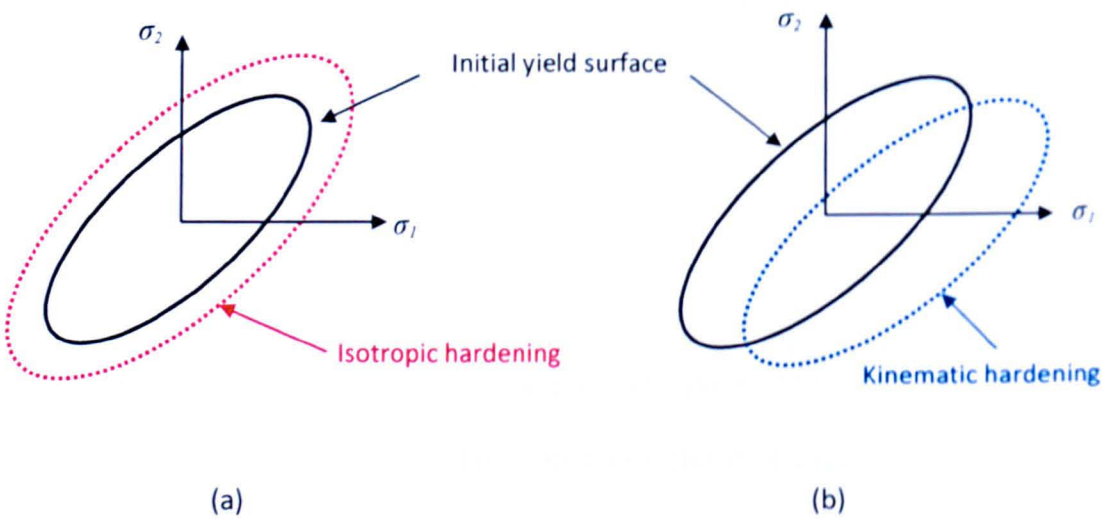

Figure 2-22: 2D illustration of isotropic (a) and kinematic hardening (b).

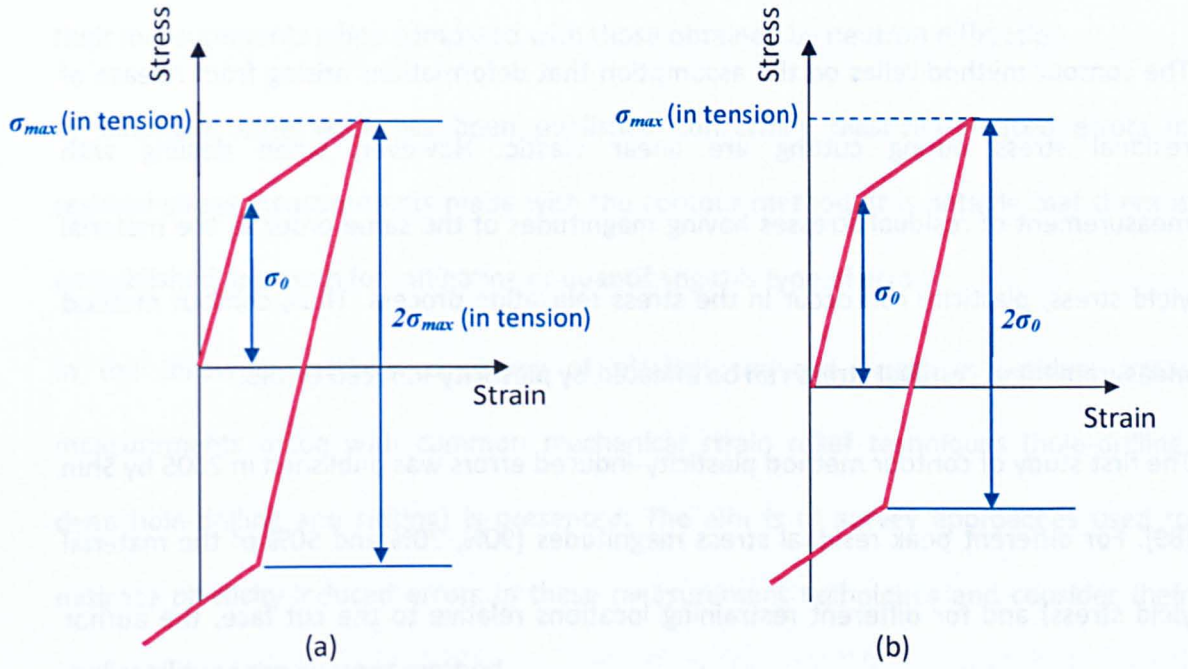

Figure 2-23: Illustration of one-dimensional isotropic (a) and kinematic hardening (b).

Flow rule

The flow rule is used to relate stresses and plastic strains after yielding occurs in the material. It determines the direction of plastic straining during plastic deformation.

After yielding, the total plastic strain consists of increments of plastic strain. Each increment of plastic strain is generated by an increment of stress. Consider a vector that represents the increment of plastic strain generated. This vector varies throughout the loading path. Since the equations governing the flow rule are based on normality conditions [88], the increment of strain is generated in a way that the plastic strain vector is normal to the yield surface during yielding.

2.6.2. Review of contour method plasticity-induced errors

The contour method relies on the assumption that deformations arising from release of residual stress during cutting are linear elastic. However, when dealing with measurement of residual stresses having magnitudes of the same order as the material yield stress, plasticity can occur in the stress relaxation process. Thus, contour method measurement of residual stress can be affected by plasticity-induced errors.

The first study of contour method plasticity-induced errors was published in 2005 by Shin [89]. For different peak residual stress magnitudes (90%, 70% and 50% of the material yield stress) and for different restraining locations relative to the cut face, the author demonstrated that plasticity effects on contour method measurements are small with secure restraining. However, the level of restraining rigidity obtained in a FE analysis is not easily achievable in practice.

Dennis et *al.* also investigated the effects of plasticity and constraint on contour method residual stresses using finite element simulations [61,90]. It was demonstrated that restraining the test component close to the cutting plane is beneficial in that less plasticity is likely to occur compared with the case where the component is restrained further away from the cut plane. In addition it was reported that the rigid restraining simulated in the finite element analysis is not feasible in practice.

Different restraining strategies are currently practiced in the contour method. One of the most effective options is to clamp the component to a stiff baseplate using fitted bolts, but care must be taken to avoid disturbing the stress field of interest by drilling the bolt holes. Prime has used a multiple-step variation of the contour method in order to avoid plasticity-induced errors in hoop stresses over a radial-axial cross section of a cylinder

[91]. However, some discrepancies attributed to plasticity or bulging were observed in their measurements when compared with those obtained by neutron diffraction.

In summary, little work has been published concerning plasticity-induced errors in residual stress measurements made with the contour method. It is notable that there is no published approach for mitigating or quantifying this type of error.

In the following sections, a review of plasticity-induced errors in residual stress measurements made with common mechanical strain relief techniques (hole-drilling, deep hole-drilling and slitting) is presented. The aim is to survey approaches used to mitigate plasticity-induced errors in these measurement techniques and consider their applicability to the contour method.

2.7. Plasticity-induced errors in some strain relief methods

As stated previously all mechanical strain relief techniques for residual stress measurements are based upon the assumption that the stress relaxation during material removal is elastic. However, when dealing with the measurement of residual stresses of magnitude approaching the yield stress of the material, this assumption can be violated. In this section the issue of plasticity-induced errors in some common mechanical strain relief techniques is covered including centre hole-drilling, deep hole-drilling and the slitting method.

2.7.1. Plasticity-induced errors in hole-drilling

The effect of plasticity in residual stress measurements made with surface centre hole-drilling is amongst the earlier plasticity investigations into mechanical strain relief techniques.

As for the contour method, the first plasticity effect study for hole-drilling technique was conducted by the means of finite element analysis [92]. The authors reported that a significant reduction in plasticity-induced errors can be obtained by using their proposed empirical relationships, which were determined by interpolation of a finite number of numerical results. It was stated that the approach enables measurement of residual stress up to 90% of the material yield stress with errors of a few percentage if the residual stress principal directions are known. Conversely, if the principal directions are unknown, measurement of high magnitude of residual stresses using the standard three-gauge rosette can be affected by up to 20%. But they reported that a noticeable improvement can be achieved (5% error) by using a new type of rosette with four radially oriented strain gauges.

Vangi *et al.* simulated the complete hole-drilling process using a 3D model for through and blind-holes [93]. From the measured strain data and von Mises effective stresses obtained from FE analysis, they proposed an iterative approach for taking into account the plasticity effect in residual stress measurements up to 90% yield stress. However, Seifi *et al.* showed that the von Mises effective stress for evaluating hole-drilling plasticity study is not complete and proposed an algorithm method to counter this effect. They reported that their approach can be applied for correcting hole-drilling plasticity-induced errors when measuring residual stress up to 97% of the yield stress.

In addition to these investigations, several other researchers have contributed to plasticity-induced errors assessment in hole-drilling technique [94-96]. However most proposed approaches are only suitable for hole-drilling and limited by the fact that residual principal directions need to be known in order to apply their approaches.

2.7.2. Plasticity-induced errors in deep hole-drilling

Unlike the surface centre hole-drilling, few publications related to deep-hole drilling plasticity assessment can be found in the open literature. This can be explained by the fact that the technique is more recent compared with centre hole-drilling and that the technique is not widely applied because it needs specialist equipment.

Nevertheless, in very recent publications [97,98], the effect of plasticity on deep hole-drilling results has been investigated analytically and numerically. A new procedure, developed by modifying the conventional deep-hole drilling to incremental deep-hole drilling, has been proposed to mitigate the plasticity-induced errors in the results of deep-hole drilling. The procedure has been successfully applied for residual stress measurement [99]. However, due to the specific nature of the deep hole-drilling technique and the new procedure (incremental cut), implementation of this approach for the mitigation of contour method plasticity-induced errors is not appropriate.

2.7.3. Plasticity-induced errors in the slitting method

Plasticity-induced errors in the slitting method of residual stress measurement is of particular interest because the technique has some similarity with the contour method, for example both techniques involve cutting the test sample into two parts using the wire EDM process.

Although the slitting method is amongst the earlier developed destructive methods, only one noticeable publication related to plasticity-induced errors assessment can be found in the open literature [25]. This work was conducted by Prime using finite element analysis and assuming elastic-perfectly plastic material behaviour.

For different stress profiles and magnitudes (compared to the material yield stress), the author simulated the slitting incremental cut for a zero cut width and determined the corresponding strains for each case. A series expansion approach was then applied to convert the strain data to residual stress assuming linear elastic behaviour. By comparing the initial residual stress state to the obtained FE predictions, an average (plasticity-induced) stress error was determined for the different stress magnitudes and profiles.

The strain data obtained from simulations were also employed to calculate the residual stress intensity factor distribution for the stress magnitude by applying Equation 2-1 given in section 2-3-1. The obtained SIF data were then normalised using the material yield stress and specimen dimensions. Based on the above assumptions (zero cut width and material with no strain hardening), the author proposed relationships between the normalised stress intensity factor and the average stress error.

One of the strengths of the developed relationships is that the average stress errors due to plasticity can be estimated without prior knowledge of the residual stress, by using the measured strain gauge data.

However, the developed relationships for slitting plasticity-induced errors estimation are not convenient for the contour method. That is because in the slitting method only one side of the test specimen is held during the cutting, while in the contour method both sides of the test sample needs to be securely restrained during the cutting process [59]. If the slitting restraining conditions are applied in contour method, this can result in bulging or plasticity-induced errors which requires another correction.

Nevertheless, since the two measurement techniques employ approximately the same cutting process, a similar approach can be developed to assess the plasticity-induced errors in the residual stress measurement made with the contour method.

2.8. Scope of this work

Based on the above review of the different types of error in the contour method it can be concluded that occurrence of plasticity in the stress relaxation during the cutting process remains largely unaddressed. There is currently no recognised way to assess and subsequently mitigate plasticity-induced errors in contour method residual stress analysis.

Work has been done to assess plasticity errors in techniques similar to the contour method, *e.g.* the slitting method; however these approaches are not directly applicable to the contour method. The objective of this thesis is to develop tools or approaches for quantifying plasticity-induced errors in the contour method of residual stress measurement.

Other errors in the contour method can be mitigated by careful experimental technique or data analysis. Anti-symmetric errors are usually removed by averaging the two sets of data from the two halves of the cut. Symmetric errors that are not dependent on the stress magnitude (*e.g.* effects of vibrations or over-burning) can be either avoided by conducting cutting trials and tuning the wire EDM cutting parameters or corrected by undertaking a stress free test cut. The bulging error or cut 'width change' can be corrected by applying the approach developed by Prime [59].

2.9. Review of cutting simulation (moving crack)

This section reviews moving crack simulation using the finite element method. This is because plasticity-induced errors are related to stress concentration and relaxation during the cutting process and the cutting process can essentially be represented as a moving blunt crack. The study of moving cracks encompasses aspects of fracture mechanics. An introduction to the finite element method and fracture mechanics is covered here, followed by a review of previous approaches applied to simulate the contour cutting process.

2.9.1. Fundamentals of the finite element method

In engineering and science many physical problems can be defined using arrays of partial differential or integral equations which are impractical to solve using classical analytical methods. The finite element method is a numerical approach by which approximate solutions can be found in a discrete manner for these partial differential and integral equations.

The finite element method essentially works by assuming a piecewise continuous function for the solution and finding the parameters of the function in a way that the errors are reduced below a threshold value. The technique involves a discretisation process where the continuum model of a given problem is divided into a finite number of elements. Each element is characterised by a certain number of nodes on which loads (e.g. pressure, temperature) and displacement are applied. The different elements of the continuum model are connected by nodes which are defined by their coordinates in a coordinate system.

The finite element method was initially developed from the need of solving complex elasticity and structural analysis problems in civil and aeronautical engineering [100] and its roots can be traced back to the work of three different groups including mathematicians [101-103], physicians [104] and engineers [100]. Nowadays, the finite element method is widely used for solving a variety of different problems including static, dynamic, solid or fluid mechanics, biomechanics and electromagnetism.

According to the behaviour of the structure to be studied, two types of finite element analysis can be used: linear and non-linear finite element analysis.

The linear finite element method

The linear finite element method is usually undertaken before the non-linear one. There are mainly three assumptions made in the linear elastic finite element method [100]:

- ✓ Displacements or deformations of the structure are presumed to be infinitesimally small, therefore negligible in the equilibrium equations for the problem resolution.
- ✓ Linear elastic behaviour is assumed for the materials of the structure;
- ✓ The structure boundary conditions are supposed to remain unchanged during the loading process.

The above three assumptions lead to a set of linear equations (Eq. 2-11) describing the structure in the linear finite element method [100].

$$Kd = F \qquad \textbf{Eq. 2-11}$$

where K is the stiffness matrix of the structure, d is the nodal displacements vector and F is the external nodal force vector.

The characteristics of the solutions for this type of problem are that the structure displacements or deformations are linearly proportional to the applied forces and that the structure's stiffness is independent of the applied load [100].

The non-linear finite element method

The non-linear finite element method is usually conducted when the structure is expected to experience non-linearity. There are three different types of non-linearity which can occur in a finite element analysis: Material non-linearity, geometry non-linearity and the status-changing non-linearity.

- ✓ Material nonlinearity is usually caused by non-linear material deformation such as elasto-plastic material, visco-elastic material and visco-plastic material behaviours;
- ✓ In geometric non-linearity, the structure deformations and rotations are no longer negligible compared to the structure's initial state.
- ✓ Contact between surfaces is the most frequent status changing non-linearity encountered in finite element modelling.

An iterative series of linear approximations with corrections are usually applied for solving non-linear problems [105]. The incremental approach was used in earlier non-linear problems [105]. However, since this approach induces significant build-up of error in the results, the Newton-Raphson approach was adopted to counter this issue [105].

Solution convergence in non-linear finite element analysis is not always easily attainable. In the commercial finite element codes, different strategies are implemented for obtaining desired convergence such as the sparse method, pre-conditioned conjugate gradient and front solvers [76].

2.9.2. Basics of fracture mechanics

Fracture mechanics is a branch of solid mechanics that studies the propagation of cracks subjected to primary loads such as forces and moments owing to service operation or secondary self-equilibrated load (*e.g.* residual stresses) or the combination of both types of load. According to the fracture behaviour of the material the field of fracture mechanics can be divided into two main parts: linear elastic fracture mechanics and elastic plastic fracture mechanics.

Linear elastic fracture mechanics was initially conceived by Griffith during World War I [106]. Because of the limitations of his proposed theory (only applicable to brittle materials), Irwin modified the theory by introducing the 'strain energy release rate' or 'crack driving force' notion [107]. Soon after, Irwin contributed to another change by introducing the concept of stress intensity factor and critical stress intensity factor [107,108].

Following Irwin's work, Rice introduced the *J*-integral concept, which is an important parameter for toughness measurement in elastic-plastic fracture [109]. It represents the 'strain energy release rate' in non-linear elastic fracture mechanics.

Linear elastic fracture mechanics focuses on predicting the critical load at which a crack in a body starts to grow. As for most elastic studies, the material being studied is usually assumed to have isotropic and linear elastic properties except in the vicinity of the crack tip where small scale inelastic behaviour can occur due to stress concentration (high stress magnitude).

There are three basic modes of loading a crack in a body: The opening mode (mode I), the sliding mode (mode II) and the tearing mode (mode III), see Figure 2-24. The opening

mode (Figure 2-24-a) is of most relevance to the contour method because it is stresses normal to the plane of interest (plane of cut) that are inferred from measurements of "the crack" surfaces (i.e. flanks created during the cutting process).

According to the ASTM standard test method for linear-elastic plane-strain fracture toughness (ASTM E399) [110], linear elastic fracture mechanics can be only used if small scale yielding conditions are met. For example to determine a valid K_{IC} (fracture toughness) using a compact tension specimen, the extent of the inelastic deformation at the crack tip should be much smaller than the specimen dimensions, the crack size and the uncracked ligament [110]. For a large crack tip plastic zone size, elastic plastic fracture mechanics should be applied [108], this latter branch of fracture mechanics being the natural extension of linear elastic fracture mechanics.

Analysis of crack behavior under an elastic-plastic regime can be achieved by applying the *J*-integral or crack tip opening displacement concepts. For a given material, these two parameters are related by a unique expression demonstrated by Shih [111]. Elastic plastic fracture mechanics is only briefly mentioned here as it is not used for the present study. The plasticity level that can be introduced by contour method cuts can be analyzed using linear elastic fracture mechanics solutions with Irwin stress redistribution and plasticity corrections.

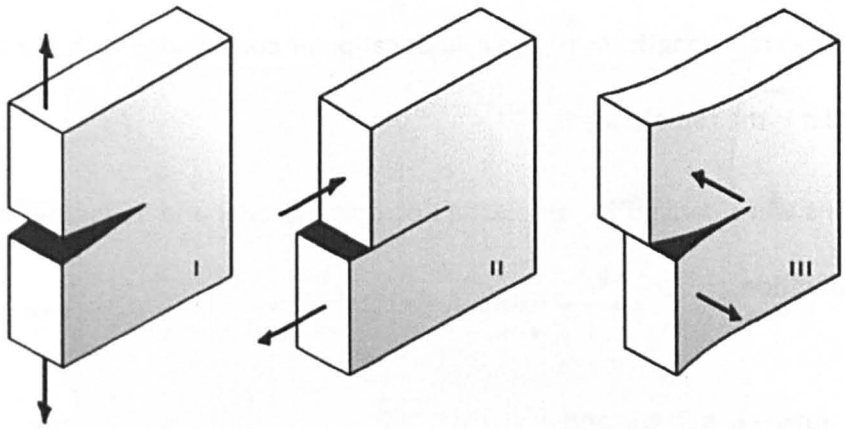

(a)-Opening mode (mode I) (b)-Sliding mode (mode II) (c)-Tearing mode (mode III)

Figure 2-24: The three basic modes of crack surface displacements in linear elastic fracture mechanics arising from direct and shear loadings [108].

Mode I crack tip stress field in linear elastic fracture mechanics

There is a wide range of publications dealing with the derivation of the mode I elastic stress field ahead of a crack tip, for example [108,112,113].

Equation 2-12 describes the elastic stress field for a crack with an infinitely sharp tip in an infinite plate biaxially loaded (Figure 2-25).

$$\sigma_X = \frac{\sigma\sqrt{\pi a}}{\sqrt{2\pi r}}\cos\frac{\theta}{2}\left(1-\sin\frac{\theta}{2}\sin\frac{3\theta}{2}\right)$$

$$\sigma_Y = \frac{\sigma\sqrt{\pi a}}{\sqrt{2\pi r}}\cos\frac{\theta}{2}\left(1+\sin\frac{\theta}{2}\sin\frac{3\theta}{2}\right) \qquad \textbf{Eq. 2-12}$$

$$\tau_{XY} = \frac{\sigma\sqrt{\pi a}}{\sqrt{2\pi r}}\sin\frac{\theta}{2}\cos\frac{\theta}{2}\cos\frac{3\theta}{2}$$

where, a is the crack length, (r, θ) are cylindrical-polar coordinates with the origin at the crack tip and σ is the remote load.

The equations were derived for an elastic isotropic material and assuming the following boundary conditions:

- ✓ $\sigma_y = 0$ for $-a < x < a$ and $y = 0$
- ✓ $\sigma_x \rightarrow \sigma$ and $\sigma_y \rightarrow \sigma$ for $x \rightarrow \pm\infty$ and $y \rightarrow \pm\infty$
- ✓ $\sigma_y \rightarrow \sigma$ for $x = \pm a$ and $y = 0$

From the expressions of Equation 2-12, it can be noticed that at the crack tip ($r=0$) a $1/\sqrt{r}$ singularity is obtained. The intensity of the stress singularity, defined by the factor $\sigma\sqrt{\pi a}$, is the so-called mode I stress intensity factor. The remaining parts of the three expressions in Equation 2-12 are functions of the geometrical position about the crack tip [108]. For the configuration shown in Figure 2-25, the stress intensity factor depends only on the remote load and the crack size.

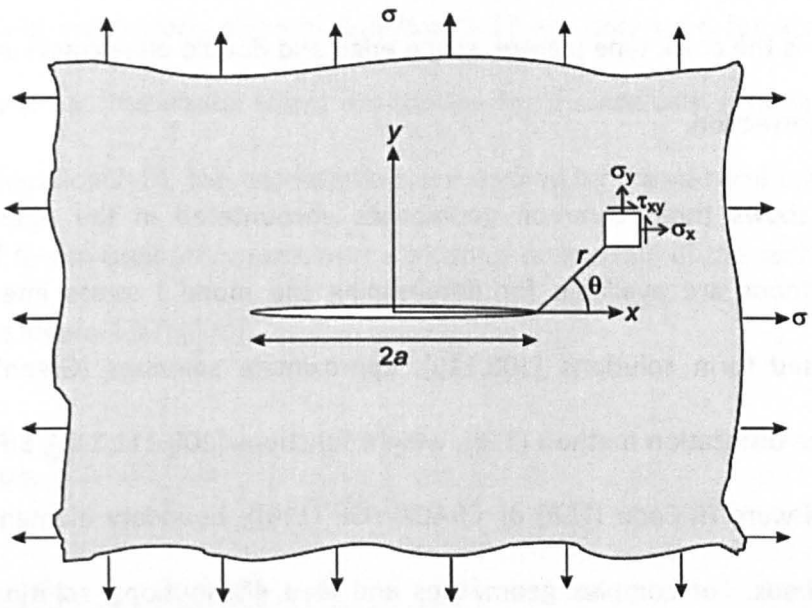

Figure 2-25: Schematic drawing showing a biaxial loaded infinite plate containing a crack [108].

The above expressions were derived for biaxial loading conditions only. For a uniaxial loading (*e.g.* in *y*-direction) the stress field must be corrected. To obtain the uniaxial crack tip stress field, the remote load is subtracted from the expression of σ_x in Equation 2-12 [114]. This correction is usually omitted because the remote load is considered to be negligible compared to the stresses near the crack tip.

It must be also noted that the crack tip stress field expressions in Equation 2-12 apply only for an infinite plate. Since the geometry of the plate can affect these expressions, the stress intensity factor needs to be corrected for different cases. Equation 2-13 gives the general form of the stress intensity factor.

$$K_I = \sigma\sqrt{\pi a} \times f\left(\frac{a}{W}\right) \qquad \textbf{Eq. 2-13}$$

where *f(a/W)* is the crack type (centre, single edge and double edge crack) and the finite width effect correction.

Figure 2-26 shows three common geometries encountered in the open literature. Different methods are available for determining the mode I stress intensity factor including closed form solutions [108,115], approximate solutions (Green's functions [108,115]), the dislocation method [116], weight functions [108,111,115], SIF handbooks [115,117], software (R-Code [118] or CRACKWISE [119]), boundary element and finite element methods. For complex geometries and load distributions, solutions found in handbooks are not suitable for determining the mode I stress intensity factor. Numerical methods are often more accurate and appropriate.

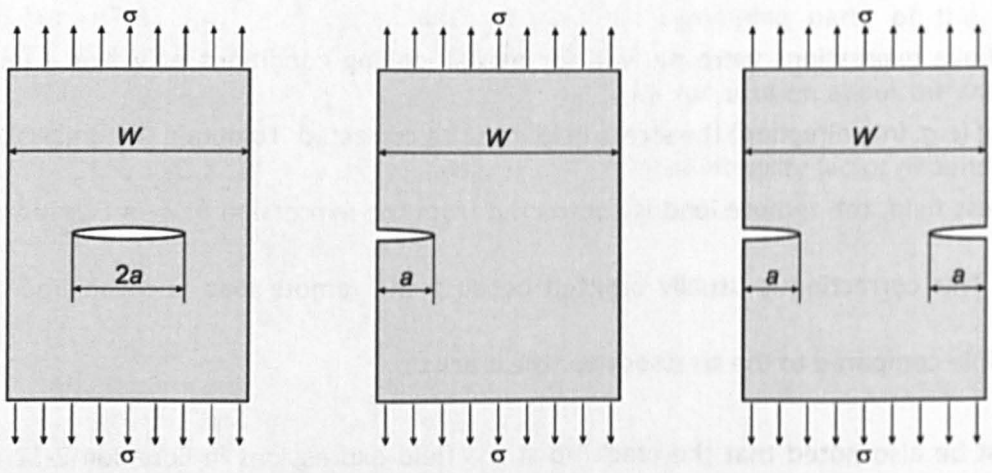

Figure 2-26: Schematic drawing showing three common cracked-plate configurations: centre crack (left), single edge notched (middle) and double edge notched (right) [108].

A blunted crack tip is introduced by wire EDM cutting (See Figure 2-27) and due to the nature of wire EDM; the cut width is greater than the wire diameter.

The stress field expressions given in Equation 2-12 are only valid for a crack with an infinitely sharp tip. The elastic stress distribution for a crack with a finite tip radius is defined by Equation 2-14. The expressions were derived by Creager and Paris by shifting the origin of the co-ordinate system over a distance of one half of the radius behind the crack tip (See Figure 2-27) [120].

$$\sigma_X = \frac{K_I}{\sqrt{2\pi r}}\cos\frac{\theta}{2}\left(1-\sin\frac{\theta}{2}\sin\frac{3\theta}{2}\right)-\frac{K_I}{\sqrt{2\pi r}}\frac{\rho}{2r}\cos\frac{3\theta}{2}$$

$$\sigma_Y = \frac{K_I}{\sqrt{2\pi r}}\cos\frac{\theta}{2}\left(1+\sin\frac{\theta}{2}\sin\frac{3\theta}{2}\right)+\frac{K_I}{\sqrt{2\pi r}}\frac{\rho}{2r}\cos\frac{3\theta}{2} \qquad \textbf{Eq. 2-14}$$

$$\tau_{XY} = \frac{K_I}{\sqrt{2\pi r}}\sin\frac{\theta}{2}\cos\frac{\theta}{2}\cos\frac{3\theta}{2}-\frac{K_I}{\sqrt{2\pi r}}\frac{\rho}{2r}\sin\frac{3\theta}{2}$$

where, K_I is mode I stress intensity factor, ρ is the blunt crack radius and (r, θ) are cylindrical-polar coordinates with the origin at the crack tip.

For this type of crack, there is no singularity in stress at the crack tip ($\theta = 0 \quad r = \rho/2$) as the maximum stress value is known, see Equation 2-15 [115,120].

$$\sigma_{Y\max} = \frac{2K_I}{\sqrt{\pi\rho}} \qquad \textbf{Eq. 2-15}$$

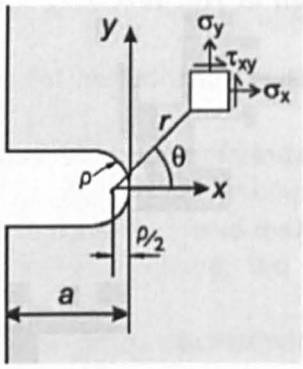

Figure 2-27: A schematic drawing of a blunt edge crack in a finite width plate along with the applied load and polar coordinate system.

Mode I crack tip plastic zone

At the crack tip, the magnitude of stress (which is singular) will exceed the material's yield stress, and this generates local plastic deformation surrounding the crack tip. The generated plastic zone size and shape are both dependent on the material's deformation properties, the state of triaxiality of the stress field at the crack tip (for example plane stress or plane strain) and the type and magnitude of the applied remote load or stress distribution within the body. The size of the plastic zone at the crack tip can be estimated using different approaches: for example by a first order approximation, by Irwin or by Dugdale's approach [108,112,113]. The shape can be approximated using a classical yield criterion: either von Mises or Tresca yield. First, details of a plane stress plastic zone size and shape are presented, followed by the case for plane strain.

First order approximation to the crack tip plastic zone size

A first order approximation to the plastic zone size can be obtained from the σ_y expression along the x-axis $(\theta=0)$ in the Equation 2-12 and Equation 2-14 for a sharp and blunt crack,

respectively [108,115]. In fact, when the stresses (σ_y) reach the material yield stress (σ_0), then $r = r_y$. Substituting these parameters in the σ_y expression allows the determination of the first approximation r_y to the plastic zone size for both cases. The sharp crack plastic zone size is readily determined, see Equation 2-16. Figure 2-28 shows the stress distribution ahead of the sharp crack tip and the corresponding first order approximation to the plastic zone size.

$$r_y = \frac{1}{2\pi}\left(\frac{K_I}{\sigma_0}\right)^2 \qquad \textbf{Eq. 2-16}$$

Contrary to the sharp crack case, the determination of the blunt crack first order approximation plastic zone size is not straightforward. After substituting the mentioned parameters (σ_0 and r_y) in the corresponding stress component (σ_y), a cubic equation has to be solved (see Equation 2-17).

The general formula for roots of a cubic equation can be readily applied to solve Equation 2-17. As only the real solution has physical significance, this expression is considered as first order approximation to the blunt crack plastic zone size (Equation 2-18). The effect of the blunt crack on the plastic zone size and the contour method predictions will be discussed in Chapter 5.

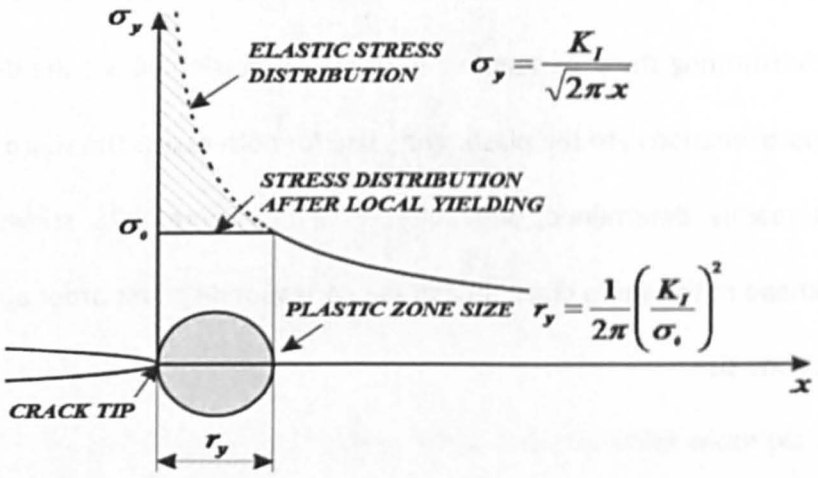

Figure 2-28: Schematic diagram showing the crack tip stress distribution and corresponding plastic zone generated according to a first order approximation approach for an edge crack subjected to a remote load distribution [108].

$$\left(\frac{2\pi\sigma_0^2}{K_I^2}\right)r_y^3 - r_y^2 - \rho r_y - \frac{\rho^2}{4} = 0 \qquad \text{Eq. 2-17}$$

$$r_y = \frac{K_I^2}{6\pi\sigma_0^2} + \frac{1}{3}\left(A + \frac{1}{2}B^{1/2}\right)^{1/3} + \frac{1}{3}\left(A - \frac{1}{2}B^{1/2}\right)^{1/3} \qquad \text{Eq. 2-18}$$

where $A = \frac{1}{8\pi^3}\left(\frac{K_I}{\sigma_0}\right)^6 + \frac{9\rho}{8\pi^2}\left(\frac{K_I}{\sigma_0}\right)^4 + \frac{3}{\pi}\left(\frac{3\rho K_I}{4\sigma_0}\right)^2$ and $B = \frac{9}{4\pi^2}\left(\frac{3\rho K_I}{2\sigma_0}\right)^4 + \frac{108\rho^3}{\pi^3}\left(\frac{K_I}{2\sigma_0}\right)^6$

It is important to note that these expressions are based on a first order approximation to the plastic zone size and as their determination is based on an elastic analysis of the crack tip stress field, the approximations are considered to be inaccurate [108,112,113].

It is difficult to define both plastic zone size and shape at the same time using simple estimation methods. In the open literature one of two approaches is usually followed. Either a better approximation of the plastic zone size (compared to first approximation to

the plastic zone size) with selected shape is determined (e.g. Irwin and Dugdale approach), or they give an impression of the shape but keep the first approximation to the plastic zone size [108]. As Irwin and Dugdale's plastic zone sizes are approximately the same [108] only the Irwin case is presented here. For the approximation to the plastic zone shape von Mises yield criterion is used here as similar results are obtained with a Tresca criterion [108].

Irwin plastic zone size

When yielding occurs, plasticity at the crack tip causes redistribution of stresses in order to satisfy equilibrium conditions. Irwin proposed that the occurrence of plasticity makes the crack behave as if it was larger than the actual physical size.

In Figure 2-29-a the shaded areas (I and II) are representative of the forces active in the elastic analysis. Because of the elastic-perfectly plastic material assumed the stresses cannot exceed the material yield stress. To maintain equilibrium the net force arising from stresses normal to the crack direction in areas I and II must be the same. Based on this equilibrium condition a more accurate plastic zone size, r_P, is estimated by Irwin as being twice that obtained in first approximation analysis for a sharp crack (Figure 2-29-b).

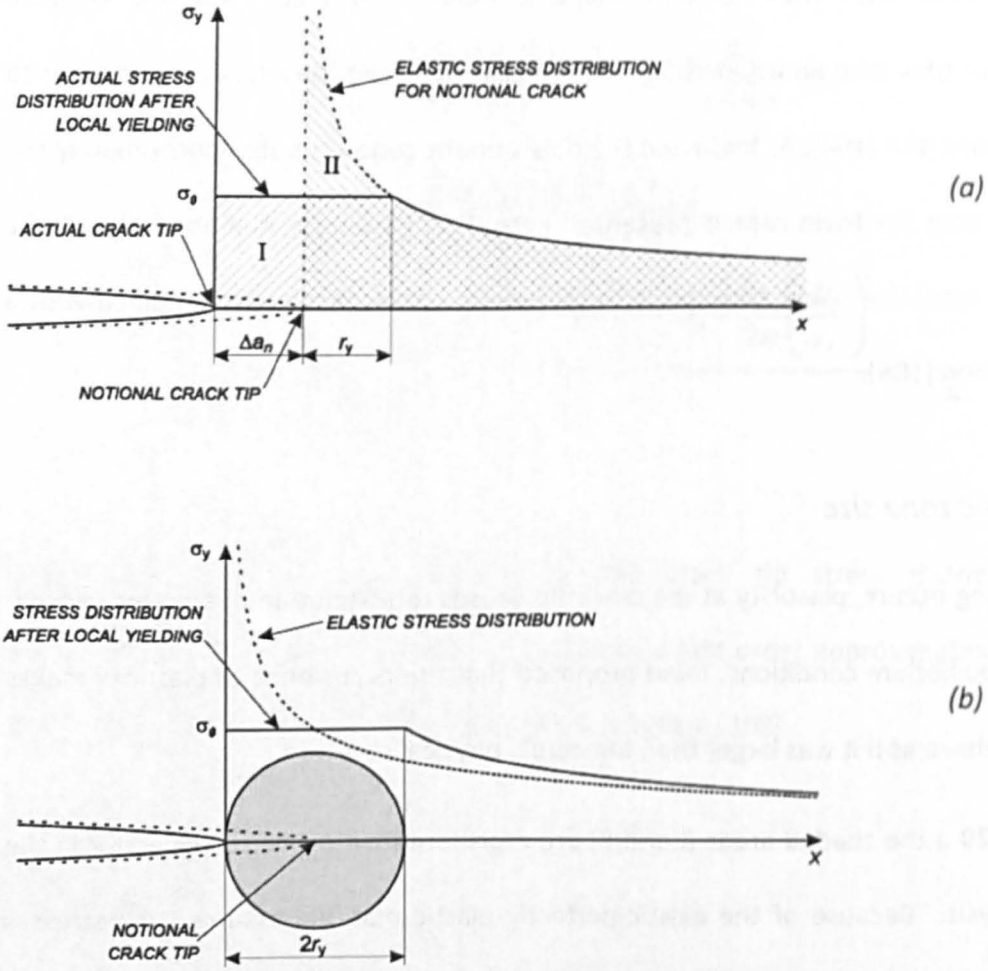

Figure 2-29: Schematic of Irwin's analysis (a) and the resulting Irwin crack tip plastic zone size (b) [108].

First order approximations to the plastic zone shape

The expressions for plastic zone size given in the above sections are for a specific direction that is the direction along the crack plane (the *x*-axis). When all directions are considered the shape of the plastic zone will be quite different.

To determine an approximation to the shape of the plastic zone ahead of crack tip under plane stress conditions the classical von Mises yield criteria is used (Equation 2-19).

$$(\sigma_1-\sigma_2)^2+(\sigma_2-\sigma_3)^2+(\sigma_3-\sigma_1)^2=2\sigma_0^2$$ **Eq. 2-19**

where σ_1, σ_2 and σ_3 are the principal stresses (See Equation 2-20) for plane stress conditions. By substituting the principal stress expressions in the yield criterion equation for plane stress conditions ($\sigma_3=0$) and by rearrangement, a first order approximation to the plastic zone shape for a sharp crack is obtained, see Equation 2-21. It can be noticed that for $\theta=0$ the value of $r(\theta)$ is the same as the approximation expression (Equation 2-16).

$$\sigma_1=\frac{K_I}{\sqrt{2\pi r}}\cos\frac{\theta}{2}\left(1+\sin\frac{\theta}{2}\right)$$

$$\sigma_2=\frac{K_I}{\sqrt{2\pi r}}\cos\frac{\theta}{2}\left(1-\sin\frac{\theta}{2}\right)$$ **Eq. 2-20**

$$\sigma_3=0$$

$$r(\theta)=\frac{1}{4\pi}\left(\frac{K_I}{\sigma_0}\right)^2\left(1+\frac{3}{2}\sin^2\theta+\cos\theta\right)$$ **Eq. 2-21**

Plane strain plastic zone size and shape

As mentioned previously the state of triaxiality of stress at the crack tip highly affects the plastic zone size and shape. From the von Mises yield criteria the plastic zone shape expression under plane strain conditions can be determined in a similar manner to the plane stress condition (Equation 2-21). Note that for plane strain conditions $\sigma_3=\nu\,(\sigma_1+\sigma_2)$; where, ν is the material Poisson's ratio.

Along the *x*-axis, assuming elastic properties with a Poisson's ratio of 0.33, a first approximation to the plane strain plastic zone size is obtained; see Equation 2-22. However, this value is considered to be underestimated [108]. For this reason Irwin proposed a nominal plane strain plastic zone size (Equation 2-23) often quoted in the literature. Figure 2-30 compares the plastic zone shape for plane stress and plane strain conditions in the crack tip region. It can be noticed that for all directions the plane stress plastic zone size is much larger than the plane strain case.

$$r(\theta)=\frac{1}{4\pi}\left(\frac{K_I}{\sigma_0}\right)^2\left((1+\cos\theta)(1-2\nu)^2+\frac{3}{2}\sin^2\theta\right) \qquad \textbf{Eq. 2-22}$$

$$r_y^{P.strain} \approx 0.11 r_y$$

$$r_y^{P.strain} \approx \frac{1}{6\pi}\left(\frac{K_I}{\sigma_0}\right)^2 \qquad \textbf{Eq. 2-23}$$

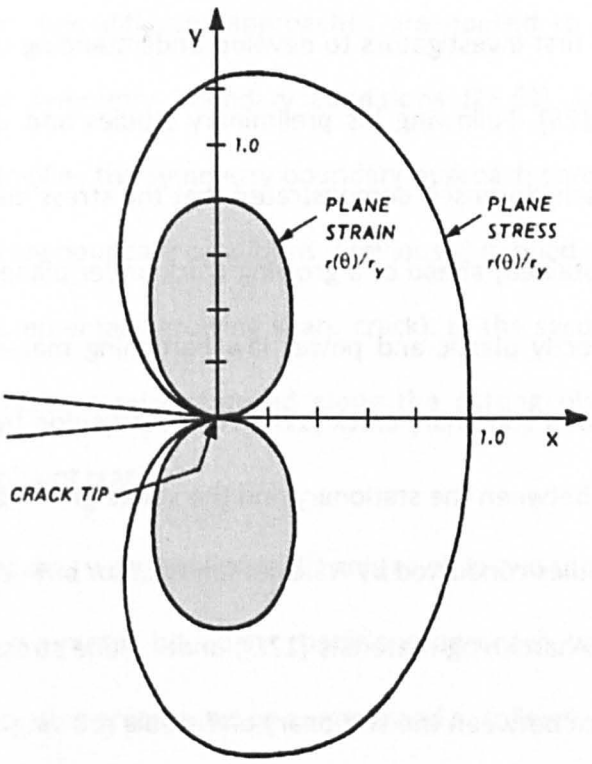

Figure 2-30: Dimensionless plastic zone shapes for the von Mises yield criterion [108].

Plastic zone associated with a stable growing crack

So far the crack tip plastic zone size and shape have been considered for a stationary crack. However, a crack does not just suddenly appear in elastic-plastic material. Likewise during the wire EDM cutting process, a crack grows step by step as material is locally eroded. The literature dealing with growing cracks is sparse compared with classical linear elastic and elastic plastic fracture mechanics. One of the reasons for this may be the complex mathematical formulation for a growing crack. Nevertheless several numerical investigations have been conducted by Rice, Sorensen, Narishaman [121-124]. Because the subject of mode-I cracking plasticity is of particular interest here, the research related to this mode only is covered.

Rice was among the first investigators to develop understanding of the mechanism of a growing crack [123,125]. Following his preliminary studies and using a finite element nodal release approach, Sorensen demonstrated that the stress distribution (from which the plastic zone is obtained) ahead of a growing crack under plane strain conditions and for both elastic-perfectly plastic and power law hardening materials is essentially the same as that ahead of a stationary crack [124]. An investigation by Sham also showed a negligible difference between the stationary and the stable growing crack tip plastic zone size [126]. Similar studies conducted by Narasimhan *et al* for both elastic-perfectly plastic [122], and power law hardening materials [121], under plane stress conditions exhibited the same resemblance between the stationary and stable growing crack plastic zone size and shape.

In summary, based on these research studies provided by different authors, it is reasonable to use the analytical expressions for the plastic zone of a stationary crack to estimate the plastic zone size for a growing crack.

2.9.3. Cutting simulation in contour method

Simulation of the contour method consists of two different steps: cutting simulation and stress back-calculation. The cutting simulation is the most critical step for plasticity assessment in the contour method. The cutting process associated with the contour method is generally modelled using a non-linear finite element analysis with an elastic-plastic material. The stress back-calculation is conducted in a linear finite element analysis by simply applying the displacements of opposite sign to a model representing the cut half-component that develop due to the release of residual stresses. Isotropic elastic constants are generally used in this second step.

In the open literature, two different approaches are applied to conduct the cutting simulation: release of symmetry boundary conditions [25,61] and material removal [89,90]. As its name implies the symmetry boundary approach consists of incrementally releasing nodal symmetry boundary conditions (previously) defined along a cut line/plane (this represents an incrementally growing sharp crack). In the second cutting approach, mesh elements are incrementally removed along the cutting plane (representing an incrementally growing blunt crack).

The two cutting approaches were applied by Dennis et *al.* in two separate publications. In their first work, the symmetry boundary conditions approach was applied [61]. The different steps of the cutting process can be summarised as follows:

- ✓ Generation of the initial state of residual stresses (by welding simulation) in a FE model representative of one half of the part geometry with symmetry boundary conditions on the plane of interest; that is on the plane along which the cutting will be conducted;
- ✓ Mapping of the initial residual stresses into a new FE model with a regular mesh grid in order to facilitate the cutting simulation process. The symmetry boundary conditions were again defined along the same plane of interest;
- ✓ Cutting simulation by incrementally releasing the nodal symmetry boundary conditions in a series of steps.

A mesh sensitivity study was conducted by the authors. Two different mesh types with reduced and full integration were analysed. It was reported that because of the resistance of linear elements to element locking [127], they behaved better than quadratic elements. The same remark was observed for reduced integration compared to full

integration. Thus, the authors conducted their cutting simulations with linear elements with reduced integration. However, no mesh sensitivity study was carried out on the mesh size, which can also affect the results.

The authors also investigated the effect of restraining the component to be cut on plasticity-induced errors by simulating the cutting process for different restraining conditions. It was reported that the degree of restraining obtained in finite element analysis is unrealistic since it is much higher compared to the sample restraining in practice.

In their second work, Dennis et *al.* [90] as well as Shin [89] used the material removal approach to perform the cutting process. Dennis et *al.* followed the same steps as in their previous work. Linear elements with reduced integration elements were used. Based upon the overall size of the FE model studied and in order to achieve a reasonable computation time, the authors reported that a 2 mm cut increment was pragmatically chosen. No explanation was given about the selected cut width (1mm). Nevertheless, it was mentioned that the results might be sensitive to these two parameters (*i.e.* cut width and increment).

Linear elements were used in the cutting simulation with a cut width of 0.254 mm. The cut increment was chosen according to the elements length in the cut direction (1 mm). However the choice of these dimensions was not explained. Different constraining locations relative to the cut plane were analysed for plasticity assessment.

Prime applied the symmetry boundary conditions release approach [25] for simulating wire EDM cutting in slitting plasticity assessment. Second order elements with reduced integration were used. It was mentioned that second order elements capture better the

stress concentration and that 'reduced integration' increases the accuracy of the results and decreases the computation time [25] . It was also reported that a mesh convergence study was conducted. However no recommendation relating to the mesh type and size was given.

In summary simulation of the contour method cutting process can be conducted by symmetry boundary condition release or material removal approaches, but the former approach neglects the effect of the finite width cut created in practice.

Linear mesh elements have been mainly used. This type of mesh element was also recommended by Dennis et *al.*[61]. However, it can be clearly seen from the review that less effort has been devoted to study the effect of mesh size on the results and the choice of cut width in the material removal approach.

In the present work, a sensitivity study on mesh size, crack width and crack tip shape will be conducted to support simulation of the contour method and the assessment of plasticity (see Chapter 5).

2.10. References

1. British Standard - BS 7910 (2005) Guide to methods for assessing the acceptability of flaws in metallic structures.

2. ASME (2013) API 579-1/ASME FFS-1- Fitness-for Service.

3. Central Electricity Generating Board (1982) Assessment of the Integrity of Structures Containing Defects: Validation. Supplement 1. CEGB Research Division,

4. Bouchard PJ (2001) Residual stresses in lifing and structural integrity assessment. In: Buschow KHJ (ed) Encyclopaedia of Materials Science and Technology Pergamon, Oxford,

5. Bouchard PJ (2001) Residual Stresses in Lifetime and Structural Integrity Assessment. In: Encyclopedia of Materials: Science and Technology (Second Edition). Elsevier, Oxford, pp 8134-8142

6. Hu Y, Yao Z, Hu J (2009) An Analytical Model to Predict Residual Stress Field Induced by Laser Shock Peening. Journal of Manufacturing Science and Engineering 131 (3):031017-031017

7. Tsui YC, Clyne TW (1997) An analytical model for predicting residual stresses in progressively deposited coatings Part 1: Planar geometry. Thin Solid Films 306 (1):23-33

8. API (2007) Fitness-for-Service. API-579 API 579-1/ASME FFS-1 Second edition

9. Bate S, Hurrell P (2010) The development of tools and methods to manage residual stresses in the future design of nuclear plant. International Journal of Pressure Vessels and Piping 87 (11):637-642

10. Ogawa K, Chidwick LO, Kingston EJ, Dennis R, Bray D, Yanagida N (2008) The Measurement and Modelling of Residual Stresses in a Stainless Steel Pipe Girth Weld / PVP2008-61542. Paper presented at the ASME Pressure Vessels and Piping Division Conference, Chicago, USA,

11. Free JA, Porter Goff RFD (1989) Predicting residual stresses in multi-pass weldments with the finite element method. Computers & Structures 32 (2):365-378

12. Withers P, Bhadeshia H (2001) Overview Residual Stress Part 1 - Measurement Techniques. Materials Sci Technol 17:355

13. Withers P, Bhadeshia H (2001) Overview Residual Stress Part 2 - Nature and Origins. Materials Sci Technol 17:366

14. Hutchings MT, Withers PJ, Holden MT, Lorentzen T (2005) Introduction to the Characterization of Residual Stress by Neutron Diffraction. Taylor & Francis Group,

15. Noyan IC, Cohen JB (1987) Residual Stress-Measurement by Diffraction and Interpretation. Springer, New York

16. Withers PJ (2007) Residual stress and its role in failure. Reports on Progress in Physics 70 (12):2211

17. Inoue T, Totten GE, Howes MAH (2001) Handbook of residual stress and deformation of steel. ASM International, Materials Park, Ohio

18. Prime MB (2012) Type of residual stress measured by the contour method. Conversation,

19. Lu J, James M, Roy G (1996) Handbook of Measurement of Residual Stresses. Prentice Hall,

20. Prime MB (1999) Measuring residual stress and the resulting stress intensity factor in compact tension specimens. Fatigue & Fracture of Engineering Materials & Structures 22 (3):195-204

21. Procter E, Beaney EM (1987) The trepan or ring core method, centre-hole method, Sach's method, blind hole methods, deep hole technique. Adv Surf Treat 4:166-198

22. ASTM (2008) Determining residual stresses by the Hole-drilling Strain-Gage Method.

23. Veqter (2013) Residual stress measurement techniques [Online]. http://www.veqter.co.uk. Accessed 3 May 2013

24. ASME (2012) Hole drilling [Online]. http://www.asminternational.org/emails/etsspraytips/090809/tssenews090809.html. Accessed 14 August 2012

25. Prime MB (2010) Plasticity Effects in Incremental Slitting Measurement of Residual Stresses. Engineering Fracture Mechanics and Technology 77:1552-1566

26. Goudar DM, Truman CE, Smith DJ (2009) Evaluating Uncertainty in Residual Stress Measured Using the Deep-Hole Drilling Technique. Strain 9999 (9999)

27. Leggatt RH, Smith DJ, Smith SD, Faure F (1996) Development and experimental validation of the deep hole method for residual stress measurement. The Journal of Strain Analysis for Engineering Design 31 (3):177-186

28. Smith DJ, Bouchard PJ, George D (2000) Measurement and prediction of residual stresses in thick-section steel welds. Journal of Strain Analysis for Engineering Design 35 (4):287–305

29. Bateman MG, Miller OH, Palmer TJ, Breen CEP, Kingston EJ, Smith DJ, Pavier MJ (2005) Measurement of residual stress in thick section composite laminates using the deep-hole method. International Journal of Mechanical Sciences 47 (11):1718-1739

30. Prime MB, Hill MR (2002) Residual stress, stress relief, and inhomogeneity in aluminium plate. Scripta Materiala 46 (1):77-82

31. Cheng W, Finnie I (2007) Residual stress measurement and the slitting method. Springer Science+Business Media, LLC,

32. Hosseinzadeh F, Toparli MB, Bouchard PJ (2012) Slitting and Contour Method Residual Stress Measurements in an Edge Welded Beam. Journal of Pressure Vessel Technology 134 (1):011402-011406

33. Schindler H, Cheng W, Finnie I (1997) Experimental determination of stress intensity factors due to residual stresses. Experimental Mechanics 37 (3):272-277

34. Prime MB (1999) Residual Stress Measurement by Successive Extension of a Slot: The Crack Compliance Method. Applied Mechanics Reviews 52 (2):75-96

35. Schajer GS, Michael B. Prime (2007) Resisdual stress solutions extrapolation for slitting method using equilibrium constants. Journal of Engineering Materials and Technology 129 (2):226-232

36. Schindler HJ, Bertschinger P (1997) Some Steps Towards Automation of the Crack Compliance Method to Measure Residual Stress Distributions. Paper presented at the 5th Int. Conference on Res. Stress, Linköping, Sweden

37. Hosseinzadh Torknezhad F, Bouchard PJ, James JA (2010) Measurements of Residual Stress in a Welded Compact Tension Specimen Using the Neutron Diffraction and Slitting Techniques. Materials Science Forum 652:210-215

38. Traore Y, Paddea S, Bouchard PJ, Gharghouri MA (2012) Measurement of the Residual Stress Tensor in a Compact Tension Weld Specimen. Experimental Mechanics:1-14

39. Fett T, Munz D (1997) Stress intensity factors and weight functions. Computational Mechanics Publications,

40. British Standard Institute Staff (2005) Non-destructive testing - Standard test method for determining residual stresses by neutron diffraction.

41. Fitzpatrick E, Lodini A (2003) Analysis of Residual Stress by Diffraction using Neutron and Synchrotron Radiation. Taylor & Francis,

42. Schajer G, Steinzig M (2005) Full-field calculation of hole drilling residual stresses from electronic speckle pattern interferometry data. Experimental Mechanics 45 (6):526-532

43. Withers PJ, Preuss M, Steuwer A, Pang JWL (2007) Methods for obtaining the strain-free lattice parameter when using diffraction to determine residual stress. Journal of Applied Crystallography 40 (5):891-904

44. Paddea S, Francis JA, Paradowska AM, Bouchard PJ, Shibli IA (2012) Residual stress distributions in a P91 steel-pipe girth weld before and after post weld heat treatment. Materials Science and Engineering: A 534 (0):663-672

45. Santisteban JR, Daymond MR, James JA, Edwards L (2006) ENGIN-X: a third-generation neutron strain scanner. Journal of Applied Crystallography 39 (6):812-825

46. Daymond MR, Bourke AM, Von Dreele RB, Clausen B, Lorentzen T (1997) Use of Rietveld refinement for elastic macrostrain determination and for evaluation of plastic strain history from diffraction spectra Journal of Applied Physics 82 (4)

47. Kröner E (1958) Berechnung der elastischen Konstanten des Vielkristalls aus den Konstanten des Einkristalls. Zeitschrift für Physik 151 (4):504-518

48. Manns T, Scholtes B (2010) Eine Software zur Berechnung diffraktionselastischer Konstanten aus Einkristalldaten. HTM J Heat Treatm Mat 65:75-84

49. Woo W, Em V, Mikula P, An G, Seong B (2011) Neutron diffraction measurements of residual stresses in a 50 mm thick weld. Materials Science and Engineering 528 (12):4120-4124

50. Winholtz RA, Krawitz AD (1995) The relaxation of residual stresses with postweld heat treatment in a high-performance weld measured with neutron diffraction. MMTA 26 (5):1287-1295

51. Prime MB (2001) Cross-Sectional Mapping of Residual Stresses by Measuring the Surface Contour After a Cut. Journal of Engineering Materials and Technology 123 (2):162-168

52. Zhang Y, Ganguly S, Stelmukh V, Fitzpatrick ME, Edwards L (2003) Validation of the Contour Method of Residual Stress Measurement in a MIG 2024 Weld by Neutron and Synchrotron X-ray Diffraction. Journal of Neutron Research 11 (4):181-185

53. Woo W, Choo H, Prime MB, Feng Z, Clausen B (2008) Microstructure, texture and residual stress in a friction-stir-processed AZ31B magnesium alloy. Acta Materialia 56 (8):1701-1711

54. Lambert TA, Murphy KD (2002) Modal convection and its effect on the stability of EDM wires. International Journal of Mechanical Sciences 44 (1):207-216

55. Hosford WF (1979) On yield loci of anisotropic cubic metals. Paper presented at the 7th North American Metalworking Conference, Deaborn, Michigan, USA,

56. DeWald AT, Hill MR (2009) Eigenstrain-based model for prediction of laser peening residual stresses in arbitrary three-dimensional bodies. Part 1: model description. The Journal of Strain Analysis for Engineering Design 44 (1):1-11

57. Richter-Trummer V, Tavares SMO, Moreira PMGP (2008) Residual stress measurement using the contour and the sectioning methods in a MIG weld: Effects on the stress intensity factor. Ciência & Tecnologia dos Materiais 20(1-2):p.114-119

58. Bueckner HF (1958) The propagation of cracks and the energy of elastic deformation. Transactions ASME 80:1225-1230

59. Prime MB, Kastengren AL (2010) The contour method cutting assumption: error minimization and correction. Paper presented at the SEM Annual conference & exposition on experimental and applied mechanics Indianapolis, Indiana, USA,

60. Cheng W, Finnie I, Gremaud M, Prime MB (1994) Measurement of Near Surface Residual Stresses Using Electric Discharge Wire Machining. Journal of Engineering Materials and Technology 116 (1):1-7.

61. Dennis RJ, Bray DP, Leggatt NA, Turski M (2008) Assessment of the Influence of Plasticity and Constraint on Measured Residual Stresses Using the Contour Method / PVP2008-61490. Paper presented at the ASME Pressure Vessels and Piping Division Conference, Chicago, USA,

62. Qu J (2002) Development of Cylindrical Wire Electrical Discharge Machining Process and Investigation of Surface Integrity and Mechanical Property of EDM Surface Layers. PhD Thesis, Faculty of North Carolina State University, Raleigh, North Carolina

63. Prime M, Sebring R, Edwards J, Hughes D, Webster P (2004) Laser surface-contouring and spline data-smoothing for residual stress measurement. Experimental Mechanics 44 (2):176-184

64. HR Machinery (2012) CMM [Online]. http://www.hrmachinery.com/machines/CMMs.htm. Accessed 14 August 2012

65. Zhang Y, Ganguly S, Edwards L, Fitzpatrick ME (2004) Cross-sectional mapping of residual stresses in a VPPA weld using the contour method. Acta Materialia 52 (17):5225-5232

66. Johnson G (2008) Residual stress measurements using the contour method. PhD Thesis, University of Manchester, Manchester

67. Renishaw (2013) Renishaw trigger probe kinematic location [Online]. http://www.renishaw.com/en/rmp60-touch-probe--6100. Accessed 12 May 2013

68. Renishaw (2013) Probe tip materials [Online]. http://www.renishaw.com/en/materials--6423. Accessed 12 May 2013

69. Renishaw (2013) Different contacts of the probe tip during measurement [Online]. http://www.touch-probe.com/kinematic-resistive-probes/factors-in-kinematic-resistive-probe-performance/. Accessed 12 May 2013

70. Pain HJ (2005) The Physics of Vibrations and Waves. Wiley,

71. Vieira M, Shimada K, Furuhata T (2003) Smoothing of Noisy Laser Scanner Generated Meshes Using Polynomial Fitting and Neighborhood Erosion. Journal of Mechanical Design 126 (3):495-503

72. Hosseinzadeh F, Bouchard PJ (2012) Mapping Multiple Components of the Residual Stress Tensor in a Large P91 Steel Pipe Girth Weld Using a Single Contour Cut. Experimental Mechanics:1-11

73. Hosseinzadeh F, Ledgard P, Bouchard PJ (2012) Controlling the Cut in Contour Residual Stress Measurements of Electron Beam Welded Ti-6Al-4V Alloy Plates. Experimental Mechanics:1-11

74. Bouchard PJ, Turski M, Smith MC (2009) Residual Stress Concentrations in a Stainless Steel Slot-Weld Measured by the Contour Method and Neutron Diffraction / PVP2009-77234. Paper presented at the ASME PVP Conference, Prague, Czech Republic,

75. MATLAB (2009) Version 7.8.0 (R2009a). The MathWorks Inc

76. Zhang Y (2004) Numerical and Experimental Exploration of the Contour Method for Residual Stress Evaluation. PhD Thesis, The Open University, Milton Keynes

77. Prime MB, Hughes DJ, Webster PJ (2001) Weld Application of a New Method for Cross-Sectional Residual. Stress Mapping. Paper presented at the Society for Engineering Mechanics Annual Conference and Exposition, Portland, Oregon, USA,

78. Pagliaro P, Prime M, Swenson H, Zuccarello B (2009) Measuring Multiple Residual-Stress Components using the Contour Method and Multiple Cuts. Experimental Mechanics 50 (2):187-194

79. DeWald A, Hill M (2006) Multi-Axial Contour Method for Mapping Residual Stresses in Continuously Processed Bodies. Experimental Mechanics 46 (4):473-490

80. Bouchard PJ, Ledgard P, Hiller S, Hosseinzadeh F (2012) Making the Cut for the Contour Method. Paper presented at the 15th International Conference on Experimental Mechanics, Porto, Portugal,

81. Hoffman O, Sachs G (1953) Introduction to the theory of plasticity for engineers. McGraw-Hill,

82. Kachanov LM (2004) Fundamentals of the Theory of Plasticity. Dover Publications,

83. Khan AS, Huang S (1995) Continuum Theory of Plasticity. 1 edn. Wiley-Interscience, New York

84. Lubliner J (2009) Plasticity Theory. Dover Publications Inc,

85. Encyclopedia Britannica (2012) Strain [Online]. http://www.britannica.com/EBchecked/media/113923/The-stress-strain-curve-illustrating-the-stretching-of-a-piece. Accessed 13 August 2012

86. Hill R (1950) The Mathematical Theory of Plasticity. OUP Oxford, Oxford

87. Smith MC, Bouchard PJ, Turski M, Edwards L, Dennis RJ (2012) Accurate prediction of residual stress in stainless steel welds. Computational Materials Science 54 (0):312-328

88. Cook RD (2001) Concepts and applications of finite element analysis. Wiley,

89. Shin S (2005) FEM analysis of plasticity-induced error on measurement of welding residual stress by the contour method. Journal of Mechanical Science and Technology 19 (10):1885-1890

90. Dennis RJ, Leggatt NA, Kutarski EA (2009) Investigation of the Performance of the Contour Residual Stress Measurement Method When Applied to Welded Pipe Structures / PVP2009-77470. Paper presented at the ASME Pressure Vessels and Piping Division Conference, Prague, Czech Republic,

91. Prime M (2011) Contour Method Advanced Applications: Hoop Stresses in Cylinders and Discontinuities. In: Proulx T (ed) Engineering Applications of Residual Stress, Volume 8. Conference Proceedings of the Society for Experimental Mechanics Series. Springer New York, pp 13-28. doi:10.1007/978-1-4614-0225-1_2

92. Beghini, M., Bertini, L., Raffaelli, P. (1994) Numerical analysis of plasticity effects in the hole-drilling residual stress measurement. Journal of testing and evaluation 22 (6):522-529

93. Vangi D, Tellini S (2009) Hole-Drilling Strain-Gauge Method: Residual Stress Measurement With Plasticity Effects. Journal of Engineering Materials and Technology 132 (1)

94. Ermini M (2000) Plasticity Effects in Residual Stress Measurement by the Hole Drilling Method. Strain 36 (2):55-59

95. Beghini M, Santus C, Valentini E, Benincasa A (2011) Experimental Verification of the Hole Drilling Plasticity Effect Correction. Materials Science Forum 681:151-158

96. Seifi R, Salimi-Majd D Effects of plasticity on residual stresses measurement by hole drilling method. Mechanics of Materials 53 (0):72-79

97. Mahmoudi AH, Truman CE, Smith DJ, Pavier MJ (2011) The effect of plasticity on the ability of the deep hole drilling technique to measure axisymmetric residual stress. International Journal of Mechanical Sciences 53 (11):978-988

98. Mahmoudi AH, Zheng G, Smith DJ, Truman CE, Pavier MJ (2013) A Procedure to Measure Biaxial Near Yield Residual Stresses Using the Deep Hole Drilling Technique. Experimental Mechanics:1-9. doi:10.1007/s11340-013-9729-2

99. Hosseinzadeh F, Mahmoudi AH, Truman CE, Smith DJ (2011) Application of deep hole drilling to the measurement and analysis of residual stresses in steel shrink fitted assemblies Strain 47 (2):412–426

100. Bathe K-J, Wilson EL (1976) Numerical methods in finite element analysis. Prentice-Hall Englewood, New Jersey

101. Collatz L (1966) The numerical treatment of differential equations. 3 edn. Springer, New York

102. Courant R (1943) Variational methods for the solution of problems of equilibrium and vibrations. Bulletin of the American Mathematical Society 49:1-23

103. Courant R, Hilbert D (1953) Methods of Mathematical Physics, vol 1. Wiley-VCH,

104. Synge JL (1957) The Hypercircle in Mathematical Physics. Cambridge University Press, London

105. Crisfield MA (1996) Non-linear Finite Element Analysis of Solids and Structures, vol 1. Wiley, London

106. Griffith AA (1921) The Phenomena of Rupture and Flow in Solids. Philosophical Transactions of the Royal Society of London Series A, Containing Papers of a Mathematical or Physical Character 221:163-198

107. Irwin GR (1957) Analysis of stresses and strains near the end of a crack traversing a plate. Journal of Applied Mechanics 24:361-364

108. Janssen M, Zuidema J, Wanhill RJH (2002) Fracture Mechanics. 2nd edn. Delft University Press, Delft

109. Rice JR (1968) A path independent integral and the approximate analysis of strain concentration by notches and cracks. Journal of Applied Mechanics 35:379-386

110. ASTM (2006) ASTM E399 - Standard Test Method for Linear-Elastic Plane-Strain Fracture Toughness K Ic of Metallic Materials.

111. Shih CF (1981) Relationships between the J-integral and the crack opening displacement for stationary and extending cracks. Journal of the Mechanics and Physics of Solids 29 (4):305-326

112. Sanford RJ (2002) Principles of Fracture Mechanics. Prentice Hall, Upper Saddle River, New Jersey

113. Unger DJ (2001) Analytical Fracture Mechanics. Dover Publications, INC., Mineola, New York

114. McClintock F, Irwin G (1995) Plasticity Aspects of Fracture Mechanics. Fracture toughness, testing and its application-ASTM STP:84-113

115. Tada H, Paris PC, Irwin GR (1985) The stress analysis of cracks handbook: by Hiroshi Tada, with the cooperation of Paul C. Paris and George R. Irwin. Paris Productions & (Del Research Corp.),

116. Feng X-Q, Shi Y-F, Wang X-Y, Li B, Yu S-W, Yang Q (2010) Dislocation-based semi-analytical method for calculating stress intensity factors of cracks: Two-dimensional cases. Engineering Fracture Mechanics 77 (18):3521-3531

117. Rooke DP, Cartwright DJ, Executive GBMoDP (1976) Compendium of Stress Intensity Factors. Stationery Office,

118. EDF Energy (2013) R-Code.V4.4. http://www.r-desk.co.uk/software. Accessed 24 February 2013

119. TWI (2013) TWI Software-Crackwise 4. http://www.twisoftware.com/crackwise. Accessed 11 May 2013

120. Creager M, Paris PC (1967) Elastic field equations for blunt cracks with reference to stress corrosion cracking. International Journal of Fracture 3 (4):247-252

121. Narasimhan R, Rosakis AJ, Hall JF (1987) A Finite Element Study of Stable Crack Growth Under Plane Stress Conditions: Part II-Influence of Hardening. Journal of Applied Mechanics 54 (4):846-853

122. Narasimhan R, Rosakis AJ, Hall JF (1987) A Finite Element Study of Stable Crack Growth Under Plane Stress Conditions: Part I-Elastic-Perfectly Plastic Solids. Journal of Applied Mechanics 54 (4):838-845

123. Rice JR (1975) Elastic-Plastic Models for Stable Crack Growth. In: May MJ (ed) Mechanics and Mechanism of Crack Growth. British Steel Corporation Physical Metallurgy Centre Publication, Sheffield, England, pp 14-39

124. Sorensen EP (1978) A finite element investigation of stable crack growth in anti-plane shear. International Journal of Fracture 14 (5):485-500

125. Rice JR (1968) Mathematical Analysis in the Mechanics of Fracture. In: Liebowitz H (ed) Fracture: An Advanced Treatise, vol 2. Academic Press, New York, pp 191-311

126. Sham TL (1983) A Finite-Element Study of the Asymptotic Near-Tip Fields for Mode I Plane-Strain Cracks Growing Stably in Elastic-Ideally Plastic Solids. In: Shih CF, Gudas JP (eds) Elastic-plastic Fracture: Second Symposium, Volume I- Inelastic Crack Analysis. ASTM STP 803, vol 1. American Society for Testing and Materials, pp I.52-I.79

127. ABAQUS (2010) ABAQUS/Standard Documentation Version 6.10.2. ABAQUS, Inc

Chapter 3: Effect of restraint on plasticity-induced errors in the contour method

The cutting process is the most critical step in the contour method of residual stress measurement because it affects all the subsequent steps and therefore has a strong influence on the measured results. As reported in the literature review chapter, if the test component is not sufficiently restrained during the cut, bulging and plasticity effects can introduce errors in the profile of stress which is determined.

The objective of this chapter is to investigate the effect of different types of restraint conditions that are applied during cutting (i.e. how the component is held) on the development of plasticity and the errors this introduces in contour method measurements. The investigation will be conducted in three different steps.

First, an introduction to the different types of restraining conditions used for contour method cuts is given. Second, residual stress measurements carried out by the contour method on a Compact Tension (CT) specimen using asymmetric restraint conditions are presented. These stress results are then compared with those obtained by neutron diffraction and the slitting method on the same component. Finally, 2D FE analysis simulating the contour method and the development of plasticity is undertaken to investigate the effect of restraint. The simulated results for different restraint conditions are compared with each other, with the CT specimen contour measurements and finally with some published contour work.

3.1. Restraint conditions in the contour method

As earlier mentioned, the test component restraining during the cutting process plays a significant role in introducing or mitigating different types of error such as bulging and plasticity effects.

Different restraining conditions are employed in the contour method to hold the cut part from movement and to control the cut faces opening/closure.

In practice the cut part restraint from movement can be achieved by using 'finger' clamp tools. Figure 3-1-a shows a schematic of a 'finger' clamp configuration. These 'finger' clamps apply a 'vertical load' on the top surface of the cut part and rely on friction to prevent lateral movement. The degree of restraining with this clamping system depends on the magnitude of the 'applied load'. Therefore, the cut parts might still move relative to the clamps, if the 'applied load' is not sufficient.

In the contour method, we want to closely control "mode I" opening/closure of the cut faces during the cut. However, in practice, close control is difficult to achieve. But ideal contour restraint conditions can be approached by rigidly clamping the specimen on both sides of the cut line (e.g. by using several fitted bolts screwed into a massive bed plate) [1]. Figure 3-1-b illustrates an example of firm restraint using fitted bolts. The efficiency of controlling the cut opening/closure depends on the distance between the bolts relative to the cut path, Figure 3-1-b [2,3].

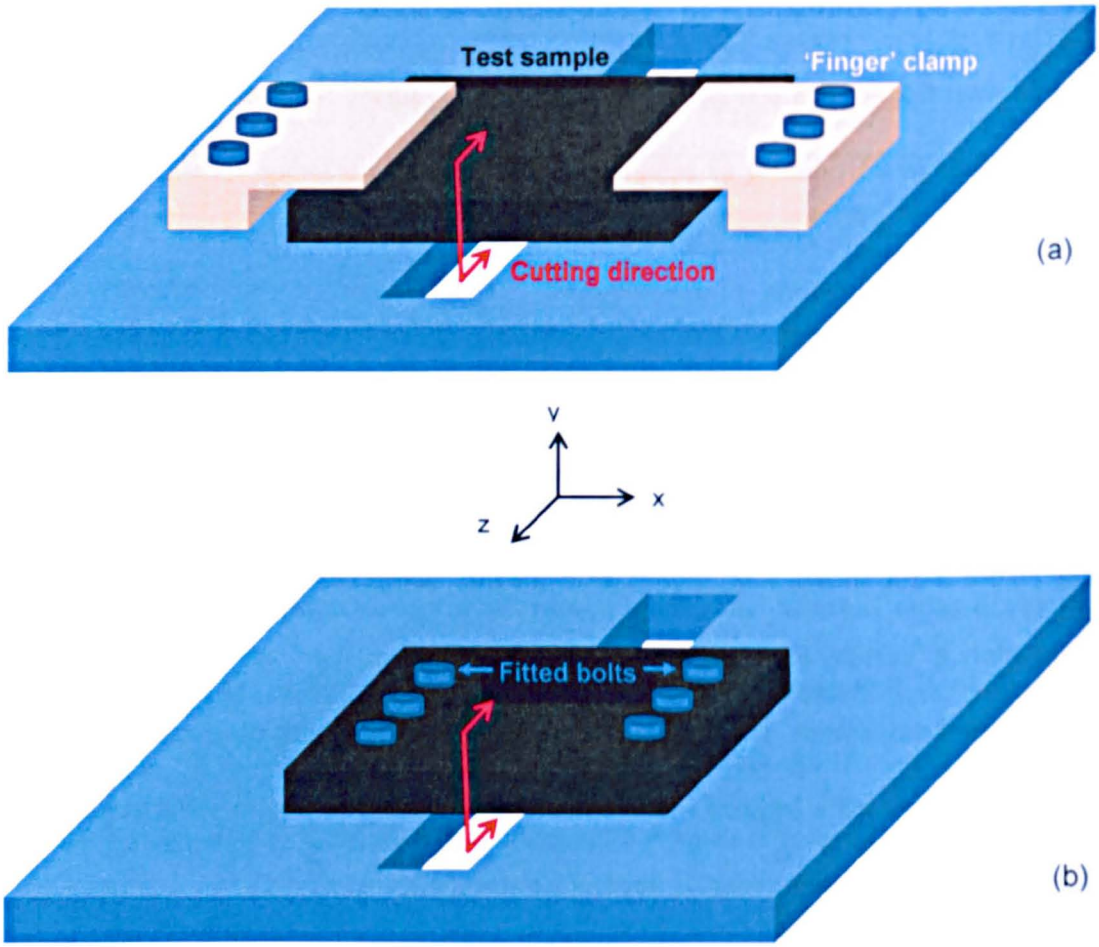

Figure 3-1: Schematic representation of 'finger' (a) and 'fitted bolts' clamping (b).

3.2. Residual stress measurement in a CT specimen blank

Creep crack growth tests in the heat affected zone (HAZ) of weldments made from Esshete 1250 stainless steel have been conducted by EDF Energy (formerly British Energy). The tests exhibited high crack growth rates and unexpectedly large crack opening displacement. The hypothesis put forward to explain these results was that the welded CT specimens contained significant levels of residual stress, which had the effect of increasing the net opening stress and crack driving force.

The material tested by EDF Energy was extracted from a manual metal arc (MMA) welded joint made from Esshete 1250 steel. In order to create CT specimens of standard

dimensions, parent material make-up pieces were electron beam welded to the extracted samples. These "composite" test specimens were designed such that crack growth would develop in the HAZ along a plane close to and parallel with the MMA weldment fusion boundary.

The primary aim of the work described here was to characterise the magnitude and nature of residual stresses along the crack propagation plane in a "composite" welded CT test specimen blank.

First, neutron diffraction was applied to measure the full residual stress tensor along the path of the crack in the HAZ of the MMA weld to assess the degree of triaxiality, the significance of shear stresses and the deviation of the principal stress directions from the component orthogonal axes. The results have been detailed in peer reviewed paper [4]. In this thesis only the direct components of the neutron diffraction strain and stress measurements associated with the component orthogonal axes are reported.

Following residual stress measurement by neutron diffraction, the distribution of the transverse component of residual stress was measured by the contour and slitting methods, in tandem. In this instance the specimen was cut incrementally (for slitting) with asymmetric restraint, that is just one side of the cut was held. The potential influence of plasticity on the slitting results is assessed using the approach of Prime [5].

Finally, the results from the contour method are compared with those obtained by neutron diffraction and slitting to assess the effect of potential plastic strains introduced owing to the lack of restraint during cutting.

3.2.1. Specimen

The T-shaped test coupon shown in Figure 3-2 was made by electron beam (EB) welding a parent metal extension piece to a cross-weld sample extracted from a purpose-made pipe butt weld. The extension piece was added to the outer surface of the pipe sample so that a CT specimen of standard dimensions could be extracted for creep crack growth testing of HAZ material, as shown in Figure 3-2. The T-shaped test coupon was 52.6 mm deep, 69.3 mm wide and 21.3 mm thick.

The pipe was made from Esshete 1250, a high manganese (6.5 %) austenitic stainless steel that had previously experienced prolonged exposure to high temperature service conditions. The multi-pass pipe butt weld was made using a manual metal arc (MMA) process with 3.2, 4 and 5 mm diameter ESAB OK 69.86 electrodes. The compositions of the service-exposed parent metal and weld consumables are listed in Table 3-1. The extension piece, also made from Esshete 1250, came from a separate source. Tensile properties for the materials were supplied by EDF Energy. The 0.2% and 1% room temperature flow stress values for the parent material were 241.1 MPa and 370 MPa, respectively. The corresponding values for the MMA weld metal were 534.5 MPa and 563.9 MPa. The elastic properties of the parent materials and weld metal were assumed to be isotropic having a Young's modulus of 204.5 GPa and a Poisson's ratio of 0.29 at room temperature [6]. The mean linear intercept grain size of the ex-service pipe parent material was measured to be 43.5 μm.

The outline geometry for a CT specimen of standard dimensions [7] with a thickness B = 19 mm is marked on the photograph of the supplied coupon in Figure 3-2. A plain rectangular block 47.5 mm ($1.25W$) wide, 45.3 mm ($1.2W$) deep and 21 mm thick was

extracted from the composite coupon by wire EDM, see Figure 3-3. The extracted block is referred to hereafter as the "CT blank."

When determining levels of strain and stress in materials using neutron diffraction, it is essential to determine the stress-free lattice parameter in reference materials representative of where the lattice strain is being measured. This was achieved by removing a 5 mm thick slice from the CT blank face (labelled A in Figure 3-3) by wire EDM and then extracting small, notionally stress-free, cubes at (y, z) positions corresponding to the neutron measurement locations. This machining operation reduced the thickness of the CT blank from 21 mm to 16 mm which is smaller than the standard CT thickness of 19 mm for W = 38 mm. This compromise was an unavoidable consequence of the imperative to secure reliable measurements of the stress-free lattice parameters. Following removal of the 5 mm slice, face A of the CT blank was polished and etched to reveal the MMA weld fusion boundary. A datum line was then scribed on this surface 2 mm from the deepest point of penetration of the MMA weld passes, for the purpose of indicating the yz measurement plane for all three residual stress measurement techniques.

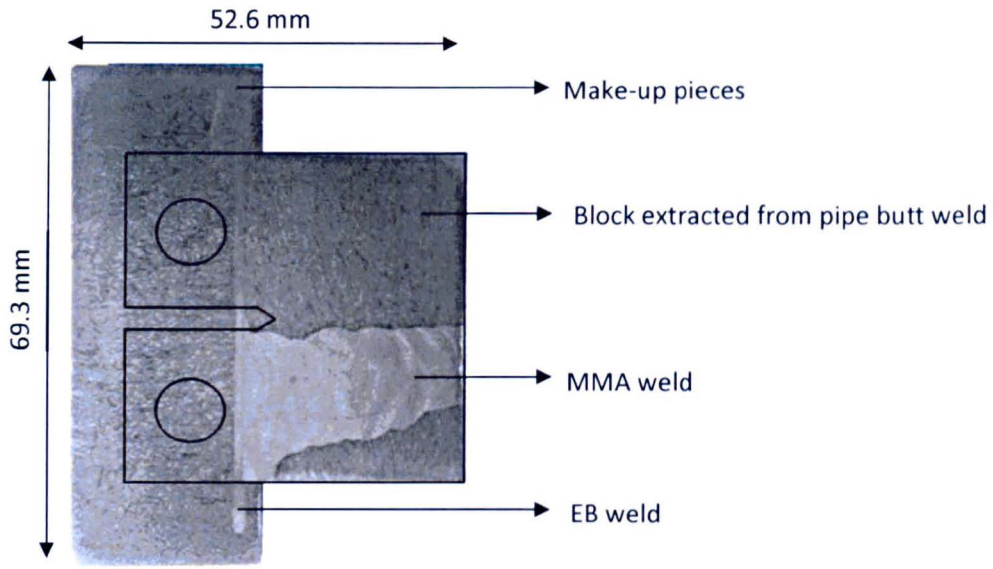

Figure 3-2: Photograph of the initial T-shaped coupon (21.3 mm thick) prior to extracting a CT specimen blank (CT specimen outline marked showing proximity of the slot tip to the MMA weld).

Table 3-1: Chemical compositions of the Esshete 1250 parent and weld metal in wt.%.

	Esshete 1250	**ESAB OK 69.86**
C	0.09	0.11
Si	0.49	0.35
Mn	6.5	7.1
P	0.019	0.021
S	0.007	0.003
Cr	15.1	16.4
Mo	1.03	1.12
Ni	10.1	8.9
Al	<0.005	<0.005
B	0.004	0.002
Co	0.03	0.044
Cu	0.1	0.05
Nb	0.78	1.07
Ti	0.008	0.013
V	0.28	0.28
W	0.01	0.03
N	0.053	0.047

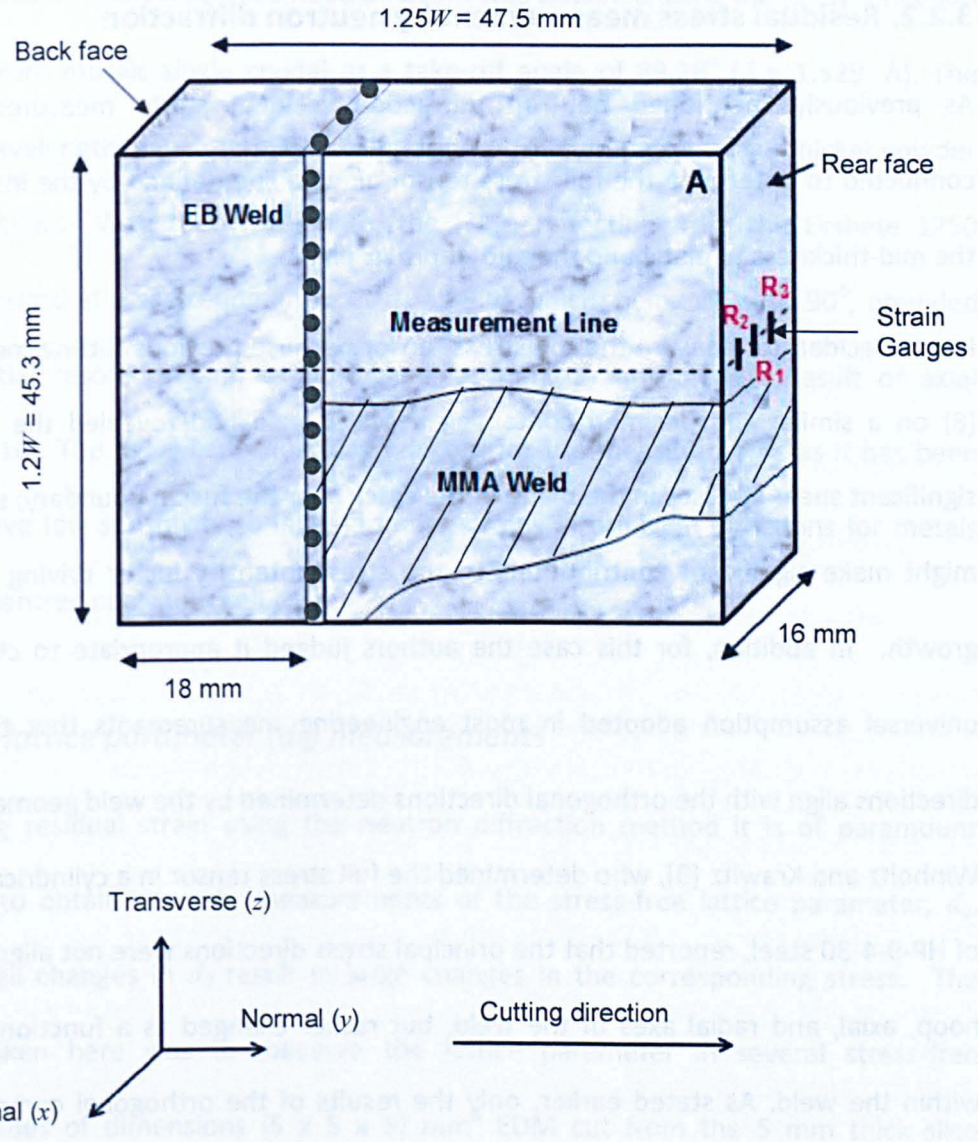

Figure 3-3: Schematic drawing showing the final dimensions of the Esshete CT blank for neutron diffraction, slitting and contour residual stress measurements. The measurement line/plane and locations of back-face strain gauges (R1, R2, and R3) applied for the slitting method are indicated.

3.2.2. Residual stress measurement by neutron diffraction

As previously mentioned neutron diffraction residual strain measurements were conducted to determine the full stress tensor along a line defined by the intersection of the mid-thickness yz plane and the mid-depth yx plane.

It was decided to measure the full stress tensor because previous slitting measurements [8] on a similar CT specimen containing a MMA weld had revealed the presence of significant shear stresses in the plane of the crack near the fusion boundary; such stresses might make significant contributions to the stress intensity factor driving creep crack growth. In addition, for this case the authors judged it appropriate to challenge the universal assumption adopted in most engineering measurements that the principal directions align with the orthogonal directions determined by the weld geometry. Indeed, Winholtz and Krawitz [9], who determined the full stress tensor in a cylindrical weldment of HP-9-4-30 steel, reported that the principal stress directions were not aligned with the hoop, axial, and radial axes of the weld, but rather changed as a function of position within the weld. As stated earlier, only the results of the orthogonal components (i.e. stress components in the test sample x, y and z directions) are reported here.

The neutron diffraction technique for the measurement of residual stresses has been explained in Chapter 2. Here the experimental procedure and the data analysis conducted to determine the stresses in the CT blank are explained.

Experimental procedure

Neutron diffraction residual strain measurements in the composite CT blank were carried out on the L3 spectrometer of the Canadian Neutron Beam Centre, National Research

Council, Canada. A monochromatic neutron beam was obtained using the {115} reflection of a germanium mosaic single crystal at a take-off angle of 89.28° (λ = 1.529 Å). The neutrons' wavelength was determined using four diffraction peaks from a nickel powder standard sample. With this wavelength, the {311} reflection from the Esshete 1250 material occurred at a scattering angle $2\theta_{311}$ = 89.5° which, being close to 90°, provided optimal spatial resolution and avoided peak asymmetry arising as a result of axial divergence [10]. The {311} reflection was selected for the measurements as it has been shown to have low sensitivity to inter-granular strains in principal directions for metals with a face-centred cubic unit cell [11].

Stress-free lattice parameter (d_0) measurements

In measuring residual strain using the neutron diffraction method it is of paramount importance to obtain accurate measurements of the stress-free lattice parameter, d_0, because small changes in d_0 result in large changes in the corresponding stress. The approach taken here was to measure the lattice parameter in several stress-free reference cubes of dimensions (5 x 5 x 5) mm^3 EDM cut from the 5 mm thick slice removed from side A (see Figure 3-3). This material was assumed to be representative of that at mid-thickness of the CT blank in the *yz* measurement plane. This size of cube was deliberately chosen to allow the proposed (2 x 2 x 2) mm^3 sampling volume to be increased if there turned out to be insufficient statistics/intensity during the experiment.

Since the d_0 measurements sampled a relatively small volume of material at the centre of the d_0 cubes, that is well away from the cut EDM surfaces, it is reasonable to assume that they were unaffected by any local residual stresses introduced by the wire EDM cutting process. Maximum residual stress levels that might remain in the d_0 reference cubes

from the original residual stress field in the uncut component can be estimated from Figure 3-4. This chart was determined from a two-dimensional FE linear elastic stress analysis simulating application of a cosine distribution of stress to opposite edges of a rectilinear body and superposition of a negative cosine stress function throughout the body. It represents an extension of the theoretical solution for a cosine distribution applied to the edge of a semi-infinite body described by Nishioka *et al.* [12] and Withers [13]. The chart gives the percentage of the maximum stress remaining in the cubes as a function of the ratio of one-half the cube's edge length to an assumed cosine residual stress wavelength. Since the wavelengths of the longitudinal, normal and transverse residual stresses in the CT specimen are about 13, 20 and 25 mm respectively, the maximum stress likely to remain in the 5 x 5 x 5 mm^3 d_0 cubes close to the centre of the EB weld is estimated to be 22, 5 and 8 MPa respectively.

Each cube was rotated about an axis normal to the external face of the cube on a simple device during the measurement, effectively averaging the lattice spacing over all specimen directions normal to the axis of rotation. This technique was adopted following the practice of Hosseinzadeh *et al.* [8] on a similar CT specimen where a wide scatter in measurements of the stress-free lattice parameter with orientation of the d_0 cube was observed which was attributed to imprecise positioning of the cubes relative to the neutron beam and the presence of large grains. Measurements were undertaken by rotating about all three cube axes and a single orientation independent value determined at each location. Although this pragmatic experimental procedure masks potential orientation dependence of d_0 owing to plastic anisotropy effects, which may well be present in the material close to the weld metal, this was judged to be a small effect as the

{311} planes are least sensitive to plasticity induced microstresses. The gauge volume used for all measurements was $(2 \times 2 \times 2)$ mm^3.

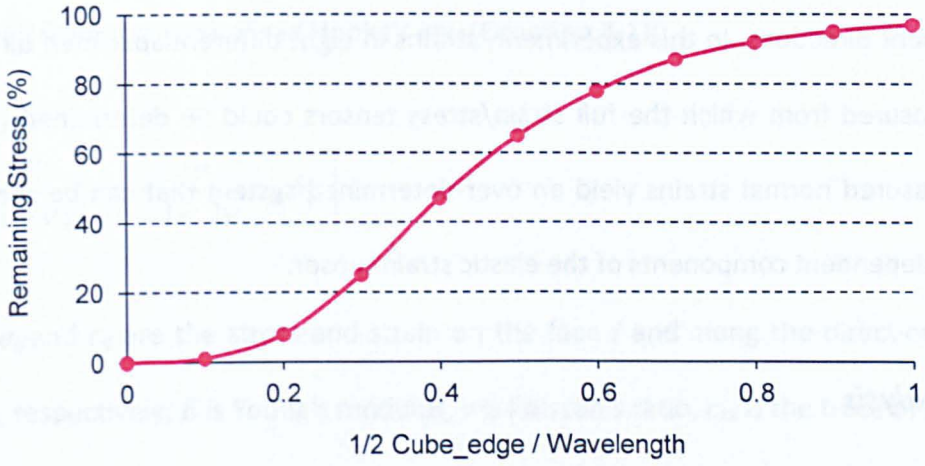

Figure 3-4: Relationship for estimating the maximum remaining residual stress at the centre of a small cube (for neutron diffraction reference lattice parameter measurements), where wavelength relates to the length-scale of a cosine distribution residual stress in the original body.

Lattice parameter measurement

A total of 23 points were selected for measurement in the *yz* plane (defined by the scribed line on face A) at mid-thickness of the CT blank. The measurement points were spaced at 2 mm intervals with the first point located 1.41 mm from the CT blank front face (Figure 3-3).

The spectrometer incident and scattered slits were carefully aligned with the centre of rotation of the sample table (the linear drives had a resolution of 0.005 mm). Neutron surface scans were then used to position the CT blank with respect to the fixed neutron gauge volume. The uncertainty in the measurement locations was in the order of 0.1 mm.

In most neutron diffraction experiments, lattice strains are measured in three orthogonal directions irrespective of whether they are principal axes. Determination of the full strain tensor at a specific location requires measurement of the lattice strain in at least six independent directions. In this experiment, strains in eight different specimen directions were measured from which the full strain/stress tensors could be determined [4]. The eight measured normal strains yield an over-determined system that can be solved for the six independent components of the elastic strain tensor.

Data analysis

The data analysis process is performed in two different steps. The first step consists of fitting the measured {311} diffraction peaks to a Gaussian distribution, determining the Bragg angle, θ_{311}, and calculating the position-dependent lattice spacings, d_{311} using Equation 2-5 in Chapter 2. The equation is shown again below.

$$\lambda = 2d\sin\theta$$

where λ is the wavelength of the incident beam, θ is the diffraction angle and d is the lattice parameter.

The stress-free reference parameter, d_0, is calculated in the same way. For each measurement point, the corresponding strain was then calculated from the measured lattice parameters using Equation 2-6 in Chapter 2 (see below).

$$\varepsilon_{xx} = \frac{d_{xx} - d_{0xx}}{d_{0xx}}$$

where ε_{xx} is the strain in the xx direction, d_{xx} is the measured lattice parameter and d_{0xx} is the unstrained lattice parameter.

Assuming isotropic elasticity, the stresses in the CT blank for all directions can be calculated from the generalised Hooke's law (Equation 3-1):

$$\sigma_{ij} = \frac{E}{(1+\nu)}\left[\varepsilon_{ij} + \frac{\nu}{1-2\nu}\varepsilon_{kk}\delta_{ij}\right] \quad \text{Eq. 3-1}$$

where σ_{ij} and ε_{ij} are the stress and strain on the face i and along the direction j of the sample, respectively, E is Young's modulus, ν is Poisson's ratio, ε_{kk} is the trace of the strain tensor and δ_{ij} is the Kronecker delta.

As mentioned earlier the full strain tensor can be determined when residual strains are measured in at least six different directions. By defining a Cartesian coordinate system related to the axes of the CT blank, one can define a rotated (primed) Cartesian coordinate system for each direction in which the normal strain is measured. In this case, the normal strain (ε'_{11}) along the x'_1 axis in the rotated coordinate system can be expressed in terms of the full strain tensor expressed in the original (unprimed) coordinate system (ε_{ij}) using the tensor transformation equation (Equation 3-2):

$$\varepsilon'_{11} = a_{1i}a_{1j}\varepsilon_{ij} \quad \text{Eq. 3-2}$$

In Equation 3-2, $a_{1m} = \cos(X'_1, X_m)$ is the direction cosine for the X'_1 axis of the rotated coordinate system with respect to the axis X_m of the unrotated specimen coordinate system. Equation 3-2 yields an expression for each measured normal lattice strain in terms of the components of the desired strain tensor. Since normal lattice strains were

determined in eight different specimen directions, eight linear equations in six unknowns were obtained, to which a least-squares procedure were applied to determine the best possible values for the six unknown components of the strain tensor.

Results

The stress-free lattice parameter distributions from the three spin axes of the eight cubes are shown in Figure 3-5. The uncertainties in these measurements were within ± 100 micro-strain. The corresponding uncertainties in the lattice parameter unit (Angstrom, Å) were about 7.44573×10^{-5} Å. It can be noticed that no significant difference is obtained between the three cube-face spin axes results. Three different regions corresponding to the make-up piece of material, the electron beam weld region and the MMA weld HAZ are observed in the profiles. The average of the data from the three sets of spin axis results is used for the strain calculations. Since direct strains were measured in 8 different specimen directions at each location, it was possible to apply a least-squares procedure to determine the best possible values for the 6 unknown components of the strain tensor. The optimised values were used for all the stress calculations.

The full stress tensor, including orthogonal and shear components, was determined for each of the 23 measurement points [4]. For the present thesis only the orthogonal components are shown and discussed.

Figure 3-6 shows the variation in longitudinal, normal, and transverse stresses along the mid-thickness measurement line in the plane yz. The uncertainty in the calculated stresses, based on the measurement of both d and d_0, was no greater than ± 25 MPa. The longitudinal stress profile shows a maximum of ~280 MPa at 19.4 mm from the front face of the CT blank. The peak stress in the transverse direction is tensile (~ 640 MPa) and

occurs at the same location. This peak is balanced by compressive stresses of up to ≈ -190 MPa in the parent metal of the extension piece and in the HAZ of the MMA weld. The peak tensile stress in the normal direction is ≈ 230 MPa in the region of the electron beam weld. As expected, the normal stress is very small close to the front and back free surfaces (20 MPa and -25 MPa).

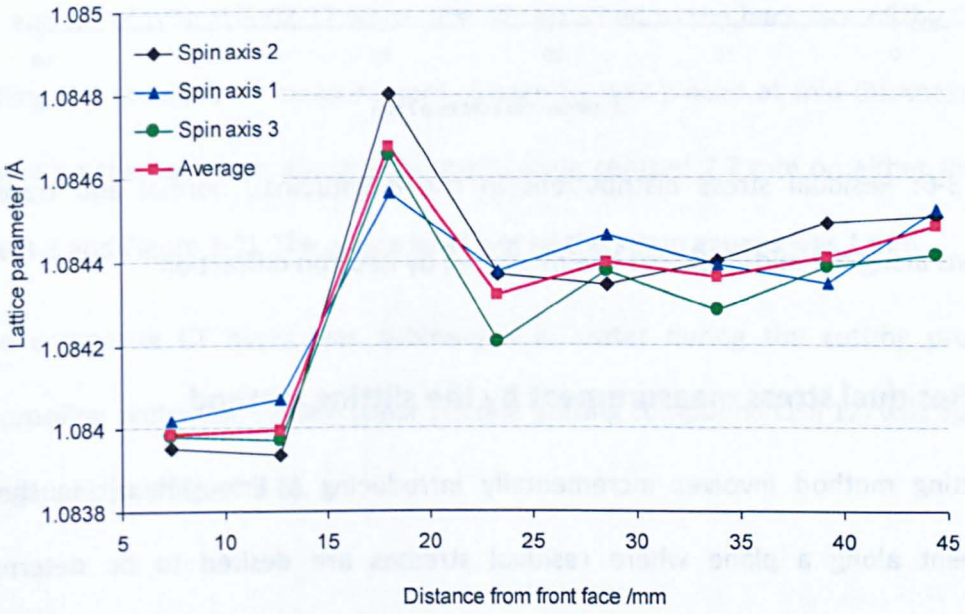

Figure 3-5: Variation of stress-free lattice parameter with distance from the front face along the measurement line. The different spin axes represent rotations about the three cube-face axes.

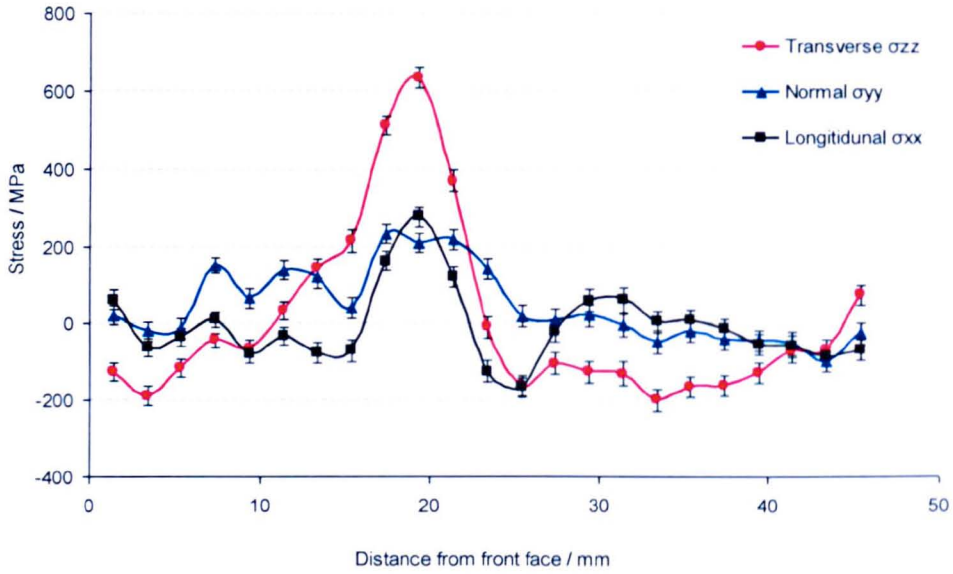

Figure 3-6: Residual stress distributions in the longitudinal, normal and transverse directions along the mid-thickness line measured by neutron diffraction.

3.2.3. Residual stress measurement by the slitting method

The slitting method involves incrementally introducing a fine slot cut in the test component along a plane where residual stresses are desired to be determined, measuring the relaxed strains at each increment of cut using strain gauges and finally back-calculating the residual stresses that were present in the test component prior to the cut using an elastic inversion process. The technique has been presented in detail in Chapter 2. Therefore, as for the neutron diffraction residual stress measurements only the experimental procedure and data analysis are described here.

Experimental procedure

The slitting experimental procedure involves sample preparation and the cutting process.

Sample preparation

The slitting method requires careful preparation before cutting by attaching strain gauges on both front and back faces of the test specimen. Measured strain data from the back face strain gauges alone are reported here because they give information about the stress distribution in the bulk of the specimen, whereas the front strain gauge results are only relevant for stresses within a couple of millimetres of the front face. Three strain gauges (R_1, R_2 and R_3) of type FLG-02-17 were carefully attached to the back face of the CT blank straddling the yz plane of measurement. Gauge R_1 was placed at mid-thickness of the specimen on the back face. Gauges R_2 and R_3 were centred 2.7 mm on either side of R_1 (Figure 3-3 and Figure 3-7). The gauge length of all the strain gauges was 1 mm.

As the composite CT blank was submerged in water during the cutting process, a waterproofing protection system (clear silicone potting compound QSil 12) was applied to all the gauges (see Figure 3-8).

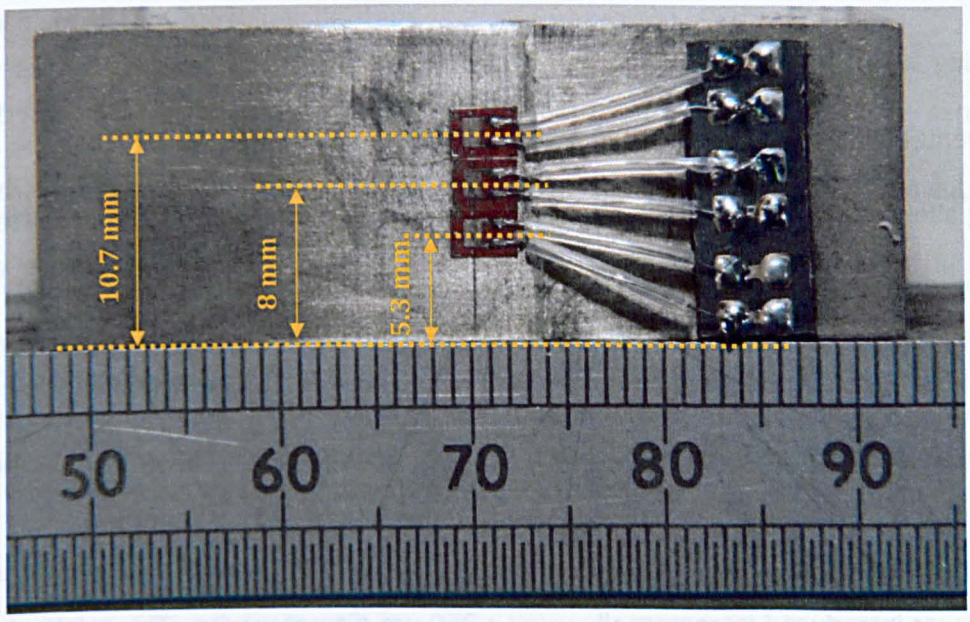

Figure 3-7: Photograph showing the strain gauges attached to the CT blank back face.

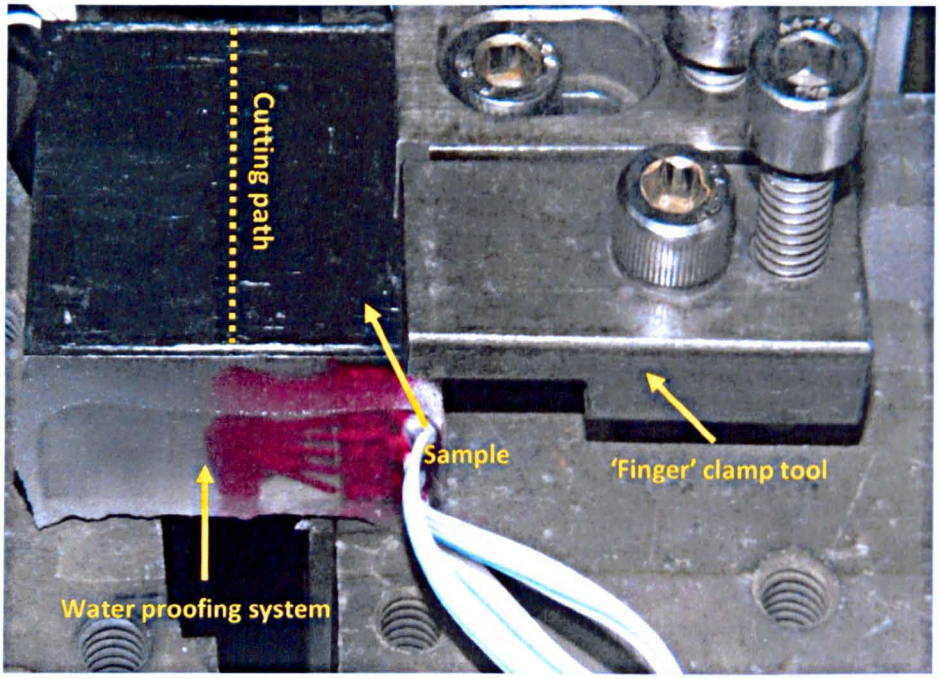

Figure 3-8: Photograph showing the waterproof system used to protect the strain gauges and the 'finger' clamp arrangement on one side of the test specimen during wire EDM cutting.

Cutting process and residual strain measurements

Following attachment of the gauges, the CT blank was cut into two halves by an incremental wire EDM process. Just one side of the CT blank was 'finger' clamped during cutting allowing the CT specimen to deform (Figure 3-8). The finger clamping system has been introduced earlier in this Chapter (see Figure 3-1-a).

The sample was submerged in de-ionised water for the wire EDM process. This minimises thermal strains and spark-induced cutting stresses, and facilitates removal of cut material by flushing.

The slit was introduced incrementally using a 250 μm diameter wire. This relatively large diameter wire was selected in order to minimise the risk of wire breakage and also to

reduce the concentration of stress at the cut tip; the latter is important because it can help to mitigate the risk of introducing plasticity during cutting.

Two different cut increments were chosen: a 0.1 mm increment from 0 up to 8 mm and from 46 mm up to 47.4 mm and a 0.2 mm increment from 8 mm up to 46 mm. The corresponding strains for each cut length were recorded after stabilisation of gauge readings to within 1-2 x 10^{-6} strain.

Stress back-calculation

As mentioned in Chapter 2, different approaches can be applied to calculate the slitting residual stresses. In the present study assessment of plasticity-induced slitting errors is of particular interest through applying Prime's published criteria [5]. Since, the criteria require stress intensity factor data (SIF), the fracture mechanics slitting analysis approach was implemented to calculate the slitting residual stresses [14-16].

Derivation of residual stresses from slitting measurements using the fracture mechanics approach consists of the following steps.

- ✓ *Determination of the influence function:* the influence function defines the sensitivity of the strain measurement point with respect to the released stress at the cut plane. The influence function can be determined using finite element analysis [8] or, for some cases, from published influence function solutions [17]. Since the CT blank dimensions are outside the range of published influence function solutions, an exact influence function was determined by finite element analysis.
- ✓ *The residual SIF calculation:* the residual stress intensity factor data were calculated using the determined influence function, the measured strain data and the material

elastic constants in Equation 2-1 of Chapter 2 The equation is reproduced below.

$$K_I = \frac{E'}{Z(a)}\frac{d\varepsilon}{da}$$

where E' is the material's generalised Young's modulus ($E' = E$ for plane stress and $E' = E/(1-\nu^2)$ for plane strain), ε is the measured strain at the cut depth a, and Z is the influence function. Because of the CT blank dimensions, a plane strain condition was assumed.

✓ *Determination of the residual stress distribution:* the weight function approach [18], defined by Equation 2-3 (given below), was applied to determine the through thickness averaged residual stress distribution along the measurement line.

$$K_I(a) = \int_0^a h(x,a).\sigma_{rx}\,dx$$

where σ_{rx} is the residual stress to be back calculated and $h(x, a)$ is the universal weight function for a given geometry. The weight function for the CT blank case (a single edge crack within a finite width rectangular plate) was determined from Equation 2-4.

Results

Figure 3-9 plots the distributions of measured micro-strain as a function of the cut length for the three back face strain gauges R1, R2 and R3. The trends and the magnitudes of the three profiles are almost identical. A peak value of 440 micro-strain was obtained at a cut depth of 17.6 mm for all the three gauges. The maximum micro-strain in terms of absolute value was measured at a cut depth of ~43 mm and is ~1140 micro-strain. The

averaged strain data from the three gauges, also plotted in Figure 3-9, were used for the rest of the data analysis.

As mentioned in the data analysis section the SIF was calculated using an exact influence function obtained by finite element analysis. Figure 3-10 shows how the residual stress intensity factor varies along the measurement plane. The calculated SIFs decrease to a minimum level of -37 MPa√m at a cut depth of 7 mm from the CT blank front face and rise to the maximum of 35 MPa√m at a cut depth of 21 mm.

The residual stress distribution based on the averaged strain data is shown in Figure 3-11. A tensile stress field is observed around the electron beam weld region balanced by compressive stresses in the make-up pieces and in the MMA weld HAZ. The peak tensile stress (~590 MPa) occurs at a depth of 19 mm from the CT blank front face.

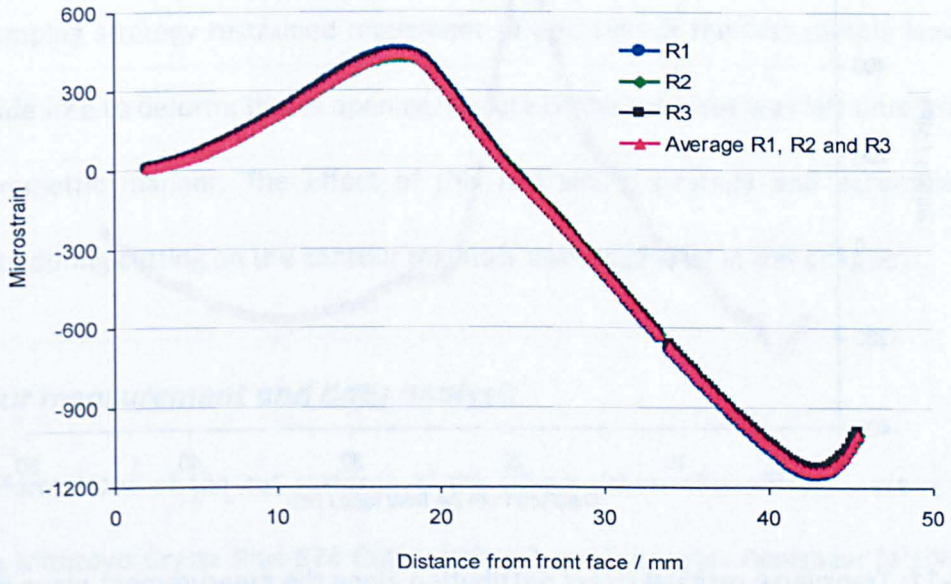

Figure 3-9: Micro-strain as a function of the cut length measured by the three back face strain gauges.

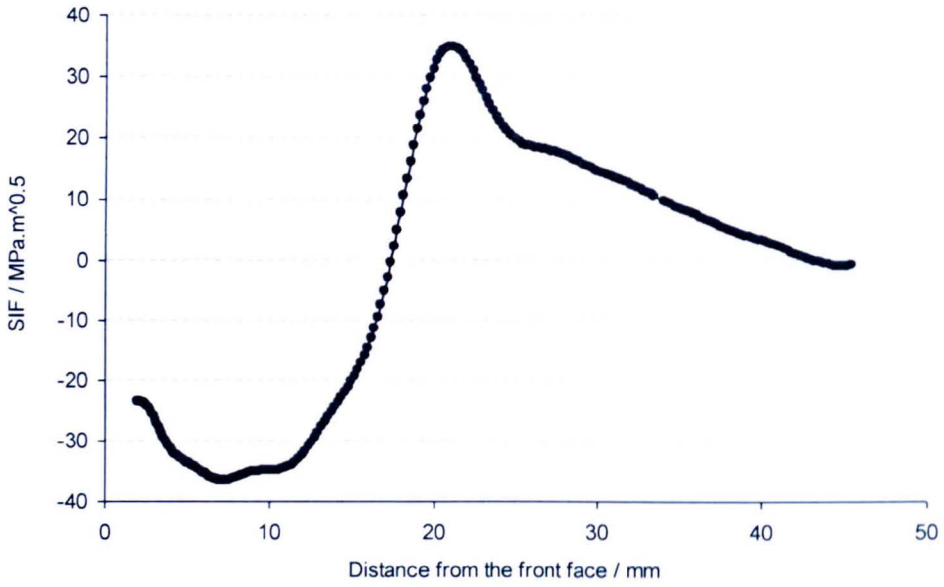

Figure 3-10: Residual stress intensity factor distribution as a function of the cut length.

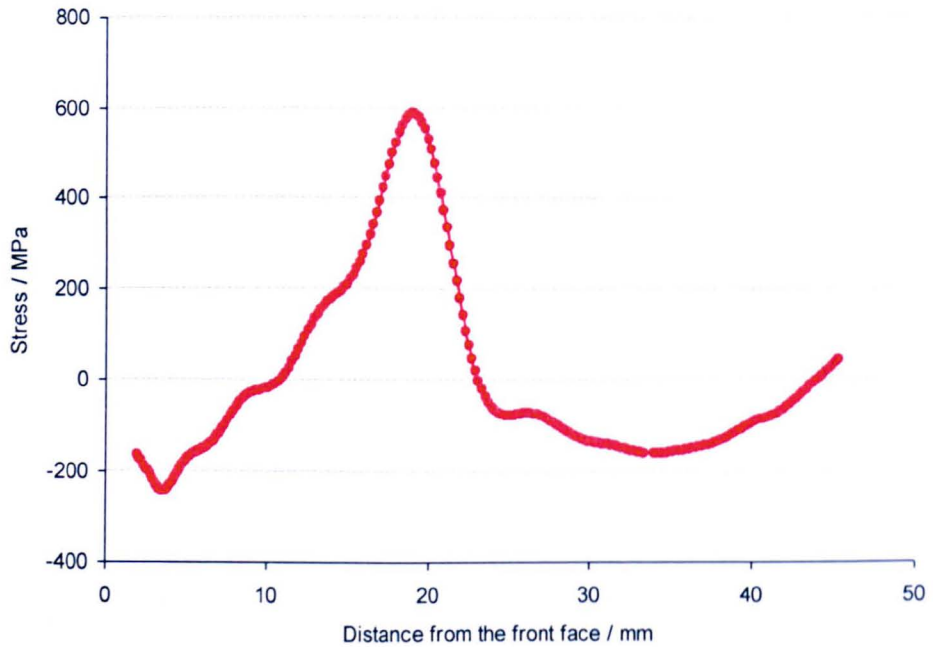

Figure 3-11: Transverse residual stress distribution along the measurement plane derived from the slitting stress intensity factor data.

3.2.4. Residual stress measurement by the contour method

The theory, the experimental procedure and the data analysis process of the contour method have been described in the literature review chapter. On completion of cutting the CT blank for the slitting method, the deformation profiles of the created cut surfaces were measured using a CMM and the data analysed in the standard way to map the transverse residual stresses using the contour method.

It is worth highlighting that the cutting process conducted to section the CT blank was not an ideal contour cut of the kind that is recommended by the practitioners of the contour method. First, an incremental cutting procedure was used for the slitting measurement and this introduced some noise into the deformed surface profiles of the cut CT blank. Secondly, only one side of the sample was clamped in order to allow the sample to deform and strains to be monitored at the back face (again for the slitting measurement). This clamping strategy restrained movement of one side of the test sample leaving the other side free to deform; that is opening/closure of the cut faces was left unrestrained in an asymmetric manner. The effect of this restraining strategy and accumulation of plasticity during cutting on the contour results is discussed later in this chapter.

Contour measurement and data analysis

The deformations of the cut surfaces of the CT specimen after slitting were measured using a Mitutoyo Crysta Plus 574 CMM with a 3 mm diameter Renishaw PH10M touch probe. The measurement spacing adopted in the thickness and length directions was 0.5 mm. Furthermore, the perimeters of both cut parts were measured as these profiles are used in the data analysis step.

The processing of the raw deformation data involves several steps. First, data from the two matching surfaces are averaged; this eliminates anti-symmetric errors (e.g., a curved cut) and the effect of shear stresses. Second, extreme outliers are removed from the dataset and the data are smoothed before mapping the deformation profile onto a finite element model of the cut component which is then used to calculate the residual stress. Different methods can be used to smooth the deformation data including 2D spline fitting, Fourier series or polynomial smoothing. In the present work two approaches were used: cubic spline fitting with different knot spacings and an implementation of a polynomial smoothing technique.

The spline fitting routine used in the present work was written in MatLab Software [19]. The routine uses the MatLab spline toolbox to join together piecewise polynomials at specified locations called "knots" which define the domain on which each polynomial is to be used. The spline toolbox also imposes both magnitude and slope continuity at the knots. The actual fitting of the spline is usually achieved by minimising the error between the data points and the fit. But the knot spacing chosen affects the resulting fitted splines. A low knot density (wide spacing) may lead to over smoothing of the measured data, while a high knot density may result in under smoothing. The maximum knot density is defined by the order of polynomial chosen (here cubic) and the measurement spacing. In practice some judgement is required, based on prior knowledge of the residual stress field, in order to select spacing appropriate for the residual stress length-scales of interest.

The polynomial smoothing technique is an iterative technique in which a locally fitted bivariate polynomial is used to update the position of each measurement point [20]. The user selects the extent and the order of the fitted polynomial. The method requires the

measured data to be meshed, but has the advantage that it may be easily applied to data on irregular physical domains. Both spline fitting and polynomial smoothing techniques have been explained in Chapter 2.

Stress back calculation

To back-calculate the residual stresses, a three dimensional model was created based on the measured outlines of the welded CT blank.

The model was meshed using linear hexahedral elements with reduced integration. The material was assumed to be isotropic with a Young's modulus of 204.5 GPa and Poisson's ratio of 0.29 [6]. To avoid rigid body motion of the cut surface the model was restrained in two directions perpendicular to the cut surface. The smoothed measured deformation profile was applied as a boundary condition to the cut face and a linear elastic stress analysis was performed to calculate the residual stresses normal to the cut face.

Results

Measured deformation data from the cut surfaces of the CT blank were processed using a conventional cubic spline approach with various knot spacings and the alternative second order polynomial smoothing approach described earlier.

In the spline fitting approach, the optimum spline knot spacing was determined by fitting a series of cubic splines to the raw data. Each of the fitted curves was then compared to the raw measurements along a number of lines [21-23]. Figure 3-12 illustrates the locations of the lines examined.

Figures 3-13 to Figure 3-15 show the results of the two best line profile fits to the data compared with the raw data. Overall, it can be seen that cubic splines with 3x3 mm knot spacing follow better the trend of the raw data compared with the 7x7 mm knot spacing.

In the next step a mesh sensitivity study was conducted to examine the effect of the mesh size on the final residual stress results. The peak transverse tensile stress (see Figure 3-6 and Figure 3-11) was taken as a reference.

Four different mesh sizes (1.5, 1, 0.75 and 0.5 mm) were analysed. From Figure 3-16, it can be seen that the results are converging as the mesh size decreases with only 9 MPa difference obtained between the peak stress results of the last two mesh sizes. Therefore, a 0.5 mm mesh size was adopted in the FE analysis for both the spline fitting and polynomial smoothing approaches. Figure 3-17 shows the corresponding mesh grid.

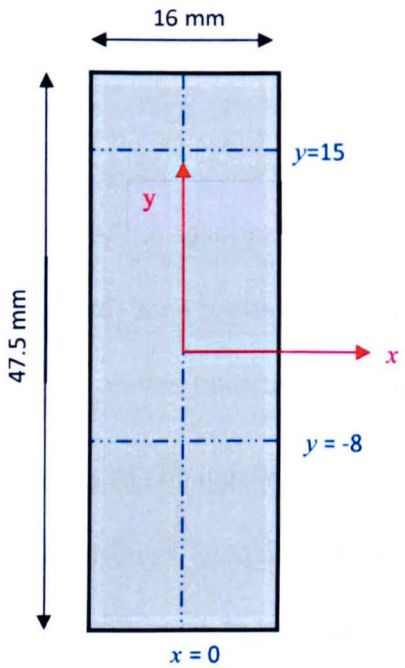

Figure 3-12: Schematic drawing showing lines along which fitted data are compared with the raw measured displacements.

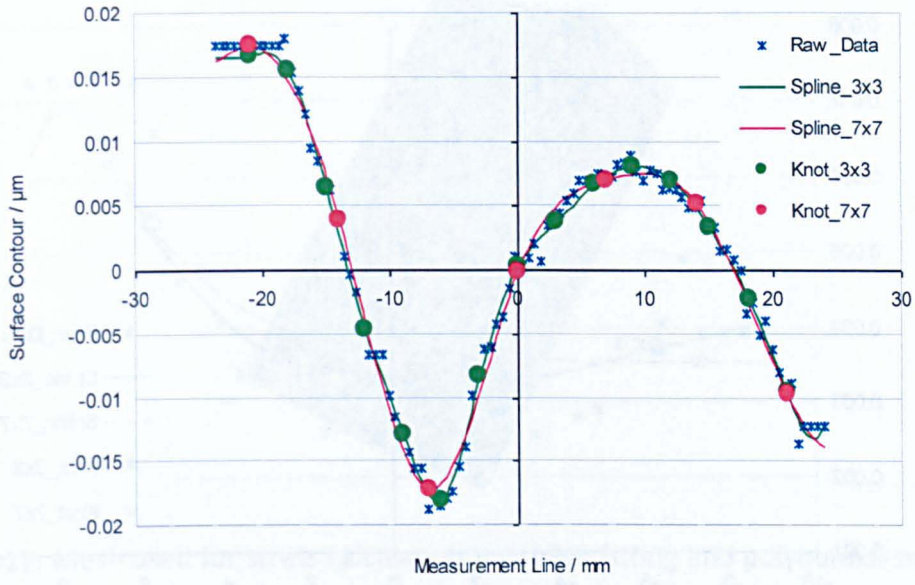

Figure 3-13: Comparison of fitted data with raw measured displacements at x = 0 mm (see Figure 3-12 for the location of x=0 mm).

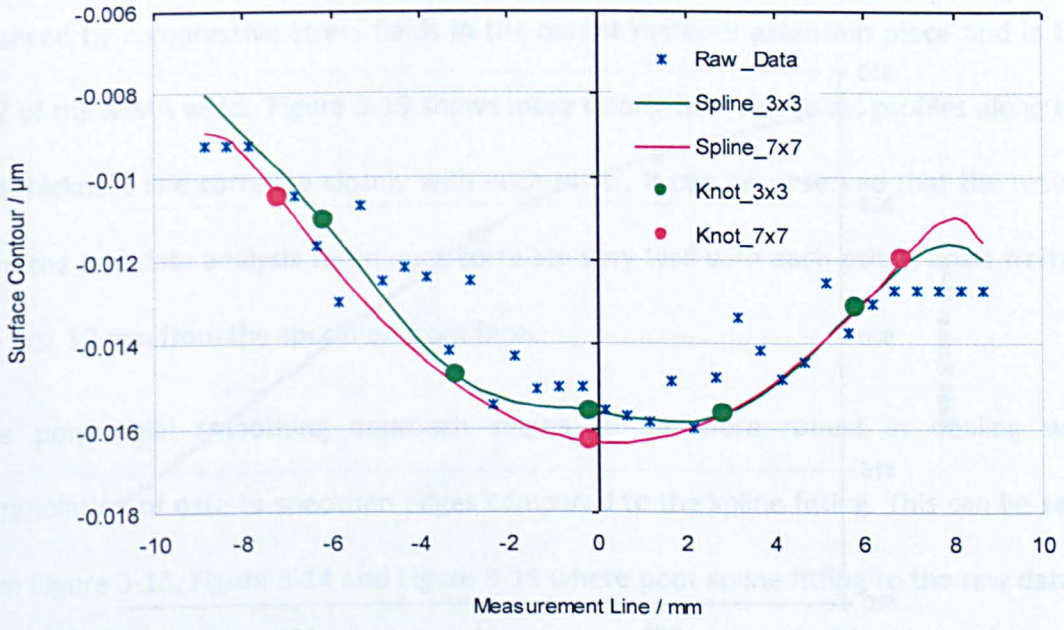

Figure 3-14: Comparison of fitted data with raw measured displacements at y = -8 mm (see Figure 3-12 for the location of y = -8 mm).

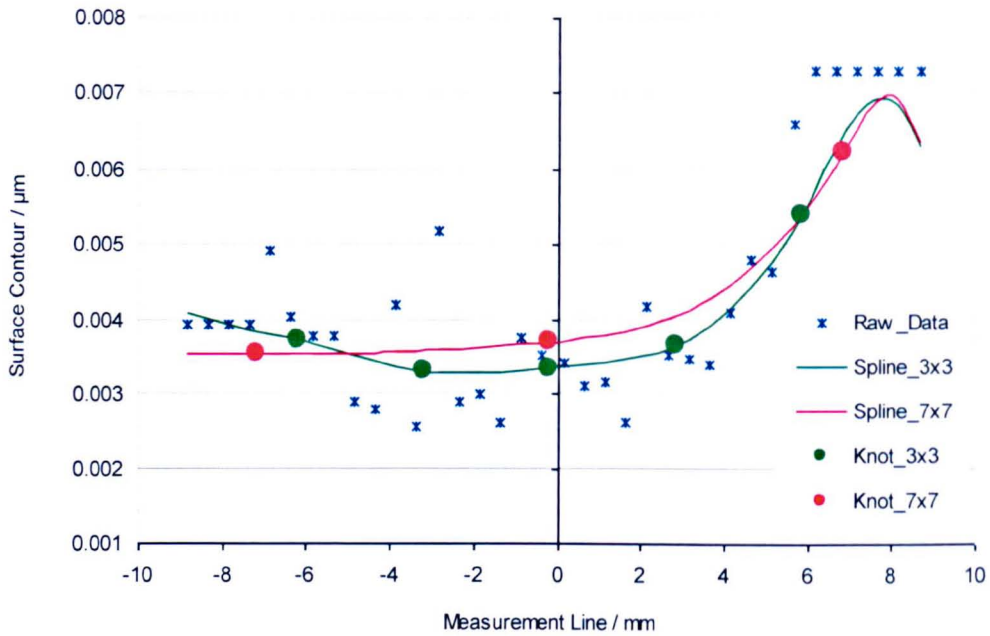

Figure 3-15: Comparison of fitted data with raw measured displacements at y = -15 mm (see Figure 3-12 for the location of y = -15 mm).

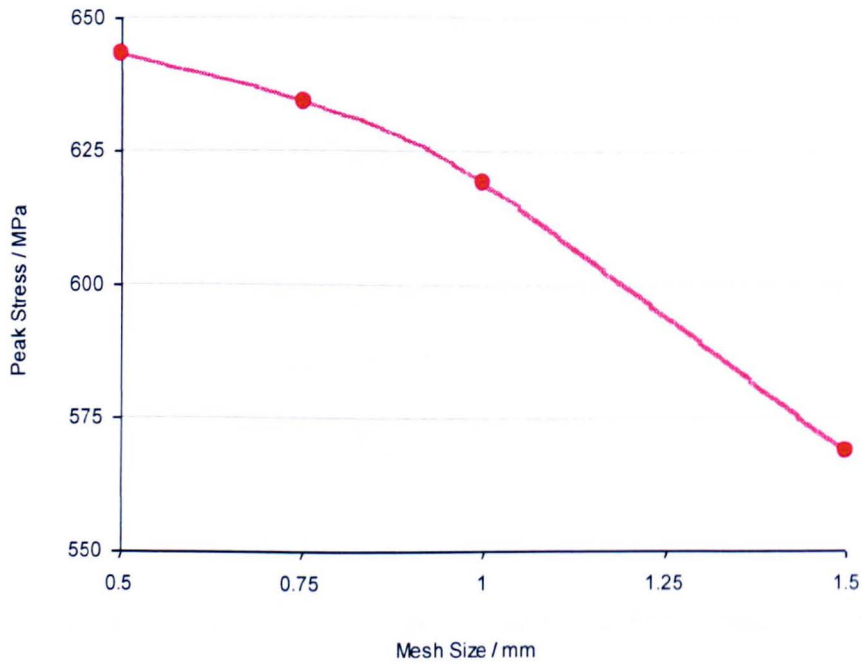

Figure 3-16: Variation of the peak tensile stress for different finite element mesh sizes.

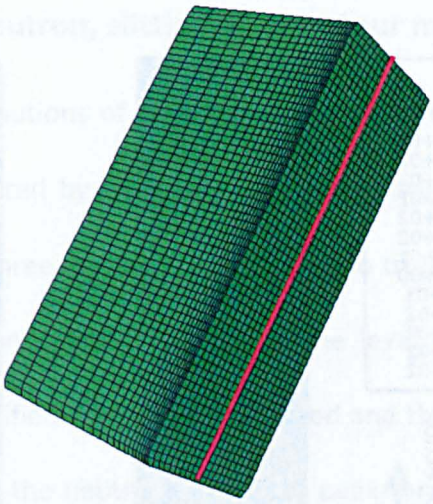

Figure 3-17: Mesh used for stress calculation for spline fitting and polynomial smoothing approaches. The red line indicates the path along which stresses are plotted.

Figure 3-18 compares residual stress distributions determined using the two data analysis methods. Both maps show a similar tensile stress region around the electron beam weld balanced by compressive stress fields in the parent material extension piece and in the HAZ of the MMA weld. Figure 3-19 shows more clearly how the stress profiles along the mid-thickness line correlate closely with each other. It can be observed that the results from the two data analysis techniques correlate very well with each other, apart from in the first 10 mm from the specimen front face.

The polynomial smoothing approach seems to be more robust in dealing with extrapolation of data to specimen edges compared to the spline fitting. This can be seen from Figure 3-13, Figure 3-14 and Figure 3-15 where poor spline fitting to the raw data is obtained approaching the edges. Therefore the results obtained from the polynomial smoothing approach were used when comparing measurements from three independent techniques (*i.e.* neutron diffraction, slitting and the contour method).

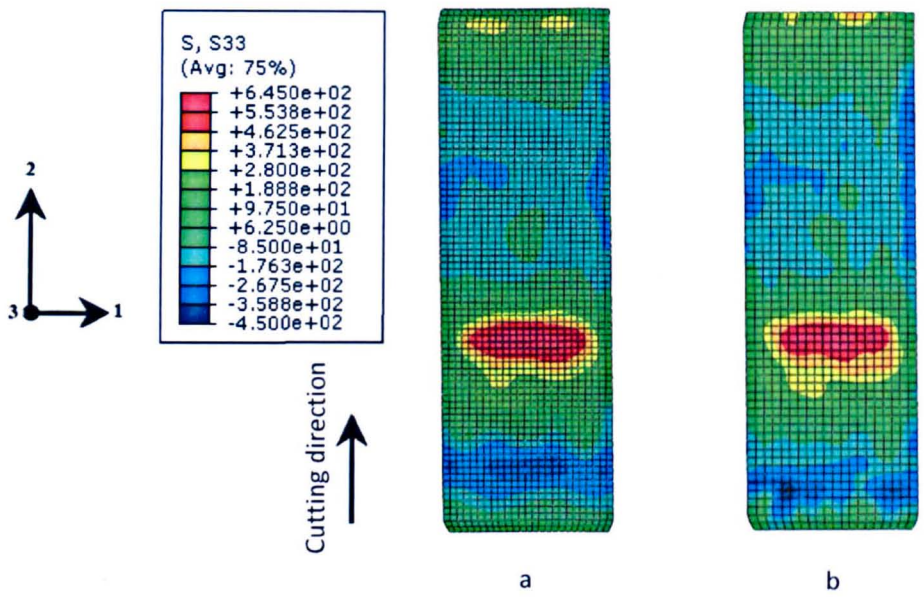

Figure 3-18: Maps of the transverse residual stresses obtained from the contour measurement using cubic splines with 3x3 mm knot spacing (a) and from a second order polynomial smoothing (b). Stress units are in MPa.

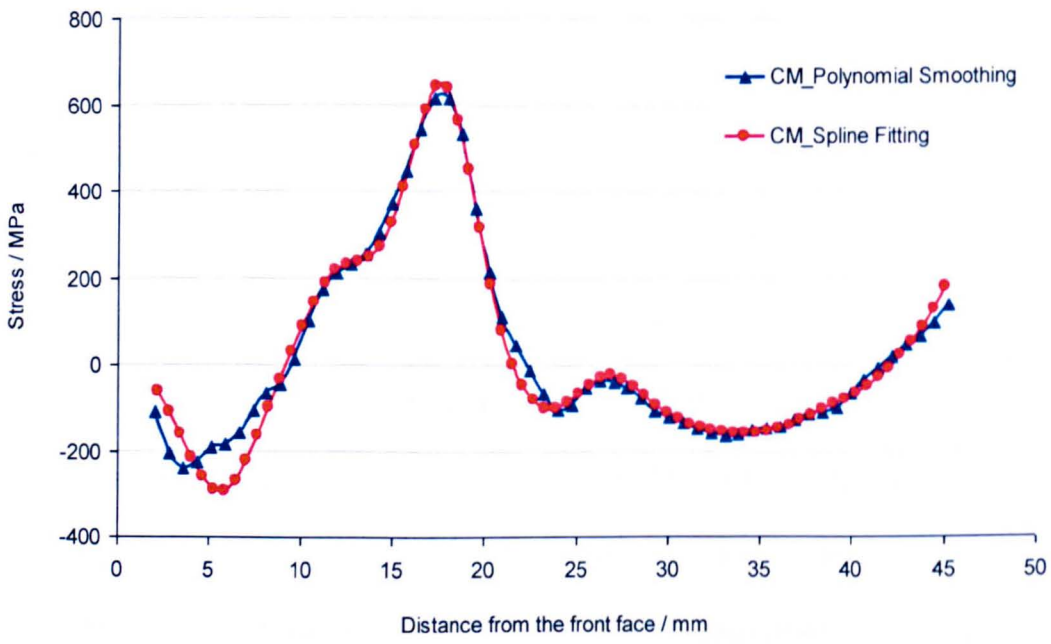

Figure 3-19: Comparison of transverse residual stress profiles along the measurement line in the CT blank using the two data analysis approaches in the contour method.

3.2.5. Comparison of neutron, slitting and contour method results

A comparison of the distributions of transverse residual stress at mid-thickness of the measurement plane measured by neutron diffraction, slitting and contour methods is shown in Figure 3-20. All three profiles follow the same trend with a peak tensile stress located around the electron beam weld region. The level of agreement of the three approaches has been quantified. The contour method and the slitting peak tensile stress magnitudes are lower than the neutron diffraction peak tensile stress magnitude by 19 MPa (3%) and 50 MPa (8%), respectively. In the contour method result, a slight shift in the location of the tensile peak towards the CT blank front face is observed.

The reduced peak tensile magnitude measured by slitting can be partially explained by the fact that the method measures averaged stresses across the thickness of the test specimen whereas the neutron diffraction measurements are averaged over a (2 x 2 x 2) mm^3 gauge volume.

The potential significance of cutting plasticity on the accuracy of the slitting stresses was assessed using the recently published approach of Prime [5] which uses SIF data to estimate a percentage error in apparent measured stress knowing the material yield stress. As it can be observed from Figure 3-10, high compressive SIFs are observed in the parent metal. In fact the maximum SIF value (-36.6 MPa.√m) occurs in this region at 7.3 mm cut depth. The stress error associated with this level of SIF is estimated to be about 15% assuming elastic-perfectly plastic behaviour with a yield stress of 241 MPa (i.e. the parent make-up piece material 0.2% proof stress). This indicative level of stress error is quite high and suggests that accumulation of plasticity in slitting is the most probable

reason why the peak tensile stress measured by slitting is slightly lower than that measured by neutron diffraction.

The outcome of the contour stress measurement is remarkably good considering the non-ideal restraint conditions (clamping on one side) and the incremental cutting procedure that had to be implemented for the slitting method measurement. Firm clamping on both sides of a contour measurement cut helps to control (reduce) the concentration of redistributed stress at the cut tip and thereby mitigate the risk of plasticity occurring and the consequent stress calculation errors [2]. The lack of restraint may explain why there is an apparent shift (about 2 mm) in the location of the peak stress in the contour measurement when compared with the slitting and neutron results. Such shifts in the peak stress location have been observed in previous contour measurements and attributed to plasticity during cutting [21,24] or elastic bulging [25], both of which are affected by the restraint conditions (see Chapter 2).

More specifically, similar shifts in peak stress position towards the cut start have been observed in previous contour method measurements at The Open University and are believed to be induced by compressive plasticity and stress redistribution associated with a large compressive SIF [21] near the start of a cut.

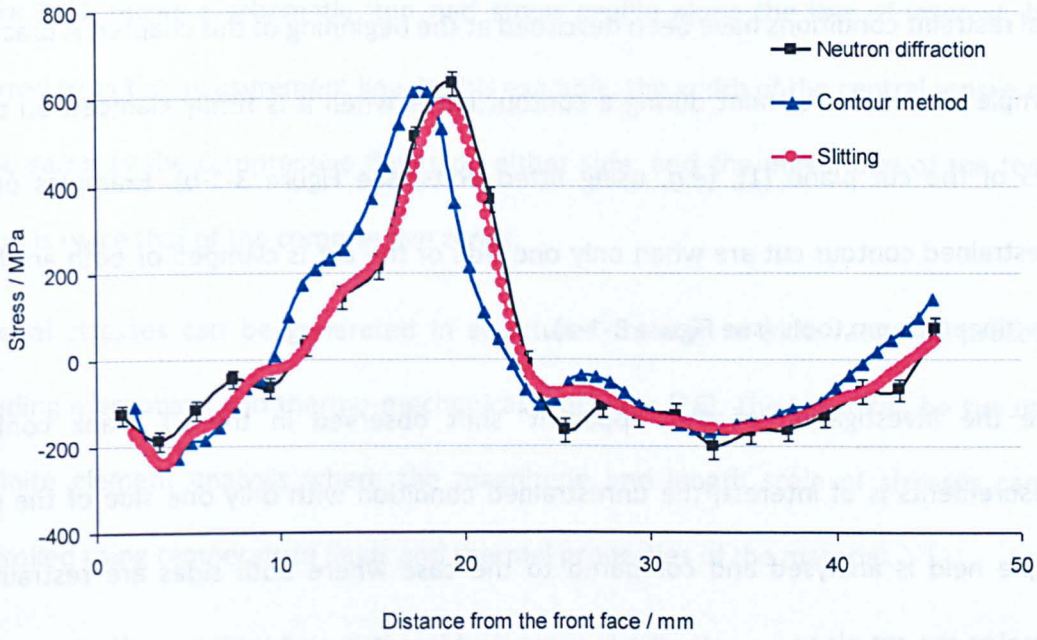

Figure 3-20: Comparison of transverse residual stress distribution in the welded CT blank specimen measured by neutron diffraction, slitting and the contour method.

3.3. Restrained and unrestrained contour cut plasticity-induced errors

The example presented above, which was effectively unrestrained (in terms of mode I crack opening/closure) during cutting suggests that an error in the stress profile measured by the contour method may have been introduced by either elastic bulging and/or plasticity [25].

In this section, the contour residual stress measurement method is simulated by finite element analysis to assess the influence of restraint on measurement errors introduced by plasticity. The hypothesis explored here is that occurrence of plasticity in the cutting/stress relaxation process can cause an 'apparent' shift in the peak stress location and changes in the profile of stress measured by the contour method, and that the severity of such errors is associated with the level and type of restraint during the cutting process.

Ideal restraint conditions have been described at the beginning of this chapter. A practical example of sample restraint during a contour cut is when it is firmly clamped on both sides of the cut plane [1], (*e.g.* using fitted bolts, see Figure 3-1-b). Examples of an unrestrained contour cut are when only one side of the cut is clamped or both are held with 'finger' clamp tools (see Figure 3-1-a).

Since the investigation of the 'apparent' shift observed in the CT blank contour measurements is of interest, the unrestrained condition with only one side of the test sample held is analysed and compared to the case where both sides are restrained, normal to the cut plane.

For both cases analysed, a well-defined residual stress distribution is first generated. The stresses are then mapped onto a new FE model. The aim of mapping is to control the level of plasticity-induced during the contour cut simulation through defining the material yield stress. Following mapping, the contour method (cutting and stress back-calculation) is simulated for the two different restraining conditions: that is completely unrestrained and restrained at a plane distance w from the cut.

3.3.1. Initial residual stress generation

A well-defined initial residual stress distribution is required for this contour simulation study. Furthermore, the defined stress distribution should be designed in a way to allow introducing controlled amounts of plasticity due to the release of both compressive and tensile stresses during cutting. An idealised 'top hat' residual stress distribution was chosen to meet these criteria.

Figure 3-21 shows a schematic 'top hat' stress profile along the line of interest, here referred to as the measurement line. In this example, the width of the central tensile zone is the same as the compressive flanks on either side, and the magnitude of the tensile region is twice that of the compressive zones.

Residual stresses can be generated in structures through a wide range of processes including mechanical and thermo-mechanical processes [26]. The latter can be simulated by finite element analysis where the magnitude and length scale of stresses can be controlled using temperature fields and thermal properties of the material.

To generate the required 'top hat' residual stress distribution a composite 2D FE model was created (see Figure 3-22). The model consisted of three sections (A, B and C), each of them 50 mm wide. The width of the three sections was chosen according to the length scale of the intended stress regions. The stress length scale is of importance here because it contributes to the level of plasticity introduced during the cutting process. The composite model was created 300 mm long.

Plane stress conditions were assumed for all analyses. This is because for the same loading and boundary conditions plasticity is more likely to occur during the cutting process for plane stress conditions than in a plane strain state [27].

The composite model was meshed with four-node plane stress elements with reduced integration (ABAQUS type CPS4R). Since, only a 'top hat' stress distribution is of interest here, and no comparison with results from other sources is needed, a mesh sensitivity study in the present case was judged to be trivial. A total of 19800 elements were generated for the model.

Two different material properties were defined for the different sections of the composite model. Section A and C were assigned the same material while section B was assigned material properties having a different yield stress and thermal expansion coefficient (See Table 3-2).

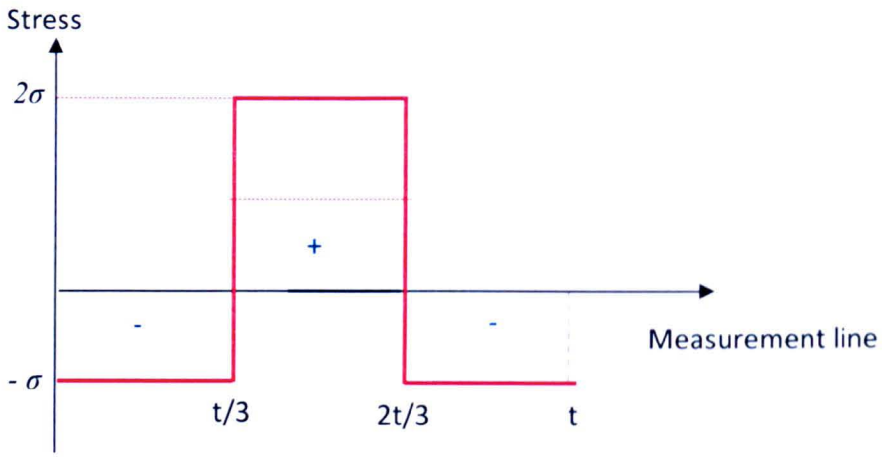

Figure 3-21: "Top hat" stress profile normal to the measurement line.

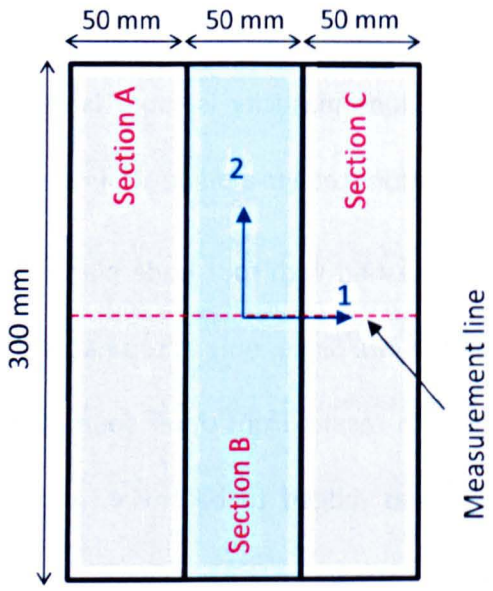

Figure 3-22: Composite model used for contour method plasticity simulations.

Table 3-2: The materials' properties used for residual stress generation in the composite plate.

	Young's Modulus (GPa)	Poisson's Ratio	Yield Stress (MPa)	Thermal Expansion Coefficient (/°C)
Material A & C	200	0.3	200	8.65×10^{-6}
Material B	200	0.3	400	1.73×10^{-5}

The yield stress value controls the magnitude of the generated stresses in the corresponding section and the relative thermal expansion coefficient for each section defines the sign of stress (tensile or compressive). For example in Figure 3-22, sections A and C have lower thermal expansion coefficient than section B, which gives compressive stresses normal to the measurement line in these two sections and tensile stresses normal to the measurement line in section B. Elastic-perfectly plastic behaviour was assumed throughout the analyses.

From Figure 3-22 it can be noticed that the composite model presents two symmetry lines in directions 1 and 2. However, because asymmetric restraining conditions will be considered in the analyses, the entire model is simulated.

The 'top hat' stress distribution along the measurement line was generated by cooling down the entire heated composite model from 1000 °C to room temperature (20 °C).

Figure 3-23 illustrates the map of the generated residual stresses in direction-1 and in direction-2 (*i.e.* normal to the measurement line). Overall, very low stress magnitude is obtained in direction-1 (Figure 23-b). However, it is the stress distribution in direction-2 that is of most interest for this study (Figure 23-a). That is because the contour method only determines stresses normal to the cut line/plane, here in direction-2.

As intended three different regions corresponding to the three sections of the composite model are obtained for the stress distribution acting normal to the measurement line: Two compressive fields are balanced by a central tensile region, see Figure 23-a.

The map of von Mises stresses and the corresponding plastic strains are shown in Figure 3-24-a and Figure 3-24-b, respectively. Although Figure 3-24-b does not indicate that yielding occurred in the plate central region, the von Mises stresses are very close to the central region yield stress (*i.e.* 400 MPa) giving a very well-defined 'top hat' stress distribution.

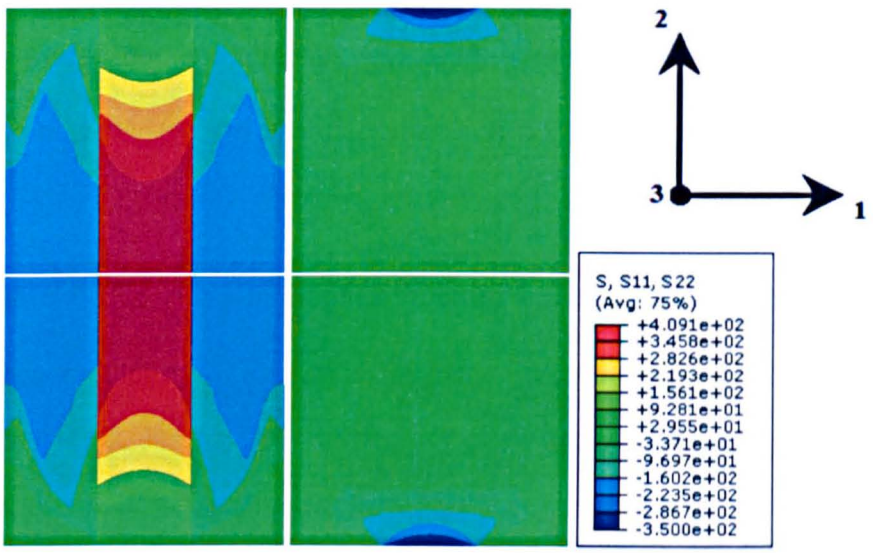

(a) (b)

Figure 3-23: Maps of residual stresses in direction-2 (*i.e.* normal to the measurement line) (a) and in direction-1 (b). Stress unit is MPa.

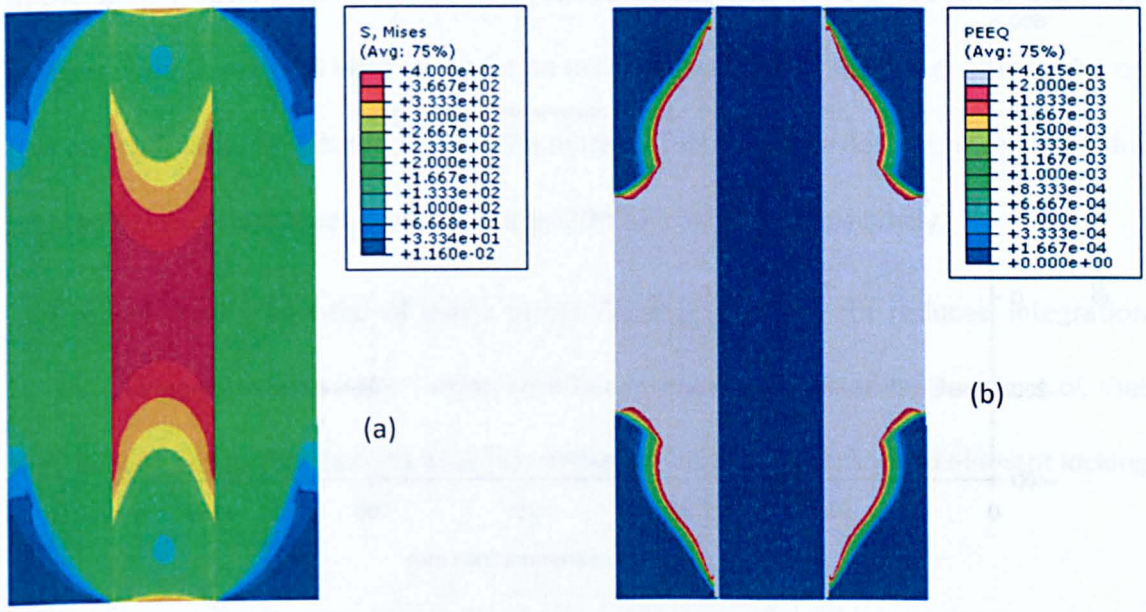

Figure 3-24: Maps of von Mises stresses (a) and the induced plastic strains (PEEQ) (b). Stress units are in MPa.

Figure 3-25 plots the stress distribution generated across the plate in the direction normal to the measurement line. It can be seen that a self-balanced residual stress field having the required characteristics is successfully generated in the composite plate. The generated stress distribution is used in the following sections for plasticity assessment.

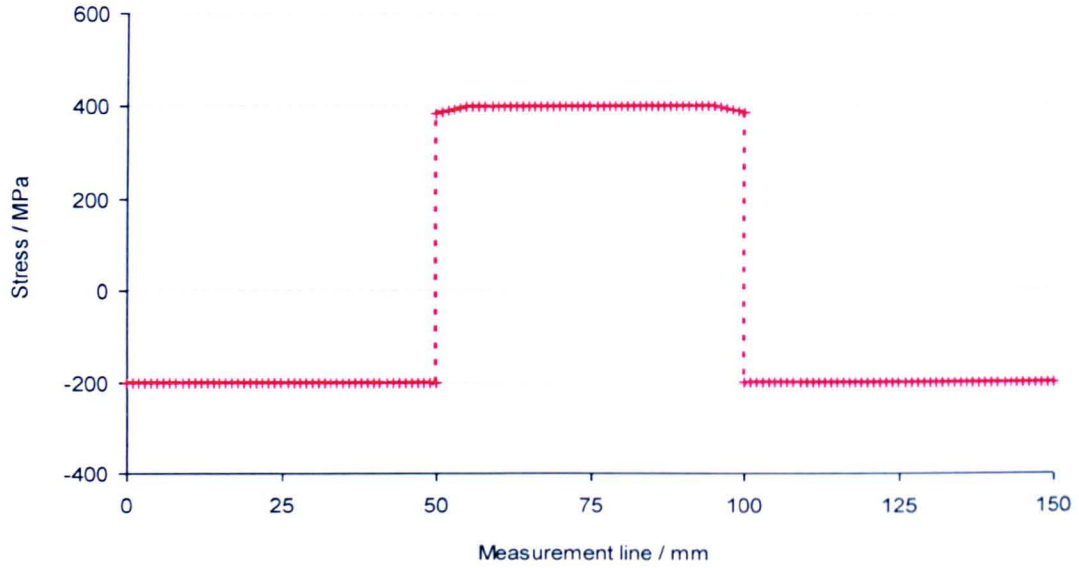

Figure 3-25: Generated residual stress distribution across the plate acting normal to the measurement line.

3.3.2. Mapping of the generated residual stresses onto a new FE model

In order to control the level of plasticity during simulation of the cutting process associated with the contour method, the model containing the idealised stress field is required to have controlled elasto-plastic properties and to have a very fine mesh in the region of the measurement line.

These conditions were met by mapping the thermally introduced residual stress field in the composite plate onto a new two-dimensional FE mesh using the MAP SOLUTION command within ABAQUS [28] and performing an equilibrium step. Single material properties were used. Plasticity in the contour cut simulation was controlled by defining the material yield stress value in the analysis after the mapping process. With a high yield stress value compared to the residual stresses magnitude, no plasticity is expected to occur while a yield stress close to the maximum residual stress is expected to result in a high level of plasticity.

In the present case, since the maximum residual stress magnitude is 400 MPa, this value was assumed as material yield stress for an initial assessment of the effect of restraint on contour cut plasticity-induced errors. The material elastic properties, *i.e.* Young modulus and the Poisson's ratio were assumed to be 200 GPa and 0.3, respectively.

The model mesh consisted of plane stress linear elements with reduced integration (CPS4R). Linear elements were chosen here because it was reported by Dennis et *al.* that they behave better than second order elements due to their resistance to element locking [3,29].

A sensitivity study was conducted on the mesh element size. Three different mesh grids were analysed with element sizes (0.5, 1, and 1.5 mm) resulting in totals of 37200, 11700 and 6900 elements.

The residual stress profiles obtained from the three FE meshes along the measurement line are very consistent as illustrated by Figure 3-26. When compared with the initial residual stress distribution, a slight difference is observed between the mapped and generated residual stresses. The locations of these discrepancies correspond to the interfaces of the three sections of the composite plate (see Figure 3-22). This might be caused by the non-structured mesh region of the models onto which the initial residual stresses are mapped (Figure 3-27). The slight difference observed between the initial and mapped stress profiles is not an issue as the mapped results are considered as the initial stress state for the rest of the plasticity assessment.

The model meshed with a 1mm element size in the cut path vicinity (see Figure 3-27) was used for assessing the different contour cutting processes.

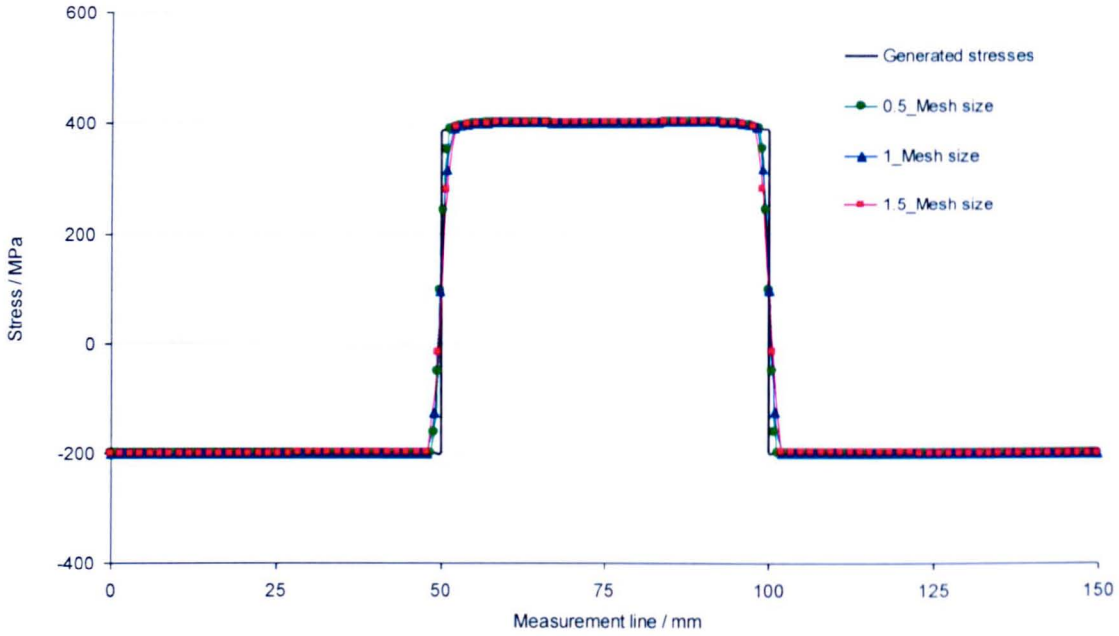

Figure 3-26: Comparison of the mapped residual stress distributions across the plate acting normal to the measurement line for different mesh sizes in the vicinity of the cut line. The original generated residual stress distribution is also shown.

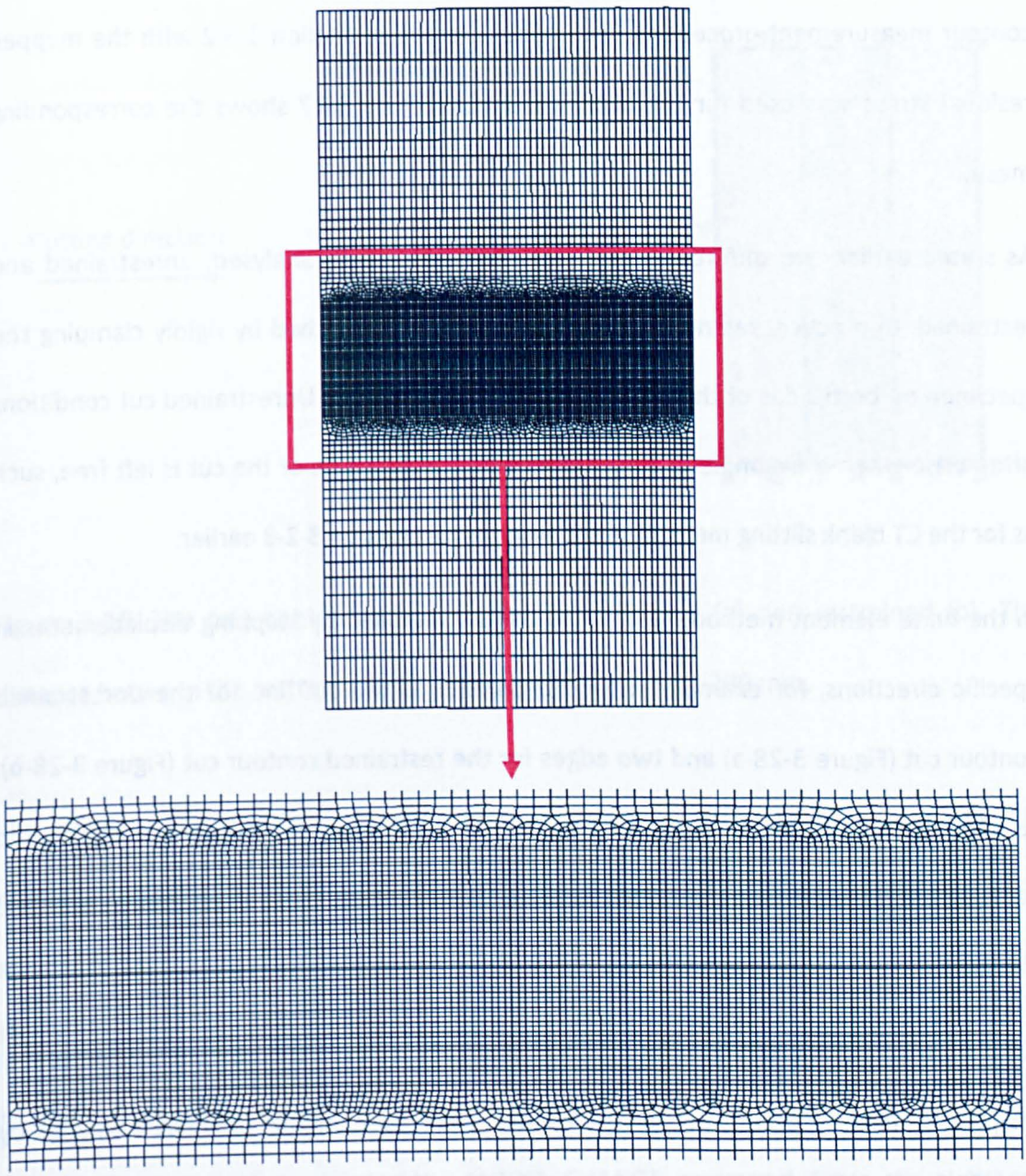

Figure 3-27: Mesh used for the different cutting processes. A close up view of the cut path vicinity mesh region is also shown.

3.3.3. The cutting process and the generated plastic strains

On completion of the mapping process, the cutting simulation was undertaken to assess the influence of sample restraint on plasticity-induced error in stresses determined by the

contour measurement procedure. The model created in section 3-3-2 with the mapped residual stress was used for the cutting process. Figure 3-27 shows the corresponding mesh.

As stated earlier two different restraining conditions were analysed: unrestrained and restrained. In practice, restrained conditions can be approached by rigidly clamping the specimen on both sides of the cut line (see Figure 3-1-b) [1]. Unrestrained cut conditions often arise when the sample is 'finger clamped' or if one side of the cut is left free, such as for the CT blank slitting measurement described in section 3-2-3 earlier.

In the finite element method, restraint is usually imposed by stopping displacements in specific directions, for example one edge parallel to the cut line for the unrestrained contour cut (Figure 3-28-a) and two edges for the restrained contour cut (Figure 3-28-b). As demonstrated by previous plasticity assessment in the contour method [3], the degree of restraint is dependent on the distance between the restrained plane and the measurement line. Here, this distance is 200 mm.

Simulation of cutting for contour method plasticity assessment has been reviewed in Chapter 2. Two different cutting approaches were used in the previous work: a) by releasing the symmetry boundary conditions [3] and b) by material removal approach [2,29]. The first approach is representative of introducing a sharp cut in a body, while a blunt cut is introduced in the body for the material removal approach. Elements are removed one after another until the completion of the cut (see Figure 3-29). This latter approach was applied in the present work.

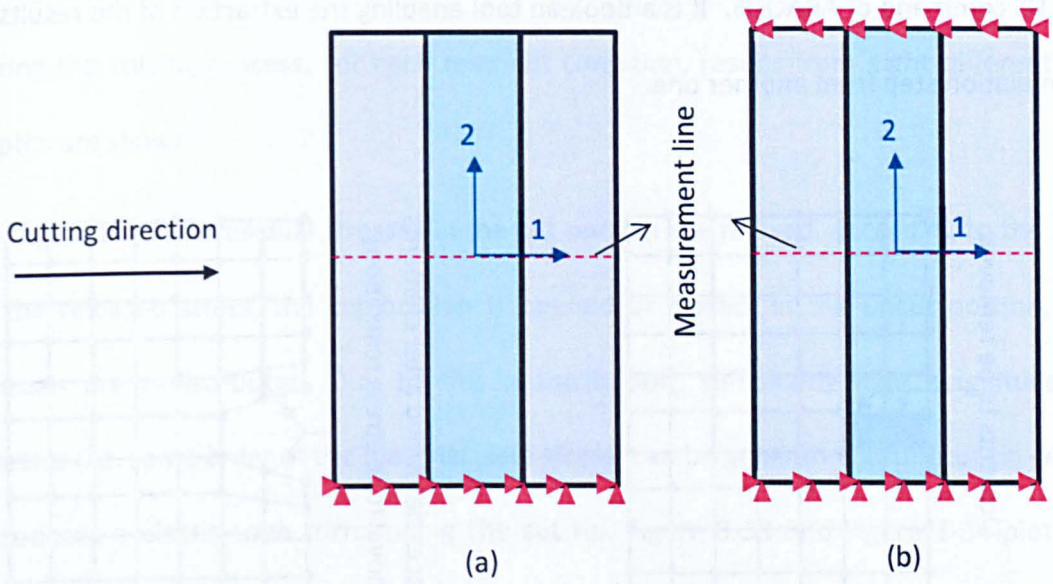

Figure 3-28: The two contour cuts analysed: unrestrained (a) and restrained (b). The distance between the restraints and the measurement line is 200 mm.

The effect of the cut width is investigated in Chapter 5. Here, to achieve reasonable computation time, a 0.5 mm cut width was selected for all cutting simulations. This is slightly wider than an EDM wire cut width of 0.39 mm for a 0.25 mm EDM wire diameter [30].

In ABAQUS, the material removal approach is performed by removing mesh elements one by one in a series of steps using the MODEL CHANGE command. Since the elements' length in the cutting direction is 1mm, and the width of the composite plate is 150 mm, the cutting process was simulated in 150 steps.

On completion of the cutting simulations, the cutting plastic strains introduced due to the release of residual stresses are extracted from the total plastic strains that include those introduced during the residual stress generation, using the CREATE FIELD OUTPUT FROM

FIELDS command of ABAQUS. It is a Boolean tool enabling the extraction of the results of a simulation step from another one.

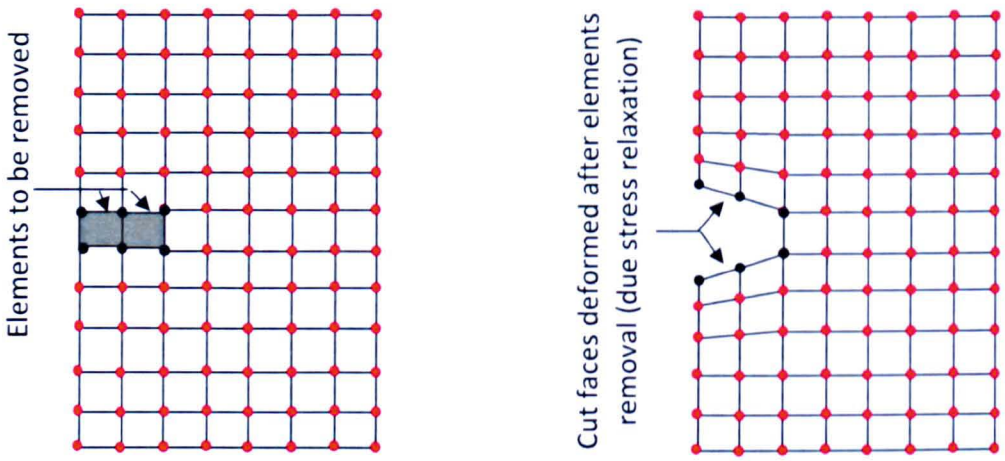

Figure 3-29: Illustration of the finite element cutting process by material removal approach.

A comparison of the plastic strains induced by the release of residual stresses for the restrained and unrestrained cases is shown in Figure 3-30. The grey regions in the maps correspond to locations with plastic strain values above 0.2 %.

In the first section of the composite plate (section A), where compressive residual stresses were generated, the total area of the induced-plastic strains is larger for the unrestrained contour cut. Conversely, in section B, the release of tensile residual stresses introduces much lower plastic strains for the unrestrained contour cut. In the last section of the composite model, no plastic strains are observed in the unrestrained model while a small plastic zone is observed in the last 10 mm of the restrained model.

Figure 3-31 and Figure 3-32 illustrate how the plastic zones in Figure 3-30 developed during the cutting process. For each restraint condition, results from eight different cut depths are shown.

During cutting, the residual stresses in the cut portion are relaxed. According to the sign of the released stress, the cut portion is opened or closed. In the uncut portion, the stresses are redistributed. Due to this redistribution, sufficiently high magnitude of stresses (i.e. same order of the material yield stress) can be generated at the cut tip which introduces a plastic zone surrounding the cut tip. Figure 3-33 and Figure 3-34 plot the stress redistribution for different cut depths of the restrained and unrestrained model, respectively. Since the induced-plastic zones are permanent, a plastic zone wake is generated during the cutting process. Considering the total area of the induced-plastic strains, the unrestrained model seems to behave better than the restrained model. However, plots of plastic strain distributions along the path of interest are required to draw robust conclusions.

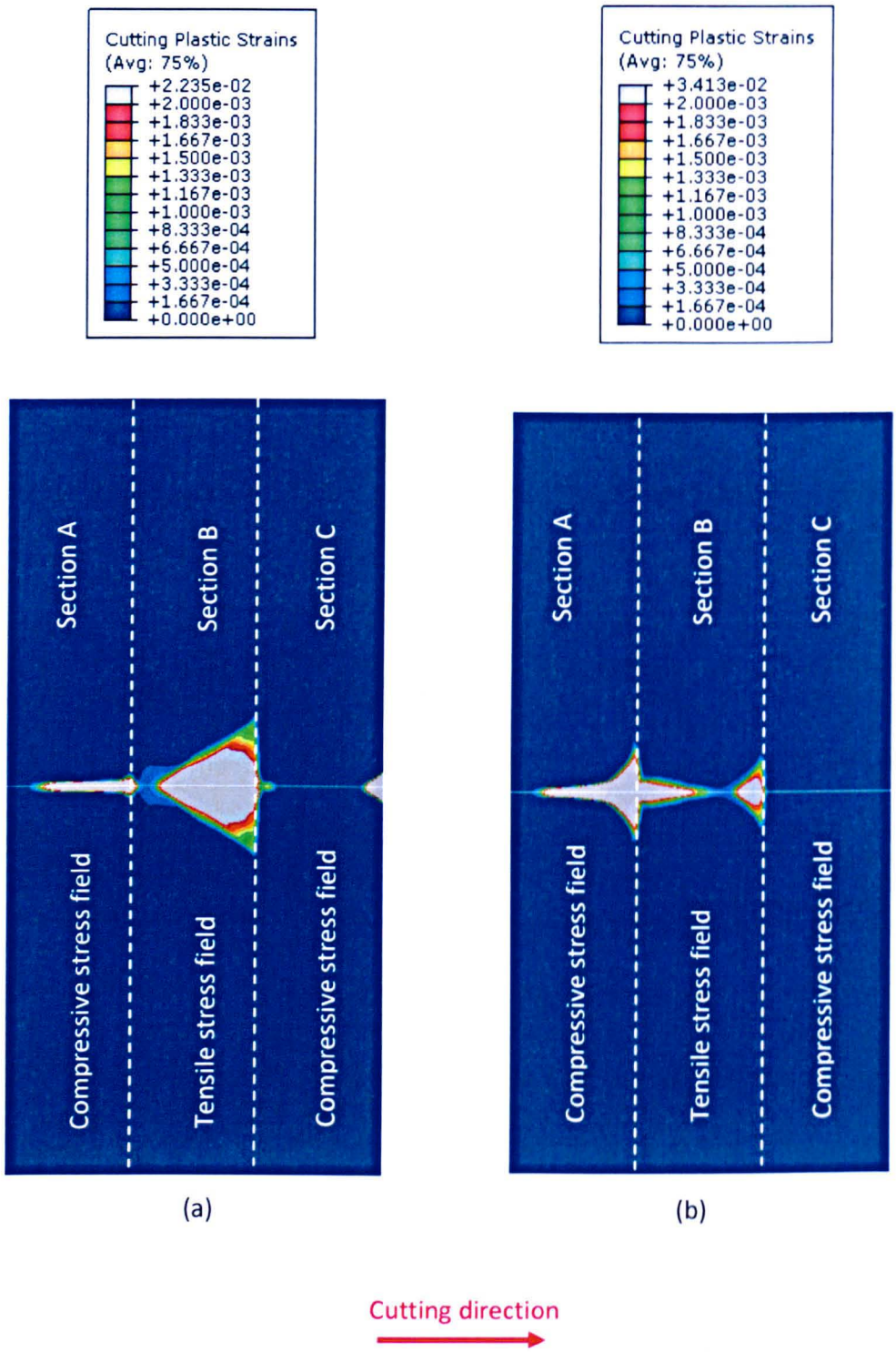

Figure 3-30: Illustration of the induced-plastic strains due to the release of residual stresses for the restrained (a) and unrestrained model (b).

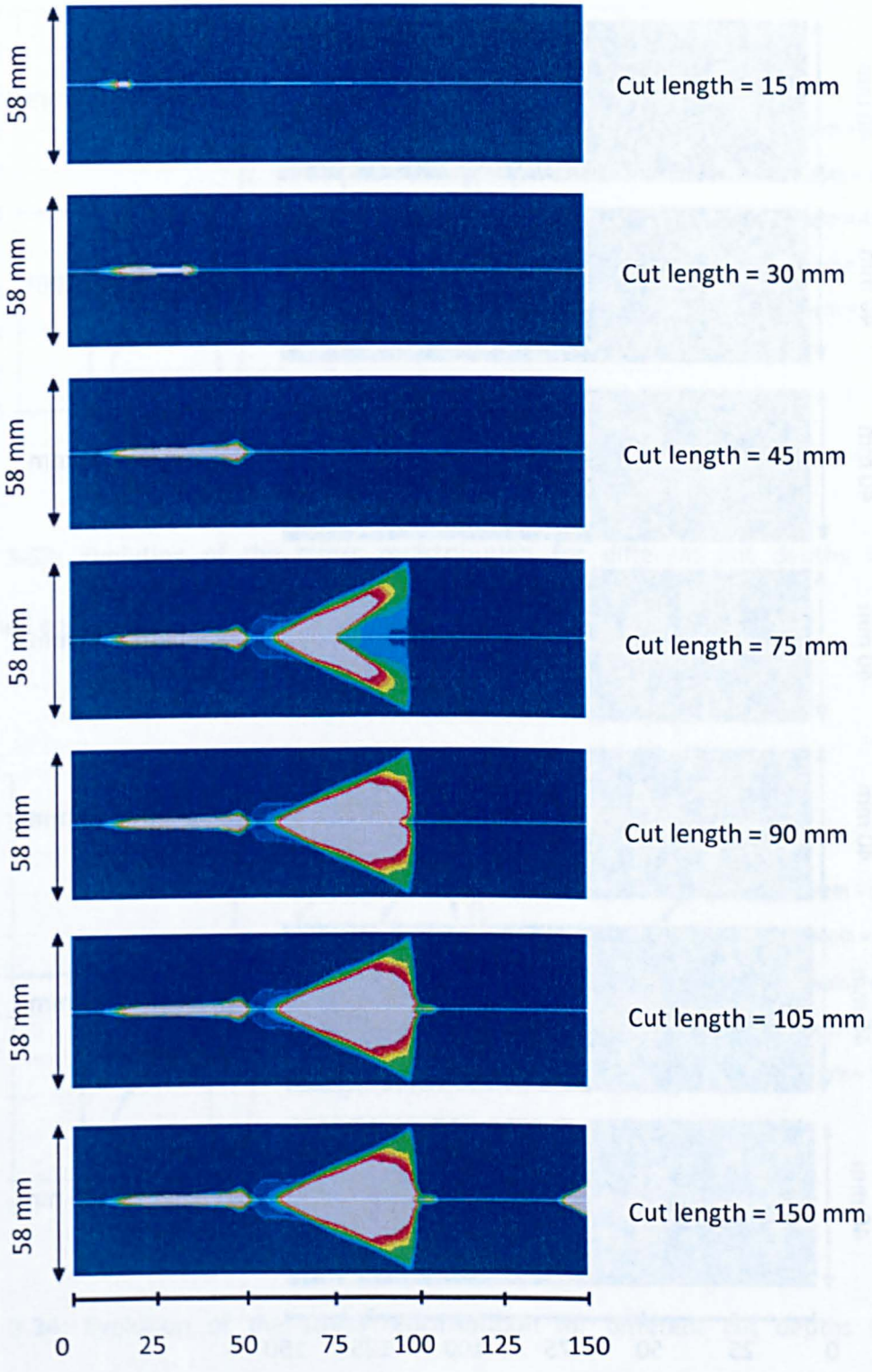

Figure 3-31: Evolution of the plastic zone during the restrained model cutting. Only a close-up view of the cut vicinity is shown. The legend is identical to the one in Fig.3-30-a.

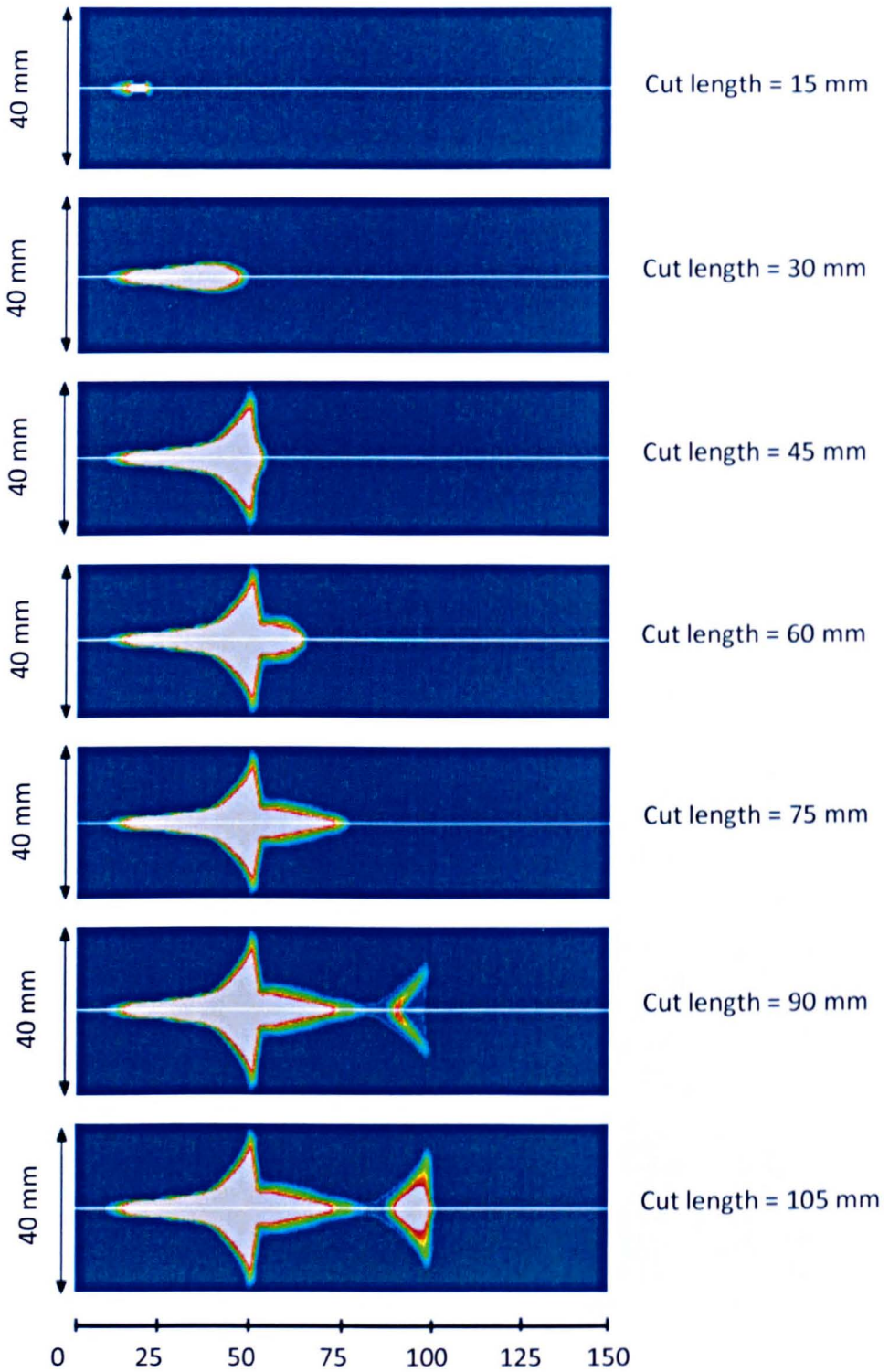

Figure 3-32: Evolution of the plastic zone during the unrestrained model cutting. Only a close-up view of the cut vicinity is shown. The legend is identical to the one in Fig.3-30-b.

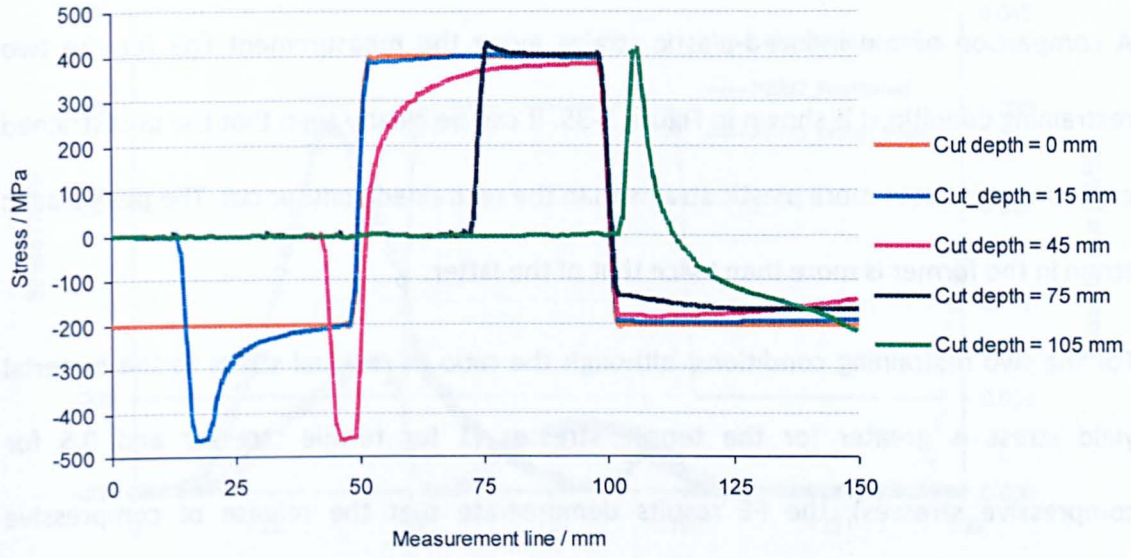

Figure 3-33: Evolution of the stress redistribution for different cut depths in the restrained contour cut.

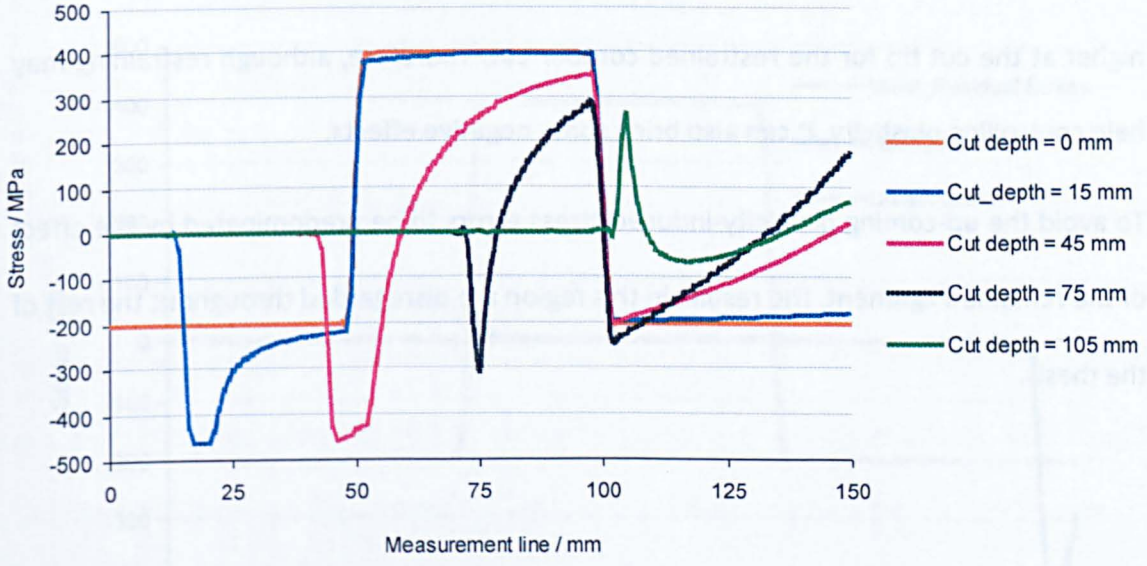

Figure 3-34: Evolution of the stress redistribution for different cut depths in the unrestrained contour cut.

A comparison of the induced-plastic strains along the measurement line for the two restraining conditions is shown in Figure 3-35. It can be clearly seen that the unrestrained contour cut induces more plastic strains than the restrained contour cut. The peak plastic strain in the former is more than twice that of the latter.

For the two restraining conditions, although the ratio of residual stress to the material yield stress is greater for the tensile stresses (1 for tensile stresses and 0.5 for compressive stresses), the FE results demonstrate that the release of compressive residual stress at the start of the cut induces higher plastic strains.

Towards the end of the restrained model contour cut, the release of compressive stresses introduces high level of cutting plastic strains. It can be seen from Figure 3-36 that the redistributed stresses in this region (*i.e.* in the remained ligament of ~5 mm) are much higher at the cut tip for the restrained contour cut. Therefore, although restraining may help controlling plasticity, it can also bring some negative effects.

To avoid the up-coming plasticity-induced stress errors to be predominated by the effect of the remained ligament, the results in this region are disregarded throughout the rest of the thesis.

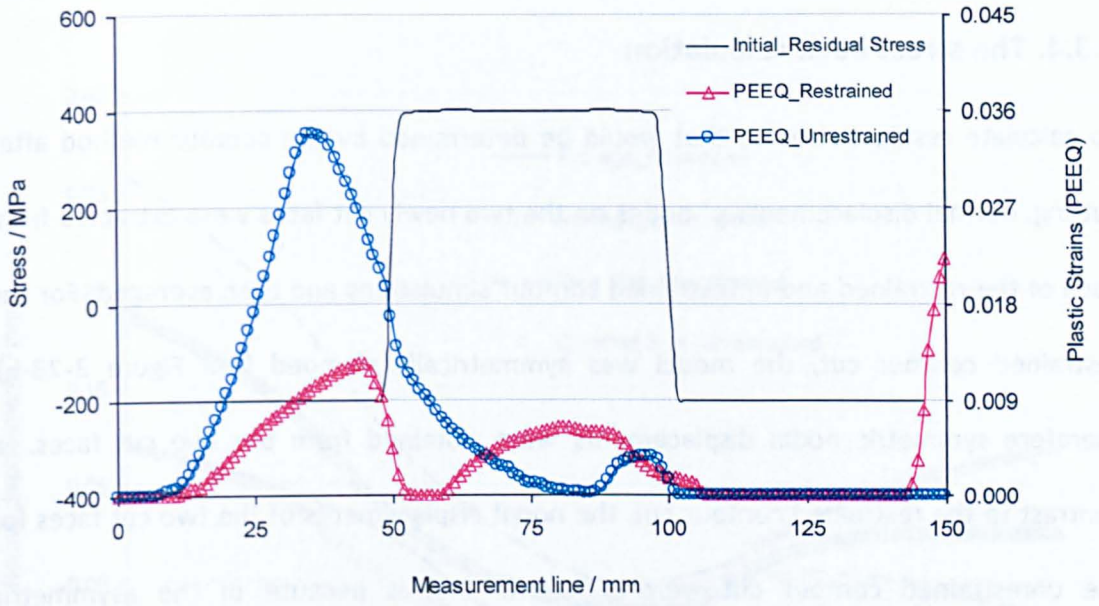

Figure 3-35: Plastic strain variation along the cutting path for the two restraining conditions.

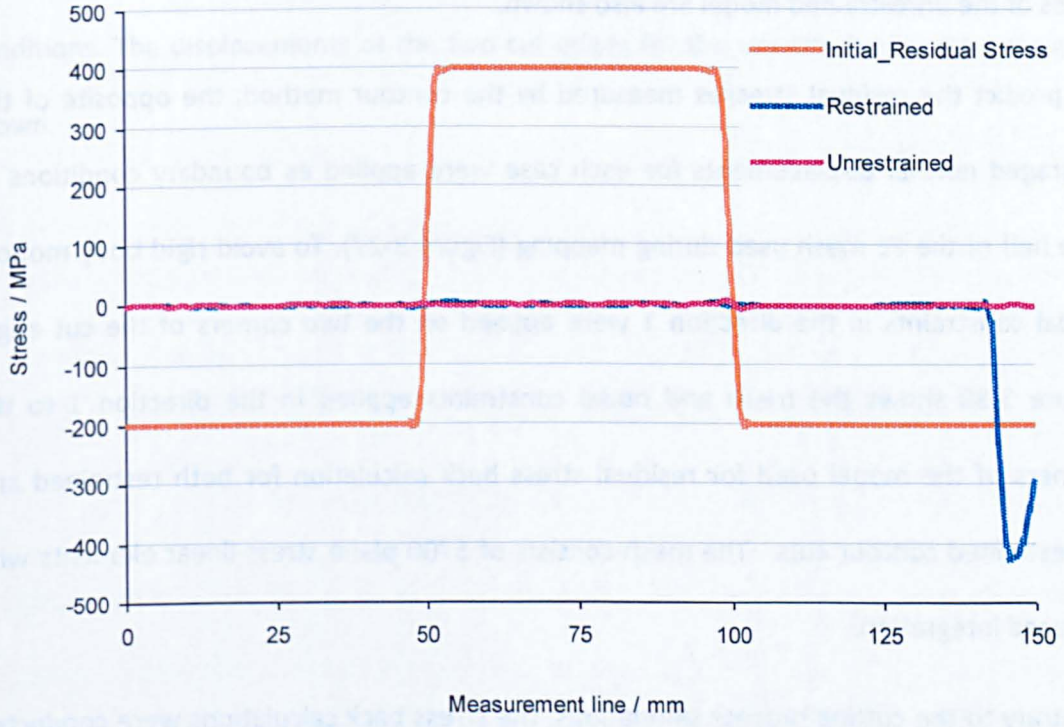

Figure 3-36: Comparison of the redistributed stresses at the cut end for the restrained and unrestrained contour cuts.

3.3.4. The stress back-calculation

To calculate residual stresses that would be determined by the contour method after cutting, normal displacements of nodes on the two newly cut faces were extracted from each of the restrained and unrestrained contour simulations and then averaged. For the restrained contour cut, the model was symmetrically clamped (see Figure 3-28-b); therefore symmetric nodal displacements were obtained from the two cut faces. In contrast to the restrained contour cut, the nodal displacements of the two cut faces for the unrestrained contour cut were different. That is because of the asymmetric restraining conditions used during the cutting process (Figure 3-28-a). Figure 3-37 illustrates the averaged normal displacements along the measurement line for both restrained and unrestrained contour cuts. The nodal displacements from the two cut faces of the unrestrained model are also shown.

To predict the residual stresses measured by the contour method, the opposite of the averaged normal displacements for each case were applied as boundary conditions to one half of the FE mesh used during mapping (Figure 3-27). To avoid rigid body motion, nodal constraints in the direction 1 were applied on the two corners of the cut edge. Figure 3-38 shows the mesh and nodal constraints applied in the direction 1 to the corners of the model used for residual stress back calculation for both restrained and unrestrained contour cuts. The mesh consists of 5700 plane stress linear elements with reduced integration.

Contrary to the cutting process simulations, the stress back calculations were conducted with linear finite element analysis. The material elastic properties, *i.e.* Young modulus and Poisson's ratio, were 200 GPa and 0.3, respectively.

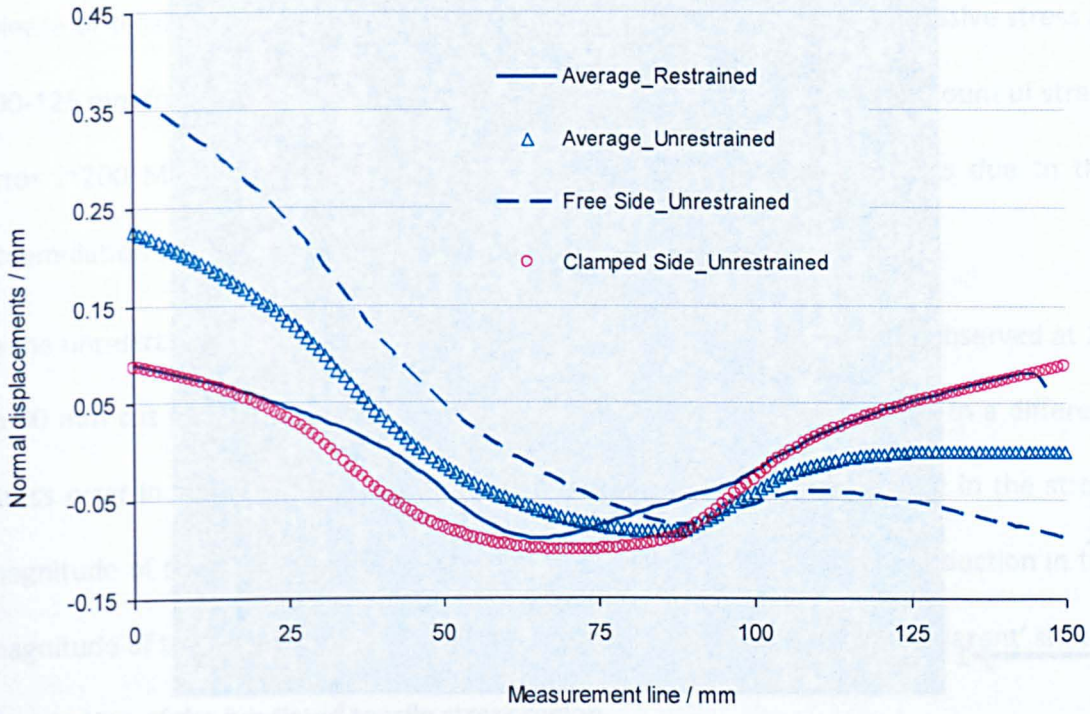

Figure 3-37: Averaged normal displacements along the cut edges for the two restraining conditions. The displacements of the two cut edges for the unrestrained model are also shown.

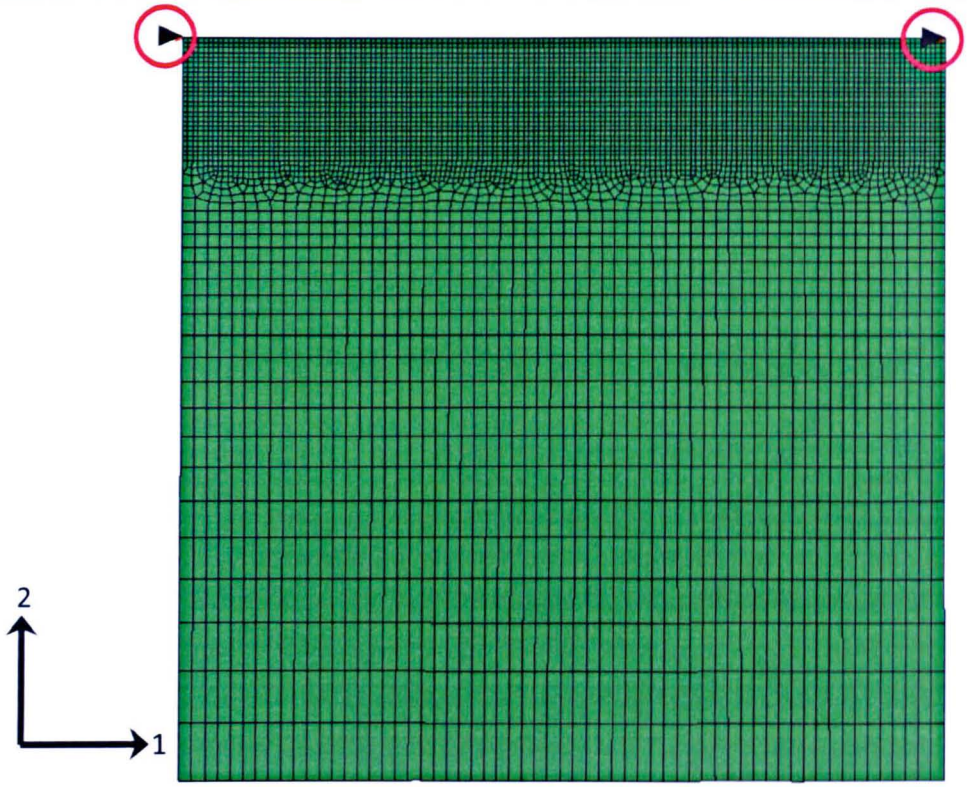

Figure 3-38: Mesh of half of the composite plate used for residual stress back calculation. The nodal constraints in the direction-1 on the cut face (within red circles) for avoiding rigid body motion are also shown.

Figure 3-39 and Figure 3-40 plot the back-calculated residual stress together with the initial stress state and their corresponding cutting plastic strain for the restrained and unrestrained contour cuts, respectively. Different effects of plastic strains on the predicted results can be observed for the two restraint conditions.

In the symmetrically restrained contour cut, the developed plastic strain from 10-55 mm cut depth induced by the release of compressive stress results in a progressive reduction in magnitude of predicted measured compressive stress (from 25-50 mm cut depth). The start of plastic strain induced by the release of tensile stresses coincides with a peak predicted tensile stress observed at ~60 mm cut depth followed by a drop in the

magnitude of predicted tensile stress (70-100 mm). The plastic strain induced by the release of tensile stress might cause the reduction in the predicted compressive stress at 100-125 mm from the start of the cut. Towards the cut end, a significant amount of stress error (~200 MPa) is introduced in the predicted contour method results due to the accumulation of plastic strain effects in the remained ligament.

In the unrestrained contour cut, a considerable amount of plastic strain is observed at 10 to 90 mm cut depth due to the release of compressive stresses. It results in a different stress error in the predicted compressive and tensile stresses: an increase in the stress magnitude of compressive stress (0-30 mm from the start of the cut), a reduction in the magnitude of tensile stress (50-87 mm from the start of the cut) and an 'apparent' shift in the location of the predicted tensile stress region.

Apart from a peak tensile stress observed at ~88 mm from the cut start, the effect of plastic strains induced by the release of tensile stresses on the predicted contour method results appears to be negligible. The peak tensile stress observed at ~ 88 mm coincides with the start of plasticity in the tensile region.

Figure 3-41 show how the absolute stress errors vary along the measurement line for the restrained and unrestrained contour cuts. The absolute stress errors were calculated by applying Equation 3-3.

$$\Delta\sigma = \left|\sigma_i\ (initial) - \sigma_i\ (predicted)\right| \qquad \textbf{Eq. 3-3}$$

where $\sigma_i\ (initial)$ is the initial stress at the measurement point i and $\sigma_i\ (predicted)$ is the predicted stress from the contour measurement method simulation at the same measurement point i.

For the restrained contour cut, significant amounts of error are introduced in the location corresponding to the drop observed in the magnitude of the predicted tensile stress (70-100 mm). The increase in the magnitude of the compressive stress towards the cut end (from ~ 132 mm) also induces high level of stress error.

In the unrestrained contour cut simulation the 'apparent' shift in location is the biggest source of errors followed by the increase in the magnitude of the predicted compressive stress (0-30 mm from the start of the cut).

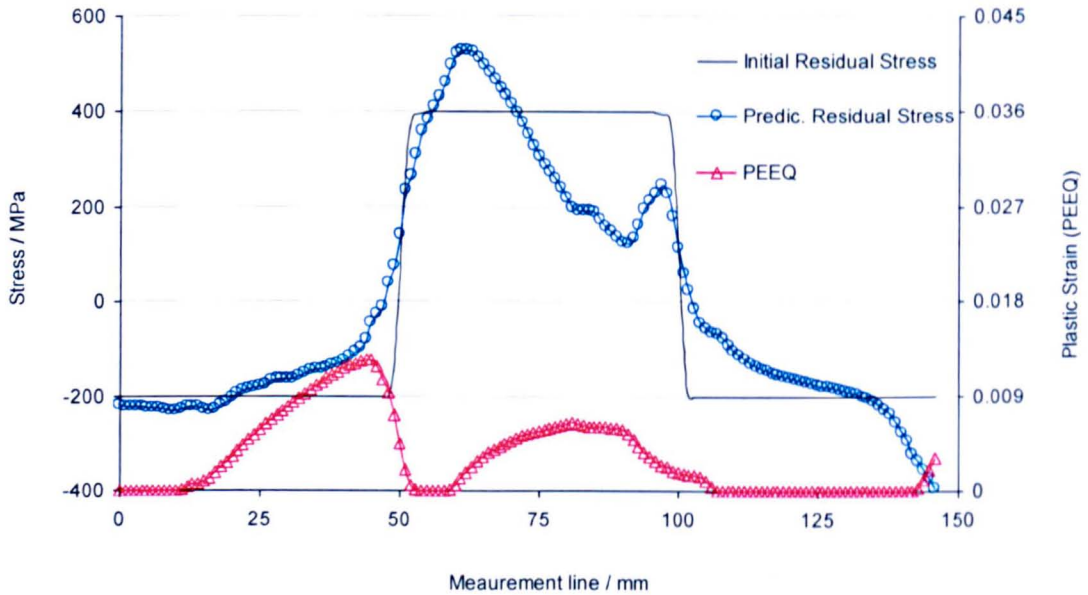

Figure 3-39: Effects of plastic strain on the predicted contour method measurements for the restrained contour cut of the composite plate.

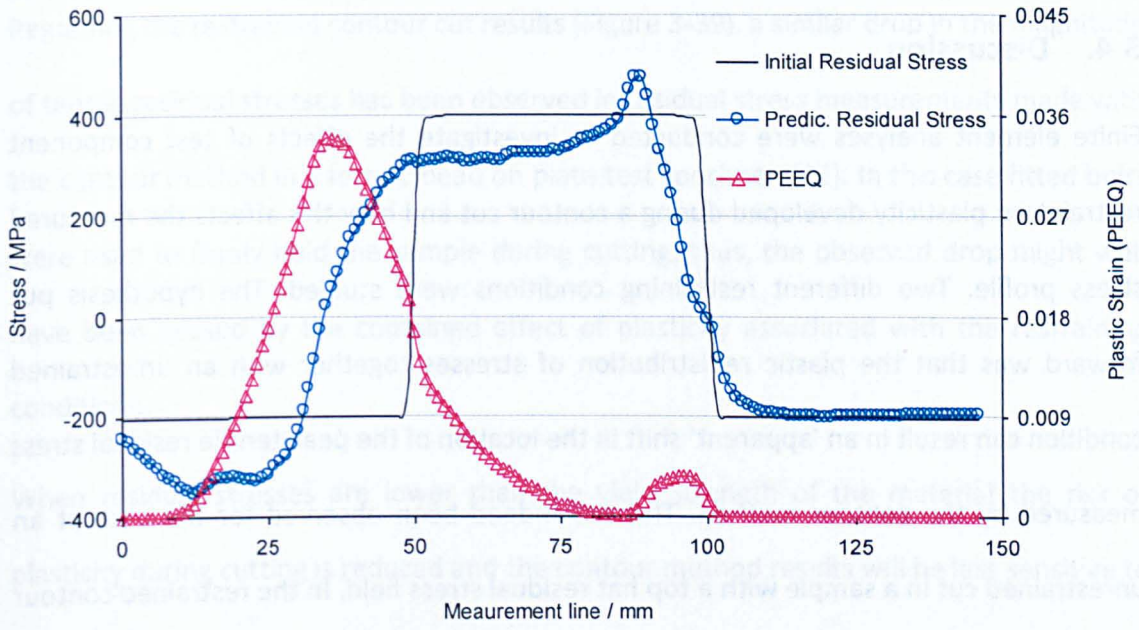

Figure 3-40: Effects of plastic strain on the predicted contour method measurements for the unrestrained contour cut of the composite plate.

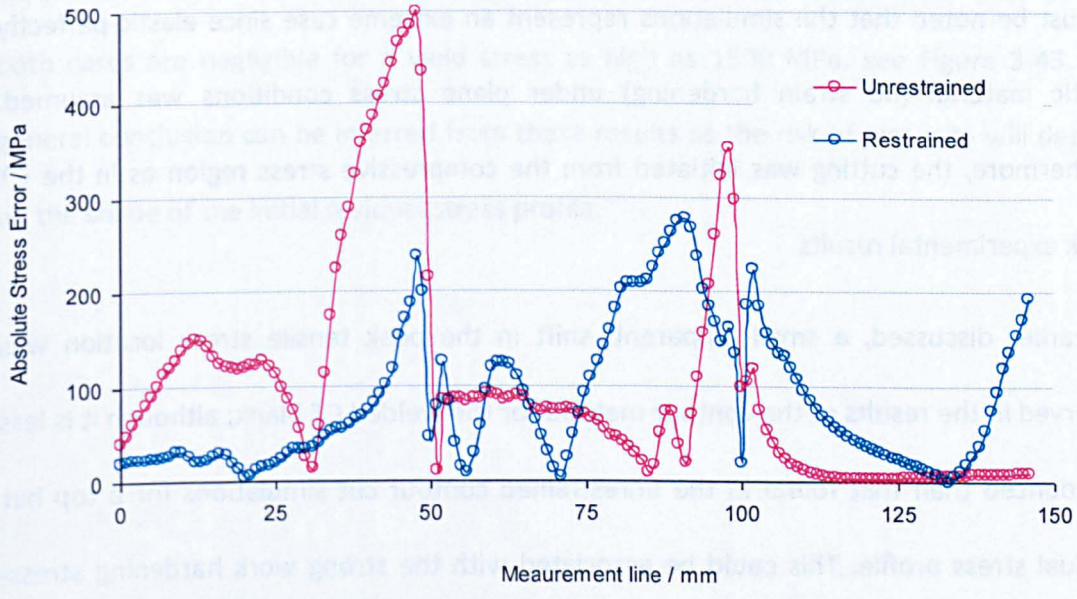

Figure 3-41: Absolute stress error variation for the two restraining conditions.

3.4. Discussion

Finite element analyses were conducted to investigate the effects of test component restraint on plasticity developed during a contour cut and how this affects the measured stress profile. Two different restraining conditions were studied. The hypothesis put forward was that the plastic redistribution of stresses together with an unrestrained condition can result in an 'apparent' shift in the location of the peak tensile residual stress measured by the contour method. This has indeed been observed for the case of an unrestrained cut in a sample with a top hat residual stress field. In the restrained contour cut the locations of the regions of compressive and tensile stress are essentially unchanged (from the original profile). However, both restraint conditions give measured stress profiles with large errors.

It must be noted that the simulations represent an extreme case since elastic-perfectly plastic material (no strain hardening) under plane stress conditions was assumed. Furthermore, the cutting was initiated from the compressive stress region as in the CT blank experimental results.

As earlier discussed, a small 'apparent' shift in the peak tensile stress location was observed in the results of the contour method for the welded CT blank; although it is less pronounced than that found in the unrestrained contour cut simulations for a top hat residual stress profile. This could be associated with the strong work hardening stress-strain behaviour of the CT blank material (Esshete 1250) [31]. Furthermore, the stress state in the CT blank specimen is closer to plane strain than plane stress conditions, which may mitigate the accumulation of plastic strains during the cutting process.

Regarding the restrained contour cut results (Figure 3-39), a similar drop in the magnitude of tensile residual stresses has been observed in residual stress measurements made with the contour method in a ferritic bead on plate test specimen [32]. In this case fitted bolts were used to firmly hold the sample during cutting, thus, the observed drop might well have been caused by the combined effect of plasticity associated with the restraining conditions.

When residual stresses are lower than the yield strength of the material the risk of plasticity during cutting is reduced and the contour method results will be less sensitive to the restraining conditions adopted. Figure 3-42 shows simulated results for an intermediate yield stress value, i.e. 800 MPa. The errors in the contour stress profile for the restrained case are small but there is still a noticeable shift in the position of the unrestrained profile (compare with Figure 3-39 and Figure 3-40) whereas the errors for both cases are negligible for a yield stress as high as 1500 MPa, see Figure 3-43. No general conclusion can be inferred from these results as the risk of plasticity will depend on the shape of the initial residual stress profile.

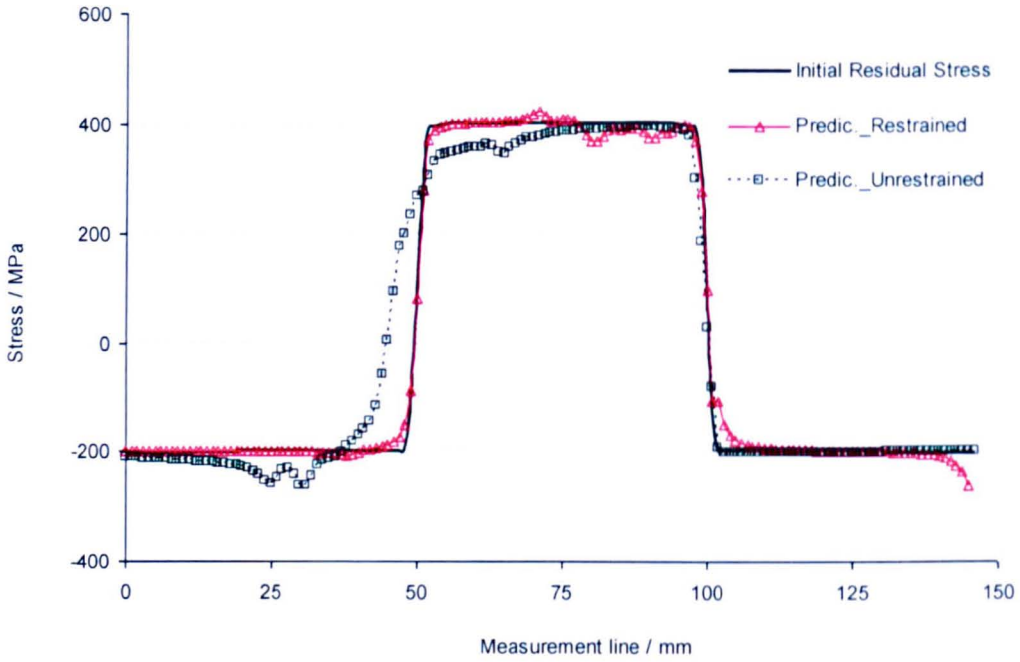

Figure 3-42: Predicted contour method results when moderate plasticity occurs in the stress relaxation process for restrained and unrestrained conditions (yield stress = 800 MPa).

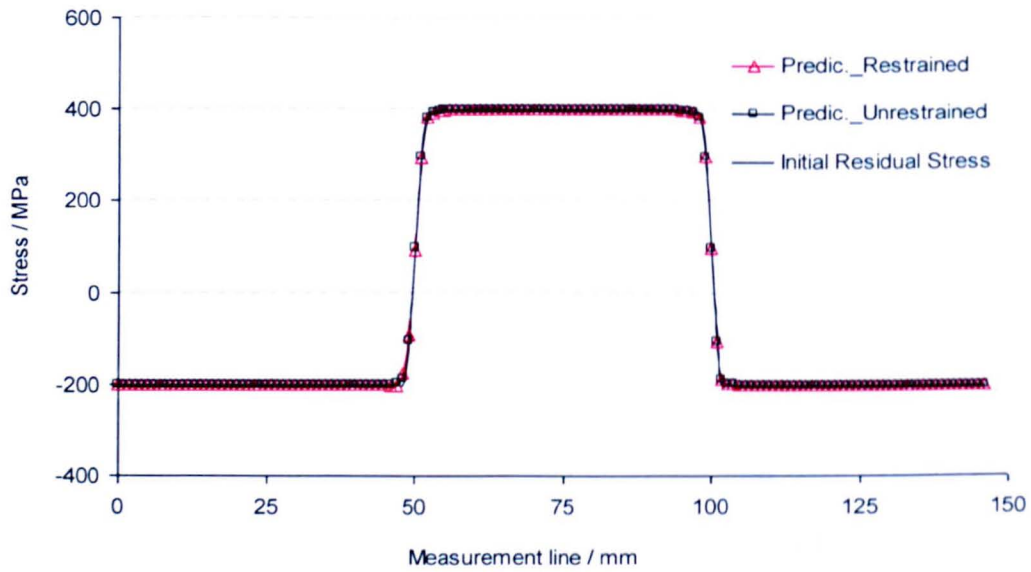

Figure 3-43: Predicted contour method results when no plasticity occurs in the stress relaxation process for restrained and unrestrained conditions (yield stress = 1500 MPa).

3.5. Conclusions

The following conclusions are made on the work carried out in this chapter:

1. The level of cut opening restraint applied in a contour measurement affects the distribution and extent of plasticity introduced and the type of error resulting in the measured stress profile.
2. When an unrestrained contour cut is conducted and the tensile residual stresses are of the same order as the yield strength of the material, the measured distribution of stress may exhibit an 'apparent' shift in the location of the measured peak residual stresses in a direction opposite to that of cutting.
3. The level of error in contour measurements is dependent on the ratio of the magnitude of the residual stresses present to the material yield strength.
4. Excellent overall agreement has been achieved between neutron diffraction, slitting and contour stress measurements in a welded CT blank specimen. A small shift in the location of the peak tensile stress of the contour measurement relative to the other measurements can be explained by development of compressive plasticity during cutting associated with the lack of restraint applied to the specimen during the measurement.

3.6. References

1. Prime MB (2001) Cross-Sectional Mapping of Residual Stresses by Measuring the Surface Contour After a Cut. Journal of Engineering Materials and Technology 123 (2):162-168

2. Shin S (2005) FEM analysis of plasticity-induced error on measurement of welding residual stress by the contour method. Journal of Mechanical Science and Technology 19 (10):1885-1890

3. Dennis RJ, Bray DP, Leggatt NA, Turski M (2008) Assessment of the Influence of Plasticity and Constraint on Measured Residual Stresses Using the Contour Method / PVP2008-61490. Paper presented at the ASME Pressure Vessels and Piping Division Conference, Chicago, USA,

4. Traore Y, Paddea S, Bouchard PJ, Gharghouri MA (2012) Measurement of the Residual Stress Tensor in a Compact Tension Weld Specimen. Experimental Mechanics:1-14

5. Prime MB (2010) Plasticity Effects in Incremental Slitting Measurement of Residual Stresses. Engineering Fracture Mechanics and Technology 77:1552-1566

6. EDF Energy (2010) AGR Materials Data Handbook. R6 Rev. 008. Gloucester, UK

7. ASTM (2001) E 1457-00: Standard Test Method for Measurement of Creep Crack Growth Rates in Metals Annual Book of ASTM Standards 3 (1):936-950

8. Hosseinzadh Torknezhad F, Bouchard PJ, James JA (2010) Measurements of Residual Stress in a Welded Compact Tension Specimen Using the Neutron Diffraction and Slitting Techniques. Materials Science Forum 652:210-215

9. Winholtz RA, Krawitz AD (1995) The relaxation of residual stresses with postweld heat treatment in a high-performance weld measured with neutron diffraction. MMTA 26 (5):1287-1295. doi:10.1007/BF02670622

10. Francis JA, Stone HJ, Kundu S, Bhadeshia HKDH, Rogge RB, Withers PJ, Karlsson L (2009) The Effects of Filler Metal Transformation Temperature on Residual Stresses in a High Strength Steel Weld. Journal of Pressure Vessel Technology 131 (4):041401-041408

11. Non-destructive testing - Standard test method for determining residual stresses by neutron diffraction DD CEN ISO/TS 21432:2005 (2005).

12. Nishioka K, Hanabusa T, Fujiwara H (1974) Theory of the X-ray residual stress analysis. Scripta Metall 8:1349-1350

13. Withers PJ (2007) Residual stress and its role in failure. Reports on Progress in Physics 70 (12):2211

14. Schindler H, Cheng W, Finnie I (1997) Experimental determination of stress intensity factors due to residual stresses. Experimental Mechanics 37 (3):272-277

15. Prime MB (1999) Measuring residual stress and the resulting stress intensity factor in compact tension specimens. Fatigue & Fracture of Engineering Materials & Structures 22 (3):195-204

16. Prime MB (1999) Residual Stress Measurement by Successive Extension of a Slot: The Crack Compliance Method. Applied Mechanics Reviews 52 (2):75-96

17. Schindler HJ, Bertschinger P (1997) Some Steps Towards Automation of the Crack Compliance Method to Measure Residual Stress Distributions. Paper presented at the 5th Int. Conference on Res. Stress, Linköping, Sweden

18. Shih CF (1981) Relationships between the J-integral and the crack opening displacement for stationary and extending cracks. Journal of the Mechanics and Physics of Solids 29 (4):305-326

19. MATLAB (2009) Version 7.8.0 (R2009a). The MathWorks Inc

20. Vieira M, Shimada K, Furuhata T (2003) Smoothing of Noisy Laser Scanner Generated Meshes Using Polynomial Fitting and Neighborhood Erosion. Journal of Mechanical Design 126 (3):495-503

21. Bouchard PJ, Turski M, Smith MC (2009) Residual Stress Concentrations in a Stainless Steel Slot-Weld Measured by the Contour Method and Neutron Diffraction / PVP2009-77234. Paper presented at the ASME PVP Conference, Prague, Czech Republic,

22. Hosseinzadeh F, Bouchard PJ (2012) Mapping Multiple Components of the Residual Stress Tensor in a Large P91 Steel Pipe Girth Weld Using a Single Contour Cut. Experimental Mechanics:1-11

23. Hosseinzadeh F, Toparli MB, Bouchard PJ (2012) Slitting and Contour Method Residual Stress Measurements in an Edge Welded Beam. Journal of Pressure Vessel Technology 134 (1):011402-011406

24. Turski M, Edwards L (2008) Boiler Spines Residual Stress Measurements Programme Task 1.2: Residual Stress Measurements on Slot Weld Specimen by the Contour Method and Neutron Diffraction. The Open University, Milton Keynes

25. Prime MB, Kastengren AL (2010) The contour method cutting assumption: error minimization and correction. Paper presented at the SEM Annual conference & exposition on experimental and applied mechanics Indianapolis, Indiana, USA,

26. Withers P, Bhadeshia H (2001) Overview Residual Stress Part 2 - Nature and Origins. Materials Sci Technol 17:366

27. Janssen M, Zuidema J, Wanhill RJH (2002) Fracture Mechanics. 2nd edn. Delft University Press, Delft

28. ABAQUS (2010) ABAQUS/Standard Documentation Version 6.10.2. ABAQUS, Inc

29. Dennis RJ, Leggatt NA, Kutarski EA (2009) Investigation of the Performance of the Contour Residual Stress Measurement Method When Applied to Welded Pipe Structures / PVP2009-77470. Paper presented at the ASME Pressure Vessels and Piping Division Conference, Prague, Czech Republic,

30. Hosseinzadeh F (2009) Measurement of Residual Stress in a Welded CT Specimen by the Slitting Method - OU/MatsEng/002 Issue 1. The Open University, Milton Keynes

31. Ganguly S, Turski M, Fitzpatrick ME, Edwards L, Smith MC, Bouchard PJ (2008) A Study of a Localised Constitutive Mechanical Property Data in a Multi-Pass Austenitic Steel Weld Specimen - PVP2008-61365. ASME Conference Proceedings 2008

32. Hosseinzadeh F, Bouchard PJ (2012) Residual stress measurment of a ferretic bead on plate benchmark test specimen using the contour method / PVP2012-78556. Paper presented at the ASME PVP Conference, Toronto, Canada,

Chapter 4: Minimisation of plasticity-induced errors in the contour method

In the previous chapter 2D finite element analyses were conducted to assess the effect of plasticity on restrained and unrestrained contour cut residual stress results. In both cases the predictions indicated that significant errors were introduced in the simulated contour measurement results, although the analyses adopted idealised conditions (*i.e.* elastic-perfectly plastic material under a plane stress condition).

In this chapter, an analogy is made between an edge cracked plate subjected to an internal load and the residual stress relaxation process that occurs during wire EDM cutting in the contour method. Furthermore, stress intensity factor analysis for different cutting/restraining strategies is used to develop a novel cutting strategy by which plasticity-induced errors in the contour method can be reduced or avoided. The stress intensity factor analysis for different cutting and restraining conditions is conducted using an idealised 'top hat' initial residual stress distribution.

4.1. Introduction

In the contour method, as the cut proceeds, the stresses acting normal to the cut faces are relaxed resulting in redistribution of the residual stress field throughout the entire body.

Assuming a release of tensile residual stresses, this process is analogous to opening mode (mode I) cracking within a body subjected to an internal load in linear elastic fracture mechanics albeit with a blunt crack tip. It can be clearly seen from Figure 4-1 that there is

an analogy between the stress relaxation process during sample cutting in the contour method and tractions on crack surfaces required to achieve displacement continuity.

As stated earlier in Chapter 2, the resulting stress field at the tip of the cut, which has a finite radius, is directly related to the mode I stress intensity factor at the tip of a sharp crack within a body [1-3]. As the cut length increases the stress field at the cut tip becomes more intense and results in local yielding. If the yielding extends sufficiently far from the cut tip this may introduce significant plasticity and resultant errors in the contour stress measurement. Therefore the plasticity-induced stress errors in the contour method are controlled by the state of the cut tip stresses which is characterised by the mode I stress intensity factor.

The consequence of this is that the stress intensity factor can be used to assess the likely hood of plasticity and extent of plasticity that may arise during contour cuts and thereby this parameter provides a means of quantifying, controlling and potentially avoiding plasticity-induced errors.

It must be noted that linear elastic fracture mechanics is usually applied for fracture assessment of components when small scale yielding conditions are met [1,2,4], that is when inelastic deformation at the crack tip is smaller than the crack size. However, in the present study linear elastic fracture mechanics is used for the purpose of plasticity-induced errors investigation and control in the contour method. Therefore, the condition of small scale yielding does not necessarily need to be demonstrated. Furthermore, as mentioned earlier, the level of plasticity during the stress relaxation process is not expected to attain levels where elastic plastic fracture mechanics has to be considered. Thus, linear elastic fracture mechanics solutions with the Irwin plasticity correction are

used hereafter for the purpose of plasticity investigation and control in the contour method. In Chapter 5, results obtained from Irwin plastic zone size expression are compared to those obtained by FE analysis in order to investigate their validity.

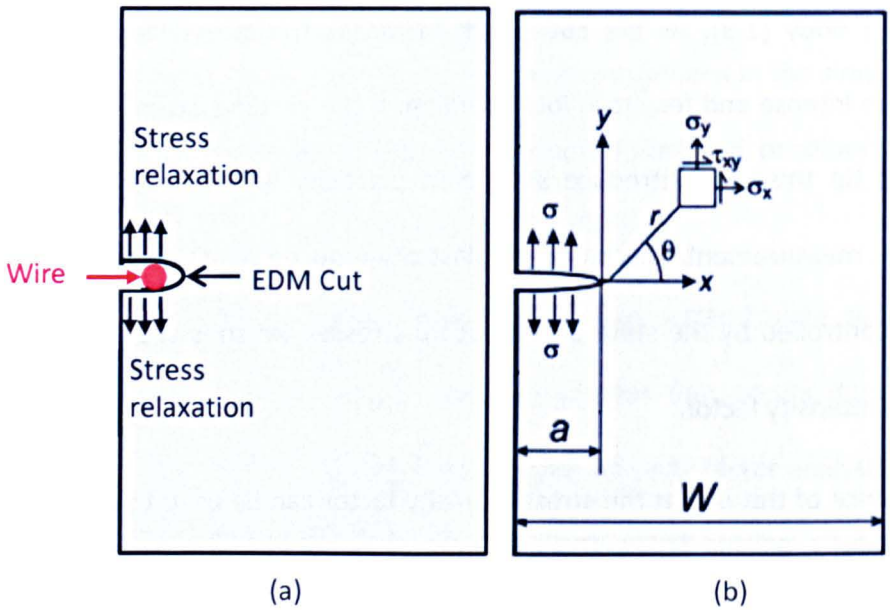

Figure 4-1: Analogy between stress relaxation during contour cutting (a) with an edge cracked plate in linear elastic fracture mechanics (b). In (a), the stresses are progressively relaxed (applied) during the cut while in (b) the internal load is instantaneously applied.

4.2. Remarks on the negative stress intensity factor

A negative stress intensity factor defines the crack tip stress concentration within a compressive stress field. Generally in fracture mechanics, negative stress intensity factor solutions are considered to be incorrect. That is because the faces of a practical crack, when anticipated to be fully or partially closed, cannot interpenetrate anywhere.

However, in a contour cut, a finite width of material is removed during the cutting process [5,6]. Thus the cut faces can displace under a compressive stress field without

contact occurring between the cut faces. Therefore, a negative stress intensity factor could well be obtained during a contour cut for residual stress measurements. Figure 4-2 illustrates the cut opening and closure under tensile and compressive stress field, respectively.

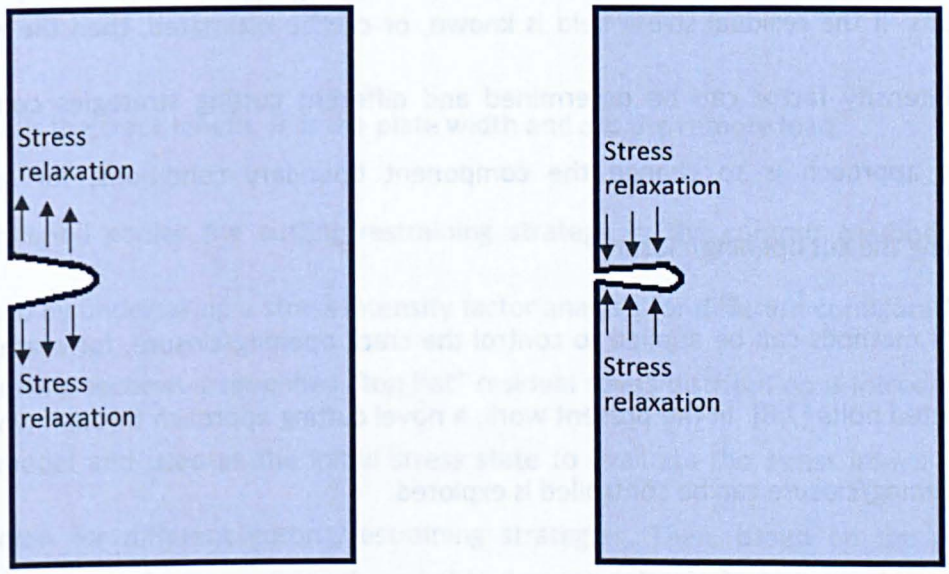

Figure 4-2: Representation of the cut opening (a) and closure (b) during the stress relaxation process and when a finite width of material is removed. Relaxation of tensile stresses tends to open the cut while the release of compressive stresses tends to close it.

4.3. Cutting/restraining optimisation

Currently most contour cuts are undertaken using an edge crack configuration. This is where the wire enters one side of the body and erodes into the body along a straight line until the cut severs the part into two pieces. However, this cutting strategy can result in high magnitude stress intensity factors associated with the residual stress field redistribution. The hypothesis explored in the present chapter is that the mode I stress

intensity factor ahead of the crack can be used to assess and, to some extent, minimise the plasticity arising in the residual stress release process during cutting.

The aim is to minimise or eliminate the risk of plasticity which may introduce errors. This might be achieved by changing the cutting path and therefore the stress redistribution conditions. If the residual stress field is known, or can be estimated, then the residual stress intensity factor can be determined and different cutting strategies compared. Another approach is to change the component boundary conditions, for example restraining the cut opening/closure.

Different methods can be applied to control the crack opening/closure, for example the use of fitted bolts [7,8]. In the present work, a novel cutting approach through which the crack opening/closure can be controlled is explored.

The approach consists of creating an embedded crack configuration (a centre crack for example, Figure 4-3-a) for the cutting process as in this case the crack opening/closure is much smaller than for a plate having an edge crack of the same length. Figure 4-3-b shows the significant reduction in the stress intensity factor for the same crack length for a centre crack configuration. The SIF results for both centre and edge cracks were determined analytically using standard solutions (Equation 4-1) [1,2] for a finite width plate uniformly loaded with a membrane stress of 100 MPa. The plate dimensions assumed were (150x100) mm^2.

$$K_I^{Edge} = \left(0.265 * \left(1 - \frac{a}{W} \right)^4 + \frac{0.857 + 0.265 * \left(a/W \right)}{\left(1 - a/W \right)} \right) * \sigma \sqrt{\pi a}$$

$$K_I^{Centre} = \left(\frac{1 - 0.5 * \left(a/W \right) + 0.370 * \left(a/W \right)^2 - 0.044 * \left(a/W \right)^3}{\left(1 - a/W \right)^{0.5}} \right) * \sigma \sqrt{\pi a}$$

Eq. 4-1

where, a is the crack length, W is the plate width and σ is the remote load.

As mentioned earlier the cutting/restraining strategy in the contour method can be optimised by undertaking a stress intensity factor analysis for different configurations. In the following sections a simplified "top hat" residual stress distribution is introduced in a 2D FE model and used as the initial stress state to evaluate the stress intensity factor distribution for different cutting/restraining strategies. Then, based on the analysed configurations, the entire contour method (cutting and stress back-calculation) is simulated to determine the 'measured' residual stress distributions and compare them with the original distribution.

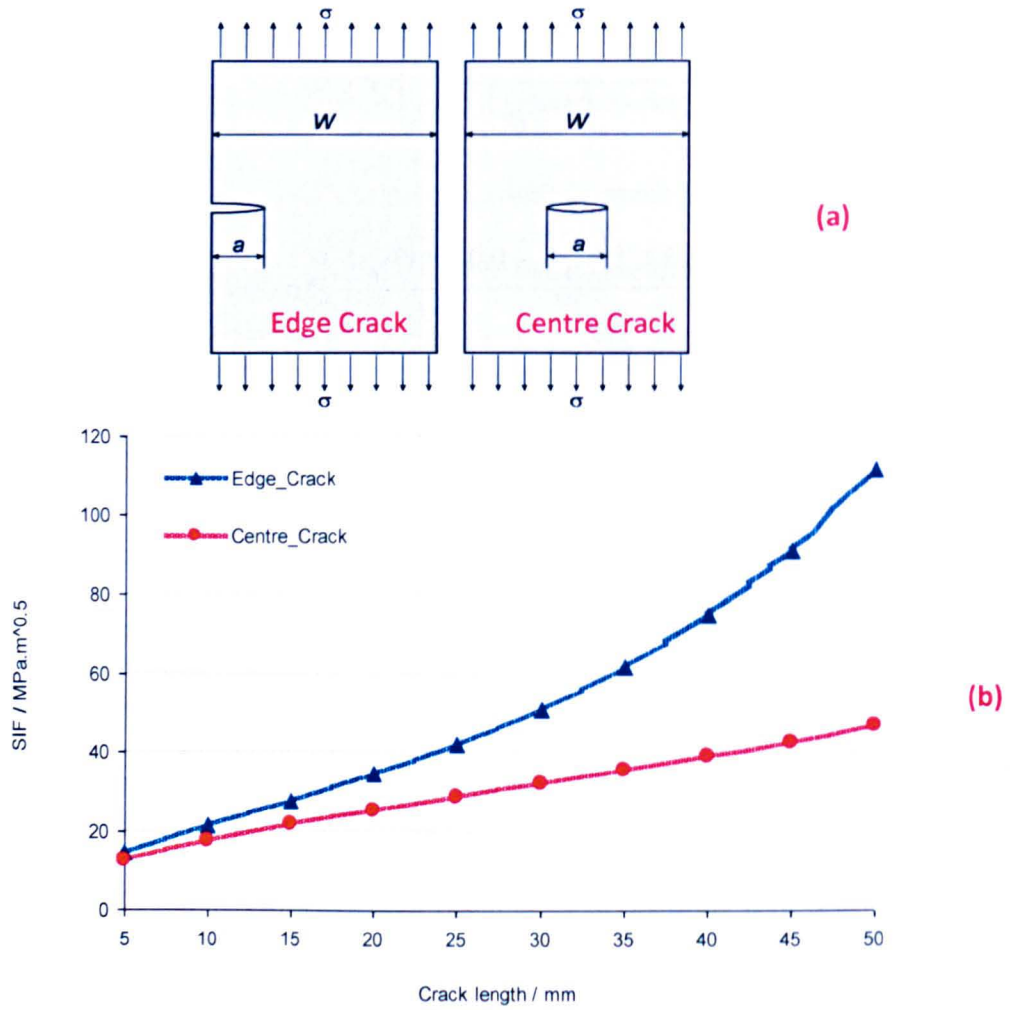

Figure 4-3: Comparison of edge and centre crack (a) stress intensity factor distribution as function of crack length (b).

4.3.1. Initial residual stress generation

The "top hat" stress distribution used here differs from the previous one in Chapter 3 only by the extent of the tensile stress region and the uniform stress magnitude for both compressive and tensile stresses. Therefore, the generation process for the two initial stress distributions is identical. The modifications in the tensile stress extent and magnitude were achieved by changing the material properties (see Table 4-1) and the

composite plate dimensions as shown in Figure 4-4. Here, the plate is 400 mm long and 200 mm wide.

The stress intensity factor analyses are conducted along a line located at the plate mid-length, referred to as the measurement line corresponding to the contour cutting path simulation. Symmetric clamping is used here because asymmetric restraining can result in different cut surface deformations which can induce a significant amount of error in measurements.

Table 4-1: The material properties used for residual stress generation in the composite plate.

	Young's Modulus (GPa)	Poisson's Ratio	Yield Stress (MPa)	Thermal Expansion Coefficient (/°C)
Material A&C	200	0.3	200	1.73×10^{-5}
Material B	200	0.3	200	3.46×10^{-5}

As shown in Figure 4-4, the geometry of the composite plate presents two symmetry lines in the directions 1 and 2. Furthermore, symmetric restraining conditions in the direction 2 will be used during the cutting process. Therefore, the model is simplified by simulating only one half of the plate using symmetry boundary conditions in the direction 2 along the measurement line. The second symmetry line in the direction 1 could be used for further simplification. However the results in this direction are not expected to be symmetric.

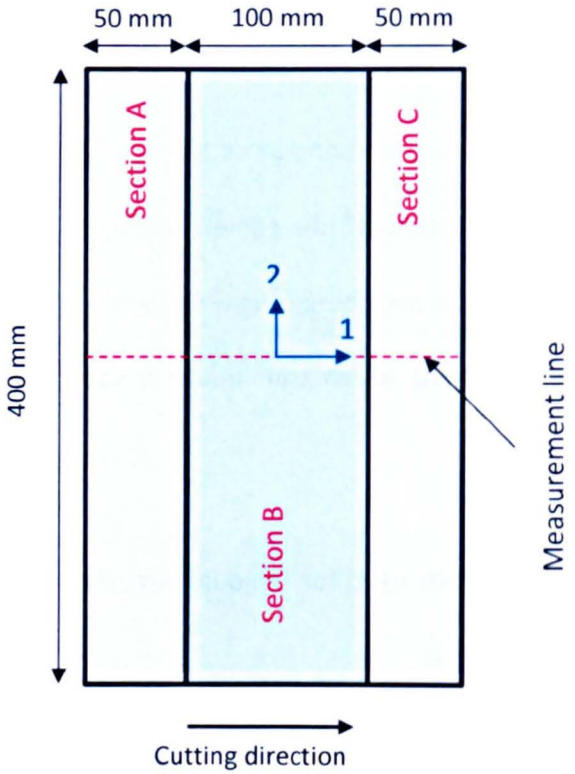

Figure 4-4: Schematic drawing of the composite plate used in the FE analysis for stress intensity factor analysis. Only one half of the plate was simulated.

Elastic-perfectly plastic behaviour under plane stress conditions is assumed for the different materials. The model, representative of one half of the composite plate, was meshed with 1 x 1 mm^2 four-node plane stress elements with reduced integration (CPS4R) using the ABAQUS FE code [9].

The residual stresses within the plate are generated by cooling down the heated model to room temperature. This is achieved by setting the initial temperature to 1000 °C and cooling it down to the room temperature assumed to be 20 °C.

Figure 4-5 and Figure 4-6 show the map and the distribution along the measurement line of the generated residual stresses, respectively. For both tensile and compressive stresses a maximum stress magnitude of ~200 MPa is obtained.

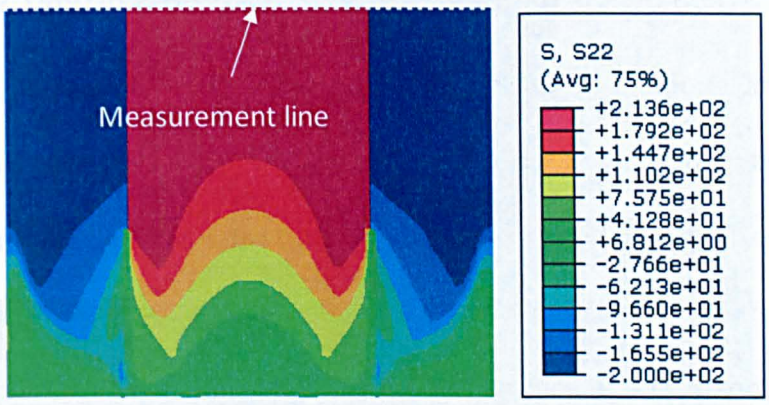

Figure 4-5: Map of generated residual stresses normal to the measurement line (*i.e.* in direction 2). Stress units are in MPa.

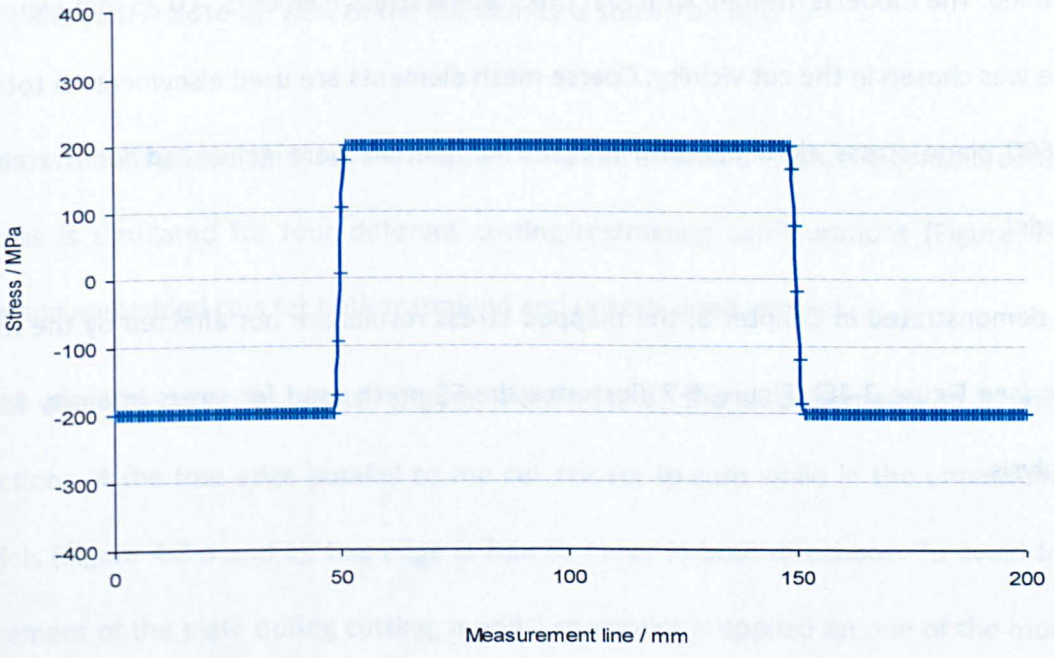

Figure 4-6: The line distribution of the residual stress component in direction 2 along the measurement line.

4.3.2. Stress intensity factor study for different cutting/restraint conditions

On completion of introducing residual stresses in the composite plate, the stresses are mapped onto a new a FE model of the same geometry. As earlier mentioned, the purpose of mapping is to define elastic (rather than elastic elastic-plastic) material properties and a fine mesh in the vicinity of the cut. Since only the residual stress intensity factor distribution is of interest, material elastic constants of 200 GPa for the Young's modulus and 0.3 for Poisson's ratio are defined for the different FE cases to be examined. To be consistent with the model used for generating the initial residual stress field, plane stress and symmetry boundary conditions along the measurement line in the direction 2 are defined. The model is meshed with first order plane stress elements. A 0.25 mm elements size was chosen in the cut vicinity. Coarse mesh elements are used elsewhere. A total of 19600 plane stress elements with reduced integration were generated for the entire model.

As demonstrated in Chapter 3, the mapped stress results are not affected by the mesh size (see Figure 3-26). Figure 4-7 illustrates the FE mesh used for stress intensity factor analysis.

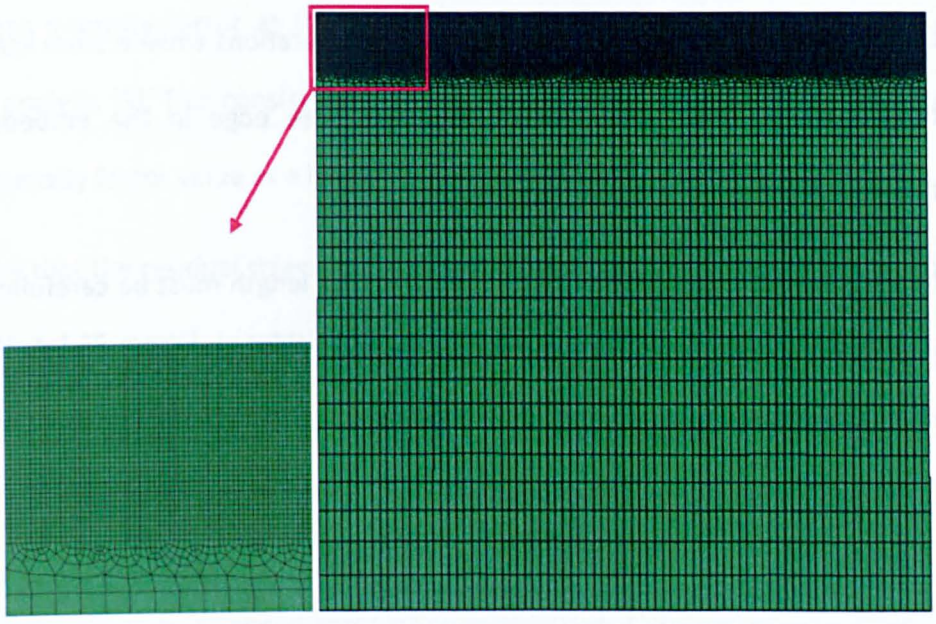

Figure 4-7: FE mesh onto which initial stress are mapped for residual stress intensity factor analysis. A close-up view of the cut vicinity is shown on left.

Once the initial residual stresses are mapped onto the above FE mesh, the contour cutting process is simulated for four different cutting/restraining configurations (Figure 4-8): edge and embedded cuts for both restrained and unrestrained regimes.

In the restrained configurations (Figure 4-8-b and d) the displacements in x and y directions of the free edge parallel to the cut are set to zero while in the unrestrained models (Figure 4-8-a and c), this edge is free to move in both directions. To avoid free movement of the plate during cutting, a nodal constraint is applied on one of the model corners.

The wire EDM cutting process was simulated by incrementally releasing the symmetry boundary conditions defined in the y-direction along the measurement line. The effect of a finite cut width that is created in a real contour cut was neglected. As illustrated in Figure 4-8-a and Figure 4-8-b, the cut is initiated from one of the model free edge

perpendicular to the cut direction in the edge cut configurations while a 5mm ligament is left between the cut start and one of the plate free edge in the embedded cut configurations (Figure 4-8-c and Figure 4-8-d).

When the results within the ligament are of interest, its length must be carefully chosen in order to avoid development of high plastic strains. This was achieved from the SIF analysis by testing different ligament sizes, as discussed later in this section.

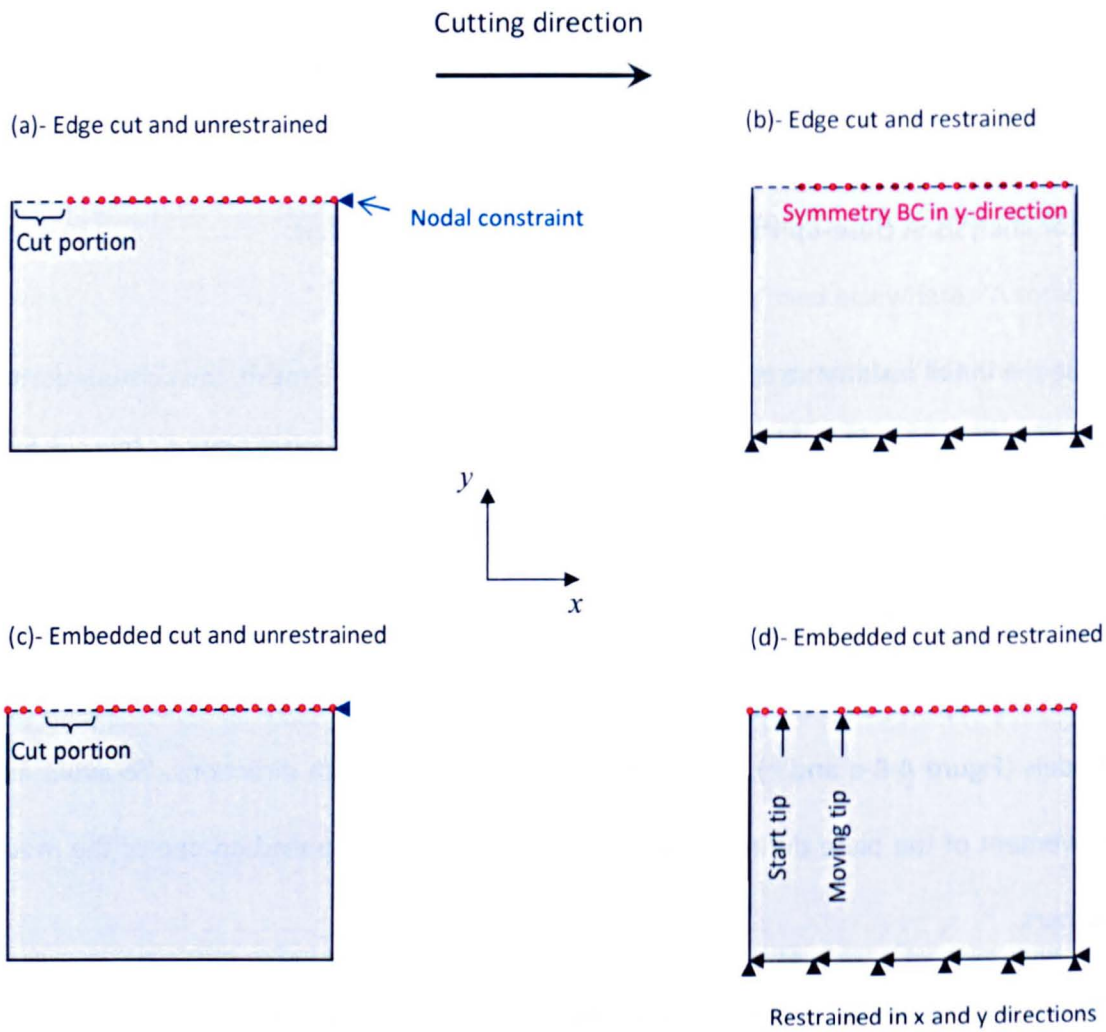

Figure 4-8: Schematic of the four cutting/restraining configurations analysed.

The stress intensity factor at the crack tip within ABAQUS is determined by contour integral analysis [9]. This consists of defining the crack and requesting the corresponding stress intensity factor value as a history output for different contours.

To ensure that the residual stress intensity factor data are unaffected by the mesh density an additional FE model, in which the cut vicinity was meshed with a 0.5 mm mesh size was used to determine the stress intensity distribution in the edge and unrestrained cut configuration. From Figure 4-9 it can be clearly seen that the results obtained from the two mesh grids are very consistent.

Figure 4-10 compares the residual stress intensity factor distributions for the four different cut/restraining configurations. For the embedded cut configurations, the results relate to the moving tips. Results for the start tip (not shown), which is associated the ligament, are only used to assess development of plasticity in the ligament.

Two groups of peaks are observed in the stress intensity factor distributions. The first group of peaks occurs at 45-50 mm cut length and are introduced by the release of compressive stresses while the second group of peaks (145-150 mm cut length) are due to the release of tensile stresses.

In the first group of peaks, the maximum compressive stress intensity factor peak is observed in the edge cut and unrestrained configuration (-108 MPa$\sqrt{m}$). Significant reduction in this peak value is obtained by restraining the edge cut model (-73 MPa$\sqrt{m}$) or by adopting the embedded cut configurations (~-60 MPa$\sqrt{m}$).

In contrast to the first group of compressive peaks, the edge and unrestrained cut gives the lowest tensile SIF peak value (33 MPa$\sqrt{m}$) for a crack length of 150 mm. The maximum tensile peak values are found with the embedded and unrestrained cut cases. Therefore,

although the embedded configuration helps to reduce the magnitude of the compressive residual stress intensity factor in some locations, further restraint is required to reduce the overall SIF distribution.

It must be noted that although residual stress intensity factor data can be used for plasticity assessment in the contour method, it is the plastic zone size distribution along the line of interest that tells us about development of plasticity during stress relaxation associated with cutting.

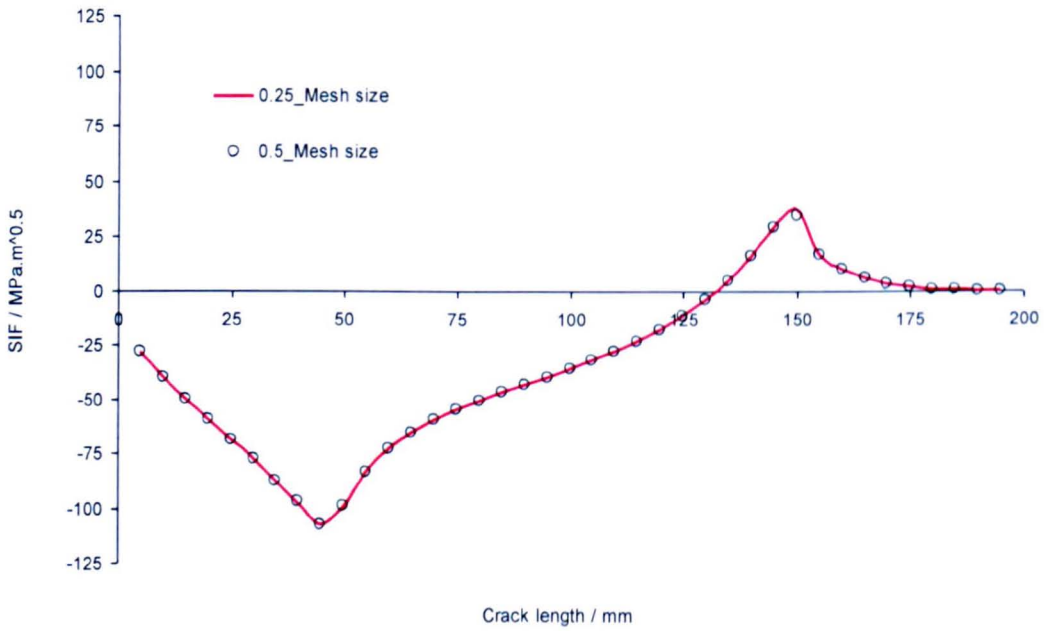

Figure 4-9: Residual stress intensity factor distribution for two different mesh sizes.

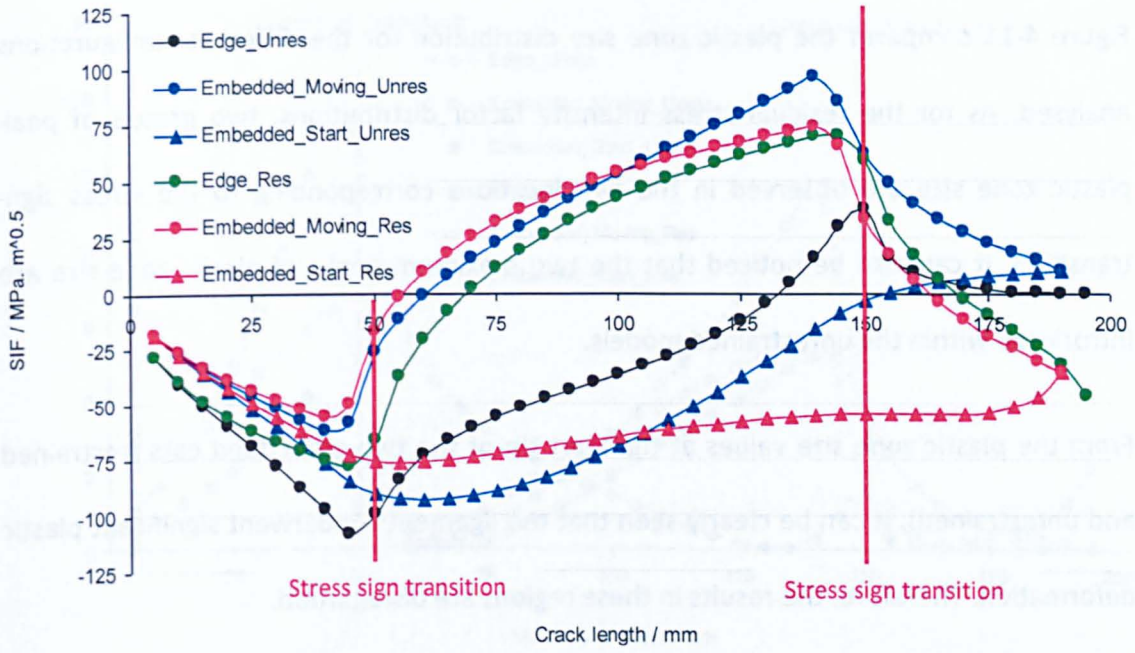

Figure 4-10: Residual stress intensity factor distribution for the four different cutting/restraining configurations assuming the idealised 'top hat' stress field.

4.3.3. Plastic zone size analysis for the different cutting/restraint conditions

Assuming an elastic-perfectly plastic material with a yield stress value of 450 MPa, the plastic zone size distribution for the four cut/restraining configurations can be readily calculated using the corresponding residual stress intensity factor data (see section 4-3-2) and by applying Irwin plastic zone size expression (Equation 4-2) [1,2].

$$r_y = \frac{1}{p\pi}\left(\frac{K_I}{\sigma_0}\right)^2 \qquad \textbf{Eq. 4-2}$$

where, K_I is the stress intensity factor, σ_0 is the material yield stress, $p=1$ for plane stress condition and $p=3$ for plane strain state.

Figure 4-11 compares the plastic zone size distribution for the different configurations analysed. As for the residual stress intensity factor distributions, two groups of peak plastic zone size are observed in the two locations corresponding to the stress sign-transition. It can also be noticed that the two maximum peaks of plastic zone size are introduced within the unrestrained models.

From the plastic zone size values at the start tip of the two embedded cuts (restrained and unrestrained), it can be clearly seen that the ligaments underwent significant plastic deformation. Therefore, the results in these regions are disregarded.

To select the optimum cutting/restraining configuration, the average plastic zone size (for all crack lengths) for the four configurations are determined and compared. An average plastic zone size of ~4 mm is found to be introduced in the unrestrained models (*i.e.* edge and embedded) while an average plastic zone size of 3.5 and 3 mm is introduced in the restrained edge and embedded cut configurations, respectively. Therefore, the embedded cut configuration combined with rigid restraining helps to mitigate plasticity during the cutting process.

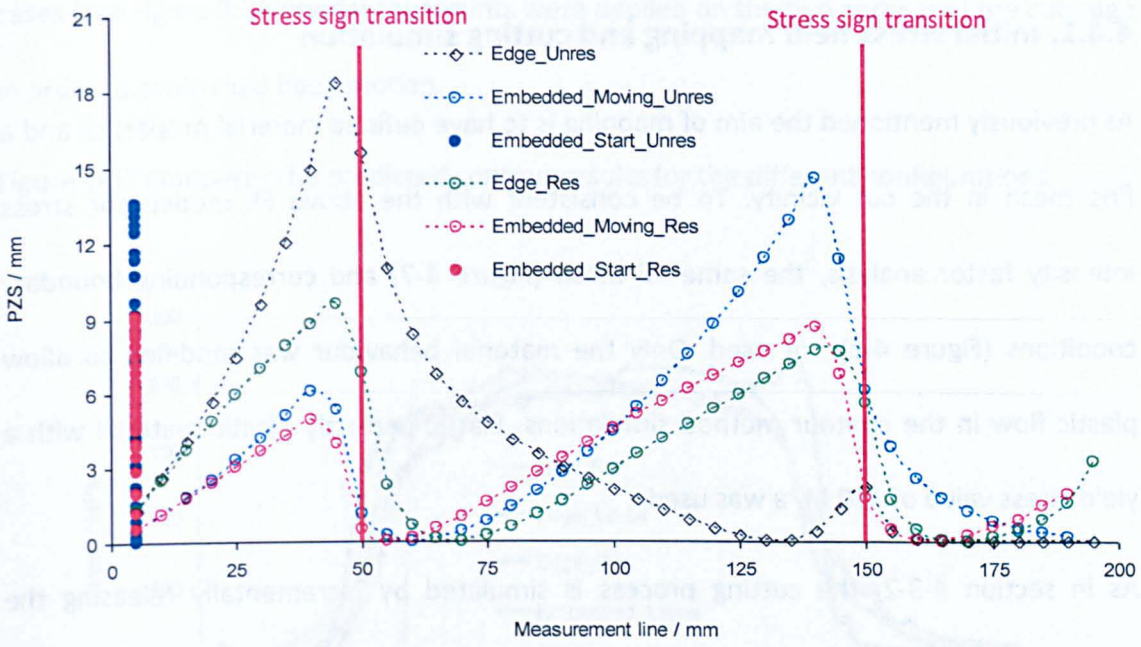

Figure 4-11: Plastic zone size distribution for the different cutting/restraining configurations assuming the idealised 'top hat' stress field.

4.4. Simulated contour residual stress for the configurations analysed

On completion of the stress intensity factor and plastic zone size analyses for the four cutting/restraining configurations, the entire contour method was simulated to determine the residual stresses in the different configurations. This is achieved in three different steps:

First, the initial 'top hat' stress distribution generated in section 4-3-1 is mapped onto a FE mesh. Second, the cutting process associated with the contour method is conducted. Finally, the displacements normal to the cut face and due to the release of residual stresses are extracted and used for residual stress back calculation. Each of these three steps has been earlier covered in detail in Chapter 3.

4.4.1. Initial stress field mapping and cutting simulation

As previously mentioned the aim of mapping is to have defined material properties and a fine mesh in the cut vicinity. To be consistent with the above FE models for stress intensity factor analysis, the same FE mesh (Figure 4-7) and corresponding boundary conditions (Figure 4-8) are used. Only the material behaviour was modified to allow plastic flow in the contour method simulations. Elastic-perfectly plastic material with a yield stress value of 450 MPa was used.

As in section 4-3-2, the cutting process is simulated by incrementally releasing the symmetry boundary conditions (*i.e.* incremental growth of a sharp crack). The effect of the cut width, neglected here, is investigated in Chapter 5.

As the element size in the cut direction is 0.25 mm and the total length to cut is 200 mm, the cutting process was simulated in a sequence of 400 steps.

4.4.2. Results and discussion

Once simulation of the cutting process was completed for the four configurations, nodal displacements normal to the cut edge were extracted from the corresponding FE models and used for residual stress back calculations, mimicking the procedure used for contour measurement.

To calculate the residual stresses linear finite element analysis is performed by applying the opposite of the extracted nodal displacements as a boundary condition to the cut edge of the FE mesh used for mapping (Figure 4-7). The material elastic constants *i.e.* Young modulus and Poisson's ratio were 200 GPa and 0.3, respectively. As in the previous

cases (see Figure 3-38), nodal constraints were applied on the two corners of the cut edge in order to avoid rigid body motion.

Figure 4-12 compares the predicted contour results for the different configurations.

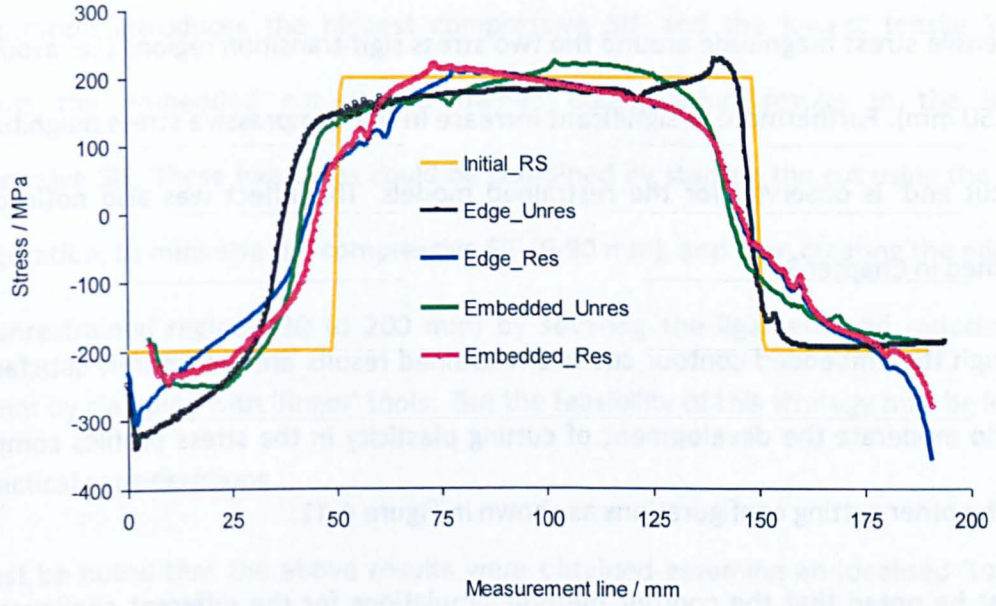

Figure 4-12: Comparison of predicted contour method residual stresses normal to the measurement line for different cutting/restraining configurations.

As discussed in Chapter 3, when dealing with measurement of high magnitude residual stresses (*i.e.* of the same order as the material yield stress), different types of restraining conditions result in different types of plasticity-induced errors in the stress profile, although some are less severe than others.

Occurrence of plasticity in the two edge-cut configurations introduces a peak compressive stress in the results of the predicted residual stress at ~ 3 mm cut depth.

In the unrestrained edge and embedded configurations, the effect of plasticity due to the release of compressive stresses tends to shift the tensile stress region towards the cut start. This was earlier observed and explained in Chapter 3.

For the restrained models, the effects of plasticity result in a reduction of compressive and tensile stress magnitude around the two stress sign-transition regions (*i.e.* around 50 and 150 mm). Furthermore, a significant increase in the compressive stress magnitude at the 'cut end' is observed for the restrained models. This effect was also noticed and explained in Chapter 3.

Although the embedded contour cut and restrained results are not entirely satisfactory, they do moderate the development of cutting plasticity in the stress profiles compared with the other cutting configurations as shown in Figure 4-11.

It must be noted that the contour method simulations for the different configurations maximised plasticity effects by assuming plane stress conditions and no strain hardening. The embedded cut and restrained configuration will perform better when measuring residual stresses in materials allowing strain hardening. In Chapter 7, an embedded restraint contour cut is applied for residual stress measurement in a three-pass slot weld specimen.

In addition to the above cutting/restraining configurations analysed, alternative combinations can be investigated for plasticity-induced errors mitigation. For example, the cutting can be initiated within the tensile stress region (e.g. at 100 mm) for different restraining conditions (see Figure 4-13). However, high stress concentration (and plasticity) is likely to develop around the pilot hole required to thread the EDM wire (see Figure 4-11) and this can considerably corrupt the measurement. This effect could be

reduced by drilling a relatively large pilot hole, but this may also disturb the stress field of interest over a certain range (~3 x the hole diameter) around the hole.

Plasticity-induced errors can also be mitigated by undertaking multiple cutting/restraining strategies. From Figure 4-10, it can be observed that the edge cut and unrestrained configuration introduces the highest compressive SIF and the lowest tensile SIF. In contrast the embedded cut and restrained configuration results in the lowest compressive SIF. These two cases could be combined by starting the cut using the latter configuration, to minimise the compressive SIF (0-90 mm), and then creating the edge cut and unrestrained regime (90 to 200 mm) by severing the ligament and reducing the restraint by clamping with 'finger' tools. But the feasibility of this strategy may be limited by practical considerations.

It must be noted that the above results were obtained assuming an idealised 'top hat' residual stress distribution having equal tensile and compressive stress magnitudes. A different initial residual stress profile will introduce different plasticity-induced stress errors.

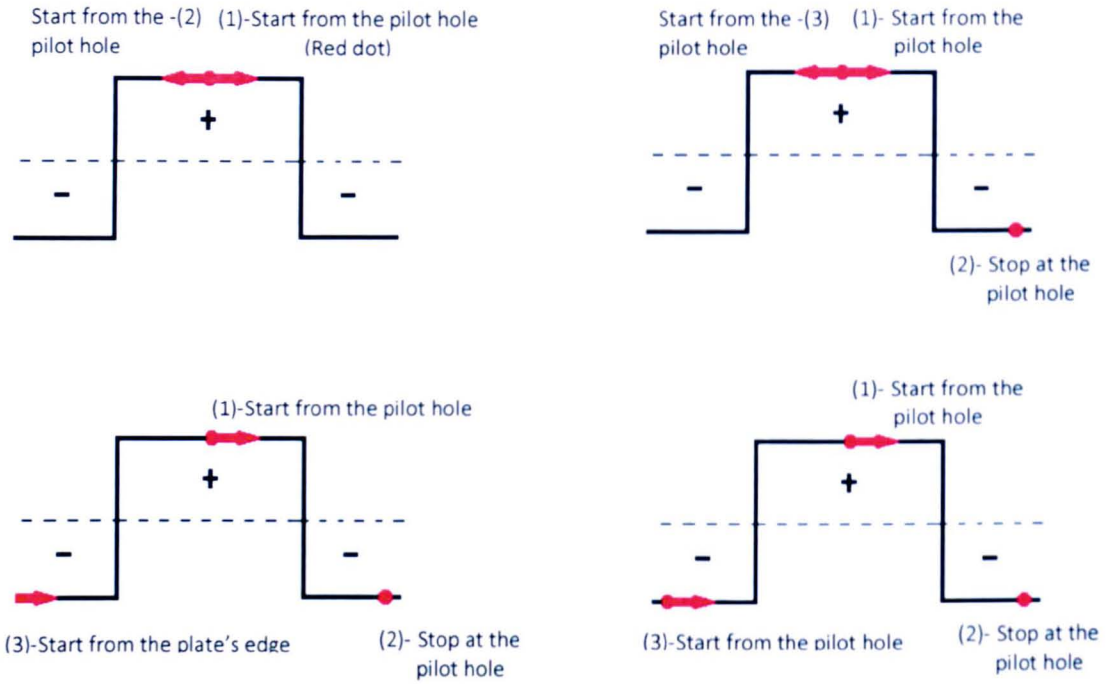

Figure 4-13: Alternative cutting strategies by initiating the cut within the tensile stress region. For each of the four cases the cutting can be conducted for different restraining conditions.

4.5. Conclusions

The following conclusions are drawn from the work carried out in this chapter:

1. The mode I stress intensity factor is a measure of the severity of the stress field ahead of the cutting wire during the contour measurement and relates to the level of plasticity introduced. The SIF variation with cut length therefore provides a convenient measure that can be used to assess the impact of different cutting and restraint strategies may have on contour measurement results.
2. A severe idealised residual stress distribution (a 'top hat') together with elastic-perfectly plastic material properties and plane stress conditions has been used to study the development of plasticity during a wire EDM contour cut idealised as a

sharp cut.

3. It is shown that a sufficiently negative SIF introduces compressive plasticity and a sufficiently tensile SIF introduces tensile plasticity. Both types of non-linear materials behaviour introduce stress errors in contour measurement simulations.
4. Different cutting path/restraint configurations have been studied using stress intensity factor distributions and non-linear simulation of contour cutting to indicate the severity and spatial extent of plasticity introduced. A novel cutting path strategy creating an embedded crack configuration has some merits especially when combined with additional measures to control the stress intensity factor associated with longer cut lengths.

4.6. References

1. Janssen M, Zuidema J, Wanhill RJH (2002) Fracture Mechanics. 2nd edn. Delft University Press, Delft

2. Tada H, Paris PC, Irwin GR (1985) The stress analysis of cracks handbook: by Hiroshi Tada, with the cooperation of Paul C. Paris and George R. Irwin. Paris Productions & (Del Research Corp.),

3. Unger DJ (2001) Analytical Fracture Mechanics. Dover Publications, INC., Mineola, New York

4. ASTM (2006) ASTM E399 - Standard Test Method for Linear-Elastic Plane-Strain Fracture Toughness K Ic of Metallic Materials.

5. Hosseinzadeh F (2009) Measurement of Residual Stress in a Welded CT Specimen by the Slitting Method - OU/MatsEng/002 Issue 1. The Open University, Milton Keynes

6. Johnson G (2008) Residual stress measurements using the contour method. PhD Thesis, University of Manchester, Manchester

7. Hosseinzadeh F, Bouchard PJ (2012) Residual stress measurment of a ferretic bead on plate benchmark test specimen using the contour method / PVP2012-78556. Paper presented at the ASME PVP Conference, Toronto, Canada,

8. Turski M, Edwards L (2008) Boiler Spines Residual Stress Measurements Programme Task 1.2: Residual Stress Measurements on Slot Weld Specimen by the Contour Method and Neutron Diffraction. The Open University, Milton Keynes

9. ABAQUS (2010) ABAQUS/Standard Documentation Version 6.10.2. ABAQUS, Inc

Chapter 5: Estimation of plasticity-induced errors in the contour method

In Chapter 4 it was demonstrated by finite element analysis that controlling the stress intensity factor distribution helps to reduce the corresponding plastic zone size; and thus plasticity-induced errors in simulated contour method results can be mitigated. However, when the magnitude of residual stresses is in the order of the material yield stress, avoiding plasticity-induced errors in contour method measurements can be very challenging.

The work presented in the first part of this chapter aims to find a plasticity error related parameter associated with simulation of the contour method cutting process which is insensitive to the mesh type/size, crack width and crack tip shape for plasticity-induced errors estimation. This is achieved by conducting sensitivity studies simulating an edge cracked plate subjected to a uniform membrane stress.

The second part of the chapter is devoted to development of procedures (referred to here as correlations) for estimating the plasticity-induced error in a residual stress measurement made using the contour method. First, a plane stress case is studied, followed by a plane strain condition. Elastic-perfectly plastic material is assumed throughout for the correlations development.

The work is based on linear elastic fracture mechanics and finite element simulations. First, the idealised top hat residual stress distribution simulated in Chapter 4 is again utilised to develop the correlations. Second, two additional 2D FE models are used to investigate the effect of specimen size on the obtained results. Finally the effect of plane stress *vs.* plane strain is explored towards the end of the chapter.

5.1. Sensitivity studies

Simulation of the cutting process associated with the contour method, and subsequent assessment of plasticity-induced errors, can be particularly sensitive to the mesh type, element size, crack width and crack tip shape. Therefore, to ensure the validity of the contour simulation procedure, three sensitivity studies were undertaken examining the crack tip plastic zone. These included the effect of the mesh size and type, the effect of the cut width and the effect of the cut tip shape. Furthermore, the influence of these parameters on the stress intensity factor was investigated.

Since previous work on moving cracks has demonstrated that it is reasonable to apply stationary crack tip plastic zone expressions to a growing crack [1,2], the sensitivity studies were conducted for stationary cracks alone.

5.1.1. The FE model used for sensitivity studies

The sensitivity studies were conducted by modelling a 2D finite width plate containing an edge crack (Figure 5-1-a). Dimensions of a plate (100 x 150) mm^2 were chosen and a 10 mm crack length selected for all sensitivity studies. The type of crack (*i.e.* sharp crack, blunt crack with a round tip or flat tip) was defined according to the sensitivity study. To simplify the analyses, one half of the cracked plate was created by defining symmetry boundary conditions in the y-direction along the line located at the plate mid-length (Figure 5-1-b). To avoid free movement of the plate during the simulation, nodal constraint was applied on one of the plate corners. The model of one half of the cracked plate was loaded on its free edge parallel to the crack direction with a membrane stress of 100 MPa. Elastic-perfectly plastic material under plane stress conditions was assumed for the sensitivity studies on the plastic zone while the material elastic constants (Young's

modulus and Poisson's ratio) were used for sensitivity studies on the SIF. The material elastic constants were 200 GPa and 0.3 for Young's modulus and Poisson's ratio, respectively. A yield stress value of 200 MPa was assumed.

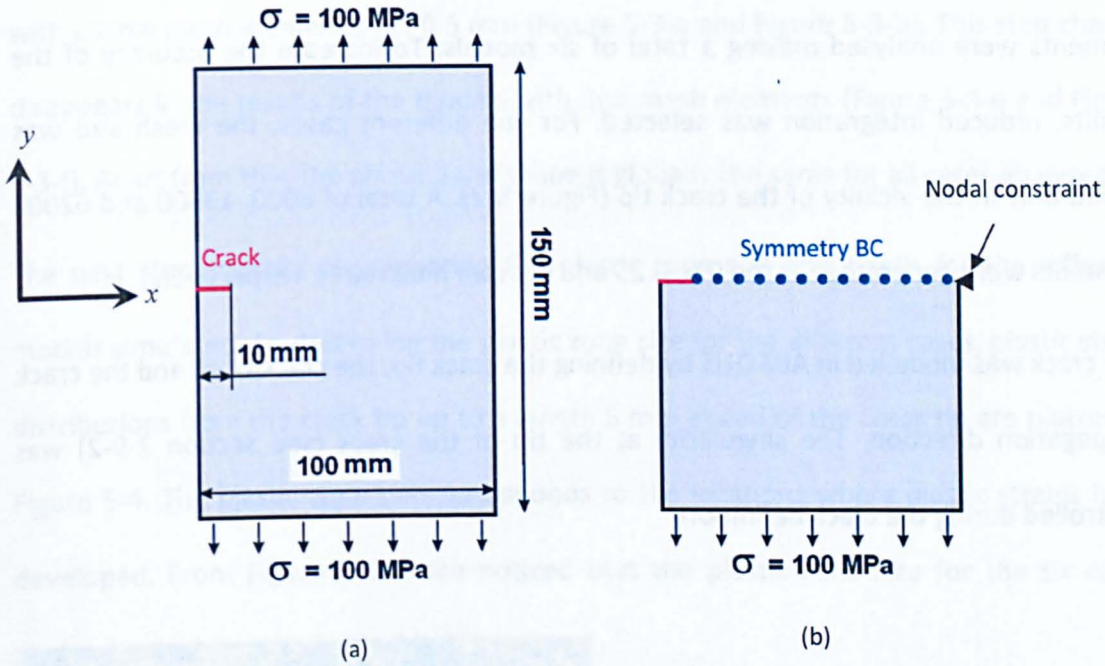

Figure 5-1: Edge cracked plate used for sensitivity studies (a). The simulations are simplified by using a symmetry boundary condition (BC) in y-direction along the plate mid-length (b).

5.1.2. Mesh sensitivity

In fracture mechanics, a stress concentration is usually generated at the tip of a crack within a stressed body. To determine the crack tip stress and strain field using the finite element method a refined mesh at the crack tip is usually required. However, this can result in a long computation time. To optimise the computation time and ensure the accuracy of the results, a mesh sensitivity study must be carried out.

The mesh sensitivity study reported here examined the crack tip plastic zone and stress intensity factor by analysing the 2D finite width plate containing a sharp edge crack (Figure 5-1).

Three different mesh sizes (0.5, 0.25 and 0.1 mm) using both first and second order elements were analysed making a total of six models. To increase the accuracy of the results, reduced integration was selected. For the different cases, the mesh size was varied only in the vicinity of the crack tip (Figure 5-2). A total of 6000, 13500 and 62000 elements were generated for the 0.5, 0.25 and 0.1 mm mesh sizes, respectively.

The crack was modelled in ABAQUS by defining the crack tip, the crack front and the crack propagation direction. The singularity at the tip of the crack (see section 2-9-2) was controlled during the crack definition.

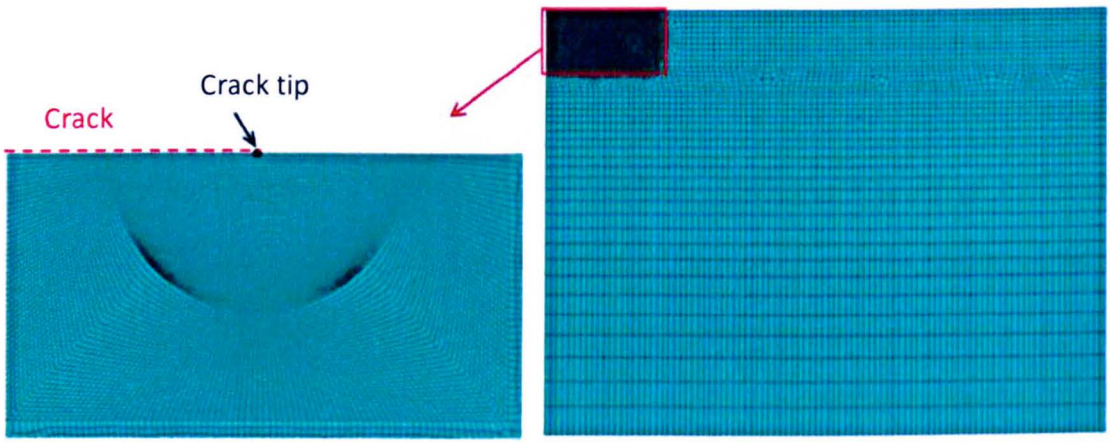

Figure 5-2: Global mesh used for the mesh sensitivity study. A close-up view of the crack tip vicinity mesh for 0.5 mm mesh size is also shown.

Figure 5-3 compares maps of generated crack tip plastic zones for the models simulated with different mesh types (first and second order) and sizes (0.5, 0.25 and 0.1 mm). The

grey regions correspond to locations with plastic strains above 0.2 %. It can clearly be seen that the crack tip plastic strains (PEEQ) increase with mesh refinement and with the order of the elements.

Looking at the shape, a step change is observed towards the tip of the crack in the models with coarse mesh elements, *i.e.* 0.5 mm (Figure 5-3-a and Figure 5-3-b). This step change disappears in the results of the models with fine mesh elements (Figure 5-3-e and Figure 5-3-f). Apart from this, the plastic zone shape is globally the same for all cases analysed.

The next step consists of comparing the plastic zone size and depth for the different models simulated. To determine the plastic zone size for the different cases, plastic strain distributions from the crack tip up to a length 5 mm ahead of the crack tip are plotted in Figure 5-4. The plastic zone size corresponds to the locations where plastic strains have developed. From Figure 5-4 it can noticed that the plastic zone size for the six cases analysed were almost identical (~ 4.1 mm).

Similarly to the plastic zone size, the strain distribution along a line perpendicular to the crack propagation is plotted for the plastic zone depth determination (see Figure 5-5). The line was selected in a way to obtain the maximum extent of the plastic strain distribution for each of the six models. A plastic zone depth of ~ 2×0.8 mm is obtained for the models with a coarse mesh (*i.e.* 0.5 mm) while an identical plastic zone depth of ~ 2×0.7 mm is measured for the models with 0.25 and 0.1 mm mesh size. No effect of the mesh type was observed on the results.

Regarding the stress intensity factor, an identical value of 21.15 MPa$\sqrt{m}$ was obtained from all six FE simulations.

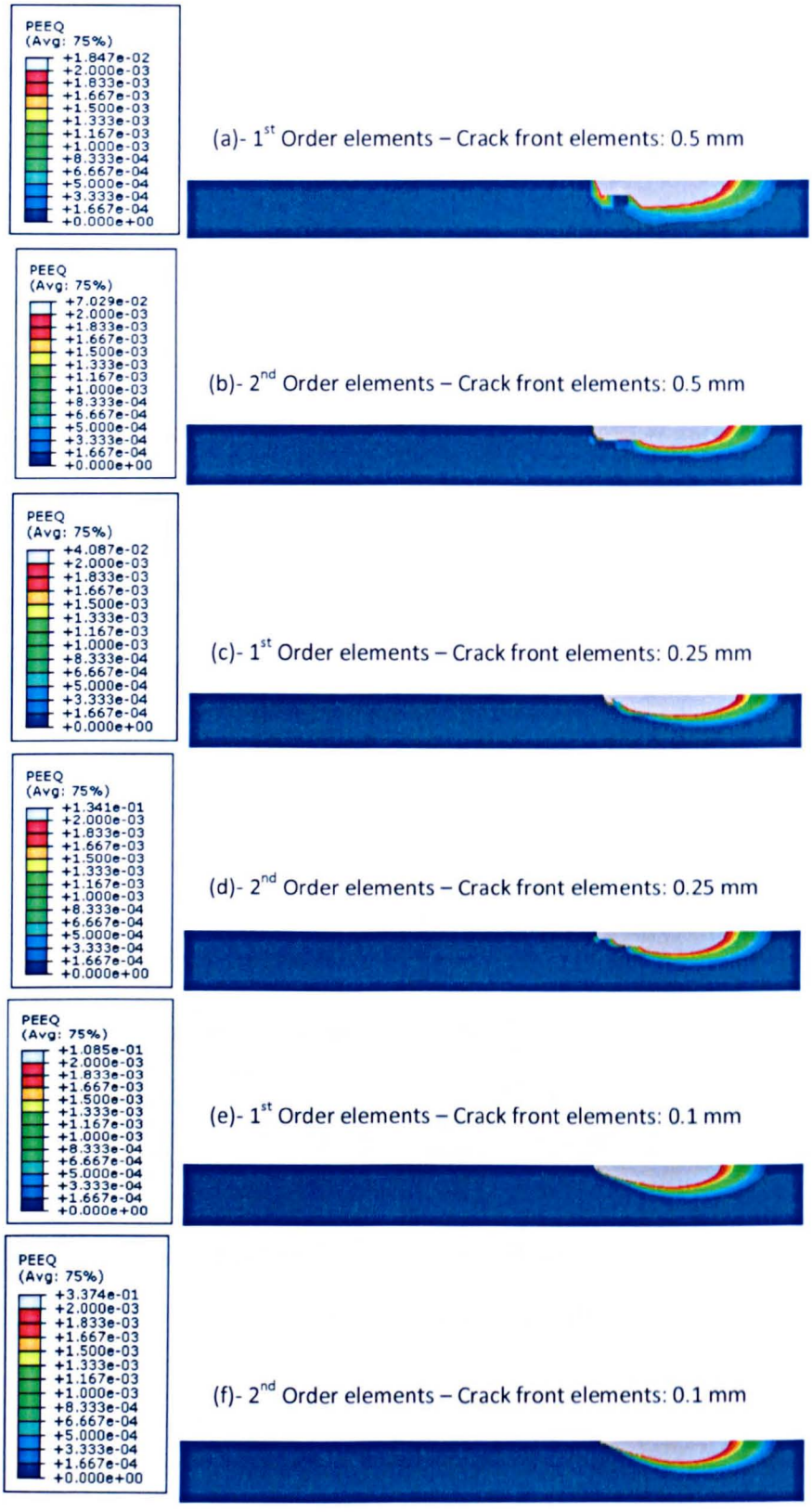

Figure 5-3: Crack tip plastic zone for different crack vicinity mesh sizes and types. Only close-up views of an area equivalent to (~15 x 1) mm^2 are shown.

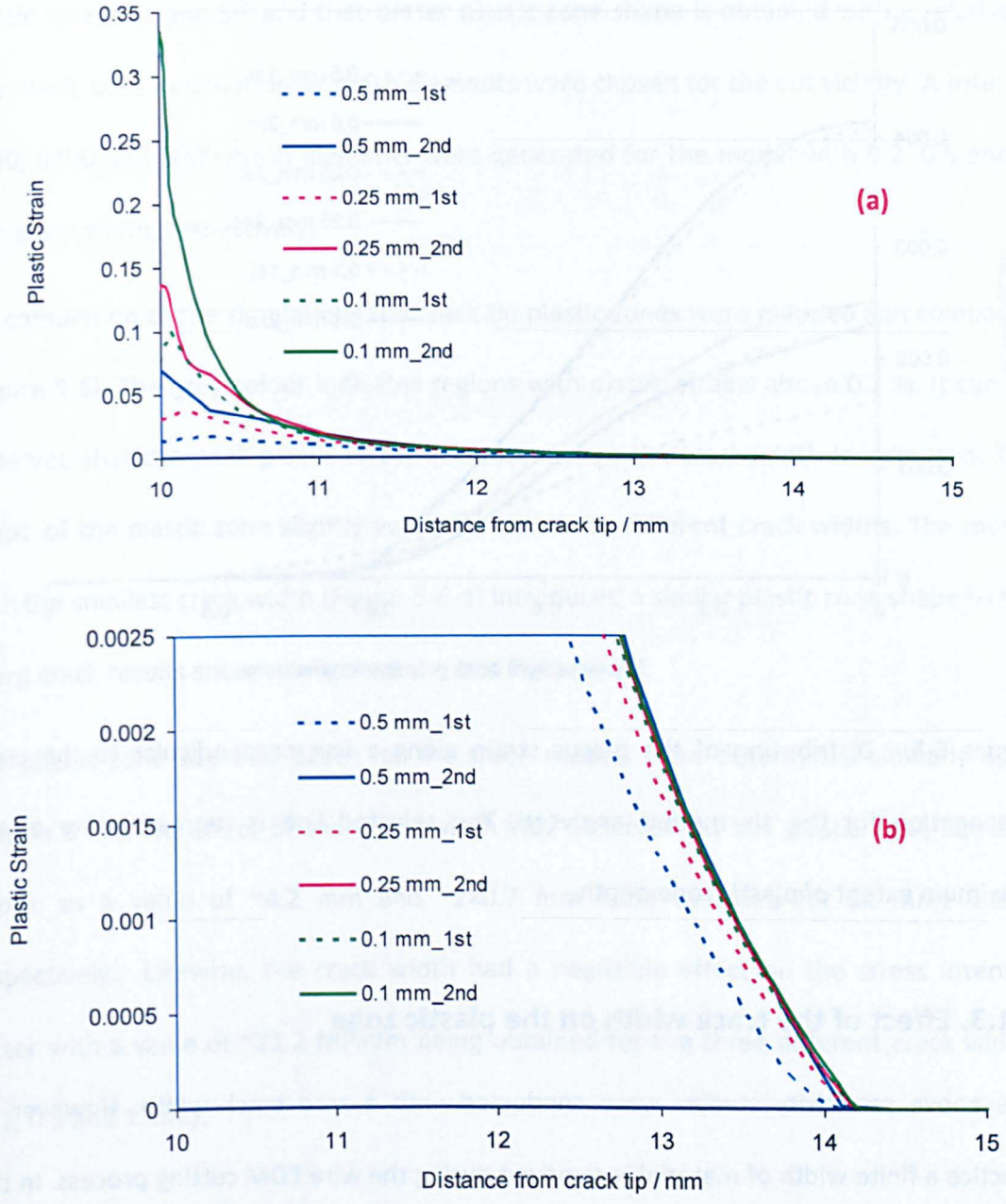

Figure 5-4: Distribution of the crack tip plastic strain for the six models analysed (a). The maximum plastic strains of the scale is lowered to 0.005 (b) in order to show the limit of plastic strains region for the different cases.

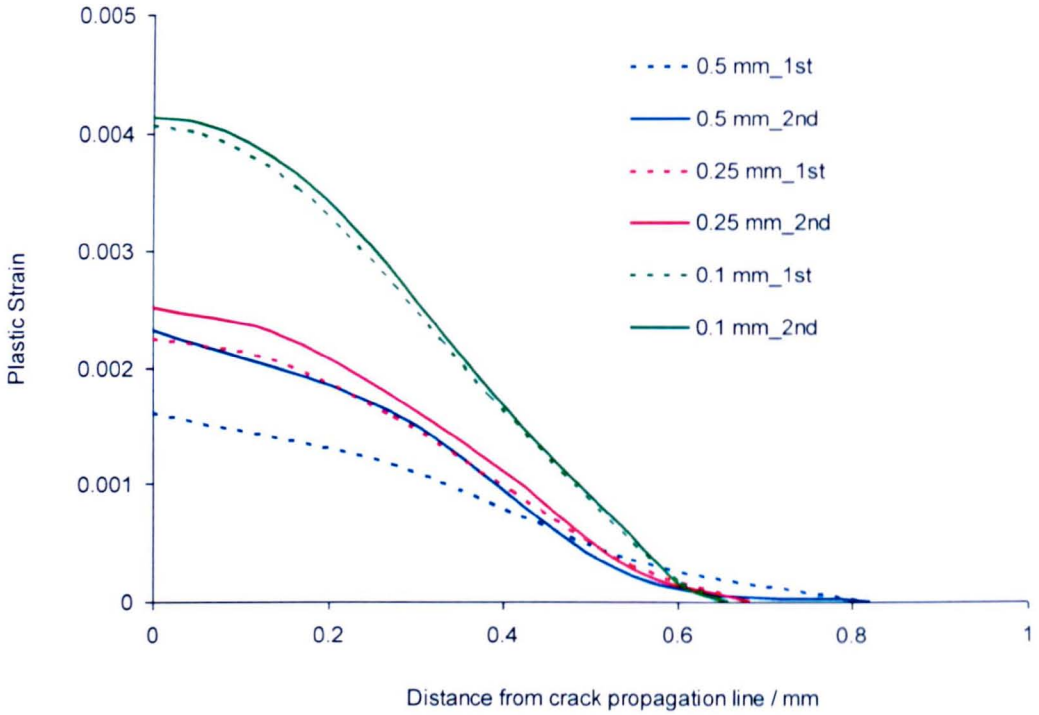

Figure 5-5: Distribution of the plastic strain along a line perpendicular to the crack propagation for the six models analysed. The selected line is representative of the maximum extent of plastic zone depth.

5.1.3. Effect of the crack width on the plastic zone

The above sensitivity studies were conducted with a zero crack width. However, in practice a finite width of material is removed during the wire EDM cutting process. In this section, the effect of the crack width on the plastic zone and the corresponding stress intensity factor is investigated by simulating the plate shown in Figure 5-1 with a finite crack width. Three different crack widths were analysed: 0.2, 0.5 and 1 mm. A rounded tip with a radius equal to one half of the corresponding crack width was chosen for each case. The cracks were defined following the same procedure as in section 5-1-2.

A similar mesh grid (global and crack tip vicinity) to the above simulations was used. Since it was demonstrated in the above section that the mesh type has negligible effect on the

plastic zone size and SIF and that better plastic zone shape is obtained with a relatively fine mesh, 0.25 mm first order mesh elements were chosen for the cut vicinity. A total of 6200, 6100 and 6000 mesh elements were generated for the model with 0.2, 0.5 and 1 mm crack width, respectively.

On completion of the simulations the crack tip plastic zones were mapped and compared (Figure 5-6). The grey colour indicates regions with plastic strains above 0.2 %. It can be observed that the peak plastic strain decreases when the crack width is increased. The shape of the plastic zone slightly varies for the three different crack widths. The model with the smallest crack width (Figure 5-6-a) introduced a similar plastic zone shape to the sharp crack results shown in Figure 5-3-e and Figure 5-3-f.

The plastic zone size and depth for the three models were determined similarly as in section 5-1-2. No effect of the crack width was observed on the plastic zone size and depth, as a value of ~4.2 mm and ~2×0.7 mm were obtained for all three cases, respectively. Likewise, the crack width had a negligible effect on the stress intensity factor with a value of ~21.2 MPa√m being obtained for the three different crack widths (0.2, 0.5 and 1 mm).

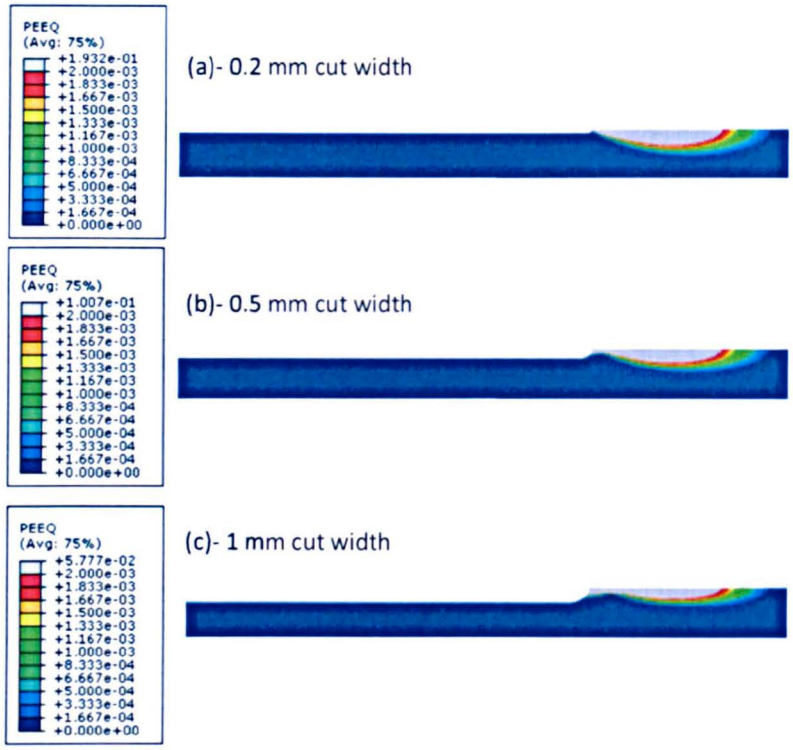

Figure 5-6: Map of crack tip plastic zone for different cut widths. Only close-up views of an area equivalent to (~15 x 1) mm^2 are shown.

5.1.4. Effect of the cut tip shape on the plastic zone

As explained earlier, the cutting simulation by material removal approach consists of removing elements one after another in a series of steps till the completion of the cut. In previously published contour method plasticity work, cutting simulation by material removal was simplified by using square/rectangular elements in the cut width [3,4]. This results in a flat cut tip during the progressive cutting process. However, in practice a rounded tip is generated by the wire EDM.

In this section the plastic zone shape and size for three different cut tip shapes are compared including a sharp, a blunt and a flat tip. To achieve this, the model shown in Figure 5-1-b was re-meshed and analysed for a 0.2 mm crack width with a flat cut tip

shape. The results were then compared to those obtained by simulating the model in Figure 5-1-b with a sharp crack and with a 0.2 mm blunt crack having a rounded tip.

Figure 5-7 compares the results from analyses of the three different crack tip shapes. The shape of the plastic zone is approximately the same for all three cases. Following the approach used in section 5-1-2 for the plastic zone parameters determination, a value of 4.2 mm for the plastic zone size and ~2×0.7 mm for the plastic zone depth were obtained for the flat tip case, which are again almost the same as the previous results. The corresponding stress intensity factor was 21.2 MPa√m.

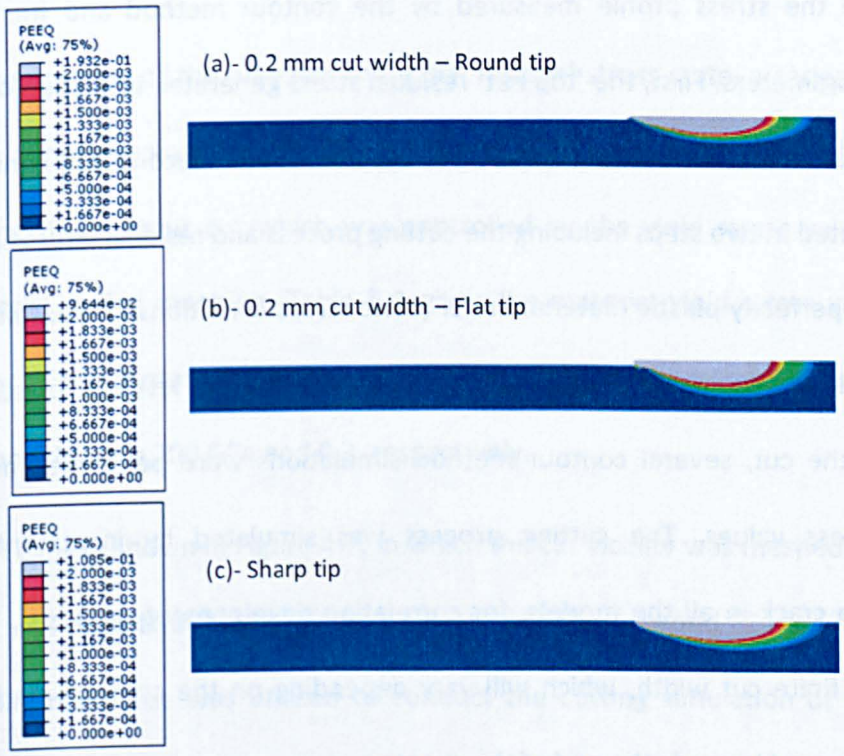

Figure 5-7: Maps of the crack tip plastic zone for different cut tip shapes. Only close-up views of an area equivalent to (~15 x 1) mm^2 are shown.

In summary, the plastic zone shape can be slightly affected by the details of how the cut width and cut tip shape are modelled and a fine mesh in the cut vicinity provides a better prediction of the plastic zone shape. However, no effect of mesh type/size, cut width and cut tip shape was observed on the plastic zone parameters (and the corresponding stress intensity factor). Therefore, these parameters can be used for contour method plasticity assessment.

5.2. Steps for plane stress correlations development

A series of contour method simulations were conducted in order to develop correlations between errors in the stress profile measured by the contour method and fracture mechanics crack parameters. First, the 'top hat' residual stress generated in section 4-3-1 was mapped onto a new FE mesh and used as an initial stress state. Second, the contour method was simulated in two steps including the cutting process and residual stress back-calculation. Elastic-perfectly plastic material under plane stress conditions was assumed. As the yield stress of the material plays a significant role in the level of plasticity generated during the cut, several contour method simulations were performed using different yield stress values. The cutting process was simulated by incrementally introducing a sharp crack in all the models, for correlation development purposes. The significance of the finite cut width, which will vary depending on the contour method practitioner, is addressed towards the end of the chapter.

On completion of the cutting simulation for each model, the size of the plastic zone in directions perpendicular and parallel to the cut path was extracted from the FE models. Then displacements normal to the cut face arising from residual stress relaxation were extracted and used for the simulated contour method residual stress back-calculation.

Plasticity-induced errors in the simulated profile were then determined by direct comparison with the initial residual stress state. Finally relationships between the average plasticity induced-error of the entire profile and averaged (along the length of the cut) plastic zone dimensions were determined.

5.3. Initial residual stress mapping and contour cutting simulation

The initial residual stress mapping and contour method simulations were undertaken following an identical procedure to that described in section 4-4 of Chapter 4. Furthermore, the 'top hat' stress distribution created in section 4-3-1 was used as initial stress state.

On completion of the mapping the initial residual stress state, a series of fifteen contour simulations were conducted. The simulations differed in the level of plasticity induced during the contour cut which was controlled by the yield stress value defined for the material during mapping. Table 5-1 gives the material yield stress values used for the series of the contour method simulations. Young's modulus and Poisson's ratio for all the FE models were 200 GPa and 0.3, respectively.

The FE mesh shown in Figure 4-7, in which the cut vicinity was meshed with 0.5 mm mesh size, was used to simulate the first eleven models. A second FE model with 0.25 mm cut vicinity mesh size was utilised to conduct the cutting simulation of the remained four models. That is because the FE mesh in Figure 4-7 was unable to capture the very small plastic zone generated in these models.

The specimen restraint during the cutting was achieved by symmetrically constraining the free edge parallel to the cut path as shown in Figure 4-8-b. The cutting process was

simulated by incrementally releasing the symmetry boundary conditions along the measurement line.

Table 5-1: The different yield stress values used for the correlation development.

FE Model	Yield Stress (MPa)
1	400
2	425
3	450
4	475
5	500
6	525
7	550
8	600
9	650
10	700
11	800
12	900
13	1000
14	1250
15	1500

5.4. Average plastic zone size and depth determination

As stated in section 2-9-2, a stress concentration at the crack tip introduces a plastic zone. The dimensions of the plastic zone in the directions perpendicular and parallel to the crack can be extracted from the FE model. The size of the plastic zone along the cut direction is usually referred to the plastic zone size (PZS) while the one perpendicular to the cutting path is named plastic zone depth (PZD), see Figure 5-8.

There are analytical solutions to calculate the plastic zone size using the stress intensity factor at the crack tip and yield stress of the material. These analytical solutions are: a

first approximation to the plastic zone size, Irwin's plastic zone size or Dugdale's plastic zone size [5,6] (See Chapter 2). A first approximation to the plastic zone size is based on elastic solutions and does not take into account the influence of plasticity [5]. To counter this, the latter two approaches are usually applied.

In contrast to the plastic zone size, no accurate expression was found in the literature to calculate the plastic zone depth. Therefore, in this study the finite element results have been used to determine both the plastic zone size and the plastic zone depth following the same approach as in section 5-1-2.

In addition, the Irwin expression for the plastic zone size has been applied to verify the numerical results. The distribution of Irwin's plastic zone size as a function of cut length along the measurement line for the present cutting/restraining configuration (Figure 4-8-b) is based on the corresponding residual stress intensity factor distribution (Figure 4-10).

The determination of the plastic zone depth is of interest here because it plays a key role in the mitigation of errors in the contour method. Indeed, when the cut width is larger than the plastic zone depth (Figure 5-9-b); no effect of plasticity will be observed on the results. Conversely if the cut width is smaller than the plastic zone depth (Figure 5-9-a), plasticity errors are introduced in the contour method results.

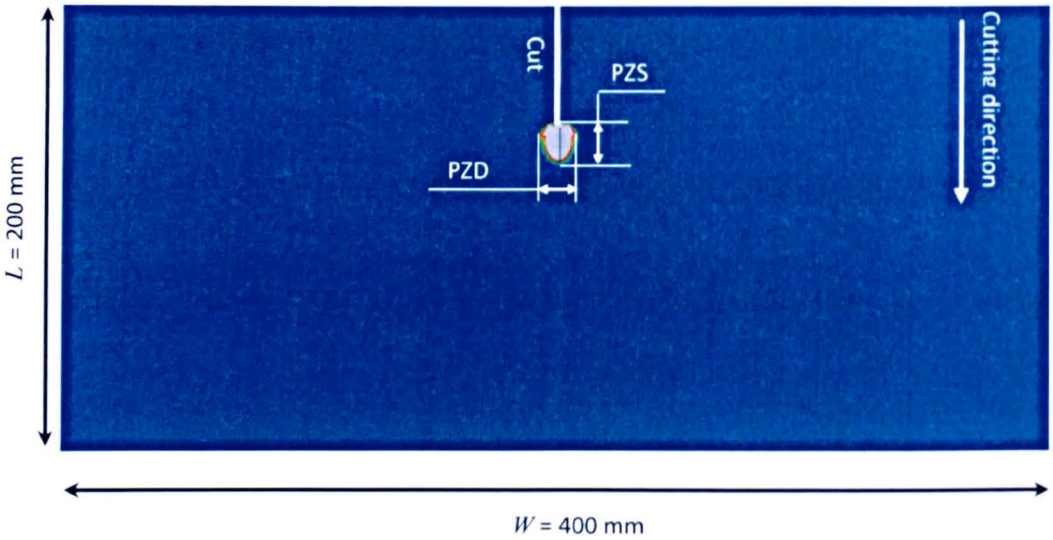

Figure 5-8: Illustration of the finite element cut tip plastic zone shape showing the plastic zone size (PZS) along the cut direction and the plastic zone depth (PZD) perpendicular to the cut.

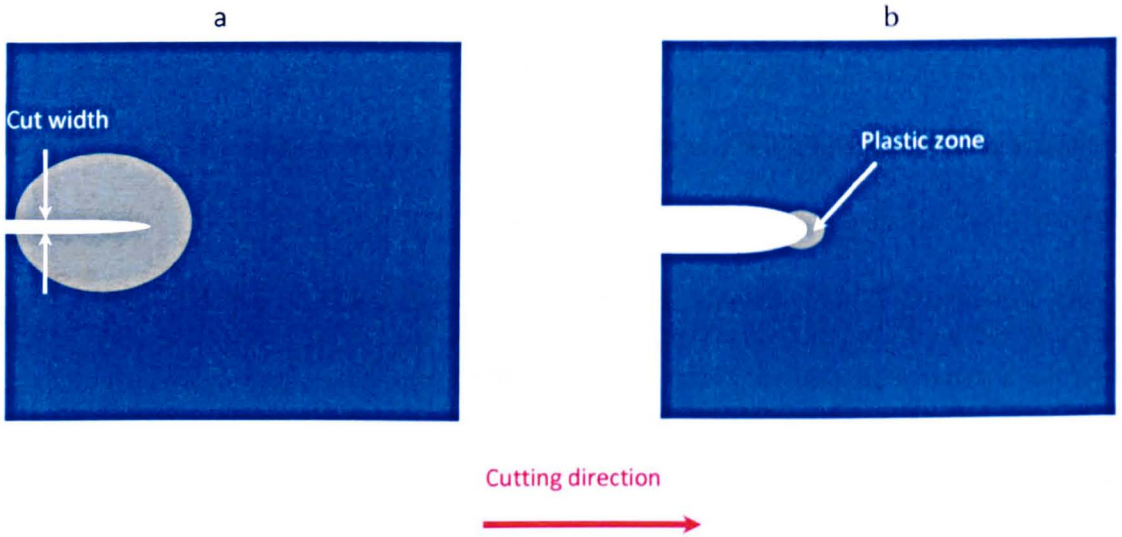

Figure 5-9: Influence of the cut width on the plastic zone while the part is being cut. A larger cut width helps in reducing the width of the plastic wake in (b) compared to the one in (a).

A comparison of the plastic zone size distribution obtained from the FE analyses after the cutting process and the plastic zone size calculated from the stress intensity factor data for three different analyses having materials with a yield stress of 500, 600 and 700 MPa is shown in Figure 5-10. The corresponding plastic zone depth distributions are plotted in Figure 5-11. The excellent correlations between the plastic zone size obtained from the FE analyses and the Irwin approach verifies the FE analyses that have been used for estimation of plasticity-induced errors for the contour method. This can also be considered as validation of the LEFM expressions assumed here that are based small scale yielding conditions.

The next step is to calculate the average plastic zone size and plastic zone depth for all cut lengths using a simple arithmetic averaging approach [7]. Figure 5-12 shows the average plastic zone size and depth distribution as a function of the material yield stress. As expected the two parameters characterising the plastic zone increase when the material yield stress is decreased.

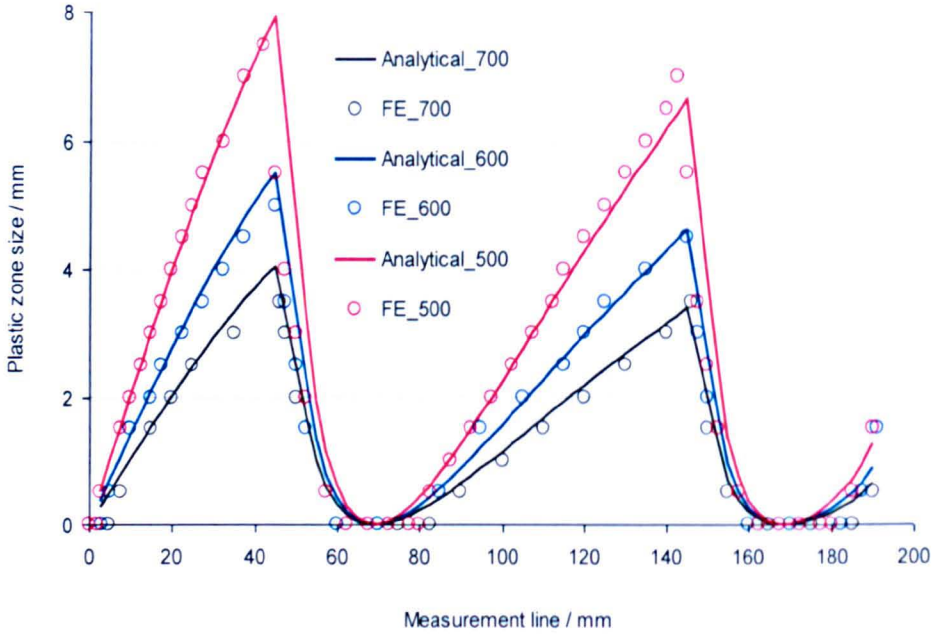

Figure 5-10: Comparison of analytical and FE plastic zone size distributions for three different yield stress values.

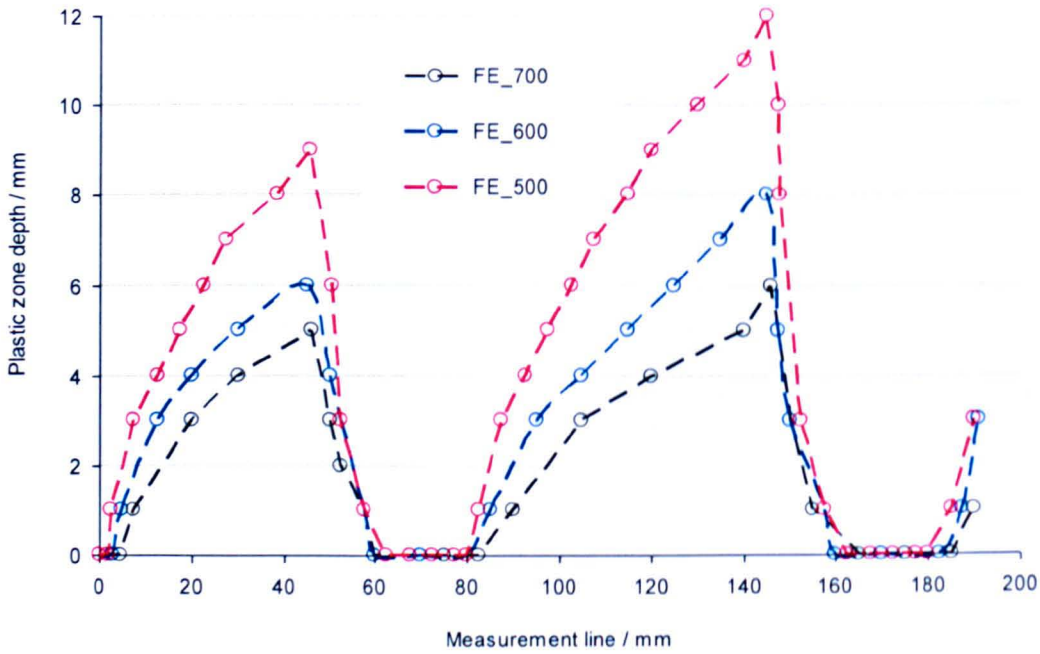

Figure 5-11: Comparison of the plastic zone depth distribution obtained from the FE analyses for three different yield stress values.

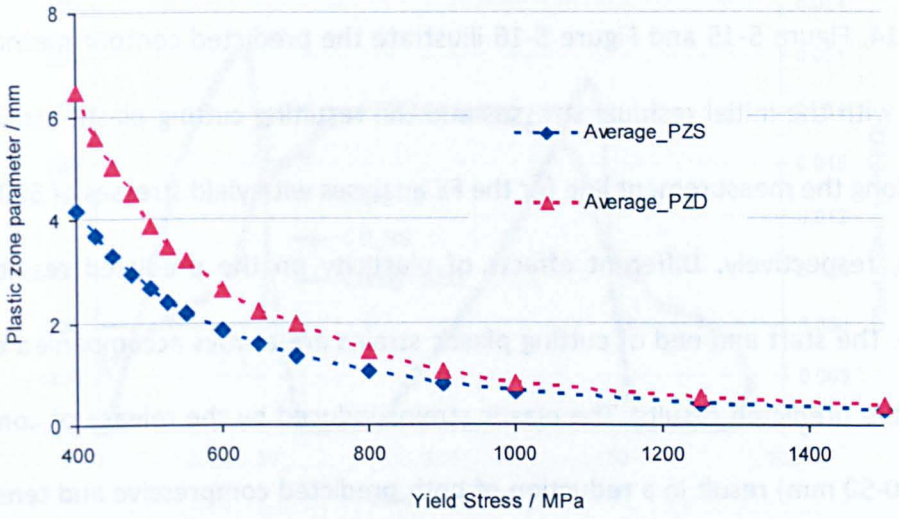

Figure 5-12: Variation of the average plastic zone size (PZS) and depth (PZD) as function of the material yield stress.

5.5. Stress back-calculation and the average error determination

The next step is the residual stress back-calculation which was carried out for the fifteen models simulated, as described in section 4-4-2. The FE models used to simulate the cutting process were again employed for the stress back-calculation.

To ensure that the contour method predictions are not affected by the mesh size, two additional FE models with 0.75 and 1 mm mesh size at the cut vicinity were simulated for the model with 500 MPa material yield stress. Figure 5-13 compares the results obtained from the FE analyses with the three different mesh sizes. It can be noticed that overall the back-calculated residual stresses are not affected by the mesh size. Furthermore, this confirms that the predicted contour method results in Chapter 3 and Chapter 4, where the simulations were conducted with a 1 and 0.5 mm mesh size at the cut vicinity, were not affected by the mesh density.

Figure 5-14, Figure 5-15 and Figure 5-16 illustrate the predicted contour method results together with the initial residual stresses and the resulting cutting plastic strains during the cut along the measurement line for the FE analyses with yield stresses of 500, 600 and 700 MPa, respectively. Different effects of plasticity on the predicted results can be observed. The start and end of cutting plastic strains are always accompanied by a peak stress in the predicted results. The plastic strains induced by the release of compressive stresses (0-50 mm) result in a reduction of both predicted compressive and tensile stress magnitude around the first stress sign-transition (*i.e.* around 50 mm). Similar remarks can be made about the plastic strains induced by the release of tensile stresses.

Finally, at the cut end, a peak compressive stress is observed in the predicted results of the three FE analyses, which is caused by accumulation of significant amounts of plastic strains in a small ligament.

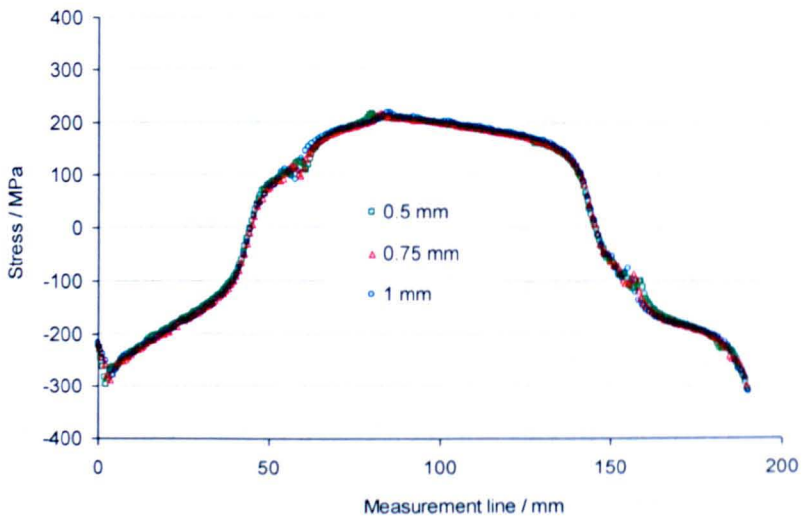

Figure 5-13: Comparison of the predicted contour method residual stress distribution along the measurement line assuming 500 MPa yield stress for different mesh sizes.

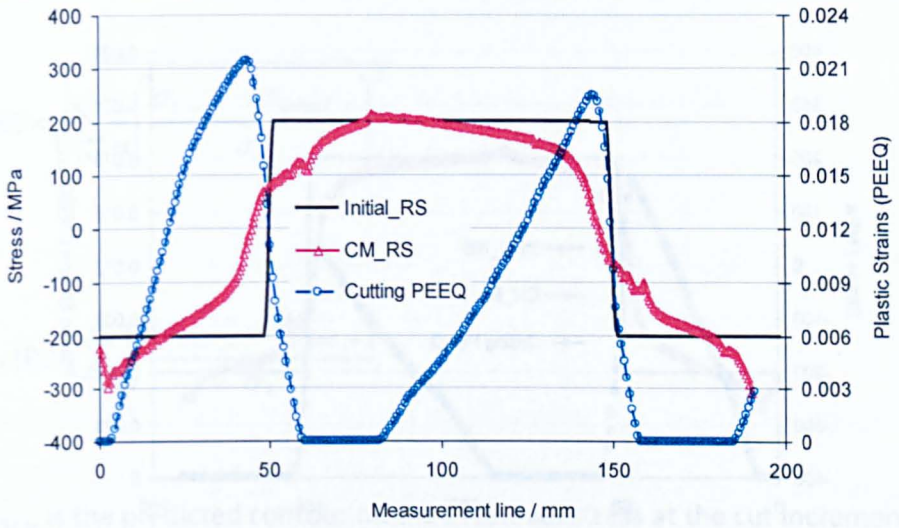

Figure 5-14: The predicted contour method residual stress distribution along the measurement line for 500 MPa yield stress together with the initial stress state and the cutting plastic strains (PEEQ).

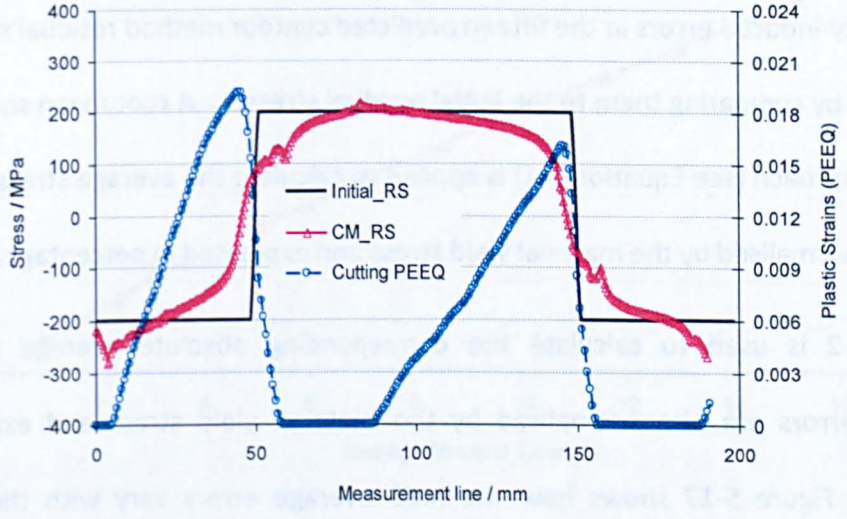

Figure 5-15: Predicted contour method residual stress distribution along the measurement line for 600 MPa yield stress superimposed with the initial stress state and the cutting plastic strains (PEEQ).

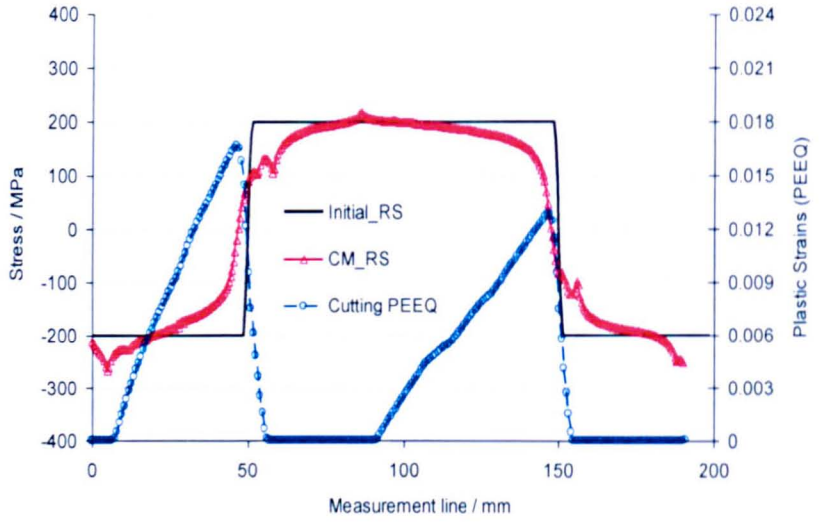

Figure 5-16: Predicted contour method residual stress distribution along the measurement line for 700 MPa yield stress superimposed with the initial stress state and the cutting plastic strains (PEEQ).

The plasticity-induced errors in the fifteen predicted contour method residual stresses are determined by comparing them to the initial residual stresses. A root mean square (RMS) deviation approach (see Equation 5-1) is applied to calculate the average stress error. The results are normalised by the material yield stress and expressed in percentage.

Equation 5-2 is used to calculate the corresponding absolute average error. The calculated errors are also normalised by the material yield stress and expressed in percentage. Figure 5-17 shows how the RMS average errors vary with the absolute average errors for the 'top hat' stress profile being analysed. The averaged absolute errors are used in the following chapter for experimental validation. For the present chapter, the distributions of the plastic zone parameters are plotted against the RMS errors.

$$\overline{\sigma}_{Error}^{RMS} = 100 \times \sqrt{\sum_{i=1}^{n} \frac{1}{n} \left(\frac{\sigma_{CM\_i} - \sigma_{Initial\_i}}{\sigma_0} \right)^2} \qquad \text{Eq. 5-1}$$

$$\overline{\sigma}_{Error}^{Absolute} = 100 \times \sum_{i=1}^{n} \frac{1}{n} \frac{\left| \left(\sigma_{CM\_i} - \sigma_{Initial\_i} \right) \right|}{\sigma_0} \qquad \text{Eq. 5-2}$$

Where σ_{CM_i} is the predicted contour method residual stress at the cut increment i, $\sigma_{Initial\_i}$ is the initial residual stress at the cut increment i, σ_0 is the material yield stress and n is the cut increment for each FE analysis.

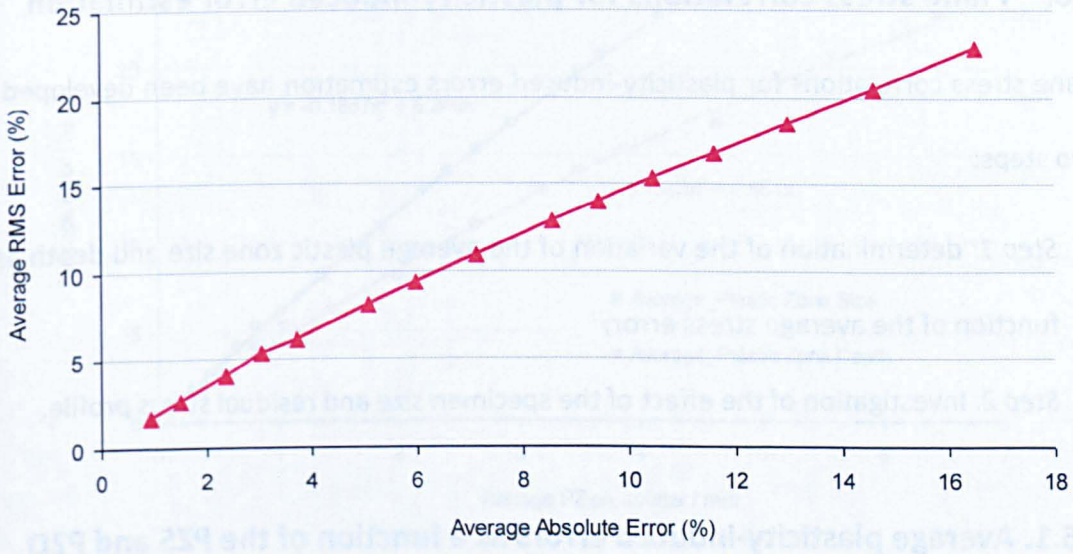

Figure 5-17: Relationship between the stress errors obtained from Equation 5-1 (RMS error) and Equation 5-2 (Absolute error).

Figure 5-18 plots the average RMS stress error variation as a function of the material yield stress. As expected the average stress error decreases when the material yield stress is increased.

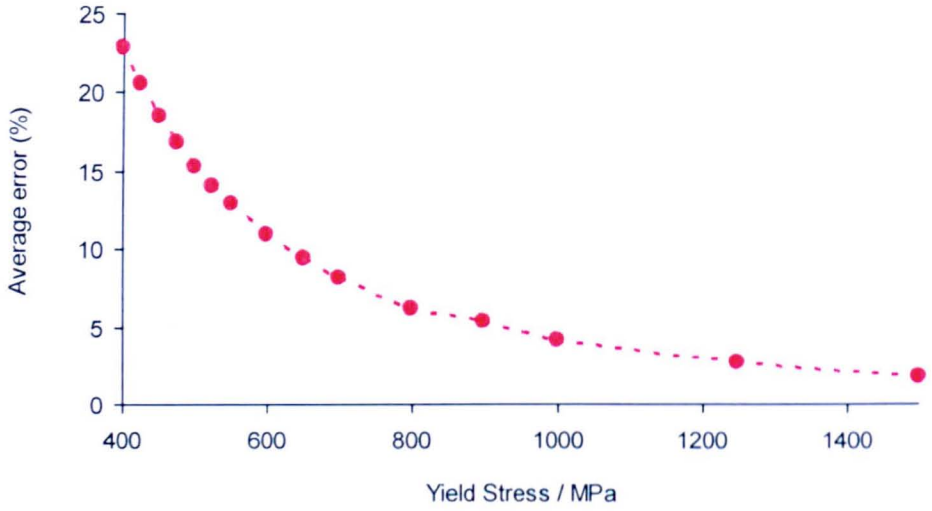

Figure 5-18: The distribution of RMS average plasticity-induced errors in the contour results as function of the material yield stress.

5.6. Plane stress correlations for plasticity-induced error estimation

Plane stress correlations for plasticity-induced errors estimation have been developed in two steps:

- ✓ *Step 1:* determination of the variation of the average plastic zone size and depth as a function of the average stress error;
- ✓ *Step 2:* Investigation of the effect of the specimen size and residual stress profile.

5.6.1. Average plasticity-induced errors as a function of the PZS and PZD

Figure 5-19 shows how the average plasticity-induced RMS stress errors increase with increase in the average plastic zone size and depth. A second order polynomial was fitted to the results to characterise the trend. From Figure 5-19 it can be noticed that in order to avoid excessive plasticity-induced errors (*i.e.* errors above 10 %) in the predicted contour method results for the 'top hat' stress profile, the average plastic zone size should not exceed 1.6 mm. The corresponding average plastic zone depth is about 2.25 mm.

When the cut tip average plastic zone size is less than 0.8 mm, the effect of plasticity error in the contour method results for the 'top hat' stress profile is negligible (*i.e.* error less than 5 %). The associated average plastic zone depth for this case is less than 1 mm. These values of the plastic zone parameters are obtained for a material yield stress of 900 MPa.

It must be noted that the relationships demonstrated in Figure 5-19 are only valid for the geometry of the plate shown in Figure 4-4 and using the 'top hat' residual stress distribution. To generalise the obtained correlations the effect of the specimen size and residual stress profile need to be investigated as covered in the following section.

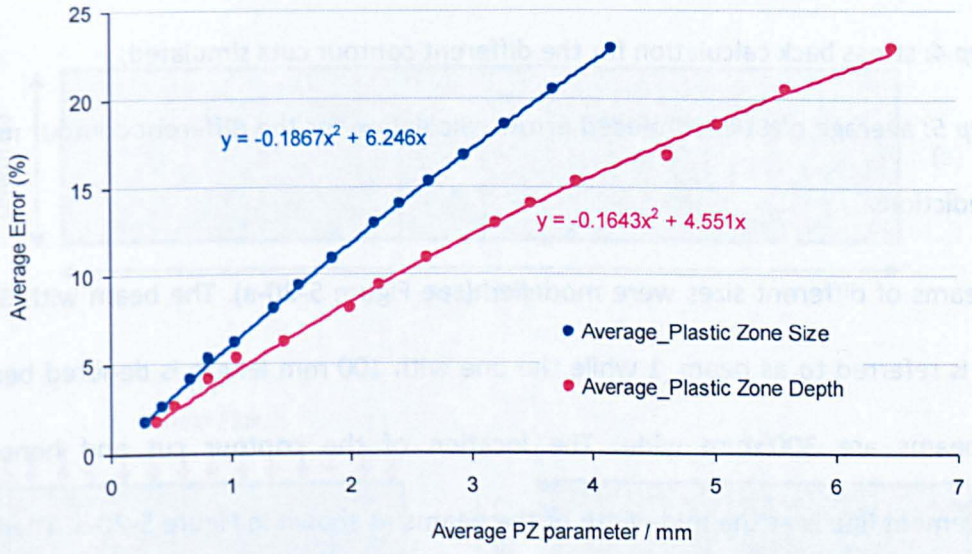

Figure 5-19: The variation in the average plasticity-induced errors as a function of the plastic zone size and depth. A second order polynomial was fitted to the results.

5.6.2. Effect of the specimen size and residual stress profile

To investigate the effect of the specimen size and residual stress profile, additional 2D contour method simulations were undertaken using different residual stress profiles as an

initial state in two beams of different sizes. The FE models were created based on previous work investigating the influence of residual stress on fracture in austenitic and ferritic steels within the EC 5th Framework ENPOWER project [8].

As for the 'top hat' stress profile, determination of the average plasticity-induced error as function of the plastic zone parameters comprised five steps:

- ✓ *Step 1:* Initial state of residual generation;
- ✓ *Step 2:* mapping and contour cut simulation for different levels of plasticity set by the material yield stress;
- ✓ *Step 3:* average plastic zone size and depth determination for the FE analyses associated with different yield stress values;
- ✓ *Step 4:* stress back calculation for the different contour cuts simulated;
- ✓ *Step 5:* average plasticity-induced errors calculation for the different contour method predictions.

Two beams of different sizes were modelled (see Figure 5-20-a). The beam with 50 mm length is referred to as beam_1 while the one with 100 mm length is denoted beam_2. Both beams are 300 mm wide. The location of the contour cut and hence the measurement line is at the mid-width of the beams as shown in Figure 5-20-a. Therefore, due to the symmetry features only one half of the beams were modelled by defining symmetry boundary conditions in the *x*-direction along the measurement line (see Figure 5-20-b). The initial state of residual stresses in the two beams was generated in two steps: a thermal analysis process followed by a stress analysis. Austenitic steel 316H physical and mechanical properties (see Table 5-2 and Table 5-3) were used. In addition to the symmetry boundary conditions defined in the *x*-direction along the measurement line,

nodal constraint was applied on one of the beam's corners to avoid model free movement during analysis (Figure 5-20-b). Heat transfer elements were used in the thermal analysis while second order plane stress elements with reduced integration were employed in the stress analysis. A uniform mesh grid of (1 x 1) mm^2 element size was created in both cases. In the thermal analysis, the heat transfer process with transient response was used.

The two beams were heated up from their top surface with a surface heat flux of 2 Watts/mm^2 for beam_1 and 4 Watts/mm^2 for beam_2 and cooled down to room temperature (assumed to be 20°C). The heating times were 24 seconds and 35 seconds for beam_1 and beam_2, respectively.

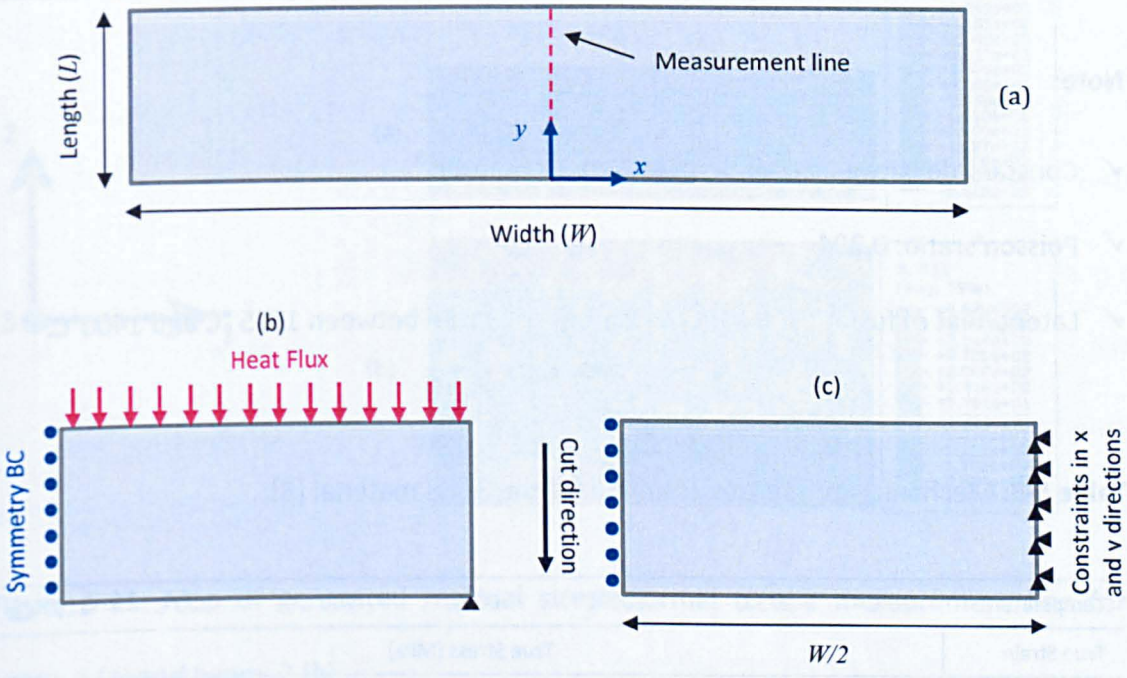

Figure 5-20: Schematic of the beam used for examining the effects of specimen size and stress profile (a). The heating edge, the boundary conditions used for the initial state of residual stress generation (b) and for contour method simulation (c) are also shown.

Table 5-2: Physical properties assumed for the 316H material [8].

Temperature (°C)	Conductivity (W / mm.K)	Specific Heat (J/Kg.K)	Expansion coefficient (/K)	Young's Modulus (MPa)
20	0.01412	488	1.46E-05	195600
100	0.01526	502	1.54E-05	191200
200	0.01669	520	1.62E-05	185700
300	0.01811	537	1.69E-05	179600
400	0.01954	555	1.74E-05	172600
500	0.02096	572	1.78E-05	164500
600	0.02238	589	1.81E-05	155000
700	0.02381		1.84E-05	144100
800	0.02523		1.87E-05	131400
900	0.02666		1.90E-05	116800
1000	0.02808		1.93E-05	100000
1100	0.0295		1.95E-05	
1200	0.03093		1.98E-05	
1300	0.03235		2.00E-05	
1400	0.03378		2.02E-05	
4000	0.03378	589	2.02E-05	

Note:

- ✓ Constant density was assumed: 7.97×10^{-06} $Kg.mm^{-3}$
- ✓ Poisson'sratio: 0.294
- ✓ Latent heat of fusion: 300 KJ/Kg, absorbed/released between 1375 °C and 1400°C.

Table 5-3: Mechanical properties assumed for the 316H material [8].

Temperature	20°C	275°C	500°C	600°C	700°C	800°C	1100°C
True Strain	True Stress (MPa)						
0	273.12	205.41	192.77	187.69	161.46	121.47	25.3
0.002	284.2	215.03	202.1	197.09	167.53	123.45	25.65
0.01	328.15	253.31	239.27	234.52	191.7	131.3	27.07
0.02	356.69	280.09	266.22	260	205.22	133.52	27.95
0.05	420	342.72	327.81	310.59	223.55	134.93	29.82
0.1	504.57	425.26	408.21	356.84	232.65	136.07	31.35

Maps of the generated residual stresses for the two beams are illustrated in Figure 5-21. Tensile residual stresses are observed towards the top and bottom edges and are balanced by compressive residual stresses in the middle of the beams. Figure 5-22 shows the depth-distribution of residual stress acting normal to the measurement line. The stress distribution is plotted along the mid-length (measurement line) from the beam top to bottom surface. Peak tensile stresses of 360 MPa and 460 MPa are obtained for beam_1 and beam_2, respectively. The maximum compressive stress is about -275 MPa for beam_1 and -305 MPa for beam_2. The created stress fields are used in the next steps for contour method simulations.

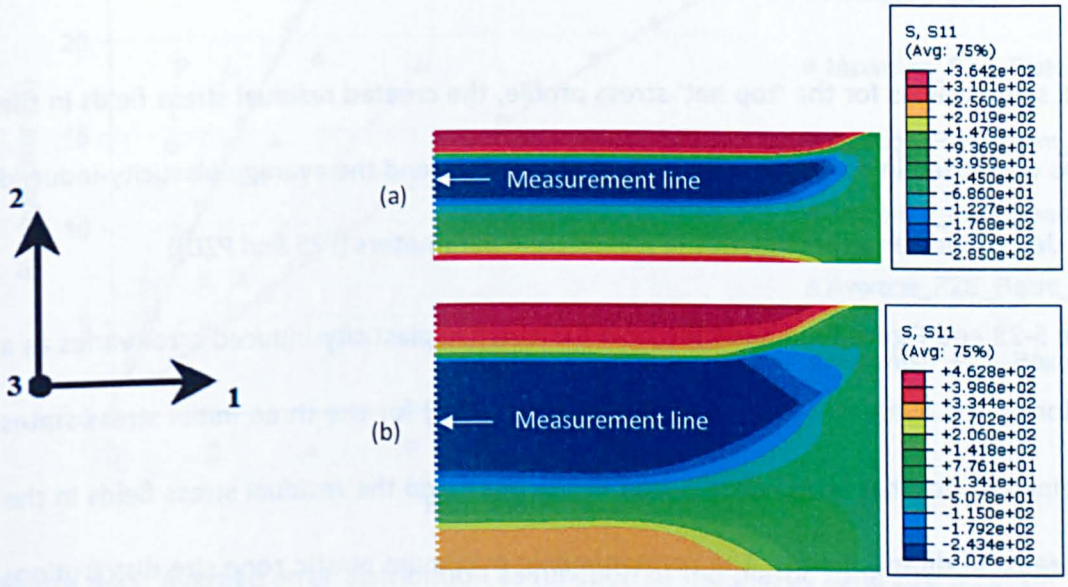

Figure 5-21: Map of generated residual stress normal to the measurement line for beam_1 (a) and beam_2 (b).

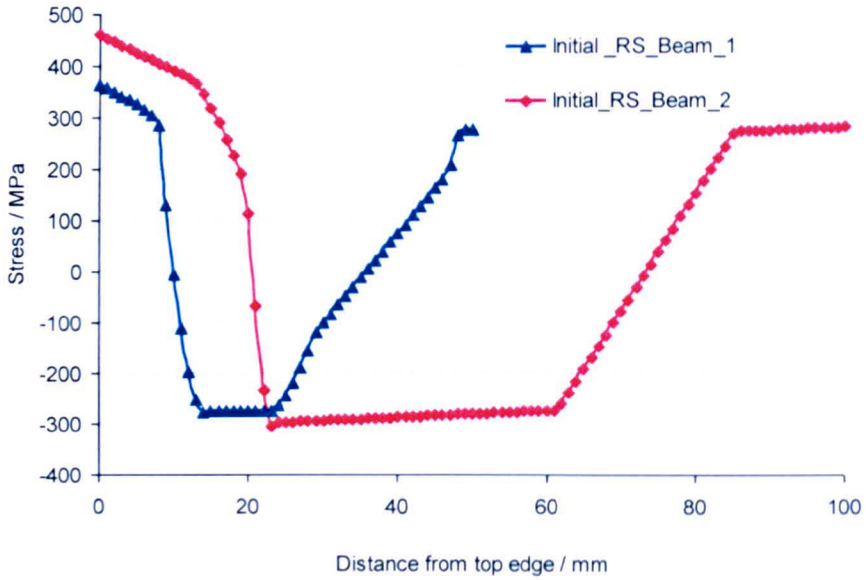

Figure 5-22: Residual stress distribution normal to the measurement line plotted along the plate mid-length (measurement line) for the two beams.

In the same way as for the 'top hat' stress profile, the created residual stress fields in the beams were used in contour measurement simulations and the average plasticity-induced error determined as a function of the plastic zone parameters (PZS and PZD).

Figure 5-23 and Figure 5-24 illustrate how the average plasticity-induced error varies as a function of the average plastic zone size (PZS and PZD) for the three initial stress states including the 'top hat stress distribution in the plate and the residual stress fields in the two beams of different sizes. The corresponding maximum plastic zone size distributions are also shown.

The relationships clearly exhibit an influence of the specimen size on the results. As it can be observed in Figure 5-23, for the same average plastic zone size, the induced average error is different for the three initial stress states. The lowest value of the average error is observed in the plate (which is larger in size) followed by beam_2. Beam_1 is the smallest in size amongst the three FE models studied, but has the highest level of induced error.

Similar features are observed for the average error distribution as a function of the plastic zone depth (Figure 5-24).

The above observations demonstrate the effect of specimen size on the different results. For a contour cut, the effective specimen size can be defined by the cut length (L) and the distance between the cut path and the clamp, $W/2$ (see Figure 5-25). The type of clamp here refers to restraining conditions that can have an effect on the size of the plastic zone introduced during the cut (e.g. use of fitted bolts). For a 'finger' clamp regime the specimen size is defined by the cut length and width.

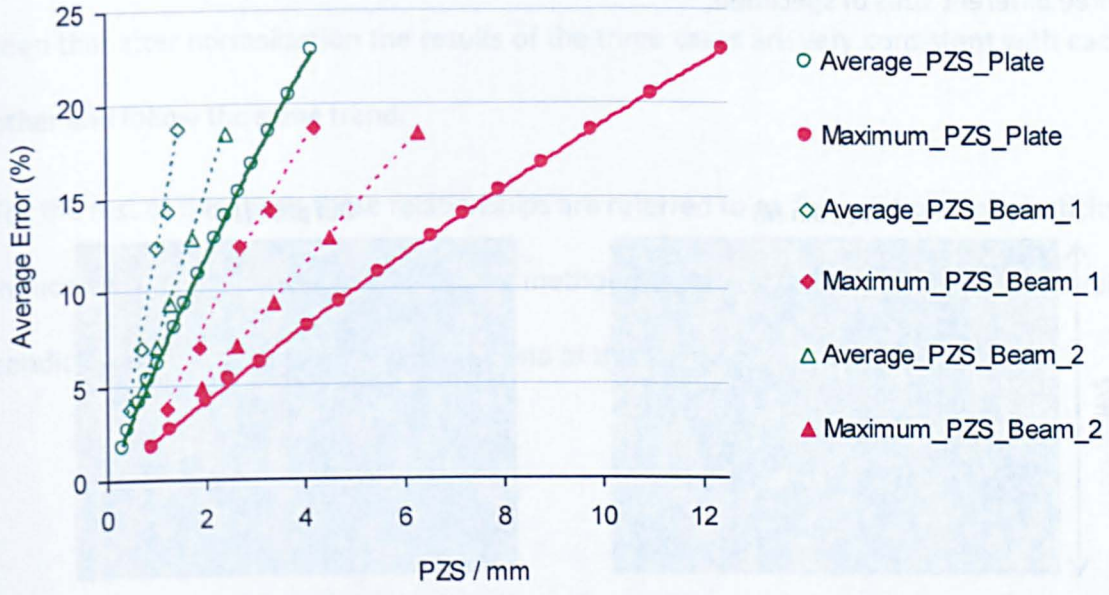

Figure 5-23: Average error distribution as function of the plastic zone size (PZS) for three different sizes of specimen.

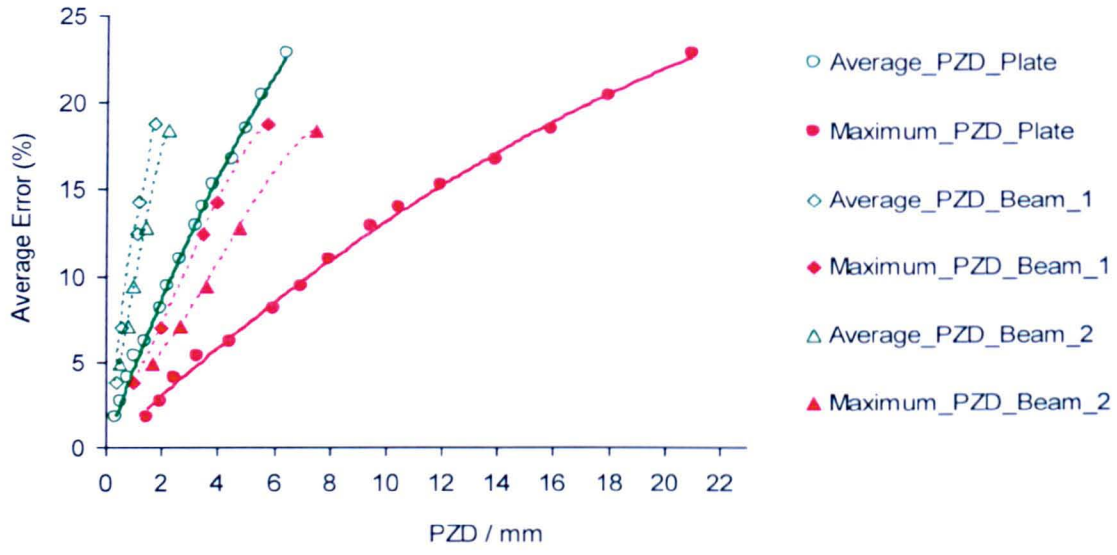

Figure 5-24: Average error distribution as function of the plastic zone depth (PZD) for three different sizes of specimen.

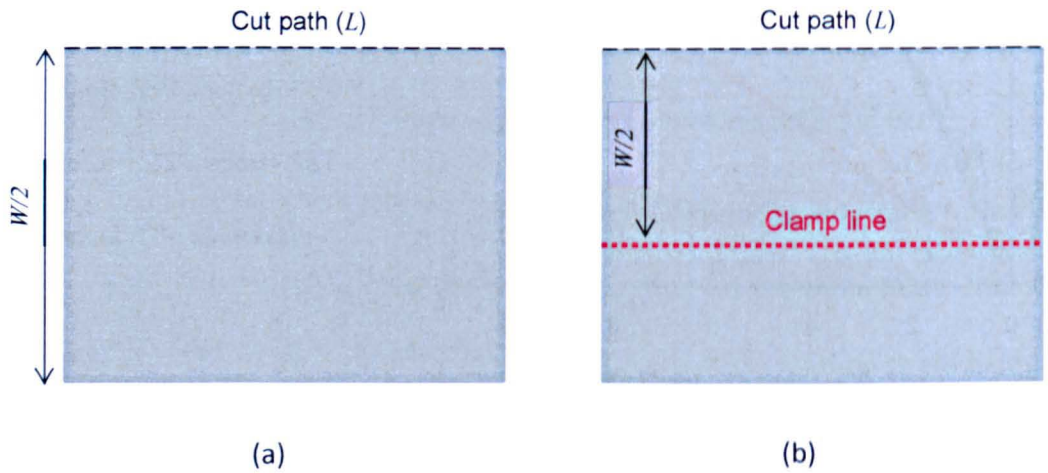

Figure 5-25: Illustration of the effective specimen size when 'finger' clamp tools (less rigid) (a) and fitted bolts (rigid) are used for restraining conditions.

To generalize the developed relationships, the plastic zone parameters must be normalized in order to eliminate the effect of the specimen size on the results. To achieve this, the plastic zone size (Figure 5-8) is normalized with respect to the root square of the

cut length (L) and the root square of the thickness over which the data are averaged, here denoted t. As the simulations were performed in 2D plane stress conditions with a unit thickness, t was set to 1 for normalization.

For the plastic zone depth, since, only half of the models (plate, beam_1 and beam_2) were simulated by using symmetry boundary conditions, half of the plastic zone depth was extracted from the different FE analyses and normalized by $\sqrt{0.5W.t}$. The normalized PZD is twice of the obtained value.

Figure 5-26 and Figure 5-27 show how the average plasticity-induced errors vary with normalized average plastic zone parameters for the three cases studied. It can be clearly seen that after normalization the results of the three cases are very consistent with each other and follow the same trend.

For the rest of this thesis these relationships are referred to as "correlations for plasticity-induced errors estimation" in the contour method for plane stress conditions. Plane strain conditions case is discussed towards the end of this chapter.

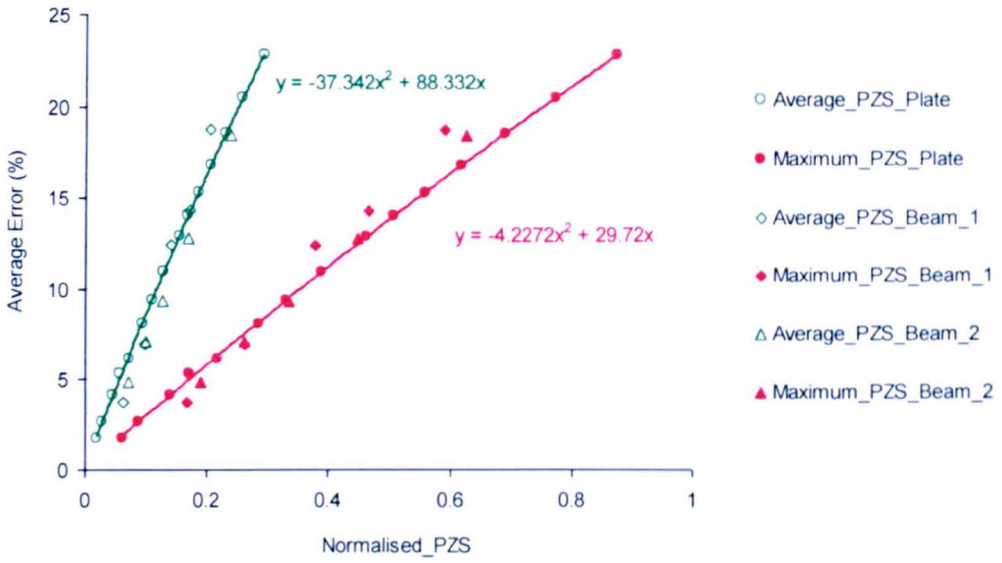

Figure 5-26: Average error distribution as function of the normalised average plastic zone size (PZS) for the three FE studied cases. A second order polynomial was fit to the results.

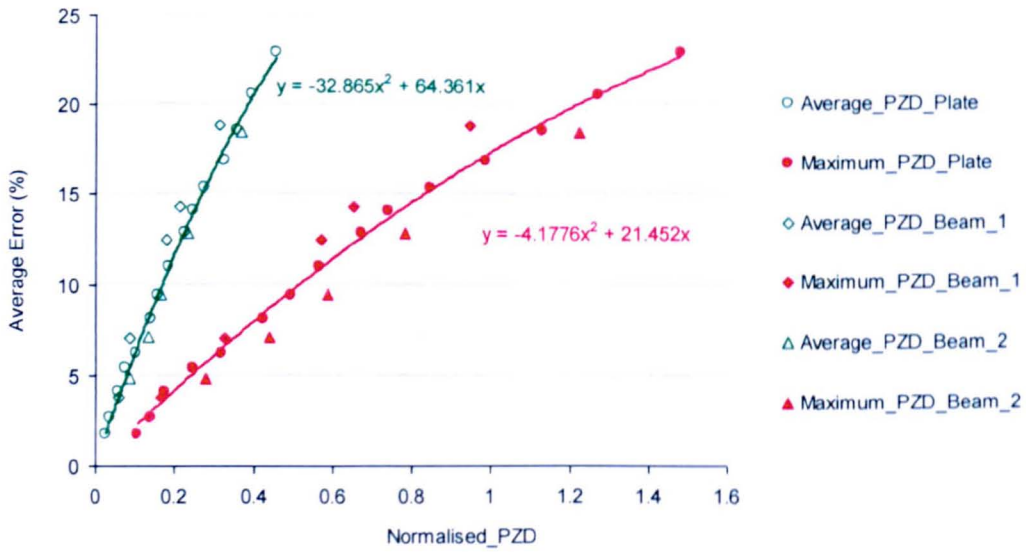

Figure 5-27: Average error distribution as a function of the normalised plastic zone depth (PZD) for the three FE cases studied. A second order polynomial was fitted to the results.

5.6.3. Plastic zone size *vs.* plastic zone depth

As stated earlier the plastic zone depth is the most important parameter that must be minimised in order to mitigate plasticity-induced stress errors in the contour method. That is because with a large plastic wake (depth), the cut vicinity tends to behave plastically; which violates the contour method elastic superposition principle. Therefore, determination of the plastic zone depth is crucial.

Unlike the plastic zone size, no accurate analytical expression for plastic zone depth was found in the open literature. In this thesis the plastic zone depths were extracted from the different FE simulations. Therefore it is important to find a relationship between the two parameters defining the plastic zone in order to facilitate the plastic zone depth determination.

Figure 5-28 shows how the normalised plastic zone depth varies with the normalised plastic zone size. A second order polynomial was fit to the results to derive an equation for the plastic zone depth analytical calculation.

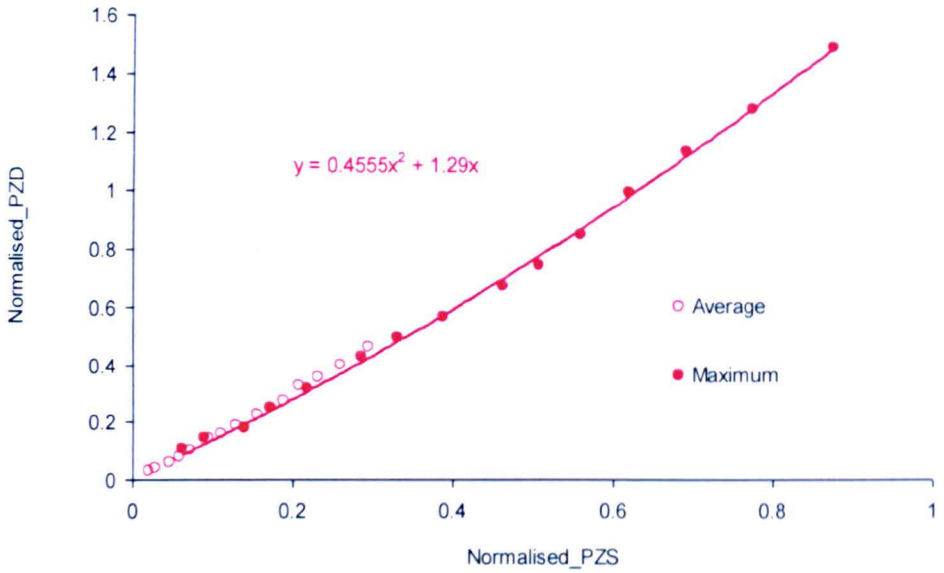

Figure 5-28: Variation of the normalised plastic zone depth as a function of the normalised plastic zone size.

5.7. Effect of the cut width

The above correlations for plane stress conditions were based on a zero cut width (*i.e.* a perfectly sharp cut). However, in practice wire EDM removes a certain amount of material.

To investigate the effect of the cut width on the plasticity-induced errors, the wire EDM cut was simulated as an incremental growing blunt crack for different material yield stress values. Apart from the material removal cutting process, all procedures conducted were identical to those followed in the above sections.

In the first instance, the sharp and the blunt cutting processes are compared by plotting the average plasticity-induced errors distribution as function of the material yield stress. Both sharp and blunt cracks were simulated for FE models having different values of material yield stress as indicated in Table 5-4. A 300 μm cut width was used for the incremental blunt cut. Figure 5-29 compares the distribution of the average error as

function of the material yield stress for the two cutting processes. It can be seen that for the different yield stress values the blunt crack helps in reducing the plasticity-induced errors in the predicted contour results.

Table 5-4: Yield stress values used for the comparison of average errors for a sharp and a blunt 300 µm width cutting processes.

FE Model	Yield Stress (MPa)
1	450
2	550
3	650
4	800
5	1000
6	1250

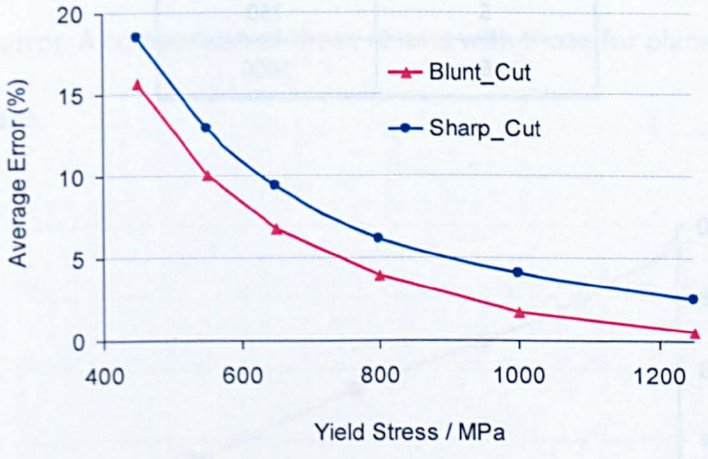

Figure 5-29: Comparison of average errors as a function of yield stress for sharp and blunt (300 µm width) cuts.

The next step was to investigate the influence of different cut widths (see Table 5-5) on the plasticity-induced errors for a selected material yield stress of 650 MPa. Figure 5-30 shows the variation of the average error as a function of the cut width. For a selected level of plasticity, it is seen that a relatively large cut width helps reducing the effect of plasticity on the predicted contour method results. This is earlier explained in section 5-4 (see Figure 5-9).

Table 5-5: Cut widths used in analyses investigating the effect of the cut width on average plasticity error in the contour method.

FE Model	Cut Width (μm)
1	0
2	150
3	300
4	500
5	750
6	1000

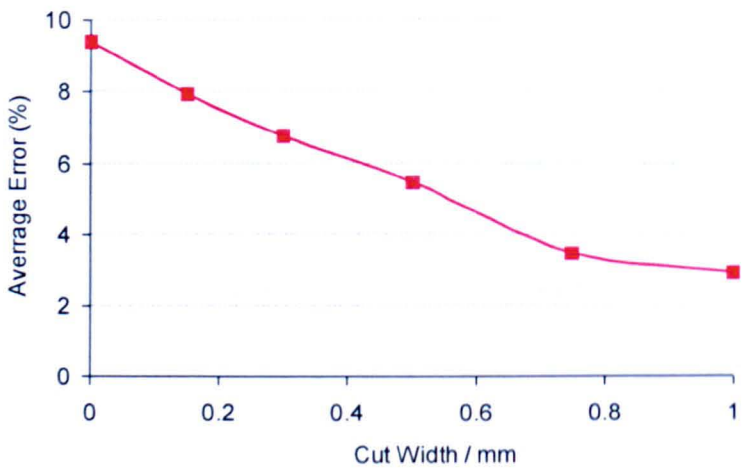

Figure 5-30: Variation of average error with cut width size for 650 MPa yield stress.

5.8. Plane strain correlations for plasticity-induced errors estimation

As mentioned earlier, the plastic zone size and shape ahead of a crack is affected by the stress state in the specimen. Therefore, it is essential to examine the viability of the developed correlations for plane strain conditions.

An identical procedure to the plane stress case was followed including generation of an initial stress state, contour method simulation, calculation of average error and determination of normalised average plastic zone parameters. The 'top hat' residual stress profile was chosen for this work using the fourteen FE models shown in Table 5-1. The plane strain condition was defined by simply meshing the models using plane strain elements.

Figure 5-31 and Figure 5-32 illustrate the plane strain plasticity correlations. It can be noticed that the plasticity-induced errors in the present case are very low. Only the errors obtained from the four highest yield stress values (i.e. 400, 425, 450 and 475 MPa) are above 5% RMS error. A comparison of these results with those for plane stress is provided in the next section.

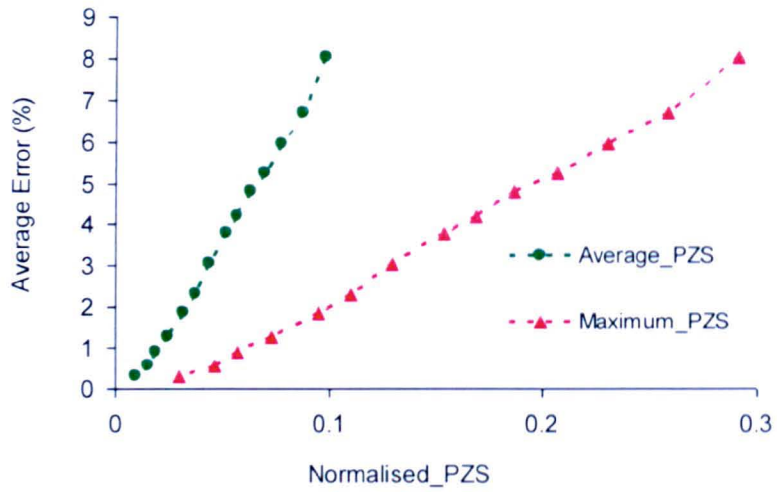

Figure 5-31: Average error as a function of normalised plastic zone size for plane strain conditions.

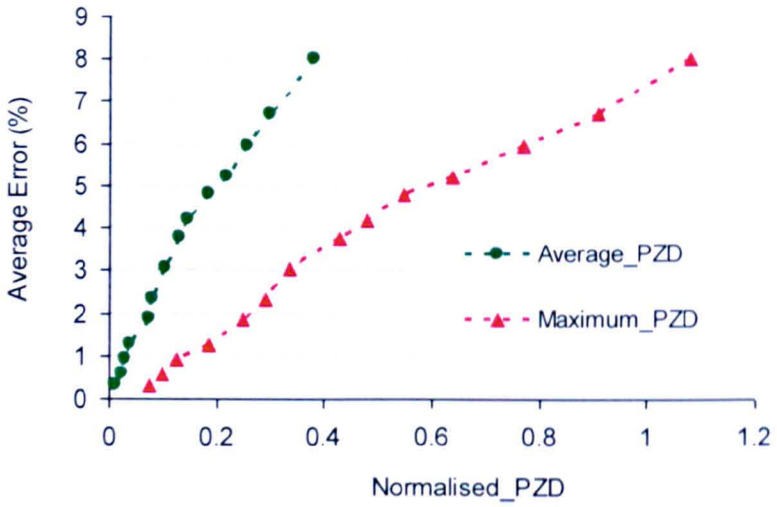

Figure 5-32: Average error as a function of normalised plastic zone depth for plane strain conditions.

5.9. Comparison of plane strain and plane stress correlations

Figure 5-33 and Figure 5-34 compare the plane stress and plane strain average error distributions as function of the normalised average plastic zone size (PZS) and depth (PZD), respectively.

The results for the two stress states in Figure 5-33 correlate very well with each other. A better interpretation can be made by plotting separately the normalised average plastic zone size and average error as a function of the material yield stress as shown in Figure 5-35 and Figure 5-36, respectively.

For a selected yield stress value, the normalised average plastic zone size in the plane stress condition is approximately three times that of the normalised average plastic zone size in the plane strain condition. A similar feature is observed for the average error distribution as a function of the material yield stress (Figure 5-36), although it is less pronounced for lower values of error.

This first comparison of the plane stress and plane strain results demonstrates that the average stress error scales approximately linearly with the normalised average plastic zone size, either in plane stress or plane strain conditions. Therefore, the plane stress average error distribution as a function of the normalised plastic zone size can be well applied to plane strain conditions.

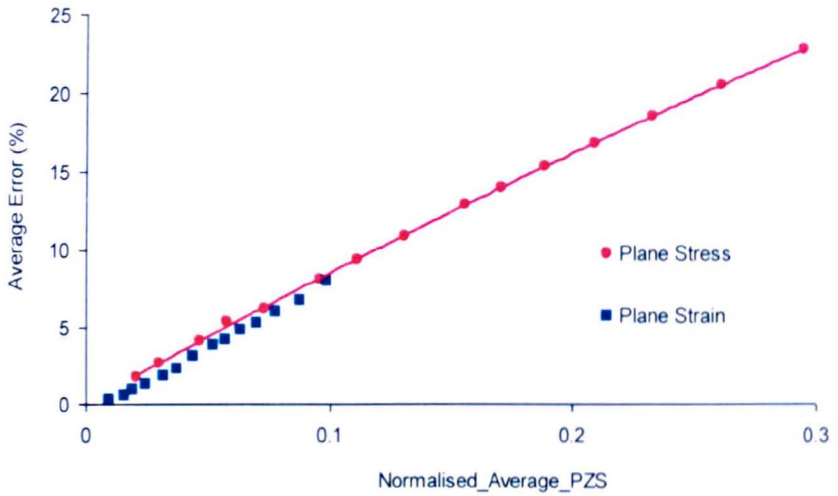

Figure 5-33: Comparison of the plane stress and the plane strain average error distribution as a function of normalised plastic zone size.

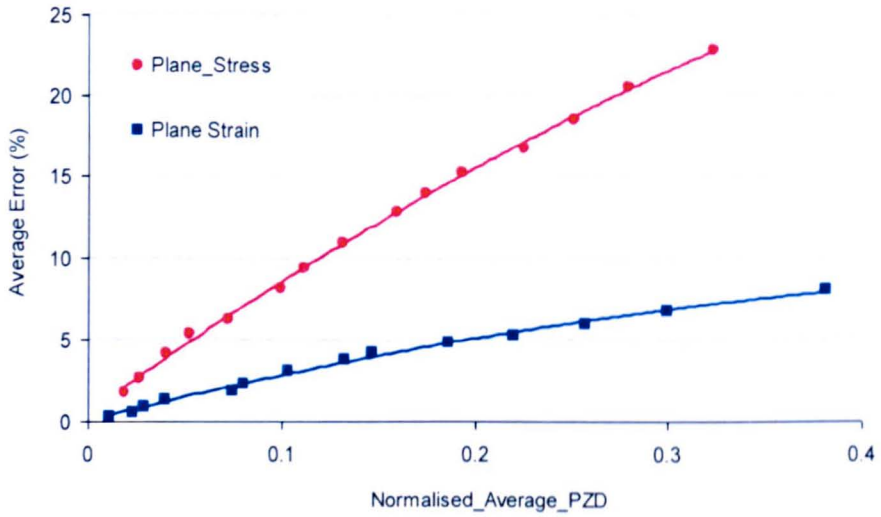

Figure 5-34: Comparison of plane stress and plane strain average error distribution as a function of the normalised plastic zone depth.

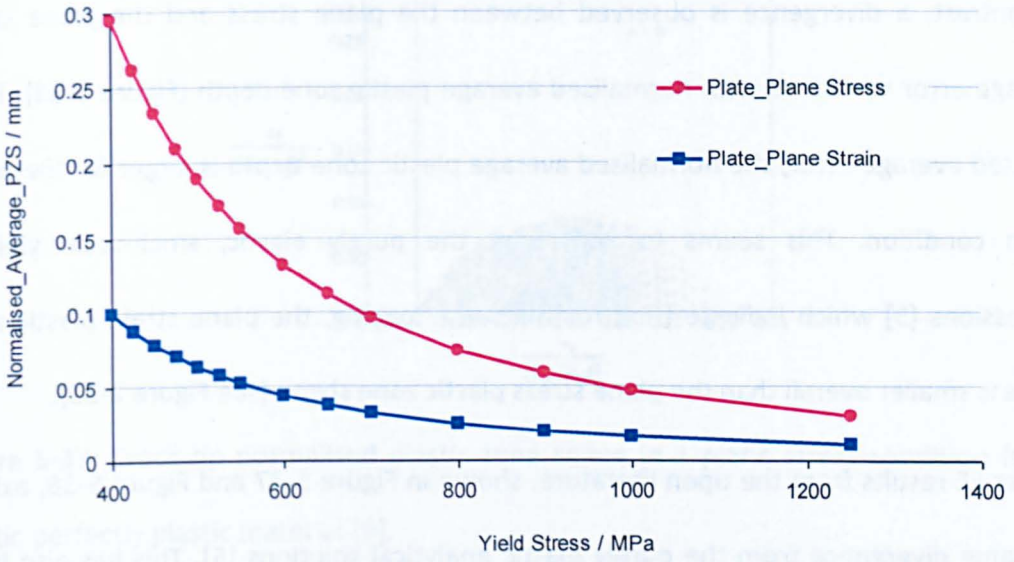

Figure 5-35: Comparison of plane stress and plane strain normalised average plastic zone size as function of the yield stress.

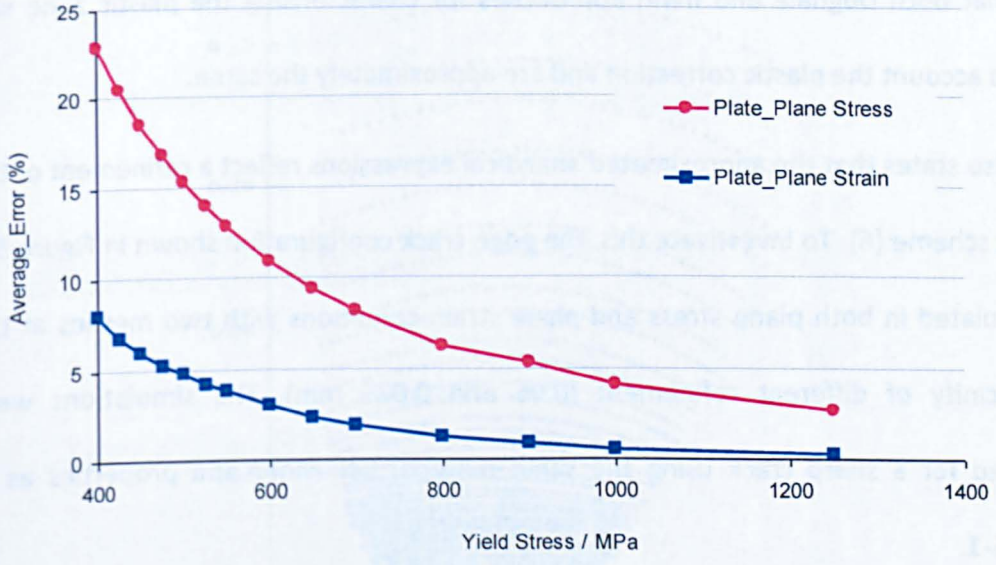

Figure 5-36: Comparison of plane stress and plane strain average error distribution as a function of the yield stress.

In contrast, a divergence is observed between the plane stress and the plane strain average error variations with normalised average plastic zone depth (Figure 5-34). For a selected average error, the normalised average plastic zone depth is larger for the plane strain condition. This seems to contradict the purely elastic, small-scale yielding expressions [5] which indicate that, for the same loading, the plane strain plastic zone shape is smaller overall than the plane stress plastic zone shape (see Figure 2-30).

Similar FE results from the open literature, shown in Figure 5-37 and Figure 5-38, exhibit the same divergence from the purely elastic analytical solutions [5]. This has also been illustrated in the book of Unger [6] where it is reported that the FE plane stress plastic zone shape is approximately the same as the Dugdale's plastic zone shape and behaves similarly to the purely elastic plane stress plastic zone shape (Figure 2-30). It must be noted that both Dugdale and Irwin approaches for characterising the plastic zone size take into account the plastic correction and are approximately the same.

Unger also states that the approximated analytical expressions reflect a refinement of the element scheme [6]. To investigate this, the edge crack configuration shown in Figure 5-1 was simulated in both plane stress and plane strain conditions with two meshes at the crack vicinity of different refinement (0.05 and 0.025 mm). The simulations were conducted for a sharp crack using the same material behaviour and properties as in section 5-1.

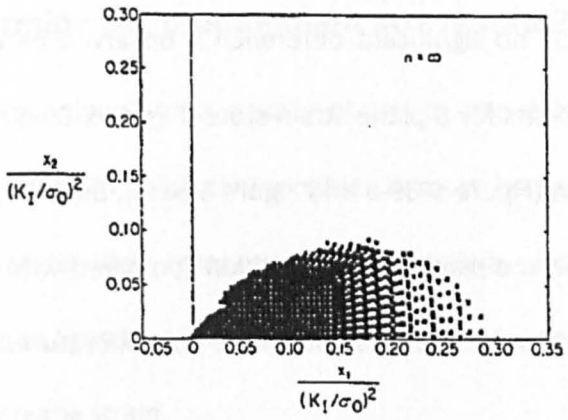

Figure 5-37: Crack tip normalised plastic zone shape in a plane stress condition for an elastic-perfectly plastic material [9].

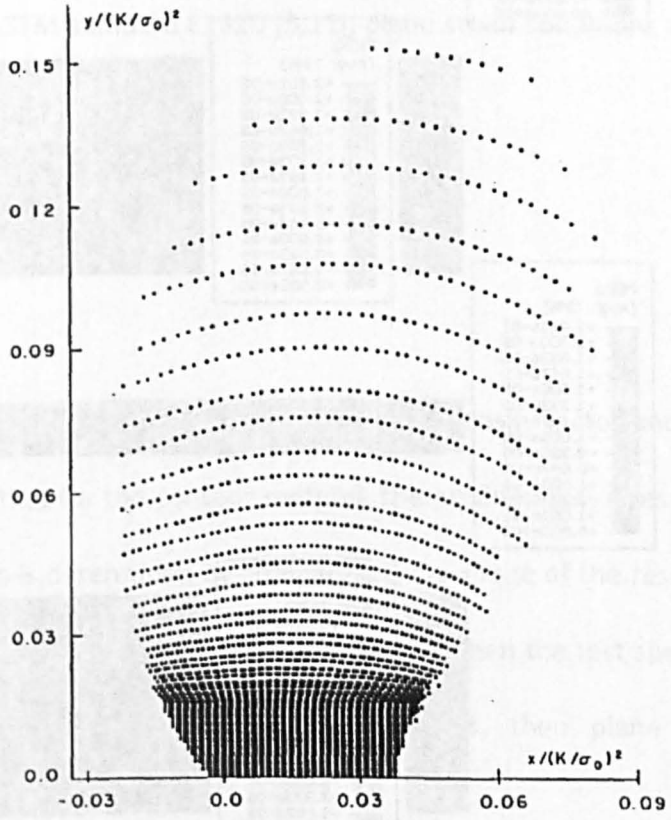

Figure 5-38: Crack tip normalised plastic zone shape in a plane strain condition for an elastic-perfectly plastic material [10].

As shown in Figure 5-39 no significant difference is observed between the results from different mesh refinements for a plane strain state (Figure 5-39-b and Figure 5-39-d) and a plane stress condition (Figure 5-39-a and Figure 5-39-c). But a larger plastic zone depth (~2.6 mm) was found in the plane strain condition compared with the plane stress state (~0.7 mm), which confirms the above results of the open literature.

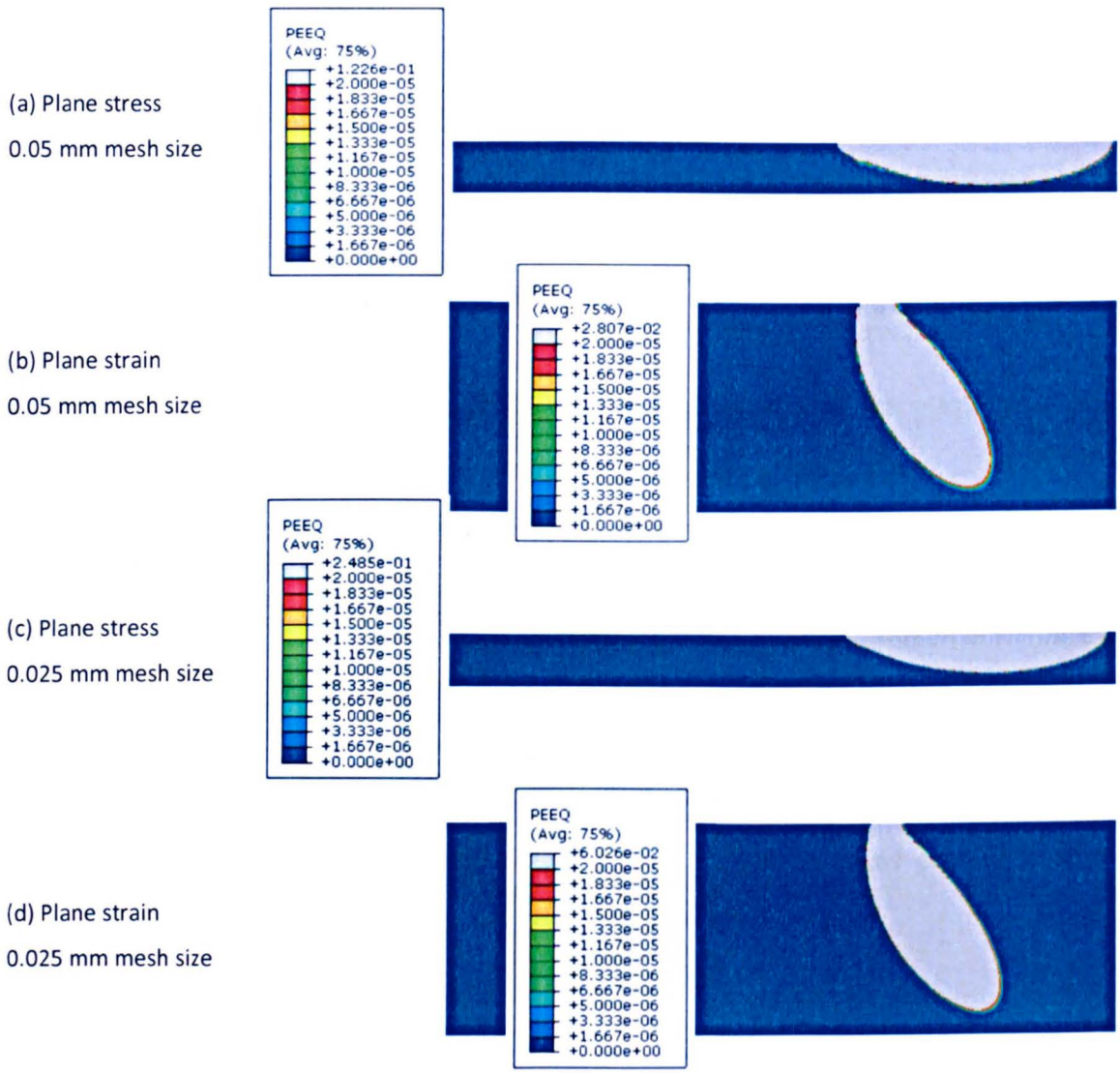

Figure 5-39: Comparison of plane stress and plane strain crack tip plastic zones for two different mesh sizes at the crack tip.

5.10. How to determine the predominant stress state?

In continuum mechanics, plane stress usually occurs in thin plates while plane strain conditions are encountered in thick components. It must be noted that this rule for determining the stress state within components may not always be accurate, and it is also not specified in the open literature how thin or thick the test component should be to assume plane stress or plane strain.

In fracture mechanics, to conduct valid fracture toughness test, the test specimen must behave elastically in a global sense [5,11], and this is an indication that the stress state ahead of the crack is under plane strain conditions [5,11].

According to the ASTM standard E1820 [5,11], plane strain conditions ahead of the crack requires that [5,11]:

$$T \geq 2.5 * \left(\frac{K_I}{\sigma_0} \right)^2 \qquad \text{Eq. 5-3}$$

where T is the specimen thickness, K_I is the stress intensity factor and σ_0 is the material yield stress. Note that for the contour method, the predominant stress state throughout the entire cut path is determined by comparing the average of the results obtained from different cut increments to the specimen thickness. When the test specimen thickness is lower than the right hand term of Equation 5-3, then plane stress conditions predominate.

5.11. Threshold plastic zone size

To design an optimum cutting/restraining strategy for contour method residual stress measurements, a threshold plastic zone size above which significant amount of errors associated with plasticity are introduced in the results is required.

As discussed earlier in section 5-6, the plasticity-induced errors can be considered negligible when the RMS average error is less than 5%. Therefore, this value is used to determine the threshold plastic zone size for plasticity-induced errors mitigation in contour method.

From Figure 5-33 of the correlations, a normalised threshold plastic zone size of ~0.05 is obtained for both plane stress and plane strain conditions.

The determined threshold plastic zone size is utilised in Chapter 7 to optimise the cutting/restraining conditions for residual stress measurement in a three-pass slot weld specimen.

5.12. Discussion

A total of 49 contour method simulations in plane stress and plane strain conditions were conducted to develop correlations for plasticity-induced stress errors estimation in residual stress measurements made with the contour method.

The finite element simulations reported in this chapter and used to develop the contour method plasticity error correlations have assumed elastic-perfectly plastic material properties. Material that hardens after first yield, for example austenitic stainless steel, will restrict the extent of plasticity during cutting and this will reduce errors in contour

measurements. Furthermore, it has been shown in section 5-7, how the finite cut width associated with the wire EDM process also helps to reduce errors introduced by plasticity.

Occurrence of plasticity in a plane stress state is more severe than for plane strain conditions. For a same yield stress value and cutting/restraining conditions, the plasticity-induced stress errors in plane stress conditions were found to be approximately three times greater than those in plane strain. Since the plane stress and plane strain plastic zone size vary in the same manner, it can be concluded that the plasticity-induced stress error approximately linearly scales with the plastic zone size. Therefore, Figure 5-26 can be used to estimate the plasticity-induced error for both plane stress and plane strain conditions.

Regarding the plastic zone depth, for a selected yield stress and cutting/restraining conditions; the plastic zone depth was found to be larger in plane strain state, although the average plasticity-induced errors were lower compared to plane stress conditions. This indicates that the plastic zone size has more effect in introducing the plasticity-induced stress errors.

As discussed in section 5-9, the plane stress plastic zone results presented here correlate with those obtained using analytical solutions. In contrast, the numerical results of the plane strain plastic zone depth seem to contradict the purely elastic, small-scale yielding expressions [5]. This can be further investigated in future. However, as mentioned earlier, when a plane strain stress state is encountered ahead of the crack/cut, the effect of plasticity is much lower in plane strain conditions compared to a plane stress state. This can be noticed from the developed plane stress (Figure 5-26) and plane strain correlations (Figure 5-31). For the plane strain case, only the results obtained from the FE analyses

with the four highest yield stress value (400, 425, 450 and 475 MPa) are above 5% RMS error.

5.13. How to use the correlations?

Estimation of plasticity-induced errors using the correlations consists of the following steps:

- ✓ *Step 1:* Get the initial stress distribution, for example from predictions or using other residual stress measurements data (slitting, neutron diffraction...).
- ✓ *Step 2:* Determine the corresponding residual stress intensity factor distribution for a designed cutting and restraining configuration.

  Step 3: Investigate the predominant stress state at the cut/crack tip by applying Equation 5-4.

$$Thickness \geq 2.5 * \left[\sum_i \left(\frac{K_I^i}{\sigma_0} \right)^2 \right] \qquad \text{Eq. 5-4}$$

  where K_I^i is the stress intensity factor at the cut increment i, σ_0 is the material yield stress. If the thickness requirement is satisfied, plane strain conditions prevail, otherwise assume plane stress conditions.

- ✓ *Step 4:* Calculate the normalised average plastic zone size for plane stress or plane strain conditions using the SIF data, the material yield stress and the sample dimensions and by applying Equation 5-5.

$$\overline{PZS}_{Norm} = \frac{1}{p\pi\sqrt{Lt}} \sum_i \left(\frac{K_I^i}{\sigma_0} \right)^2 \qquad \text{Eq. 5-5}$$

where $p=1$ for plane stress and $p=3$ for plane strain condition, L is the length of cut, t is the thickness over which the residual stress data (used to calculate the SIF) are averaged.

For example, when residual stress measurements obtained from the slitting method are used for calculating the SIF distribution, t is equal to the sample's thickness. That is because the slitting method measures residual stresses averaged over the entire specimen thickness. In the case of neutron diffraction results, the side of the gauge area over which the results are averaged, is used (see Chapter 6 and Chapter 7). When analytical or FE line profile results are employed to calculate the SIF data, a unit distance ($t=1$) is assumed for normalisation. For a more generalised case, which is also the worst case for assessing plasticity effect, a unit distance $(t=1)$ can be assumed in the normalisation. However, for the validation process (Chapter 6 and Chapter 7), the correct value of t is utilised.

✓ *Step 5:* Estimate the average stress error from Figure 5-26 and corresponding normalised plastic zone depth using Figure 5-27 for plane stress state and Figure 5-32 for plane strain conditions.

✓ *Step 6:* To take into account the cut width effect, measure and normalise the removed wire EDM cut width (see Equation 5-6). Subtract the obtained value from the estimated normalised plastic zone depth of step 5.

$$Cut\_Width_{Norm} = 2 \times \frac{\frac{1}{2} Cut\_Width}{\sqrt{\frac{1}{2} W t}} \qquad \text{Eq. 5-6}$$

where $1/2W$ is the distance from the cut path to the clamp, t is the distance over which the residual stress data (used for the normalising the PZS) are averaged.

✓ *Step 7:* Re-estimate the average stress error from Figure 5-27 (plane stress state) and Figure 5-32 (plane strain state) of the correlations using the corrected normalised average plastic zone depth of step 6.

5.14. Conclusions

The following conclusions are made on the work carried out in this chapter:

1. The size and shape of the plastic zone ahead of a contour cut is not affected by how the cut is idealised (i.e. the width and crack tip shape) in the finite element model. However, a better shape is obtained with a model having a fine mesh in the crack vicinity.
2. Correlations for estimating plasticity-induced errors in the contour method measurements for both plane stress and plane strain conditions have been developed based on elastic-perfectly plastic material behaviour (i.e. no strain hardening) with symmetric contour cut restraining conditions.
3. It was found that the plasticity-induced errors for plane strain conditions are lower compared to plane stress.
4. The normalised average PZS (rather than the normalised average PZD) was found to be the most important parameter determining the introduction of plasticity-induced stress errors.
5. The effect of a finite cut width helps to reduce the lateral extent of the plastic wake and hence will help reduce plasticity-induced errors in contour measurements.
6. A normalised threshold plastic zone size from which plasticity starts to become significant is proposed for plasticity-induced errors mitigation in the contour method.

5.15. References

1. Sham TL (1982) Finite-element study of the asymptotic near-tip fields for Mode I plane strain cracks growing stably in elastic ideally plastic solids.

2. Narasimhan R, Rosakis AJ, Hall JF (1987) A Finite Element Study of Stable Crack Growth Under Plane Stress Conditions: Part I-Elastic-Perfectly Plastic Solids. Journal of Applied Mechanics 54 (4):838-845

3. Shin S (2005) FEM analysis of plasticity-induced error on measurement of welding residual stress by the contour method. Journal of Mechanical Science and Technology 19 (10):1885-1890

4. Dennis RJ, Leggatt NA, Kutarski EA (2009) Investigation of the Performance of the Contour Residual Stress Measurement Method When Applied to Welded Pipe Structures / PVP2009-77470. Paper presented at the ASME Pressure Vessels and Piping Division Conference, Prague, Czech Republic,

5. Janssen M, Zuidema J, Wanhill RJH (2002) Fracture Mechanics. 2nd edn. Delft University Press, Delft

6. Unger DJ (2001) Analytical Fracture Mechanics. Dover Publications, INC., Mineola, New York

7. Medhi J (1992) Statistical Methods: An Introductory Text. John Wiley & Sons,

8. Smith MC (2003) ENPOWER Task 2.2: design of a beamtype fracture specimen containing a residual stress field.

9. Narasimhan R, Rosakis AJ (1988) A finite element analysis of small-scale yielding near a stationary crack under plane stress. Journal of the Mechanics and Physics of Solids 36 (1):77-117

10. Sham TL (1983) A Finite-Element Study of the Asymptotic Near-Tip Fields for Mode I Plane-Strain Cracks Growing Stably in Elastic-Ideally Plastic Solids. In: Shih CF, Gudas JP (eds) Elastic-plastic Fracture: Second Symposium, Volume I- Inelastic Crack Analysis. ASTM STP 803, vol 1. American Society for Testing and Materials, pp I.52-I.79

11. ASTM (2006) ASTM E399 - Standard Test Method for Linear-Elastic Plane-Strain Fracture Toughness K_{Ic} of Metallic Materials.

Chapter 6: Experimental validation of correlations for plasticity-induced errors estimation in the contour method

Correlations for estimating plasticity-induced errors in residual stress measurements made with the contour method have been developed in Chapter 4. However, for confidence in their accuracy and application, experimental validation is required. The purpose of the present chapter is to report the detailed experimental work performed and results obtained which demonstrate that appropriate correlations have been developed.

As cutting plastic strains developed in plane stress conditions are of more concern than those in plane strain (see Chapter 5), the experimental validation is mainly carried out with test specimens having dimensions such that an approximate plane stress state prevails. A series of test specimens is designed with different residual stress distributions introduced by using different patterns of laser line welds. Neutron diffraction and the contour method are applied to quantify the residual stress distribution along the plane/line of interest in each test specimen. The differences between the measured stresses are then assessed and used to validate the plasticity-induced error correlations.

6.1. Test specimens design

The test specimens design was conducted in different steps including material characterisation, geometry selection, laser welding layout optimisation and residual stress and strain prediction by the finite element method. The test specimens were

designed to approach the assumptions made during the correlations development that is plane stress conditions and elastic-perfectly plastic material stress-strain properties.

6.1.1. Material

As the correlations for plasticity-induced errors estimation were developed assuming elastic-perfectly plastic material properties, a material with properties representing this idealised case was chosen. Bright steels are amongst the few materials having approximately elastic-perfectly plastic behaviour. Therefore, this type of material is used for all the test specimens. The bright steel chosen is designated in British Standard BS 970:1991 as 080A15. The chemical composition of the material, shown in Table 6-1, was supplied by ACENTA [1].

The as-received plates (500 x 200 x 6) mm^3 were cut into two halves of (250 x 200 x 6) mm^3. Specimens for tensile testing and Young's modulus measurement were extracted from one of the cut plates. All the cutting processes were achieved by wire EDM. On completion of these preliminary cuts, the plates and specimens for the material's mechanical properties characterisation (yield stress and Young's modulus) were placed in a furnace and heated up to 600 °C for a stress relief heat treatment. This heating temperature was maintained for about 10 hours in order to obtain a uniform temperature distribution through all the specimens, and then air-cooled down to ambient temperature.

Table 6-1: Chemical compositions of the 080A15 steel in wt.%.

C	Si	Mn	P	S
0.16	0.22	0.75	0.016	0.029

Mechanical properties

To assess the mechanical properties of the plates, tensile testing was carried out using an Instron 5969 Universal machine equipped with a 50 kN load cell. Friction grips were used to hold the sample during the test. The test specimen was cut in size according to ASTM E8/E8M-11 Standard [2] (see Figure 6-1). Figure 6-2 shows the measured engineering stress-strain curves for the three samples tested. It can be observed that the results obtained from samples 2 and 3 are more consistent with each other compared to the results from sample 1. This might be related to material inhomogeneity as the three samples were extracted from different locations of the plate. The material yield stress was determined by taking the stress value corresponding to the 0.2% plastic strain for the different curves and Young's modulus derived using the classical approach (*i.e.* by taking the slope of the elastic region). The average value of the yield stress and Young's modulus from the three curves was 550 MPa and 211 GPa, respectively. The yield stress obtained is found to be in the range of drawn bright steel yield stress [3].

To increase the level of confidence in the elastic properties, Young's modulus was measured using a different technique developed by IMCE [4]. The equipment shown in Figure 6-3 determines the flexural vibration frequency from which Young's modulus can be calculated using the mass and dimensions of the test sample, here a block of dimensions (50.010x9.995x6.316) mm^3. The experimental procedure consists of mechanically hand tapping the block using a small flexible hammer. The hand tap causes flexural vibrations of the beam which are detected by a USB-microphone. The frequency signal is analysed using software.

For a series of three tests with a 0.3 Poisson's ratio assumed, consistent values of Young's modulus were obtained (210.5, 210.48, 210.57 GPa). The average of these three measurements, ~210.5 GPa, is used in the validation studies presented in this Chapter.

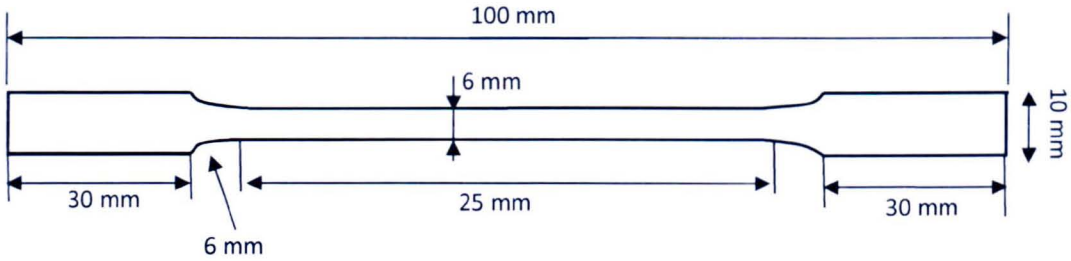

Figure 6-1: Schematic of the flat tensile test specimen used for tensile testing. The specimen gauge section was (6×6) mm^2.

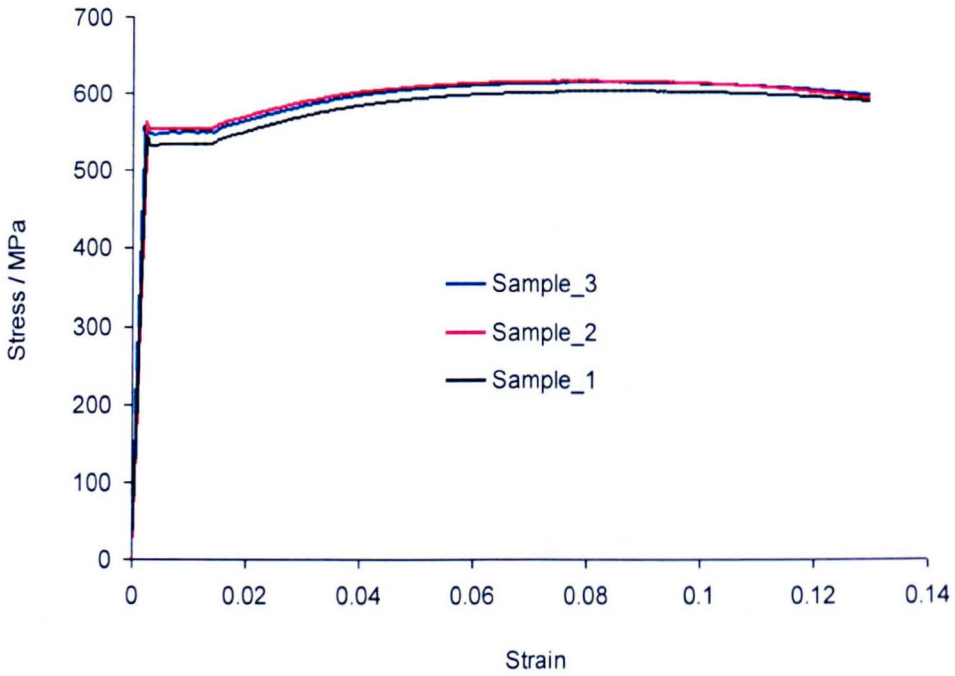

Figure 6-2: Tensile test engineering stress-strain curves for the 080A15 material after heat treatment. The average yield stress, from the three measurements, was 550 MPa and the average Young's modulus 211 GPa.

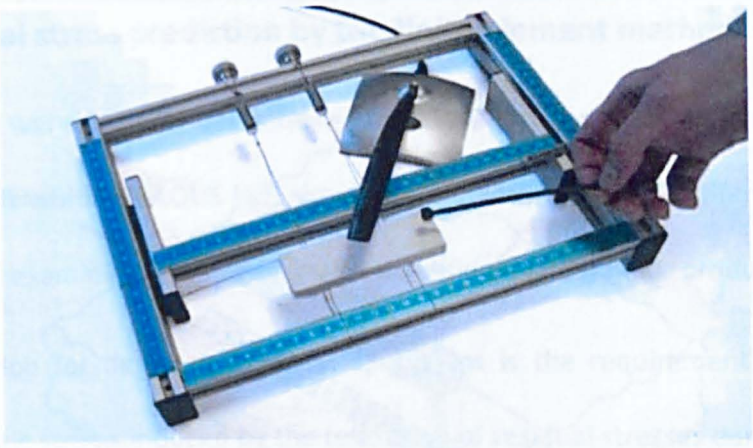

Figure 6-3: Photograph of the equipment used for Young's modulus measurement [4].

6.1.2. Introduction to laser welding

L.A.S.E.R. (***L***ight ***A***mplification by ***S***timulated ***E***mission of ***R***adiation) welding [5-7] is a non-contact welding process for joining materials. The process consists of generating a sharp and focused beam of high intensity light (*i.e.* energy) that melts a very small area of the material at a very high rate.

Two different types of laser sources are mainly used in laser welding: CO_2 (Carbon dioxide) and Nd:YAG (Neodymium-doped yttrium aluminium garnet) [8]. The CO_2 laser can be applied to almost any type of material while the Nd:YAG lasers work only for a limited number of materials [9]. The most important parameters which can be controlled during laser welding are the laser travelling speed (welding speed), the spot size and the power density [6,7,10]. Figure 6-4 shows a schematic representation of the laser welding process.

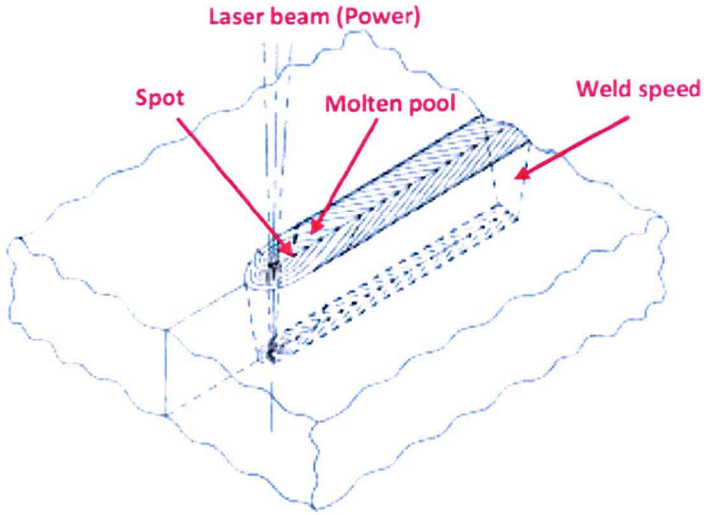

Figure 6-4: Schematic representation of the laser welding process [11].

There are different laser welding modes including the keyhole and conduction modes [7]. The former regime can be obtained when welding is conducted with high power density, giving a high penetration, while the latter one is obtained with a low power density. The advantages of the keyhole mode remain in its deep penetration and relatively small heat affected zone. However, the keyhole mode welding can sometimes lead to several types of weld defect such as porosity and spatter [12-16]. The conduction mode enables a high flexibility and control over its heat input [6]. Contrary to the keyhole mode, no porosity, cracking or spatter issues accompany the process. The two main disadvantages attributed to the conduction mode are the small penetration depth of the weld and the coupling efficiency of the process [12].

Since for the present project control of the heat affected zone and associated welding plastic strains is of high important, the keyhole welding mode is selected.

6.1.3. Residual stress prediction by the finite element method

Test specimens were carefully designed by undertaking two-dimensional non-linear finite element analysis within ABAQUS [17] simulating the introduction of different patterns of laser welds and examining the plastic strain and residual stress fields produced.

The first criterion for designing the test specimens is the requirement to control the amount of plastic strains induced by the relaxation of residual stresses during the contour cutting process. Three different levels of cutting plastic strains induced by the release of different magnitudes of compressive residual stresses have been studied: high, moderate and negligible. The validation process has also examined cutting plastic strains induced by the relaxation of tensile residual stresses in more complex laser welded test specimens.

To avoid mixing any plastic strains introduced by manufacture of the test plates (*i.e.* laser line heating) and the contour method cutting process, a second design criterion was imposed, that is cutting plasticity must develop in parent material plastically unaffected by the laser welding. This condition is also desirable for reliable measurement of residual stresses by neutron diffraction.

To ensure that the induced residual stress fields in the test specimens met the two criteria defined above, a series of finite element simulations were undertaken. These included thermal analysis, stress analysis and contour method cutting simulation for checking the resulting level of plasticity.

Thermal analysis

The thermal analysis consists of simulating the heat transfer in the plates heating during laser welding and subsequent cool down. The transient heat transfer mode was used for the simulations [17]. To achieve the heat transfer simulation, the material's physical-thermal properties such as thermal conductivity, specific heat, latent heat, linear thermal expansion coefficient, latent heat and density are required.

To obtain more reliable results, temperature dependency is taken into account for the thermal conductivity, specific heat and the linear thermal expansion coefficient. In the open literature the exact values for bright steel (080A15) physical-thermal properties with temperature dependency are not easily accessible. Therefore, general physical-thermal properties of a carbon steel from the open literature from the MPC database developed for ASME Div II_Rewrite [18] have been assumed (Table 6-2).

As stated earlier, the validation process is conducted with test specimens having different expected levels of cutting plastic strains induced by the relaxation of compressive and tensile residual stresses. To achieve this, test specimens with different welding configurations were analysed. Four different welding configurations were finally retained for the present project: three plates with parallel heating zones (Figure 6-5-a) and one with inclined heating zones (Figure 6-5-b). The plates with parallel heating zones are used for the validation process where the cutting plastic strains are induced by the release of compressive residual stresses while the plate with inclined heating zones is used for the validation process where cutting plastic strains are induced by the release of tensile residual stresses.

The three plates with parallel heating zones were only different by the distance y between the two heating zones, which is 38 mm, 54 mm and 100 mm for plate_0, plate_1 and plate_2, respectively. The distance y between the two parallel heating zones controls the magnitude of residual stresses and the amount of cutting plastic strains to be induced by the release of the corresponding residual stresses. The smaller the y-value is, the higher are the magnitude of residual stresses and cutting plastic strains. The length of the heating zones introduced by laser welding was 100 mm for the plates with parallel heating zones and 96 mm for the plate with inclined heating zones. A 1 mm heating spot was assumed for all the plates. Because of the symmetric plane along the measurement line, only one half of each plate design was simulated. Symmetry boundary conditions were defined along the measurement line and about the y-axis.

Table 6-2: Physical properties assumed for the laser heating thermal analysis.

Temperature (°C)	Conductivity (W / mm.K)	Specific Heat (J/Kg.K)	Expansion coefficient (/K)	Young's Modulus (MPa)
20	0.0586	460	1.18E-005	210500
100	0.058	480	3.75E-005	
200	0.052	500	3.9E-005	
300	0.049	550	4.1E-005	
400	0.0435	635	4.255E-005	
500	0.04	710	4.35E-005	
600	0.035	790	4.45E-005	
700	0.03	880	4.65E-005	
800	0.026	990	4.8E-005	
900	0.021	1050	5E-005	
1000	0.018	1140	5.2E-005	
1100	0.015	1200	5.4E-005	
1200	0.01	1300	5.5E-005	
1300	0.008	1400	5.65E-005	
1400	0.004	1500	5.8E-005	
1500	0.0015	460	5.95E-005	2105

Note:

- ✓ Constant density was assumed: 7.85×10^{-06} $Kg.mm^{-3}$
- ✓ Poisson'sratio: 0.3
- ✓ Latent heat of fusion: 300 KJ/Kg, absorbed/released between 1475 °C and 1500°C.

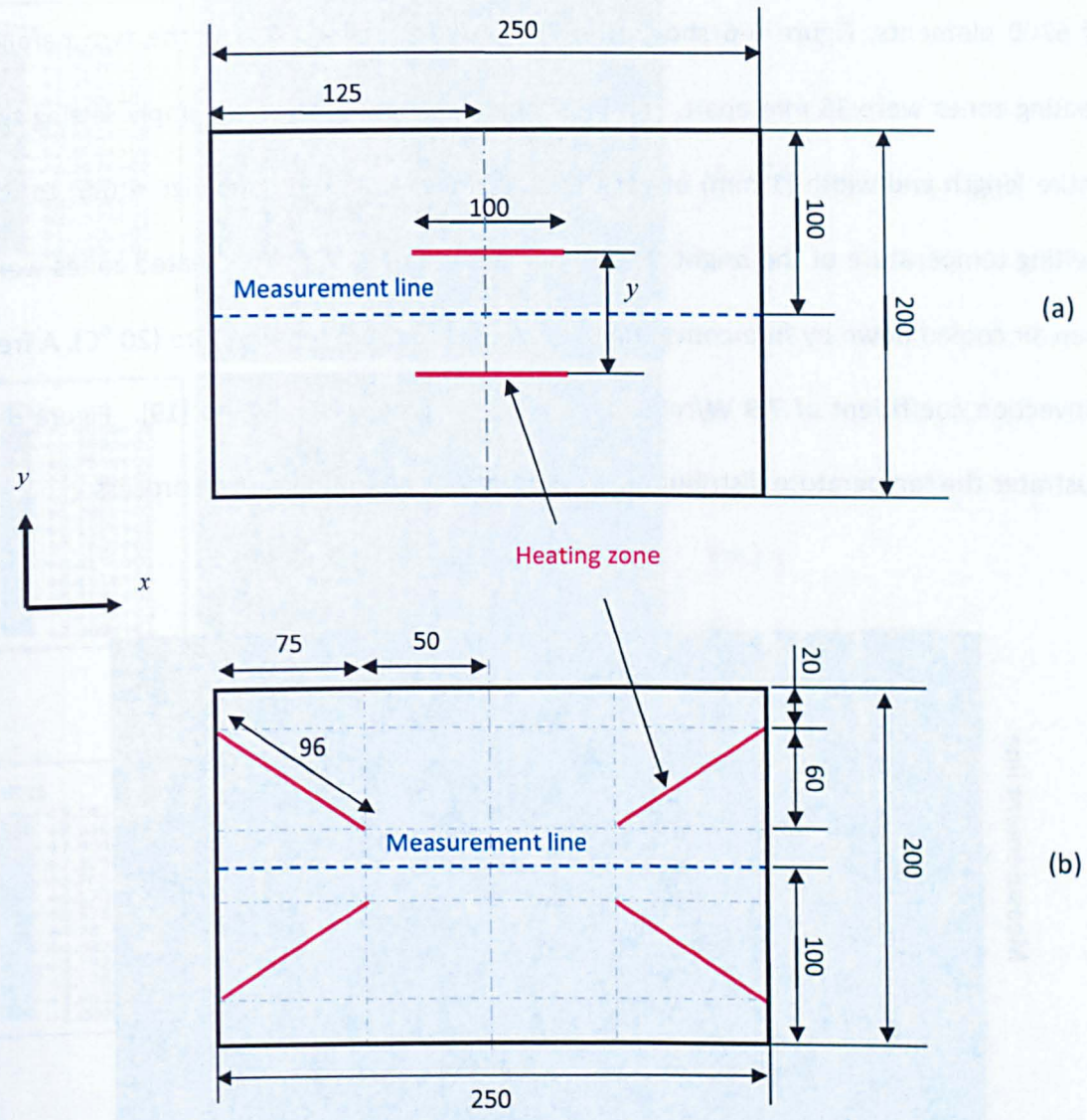

Figure 6-5: Schematic representation of the plates showing the heating zones and the measurement line. Three plates with two parallel heating zones (a) and one with four inclined heating zones (b) are simulated. The plates' thickness is 6 mm. All dimensions are in mm.

The plates were meshed with second order heat transfer elements (DC2D8). A global mesh size of 2 mm was chosen with finer mesh elements in the vicinity of the heating zones. The mesh grid is coarsened towards the plate centre and free edges giving a total

of 6300 elements. Figure 6-6 shows the FE mesh for plate_0 where the two parallel heating zones were 38 mm apart. The laser heating was simulated by simply setting the entire length and width (1 mm) of each heating zone (Figure 6-5 and Figure 6-6) to the melting temperature of the bright steel, assumed to be 1500 °C. The heated zones were then air cooled down by free-convection heat losses to room temperature (20 °C). A free convection coefficient of 7.9 W/m^2K for mild steel in air was assumed [19]. Figure 6-7 illustrates the temperature distribution for different stages of the cooling process.

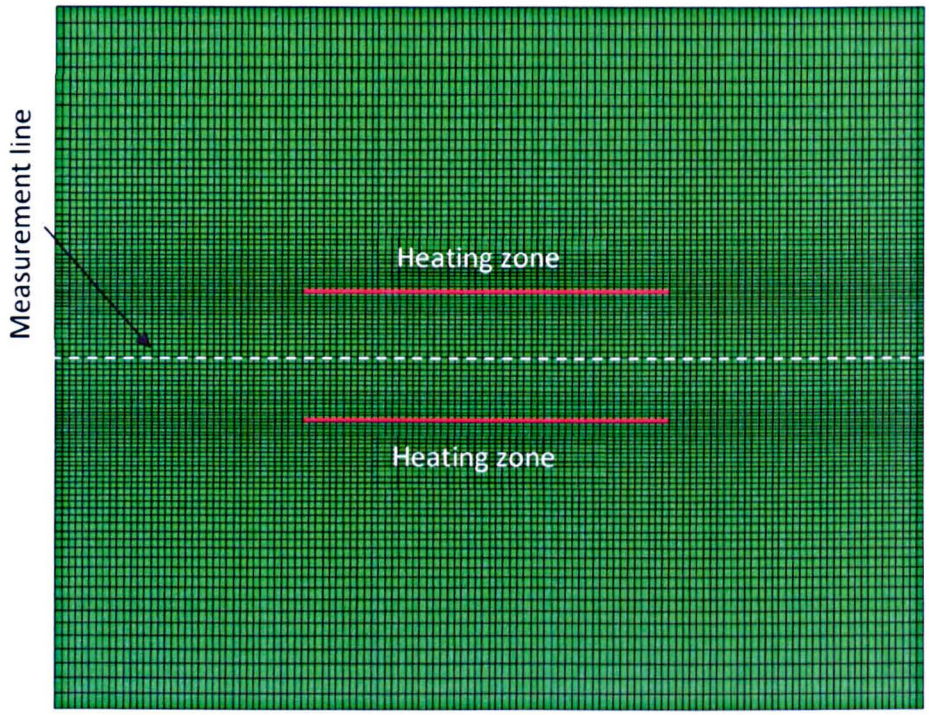

Figure 6-6: Illustration of the mesh used for the thermal analysis for plate_0. The vicinity of the heating regions is meshed with finer elements. The mesh size is coarsened towards the plate centre and free edges parallel to the heating zones. Only one half of the plate was simulated.

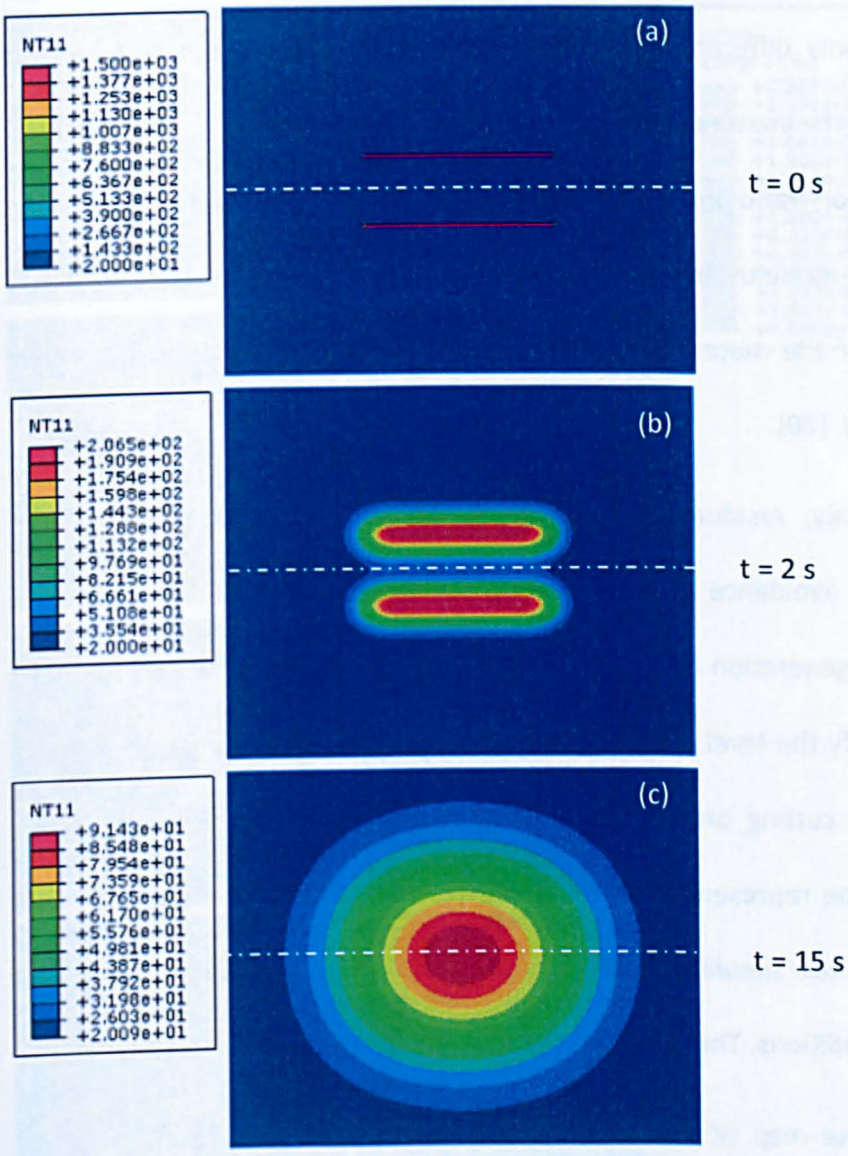

Figure 6-7: Temperature distribution for different cooling stages for the plate_0. Step (a) shows the heating regions molten. Only one half of the plate was simulated. Temperature units are in °C.

Mechanical analysis

Once the thermal analysis is completed, the temperature distribution history of the different plates was mapped into new FE models to generate the evolution of residual stress distribution due to the laser heating process. The models used in the thermal and

stress analysis were only different by the mesh type used (here plane stress mesh elements, CPS8R) and the material properties defined. Mechanical properties such as Young's modulus, Poisson' ratio and elastic-plastic stress-strain data were required in the stress analysis. Young's modulus and yield stress temperature dependency data for mild steel were assumed for the material used. The data were determined from the paper published by Chen et *al.* [20].

As mentioned previously, residual stresses in the different plates were generated according two criteria: avoidance of laser heating plastic strains in the vicinity of the measurement line and generation of different levels of plastic strains during the contour cutting process. To verify the level of plasticity introduced by a contour measurement it was assumed that the cutting process would be conducted in practice using 'finger' clamping which could be represented by minimum restraint in the FE modelling. The EDM cutting process was simulated as an incremental sharp cut by releasing the symmetry boundary conditions. The finite width of a real EDM cut was neglected.

Figure 6-8 illustrates the map of predicted plastic strains induced by both the laser heating and contour cutting processes. It can be observed that higher cutting plastic strains are predicted with the more closely spaced heating zones. Since the induced cutting plastic strains are dependent on the stress magnitude, the predicted residual stress magnitude for the plates with parallel heating zones are expected to vary similarly.

Figure 6-8: Illustration of the predicted plastic strains induced (grey regions) by the laser heating process (a) and with the additional plastic strains introduced by the cutting process (b) for the different plates simulated.

Maps of the predicted residual stresses normal to the measurement line (*i.e.* the transverse component of residual stresses) are shown in Figure 6-9 and Figure 6-10 for

the plate with inclined heating zones and the plates with parallel heating zones, respectively. The transverse component of residual stresses is of interest here, because the standard contour method can only measure the stresses normal to the cut faces.

Tensile residual stresses are obtained around the heating zones balanced by some compressive stresses adjacent to the ends of the heating zones. In the plates with parallel heating zones the magnitude of the stresses along the measurement line decreases when the distance between the heating zones is increased.

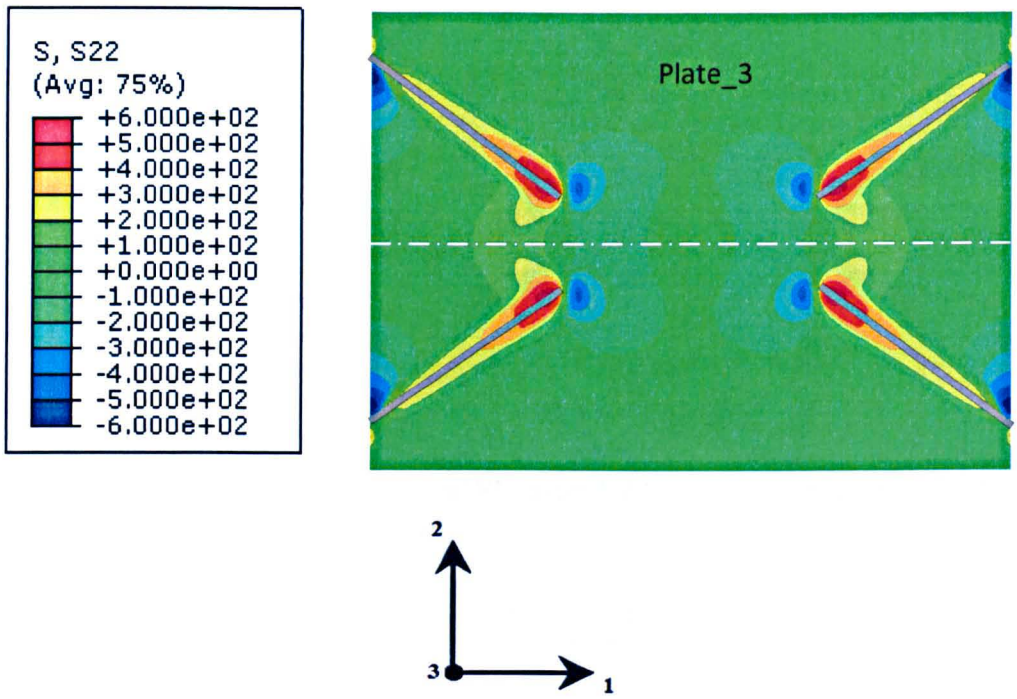

Figure 6-9: Illustration of the predicted map of transverse residual stress in the plates with inclined heating zones. The heating zones (in grey) are also shown. Stress units are in MPa.

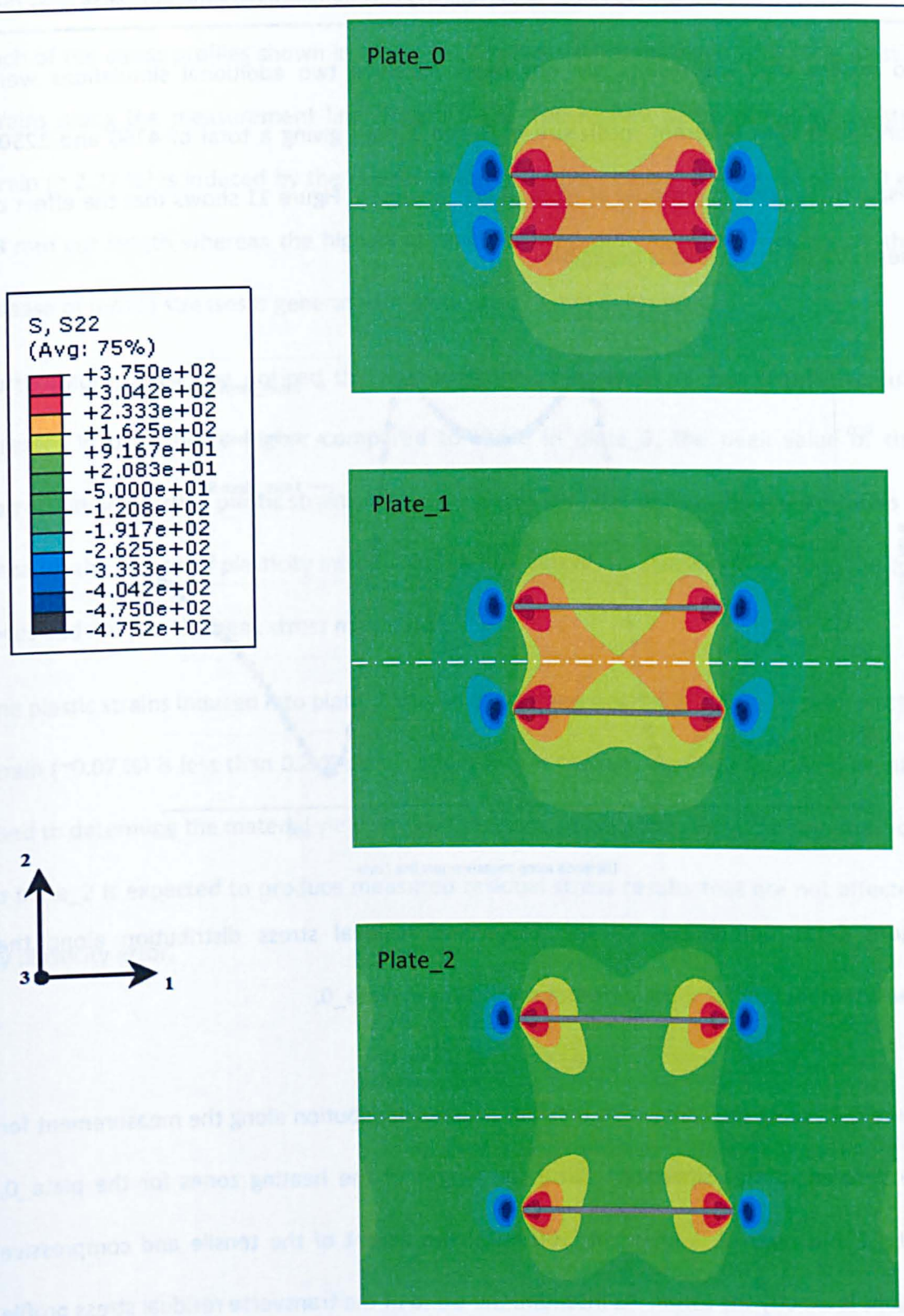

Figure 6-10: Illustration of the predicted maps of transverse residual stress in the three designs of plates with parallel heating zones. The heating zones (in grey) are also shown. Stress units are in MPa.

To ensure that the results are not mesh sensitive two additional simulations were conducted with different mesh size of 3 and 1 mm; giving a total of 4150 and 12500 respectively. Only the model of plate_0 was analysed. Figure 11 shows that the effect of mesh size on the results is negligible.

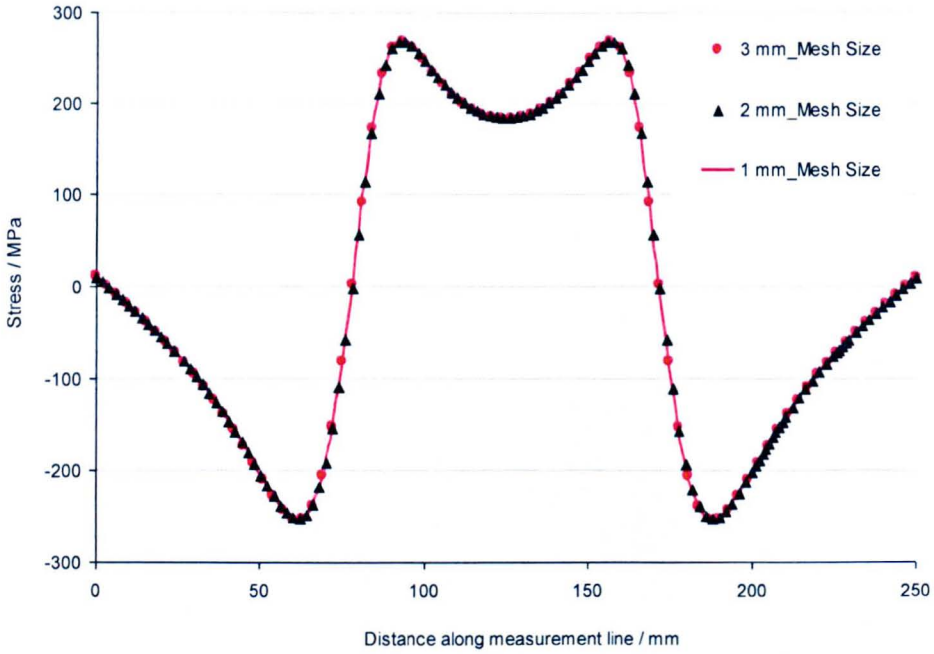

Figure 6-11: Comparison of the transverse residual stress distribution along the measurement line for three different mesh sizes in plate_0.

Figure 6-12 plots the transverse residual stresses distribution along the measurement for the different plates simulated. Since the length of the heating zones for the plate_0, plate_1 and plate_2 is identical (100 mm), the extent of the tensile and compressive regions is exactly the same. As intended the trend of the transverse residual stress profile obtained in plate_3 (with inclined heating zone) is approximately the opposite of those generated in the plates with parallel heating zones, although the magnitudes change.

Each of the stress profiles shown in Figure 6-12 induces different levels of cutting plastic strains along the measurement line (Figure 6-13). The highest value of cutting plastic strain (~ 2.77 %) is induced by the release of compressive residual stresses in plate_0 at 68 mm cut length whereas the highest cutting plastic strain (~ 0.44 %) induced by the release of tensile stresses is generated in plate_3 at 73 mm cut length.

Furthermore, it can be noticed that although the magnitudes of the tensile residual stresses in plate_0 are higher compared to those in plate_3, the peak value of the corresponding cutting plastic strains in the two plates is of the same order (~0.4 %). This is because the degree of plasticity introduced is a function of the stress profile along the cut faces and not just the peak stress magnitude.

The plastic strains induced into plate_2 can be considered negligible since the peak plastic strain (~0.07 %) is less than 0.2 % plastic strain that is the non-linearity threshold usually used to determine the material yield stress. Therefore, application of the contour method to plate_2 is expected to produce measured residual stress results that are not affected by plasticity error.

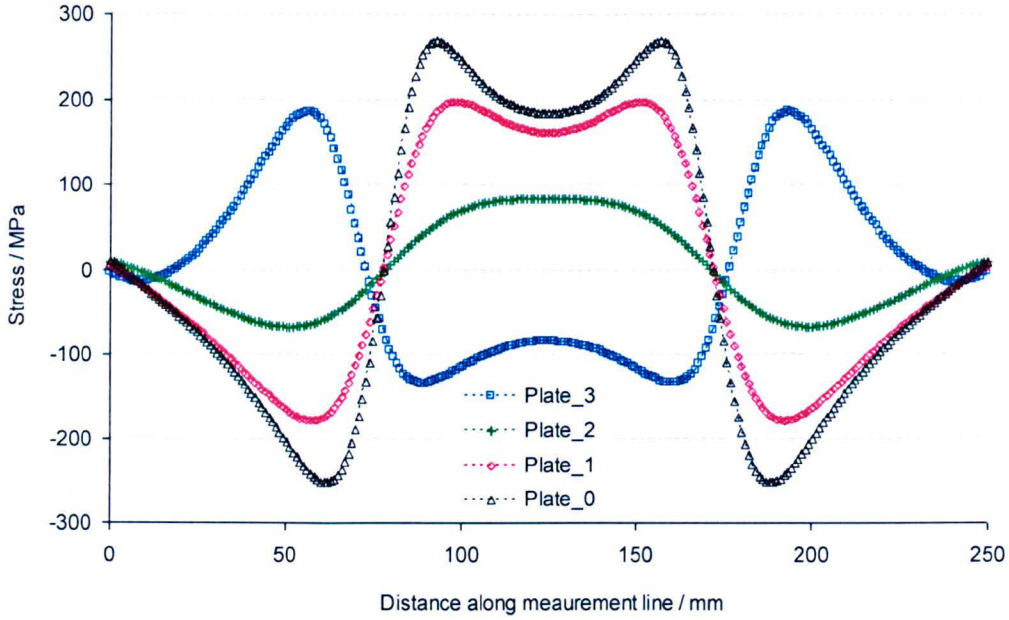

Figure 6-12: Comparison of the predicted transverse (*i.e.* perpendicular to the welding direction) component of residual stresses along the measurement line in the different laser welded plates.

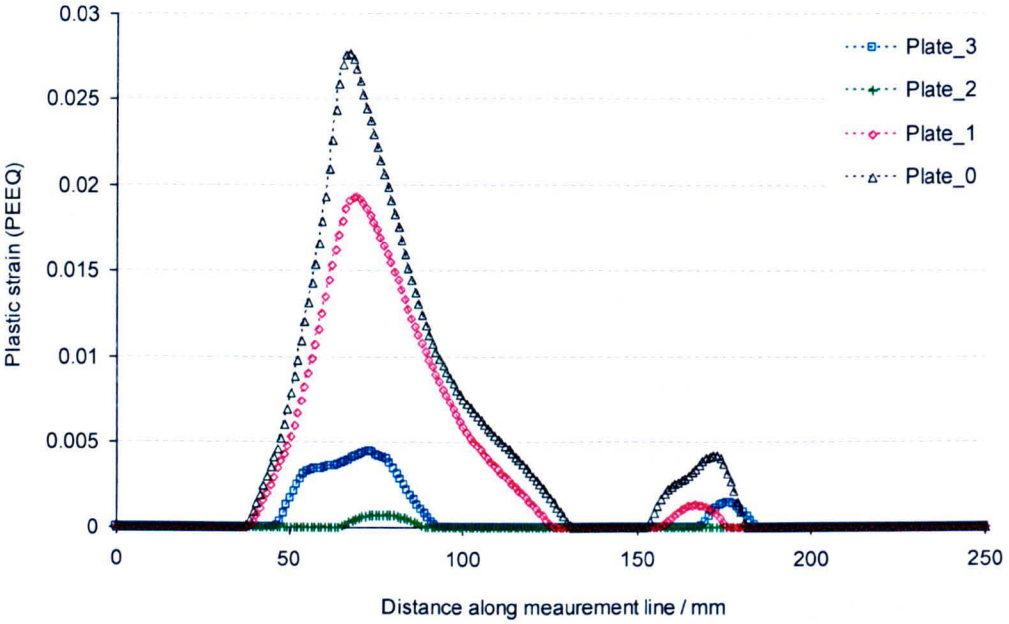

Figure 6-13: Comparison of predicted plastic strains (PEEQ) induced by the cutting process along the line of the cut for the different welded plate configurations simulated.

6.1.4. Manufacture of laser welded plates

A set of laser welded plates were made based on the finite element results. The laser heating process was conducted for the author at the Welding Engineering and Laser Processing Centre at Cranfield University.

The different heating modes and parameters of the laser welding process have been described earlier in this chapter. Since the heat affected zone and associated plastically strained region generated in conduction mode is usually greater compared to keyhole mode, this latter regime was applied to create the required heated zones.

A CO_2 fibre laser source of type IPG YLR-8000 CW with a maximum power of 8 kW was used. However, only 3kW power was applied for the present work. The optical arrangement was made in a way to produce a 1 mm diameter welding spot for all the plates. The laser beam travelling speed was about 0.5m/min. Once the heating process was completed, the plates were free air-cooled down to ambient temperature. Figure 6-14 and Figure 6-15 show the picture of one the plates with parallel heating zones (plate_0, y = 38 mm) and the plate with inclined heating zones (plate_3), respectively. Fairly uniform laser heating zones were obtained with all four plates, although a close-up view on the back face of plate_0 shows a slight non-uniformity in the width of the bottom of the heated zone (See Figure 6-14-b) which may have affected residual stress field introduced.

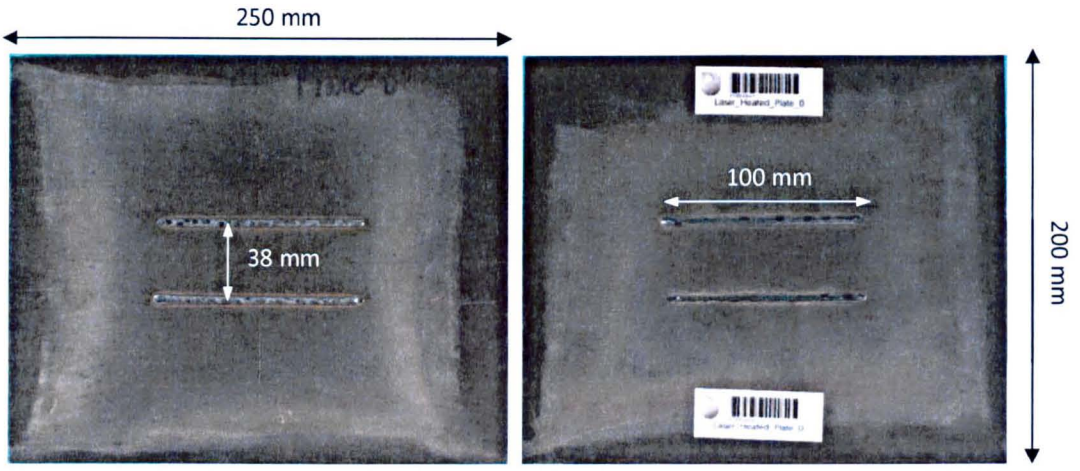

Figure 6-14: Photo showing the front face (a) and back face (b) of one of the plates with parallel heated zones (plate_0, y = 38 mm).

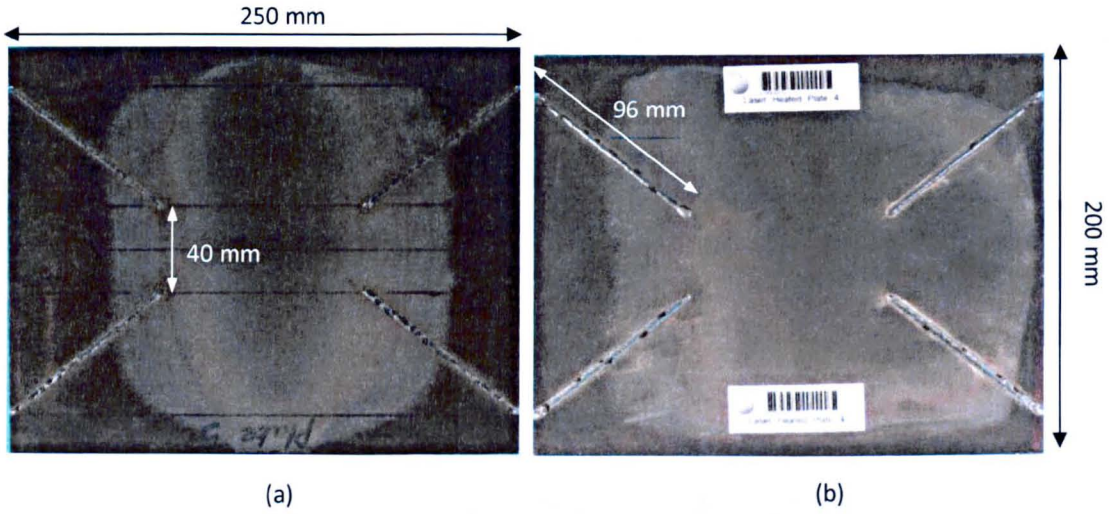

Figure 6-15: Photo showing the front face (a) and back face (b) of the plate with inclined heated zones (plate_3).

6.2. Residual stress measurement

On completion of the test specimens design and manufacture, residual stress measurement by neutron diffraction and contour method was undertaken for each of the plates.

First, neutron diffraction, a non-destructive technique, was used to determine the orthogonal (*i.e.* longitudinal, transverse and normal) components of residual stresses along the measurement line at the plates' mid-thickness. Following neutron diffraction measurements, the contour method was applied to determine the transverse component of the residual stresses on the cut plane along the same measurement line of each plate.

6.2.1. Residual stress measurement by neutron diffraction

The neutron diffraction residual stress measurements were performed at two different facilities: the Australian Nuclear Science and Technology Organisation (ANSTO), Australia and the ISIS facility of the Rutherford Appleton Laboratory, UK. The residual stress distributions in plate_1 and plate_2 were measured at the ANSTO facility and the residual stress distributions in the remaining two plates (plate_0 and plate_3) were quantified at ISIS.

Plate_1 and plate_2 residual stress measurement

The residual strain measurements in plate_1 and plate_2 for the three orthogonal (*i.e.* longitudinal, transverse and normal) components were carried out on the Kowari strain scanner instrument at ANSTO by PhD student Sanjooram Paddea with close support from the author. At this facility, the neutrons are produced by fission from the OPAL nuclear reactor.

Prior to the experiment, stainless steel spheres (providing reference fiducial points) were attached to each plate around the measurement line and a model of the sample was created by laser scanning. The fiducial points act as reference locations on the sample that can be seen when the sample is in position on the instrument. The SSCANSS (Strain SCANning Simulation Software) [21] together with a laser touch probe was used for the plates' alignment; giving a measurement positioning accuracy of ~50 μm.

The lattice parameter was measured in three orthogonal directions at 45 points along the measurement line located at the mid-thickness of each plate. A spacing of 5 mm was chosen between the measurement points giving a total measurement length of 225 mm. Due to the sample clamping arrangement; the remaining 25 mm length of plate was not accessible for measurement. Stress profile data for this region were inferred by assuming symmetry conditions about the plate mid-length. The first measurement point was located at 5 mm from one of the plate free edges (width) perpendicular to the measurement line.

The {211} diffraction plane was selected for the measurements as this is relatively insensitive to the inter-granular strains in ferritic materials such bright steel grade 080A15 [22].

The gauge volume (2 x 2 x 2 mm^3) for all the measurements was obtained by controlling, through slits, the incoming beam. Since the predicted stresses close to the plates' edges are negligible (See Figure 6-12 for the transverse stress component) and as no variation in the chemical composition along the measurement line was expected; far field orientation dependent lattice parameters (*i.e.* in transverse, longitudinal and normal directions) were used as reference measurements (*i.e.* stress free lattice parameter). A single peak fitting

was applied using the in-house software to determine the lattice parameters. The corresponding elastic strain is calculated using the Equation 2-6 in Chapter 2 (see below).

$$\varepsilon_{xx} = \frac{d_{xx} - d_{0xx}}{d_{0xx}}$$

where ε_{xx} is the strain in the xx direction, d_{xx} is the measured lattice parameter and d_{0xx} is the unstrained lattice parameter.

Finally the orthogonal components of residual stresses were calculated using the Hooke's Law for isotropic material (Equation 2-7 in literature review Chapter).

$$\sigma_{xx} = \frac{E}{(1+\nu)(1-2\nu)}[(1-\nu)\varepsilon_{xx} + \nu(\varepsilon_{yy} + \varepsilon_{zz})]$$

$$\sigma_{yy} = \frac{E}{(1+\nu)(1-2\nu)}[(1-\nu)\varepsilon_{yy} + \nu(\varepsilon_{xx} + \varepsilon_{zz})]$$

$$\sigma_{zz} = \frac{E}{(1+\nu)(1-2\nu)}[(1-\nu)\varepsilon_{zz} + \nu(\varepsilon_{xx} + \varepsilon_{yy})]$$

where σ_{xx} is the relevant stress direction (longitudinal, normal, transverse) and E (223.3 GPa) and ν (0.276) are the lattice plane specific Young's modulus and Poisson's ratio, respectively. These were calculated using open source DECcalc software [23] by applying the Kroner model [24]. The single crystal elastic constants c_{ij} were obtained from work published by Adams *et al.* [25].

Plate_0 and plate_3 residual stress measurement

Residual stress measurements for the longitudinal, transverse and normal components in the remaining two plates (plate_0 and plate_3) were conducted by the author on the

ENGIN-X beam-line at ISIS. In contrast to the previous neutron diffraction facilities used to support this thesis (NRC/CNBC, Canada and ANSTO, Australia), pulsed neutron beams with spectrum of wavelengths produced by a spallation process are used at ISIS. Hence, the time of flight (TOF) approach [22] is applied to calculate the lattice parameters.

The plates were carefully aligned using theodolites. To be consistent with the previous diffraction measurement carried out at ANSTO on plate_1 and plate_2, the same gauge volume (2 x 2 x 2) mm^3 and measurement points (45 points) with 5 mm interval were used for the present experiment. Furthermore, the far field orientation dependent lattice parameters (*i.e.* in transverse, longitudinal and normal directions) were used as a reference measurement (*i.e.* stress free lattice parameter). The Rietveld technique [26], using the in-house software (OpenGenie), was applied to fit an average lattice parameter to all the measured diffraction peaks.

The three orthogonal components of residual stresses in the plates were calculated using the same equations applied for the previous neutron diffraction (Eq. 2-6 and Eq. 2-7 for strain and stress calculation, respectively). In this case bulk elastic constants of 210.5 GPa and 0.3 for Young's modulus and Poisson's ratio, respectively were used.

Results

The orthogonal components of residual stresses along the measurement line for plate_0, plate_1, and plate_2 are plotted in Figure 6-16, Figure 6-17 and Figure 6-18, respectively.

As intended the distribution of the transverse component of residual stresses for the three plates with parallel heating zones shows a similar profile to the 'top hat' stress distribution used for the correlations development. For plate_0, the tensile region of the

transverse residual stresses is seen to increase with distance. From the picture of plate_0 in Figure 6-14-b, it can be seen that the width of one the two heating zones increases from the plate's left to its right side. This is probably associated with the direction of laser heating and that the steady state conditions were not reached during the welding process. Indeed an increase in tensile stress has been observed in predictions and measurements of residual stress in a single weld bead on plate benchmark sample [27].

The peak value of the transverse residual stresses in plate_1 (190 MPa) is approximately two-thirds of that observed in plate_0 (300 MPa), and plate_2 (100 MPa) is about one-third of plate_0. Maximum values of compressive stress of -270 MPa, -160 MPa and -70 MPa were found in plate_0, plate_1 and plate_2, respectively.

The longitudinal and normal components of residual stress in the three plates generally exhibit low magnitudes compared with the transverse stress component. The low magnitude of the normal stress component validates the plane stress conditions assumed during the plates design.

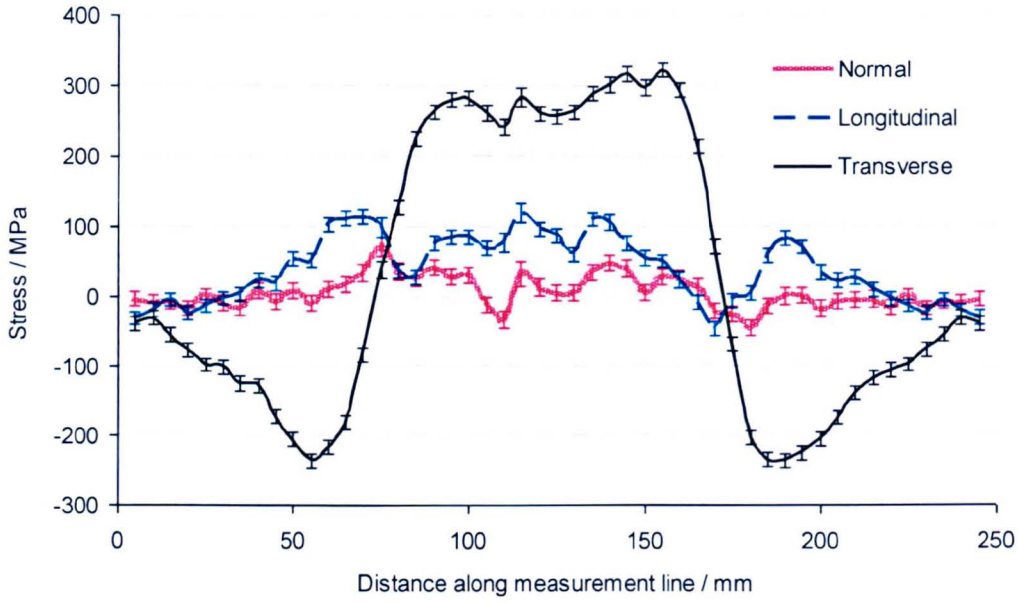

Figure 6-16: Variation in orthogonal components of residual stress measured by neutron diffraction along the measurement line at the mid-thickness of plate_0.

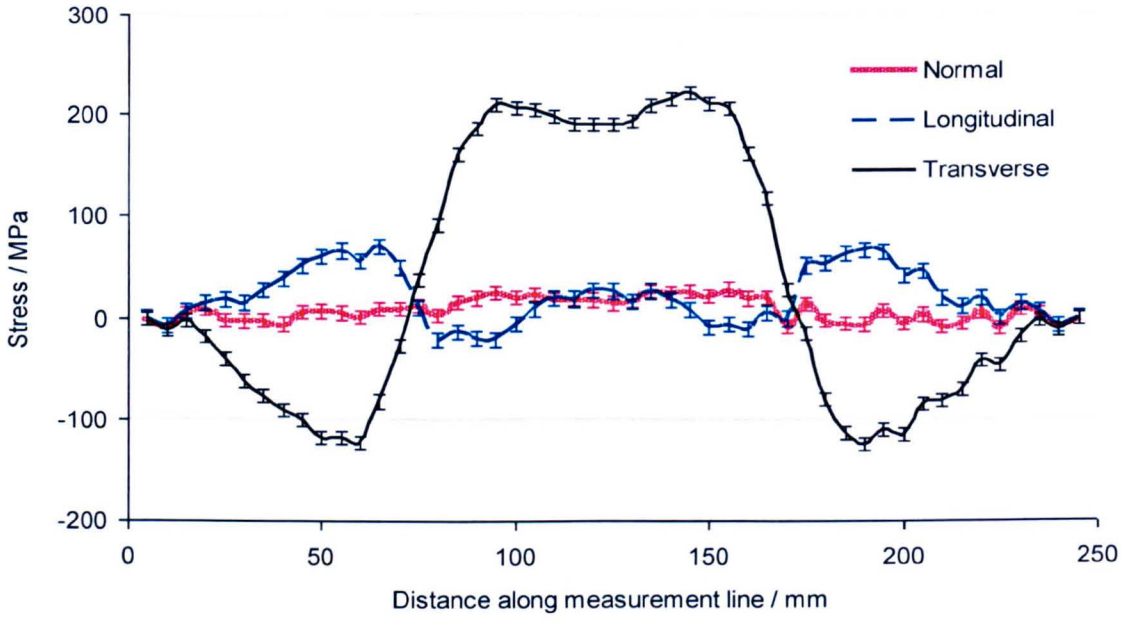

Figure 6-17: Variation in orthogonal components of residual stress measured by neutron diffraction along the measurement line at the mid-thickness of plate_1.

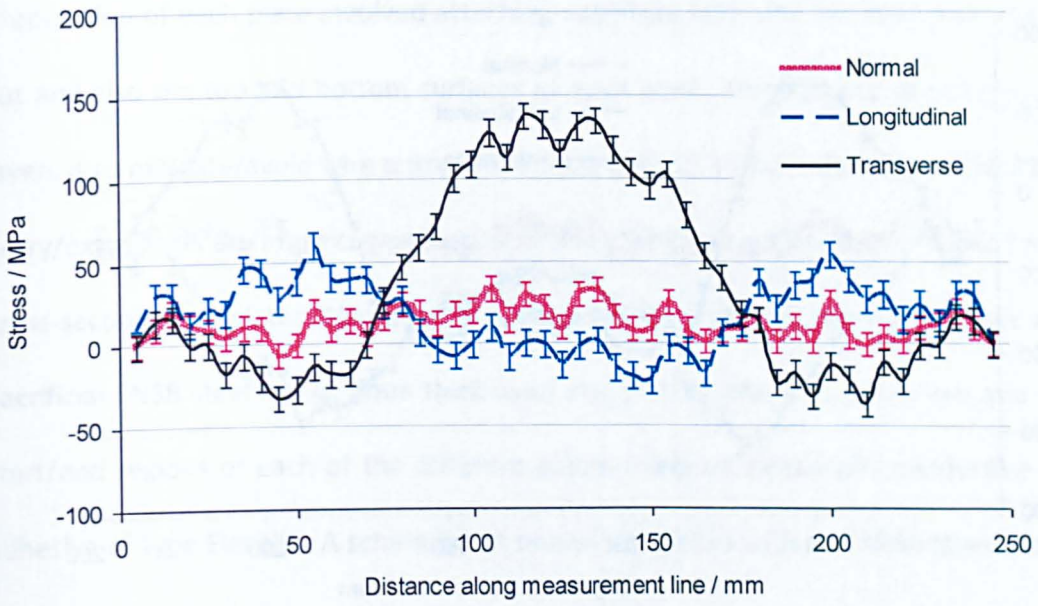

Figure 6-18: Variation in orthogonal components of residual stress measured by neutron diffraction along the measurement line at the mid-thickness of plate_2.

Figure 6-19 shows how the transverse, longitudinal and normal components of residual stresses vary along the measurement line in plate_3 (*i.e.* the plate with the inclined heating zones). The trend of the transverse residual stresses is approximately the opposite of the distribution of the transverse stress component measured in the plate_1 (See Figure 6-17). A maximum stress value of +/-160 MPa was measured for the tensile/compressive stresses. The profile of the longitudinal component of residual stresses exhibits a profile similar to a 'w-shape'. Only compressive stresses were measured for this stress component, with a maximum value of -300 MPa at 70 mm. The normal component of residual stress has negligible magnitude compared to the other components (between -40 MPa to 10 MPa), which confirms the plane stress conditions assumed.

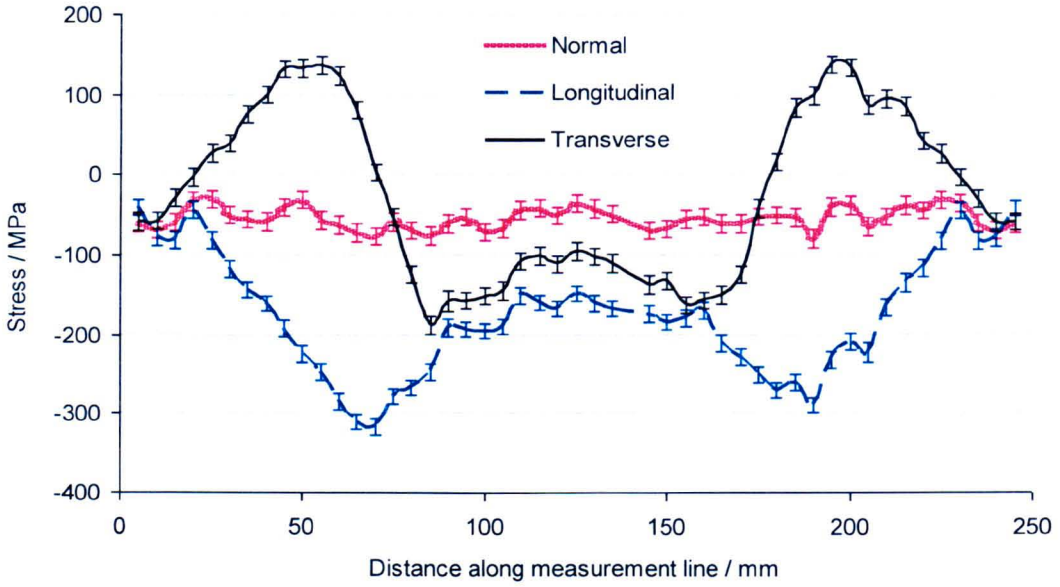

Figure 6-19: Variation in orthogonal components of residual stress measured by neutron diffraction along the measurement line at the mid-thickness of plate_3.

6.2.2. Residual stress measurement by the contour method

The transverse component of the residual stresses distribution in the four plates was measured using the contour method in order to access the influence of cutting plasticity and validate the correlations developed in Chapter 5. The theory and the technical aspects of the contour method have been covered in the literature review chapter (Chapter 2) and an application example (CT blank specimen) presented in Chapter 3. Therefore, only brief description will be given here about the experimental procedure and data analysis for the contour method.

Experimental procedure

The experimental procedure involves preparation of test component, cutting it and then measuring the normal deformation 'contour' of the cut surfaces.

Preparation of each plate involved attaching sacrificial layers to the start and end of the cut and also the top and bottom surfaces of each plate. The purpose of using sacrificial layers is to mitigate/avoid wire entry/exit effects and cut start/end artefacts [28,29]. Wire entry/exit effects are more concerning here since the measured contour results for a thin cross-section (the plates' thickness is 6 mm) can be strongly altered by edge effects. Sacrificial EN3B steel layers, 6mm thick were attached on the wire entry/exit and the cut start/end regions of each of the different plates using an electrically conductive epoxy-adhesive of type Elecolit. A schematic of one of the plates with sacrificial layers attached is shown in Figure 6-20.

Once the sacrificial layers were attached, each of the different plates was symmetrically finger clamped in the Agie Charmilles FI 440 CCS wire EDM workspace for the cutting process. A thin wire of 0.15 mm diameter with 'skim' cut setting parameters was used to conduct the plates' cutting. The plates were submerged into water in order to help with flushing away cutting debris. Figure 6-21 shows a photo of one of the plates (plate_3) with the sacrificial layers and clamped in wire EDM workspace.

Following cutting of the plates, the sacrificial layers were carefully removed prior to measuring the distortion of the surfaces. A Mitutoyo Crysta Plus 574 CMM equipped with a 3 mm diameter Renishaw PH10M touch probe was used to measure the deformation of the cut surfaces. A measurement density of 4 points/mm (*i.e.* 0.25 mm measurement spacing) was chosen in both thickness and length directions.

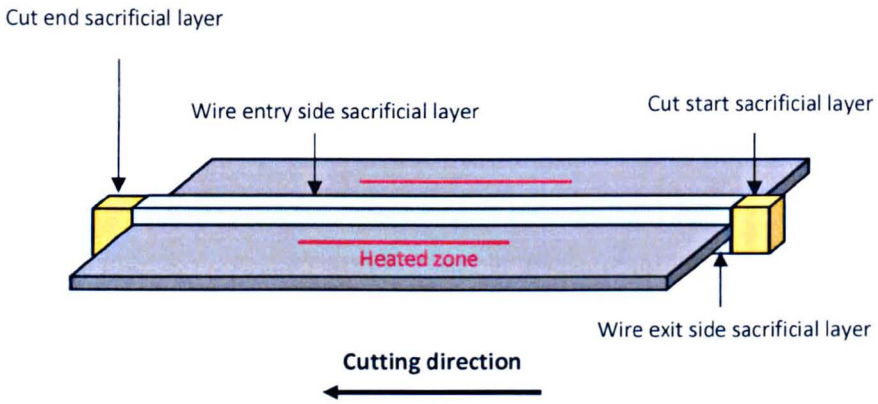

Figure 6-20: Schematic of one the plates with parallel heating zones showing the sacrificial layers attached.

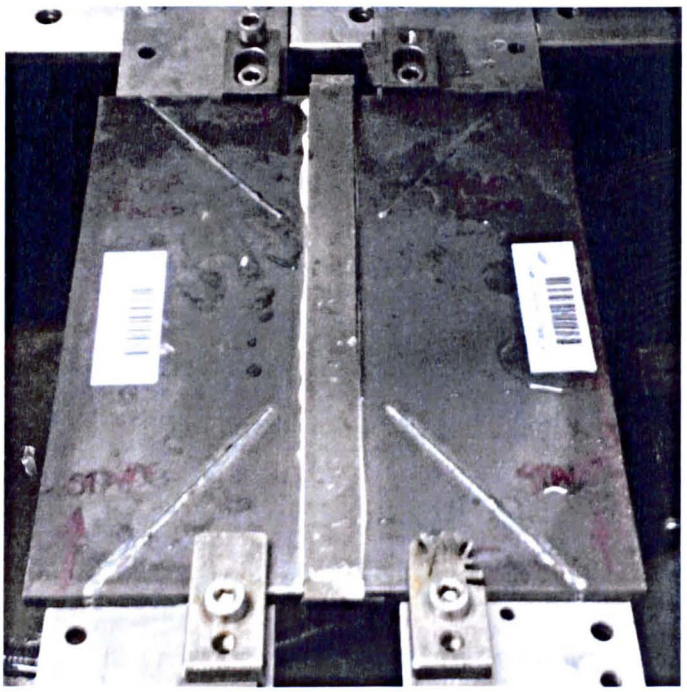

Figure 6-21: Photo showing plate_3 with sacrificial layers, 'finger' clamped in the wire EDM workspace.

Data analysis and residual stress back-calculation

On completion of the contour measurement of the cut surfaces for the different plates, a conventional spline fitting approach was applied for the data analysis (see Chapter 2). This consisted of averaging the data of the two cut surfaces, removing noise and outliers and fitting a cubic spline to the cleaned data [29-31].

Figure 6-22 shows the averaged deformation data for the four plates. Although some cutting artefacts occurred during plate_2 cutting, no major cleaning had to be performed on the averaged data. The cutting artefacts observed in the plate_2 raw data were anti-symmetric; therefore, they were predominantly cancelled out by the averaging process.

The shapes of the cut faces' deformation for plate_1, plate_2 and plate_3 are approximately symmetric about their mid-length plane. This is consistent with the profile of the corresponding relaxed transverse residual stress measured by neutron diffraction and predicted by the finite element method. In contrast, the measured profile of plate_0 shows some asymmetry suggesting that there may be significant plasticity effects affecting the results.

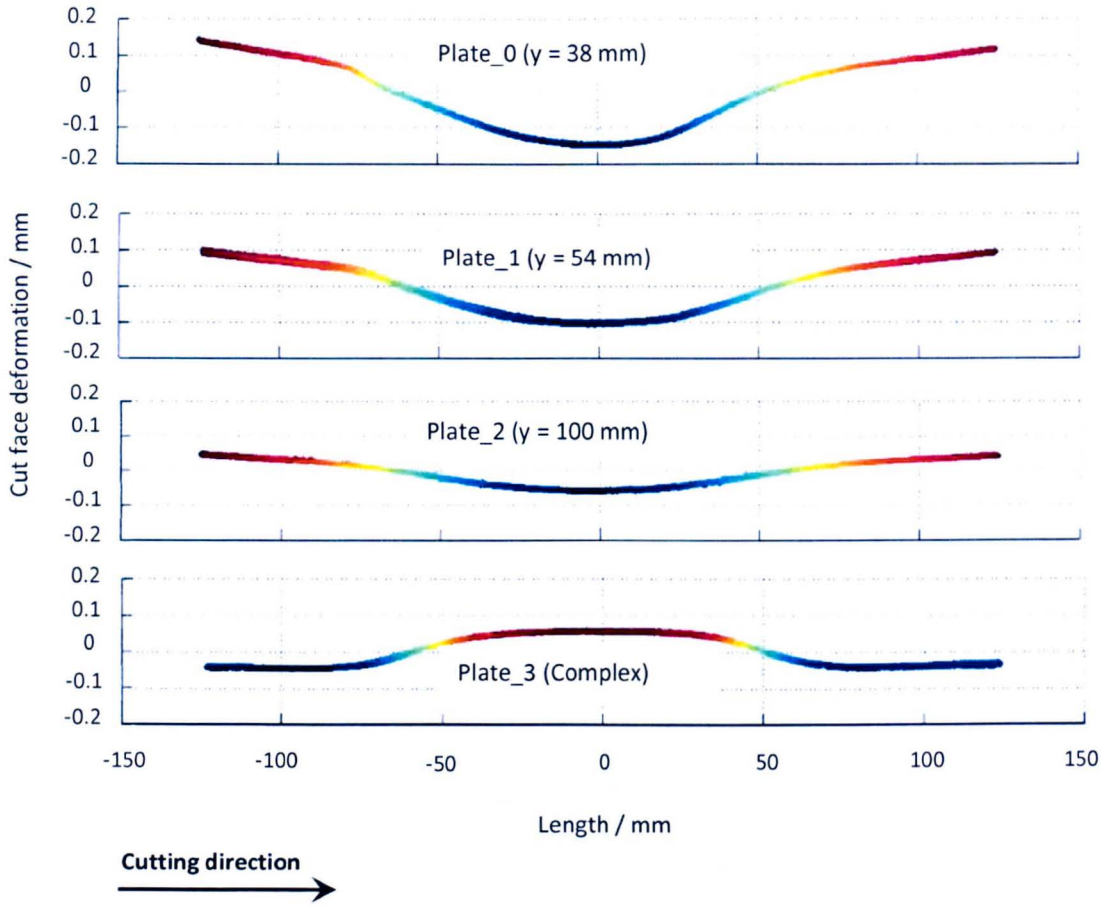

Figure 6-22: Averaged deformations of the cut faces measured by CMM for the different laser heated plates.

To back calculate the transverse component of residual stresses, linear FE analysis was carried out for the different plates. The 3D FE model of half of each plate was generated based on their corresponding outline measured using the CMM. A non-regular mesh, which consists of linear hexahedral elements with reduced integration (C3D8R), was used. The mesh elements in the vicinity of the cut surface were finer and progressively coarsened towards the free face parallel to the cut surface (See Figure 6-23).

The material (bright steel) elastic properties (i.e. Young's modulus of 210.5 GPa and Poisson's ratio of 0.3) were defined.

Best spline fit interpolation functions to the deformation data were derived using the published criteria of Prime [32], that is a series of finite element simulations for each plate was performed by applying the opposite of the fitted data to the cut face to calculate the residual stresses. An optimum spline fit was chosen corresponding to the minimum average stress error calculated for sequentially refined fitting functions (knot spacings). The average stress error is calculated using based on the standard deviation approach (see Equation 6-1).

$$\overline{\partial\sigma}(j)=\frac{1}{\sqrt{n}}\sqrt{\sum_{i=1}^{n}\left[\frac{1}{\sqrt{2}}|\sigma(i,j)-\sigma(i,j-1)|\right]^2} \qquad \textbf{Eq. 6-1}$$

where $\sigma(i,j)$ is the stress at node i for the smoothing spline solution designated j, j-1 refers to the previous, coarser smoothing-spline solution, n is the number of FE nodes on the cut surface in the model.

From Figure 6-24 it can be seen that overall 4×4 mm and 7×7 mm knot spacings (in the thickness and length directions) behave better than the other splines. However line plot results along the measurement line for plate_0 (Figure 5-25) shows that 4x4 knot spacing over-fits the raw measurements. Therefore, the 7×7 mm knot spacing is used for fitting the raw measurements of the four plates.

To provide a more meaningful comparison of measured localised transverse stresses, the contour method results are averaged over the gauge volume used for the neutron diffraction measurements (2×2×2) mm^3. This consisted of extracting the contour method

residual stress from an area representative of the neutron diffraction gauge volume on the cut face and taking an average for that region to produce the final measurement. The approach was developed and written in a MatLab script by Turski et *al.* [33,34]. For a (2×2×2) mm^3 gauge volume, the contour method results were averaged over an area of (1.4×1.4) mm^2.

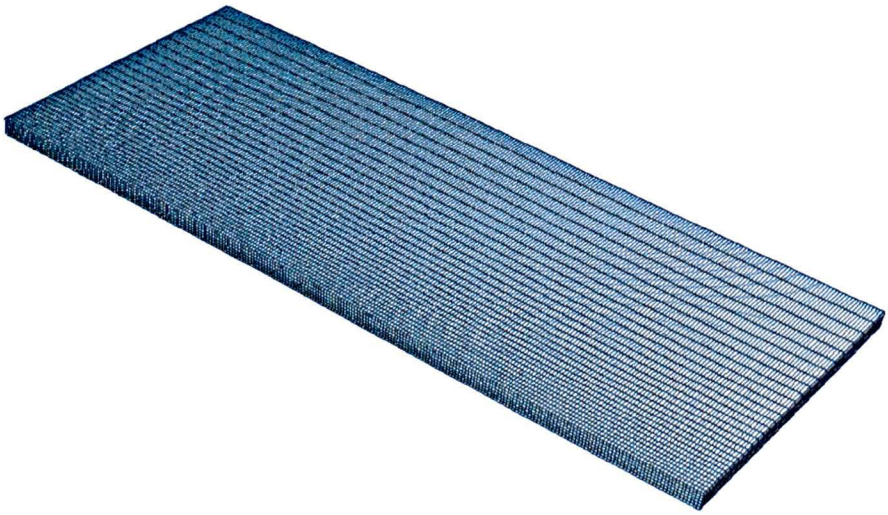

Figure 6-23: Illustration of the mesh of the 3D finite element model used for the contour method stress back-calculation.

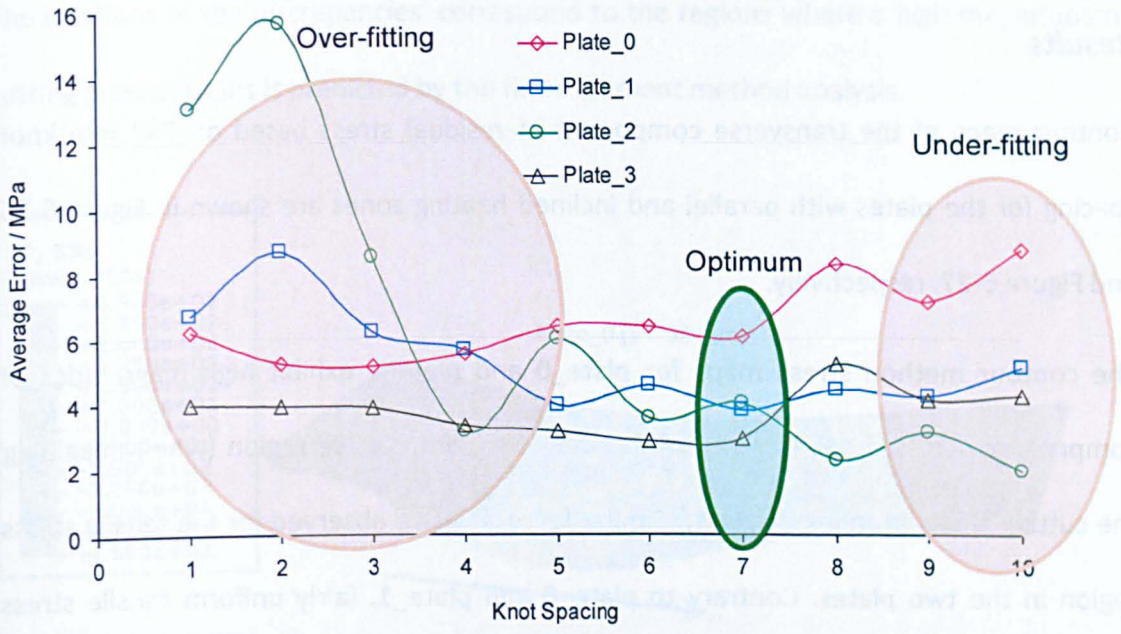

Figure 6-24: Average stress error as function of the knot spacing for the different plates.

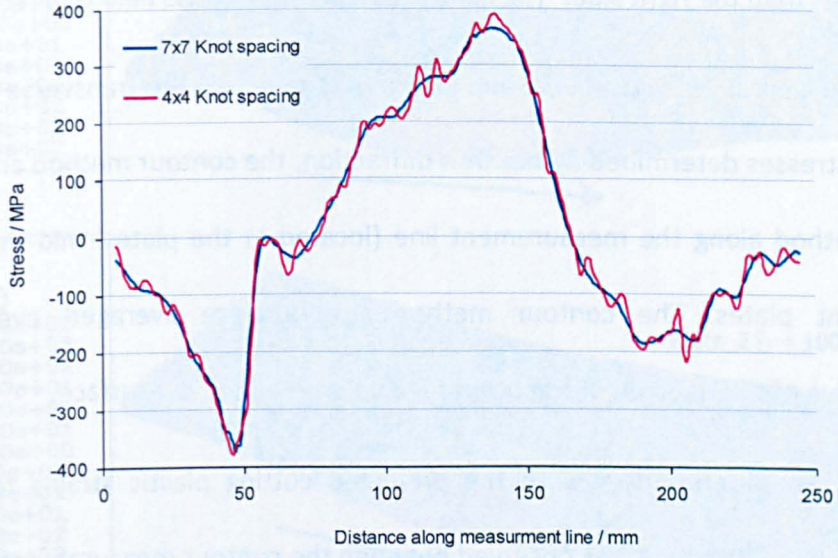

Figure 6-25: Comparison of plate_0 transverse residual stress distribution along the measurement line for 4×4 mm and 7×7 mm knot spacing.

Results

Contour maps of the transverse component of residual stress based on 7×7 mm knot spacing for the plates with parallel and inclined heating zones are shown in Figure 6-26 and Figure 6-27, respectively.

The contour method stress maps for plate_0 and plate_1 exhibit high magnitudes of compressive stresses towards the end of the first compressive region (when imagining the cutting starts from left to right). Similar features were observed for the tensile stress region in the two plates. Contrary to plate_0 and plate_1, fairly uniform tensile stress region balanced by two compressive stress fields are observed for plate_2. For plate_3 (Figure 6-27), the magnitude of the tensile stresses observed in the left side of the plate is slightly higher than the right side. The central compressive stress field is fairly uniform.

Figure 6-28, Figure 6-29, Figure 6-30 and Figure 6-31 compare the transverse component of residual stresses determined by neutron diffraction, the contour method and the finite element method along the measurement line (located at the plates' mid-thickness) for the different plates. The contour method results were averaged over an area representative of the neutron diffraction gauge volume on the cut surface.

The results are superimposed with the predicted cutting plastic strains for a better explanation of the discrepancies observed between the contour measurements and those obtained by neutron diffraction and finite element method. For all four plates, a very good correlation between the neutron diffraction and the FE results is obtained.

The distribution of the transverse residual stresses measured by the contour method in plate_0 shows some differences compared to the neutron diffraction and the FE results.

The locations of the discrepancies' correspond to the regions where a high magnitude of cutting plastic strains is predicted by the finite element method analysis.

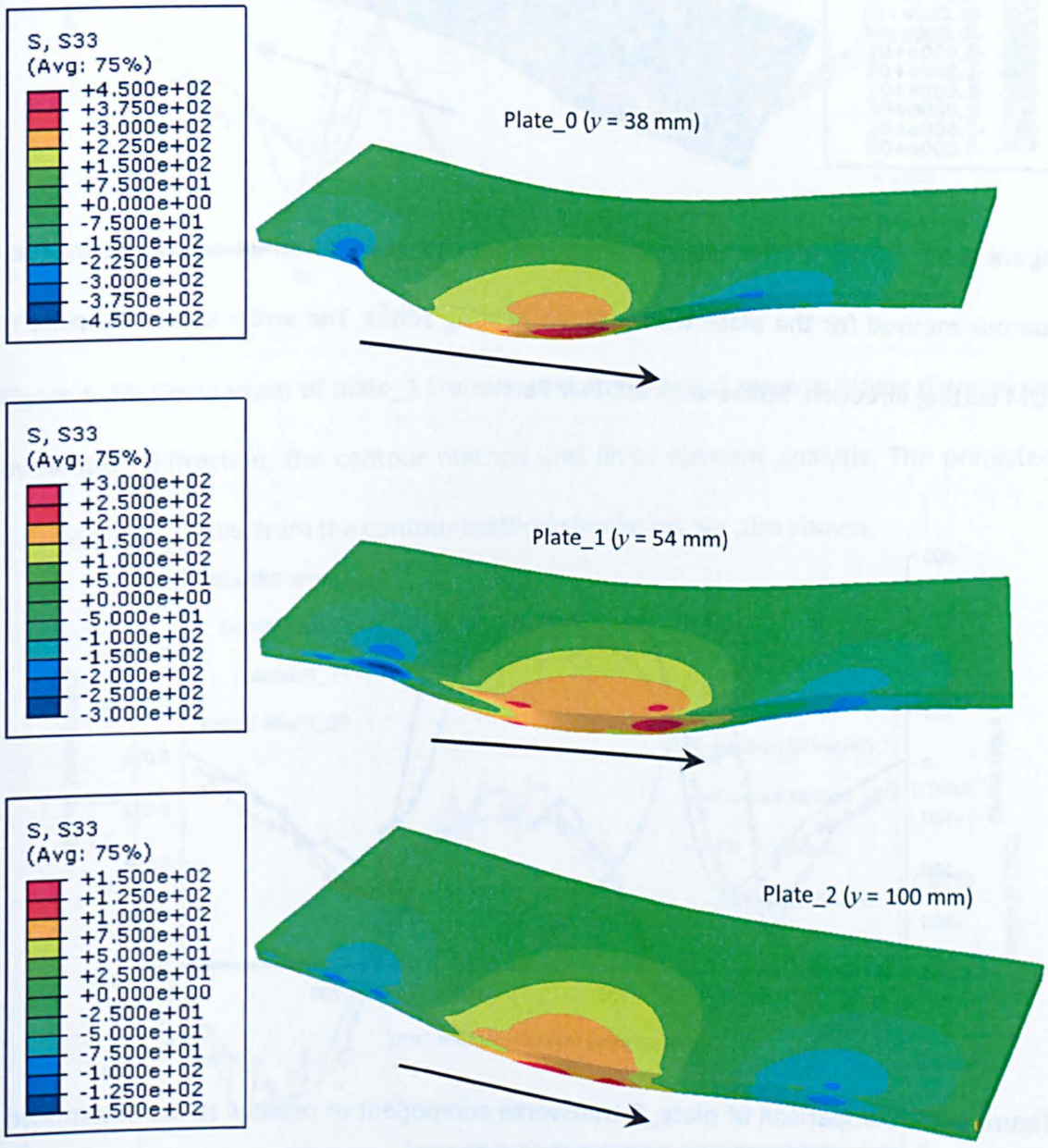

Figure 6-26: Map of the transverse component of residual stress measured by contour method for the plates with parallel heating zones. The arrows show the plates' EDM cutting directions. Stress units are in MPa.

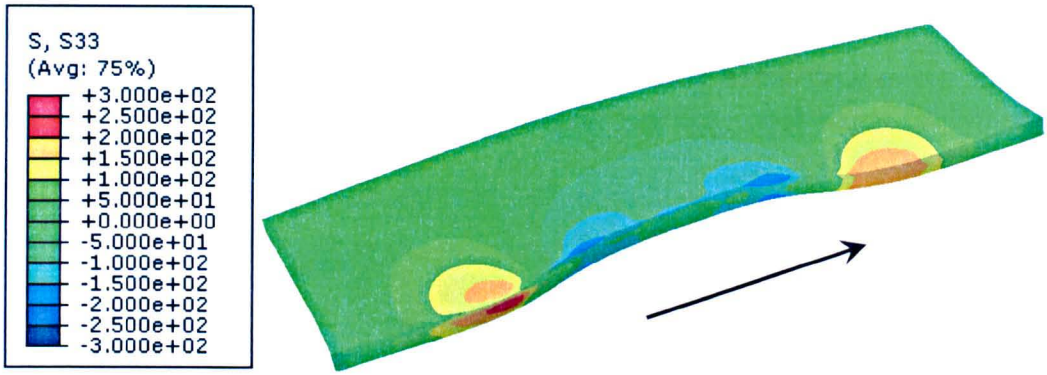

Figure 6-27: Map of the transverse component of residual stress measured by the contour method for the plate with inclined heating zones. The arrow shows the plate's EDM cutting direction. Stress units are in MPa.

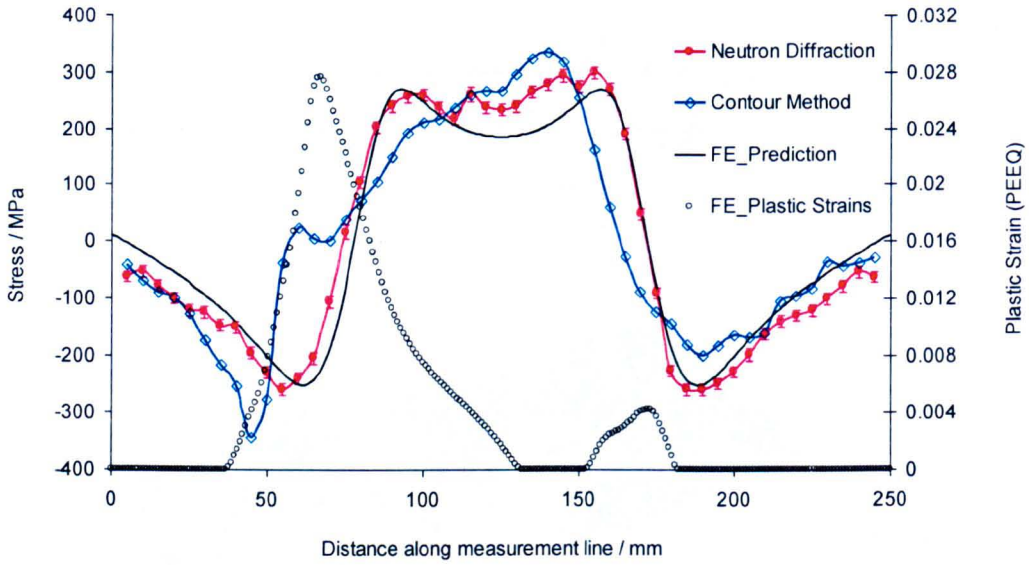

Figure 6-28: Comparison of plate_0 transverse component of residual stress determined by neutron diffraction, the contour method and finite element analysis. The predicted cutting plastic strains from the contour method simulation are also shown.

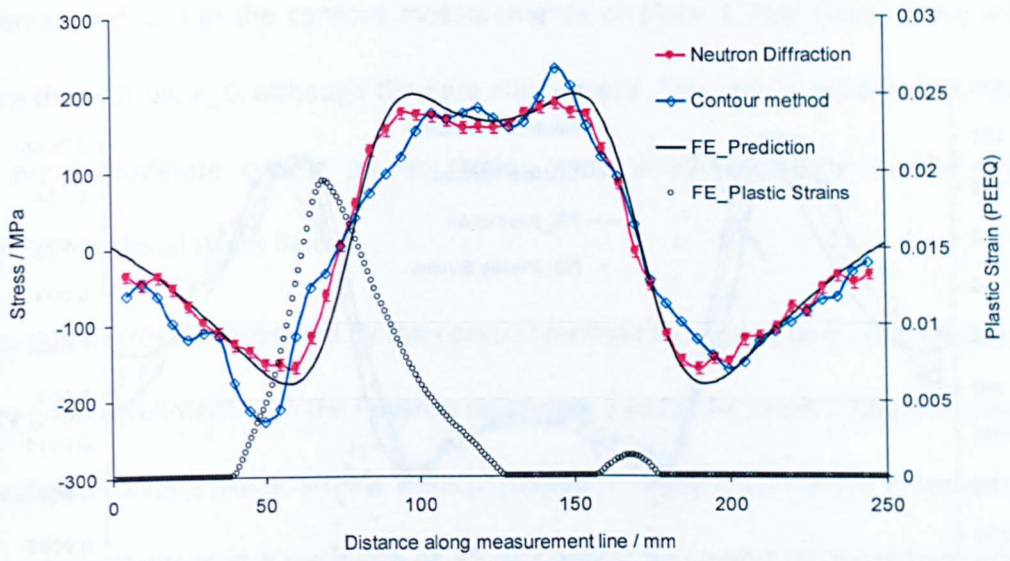

Figure 6-29: Comparison of plate_1 transverse component of residual stress determined by neutron diffraction, the contour method and finite element analysis. The predicted cutting plastic strains from the contour method simulation are also shown.

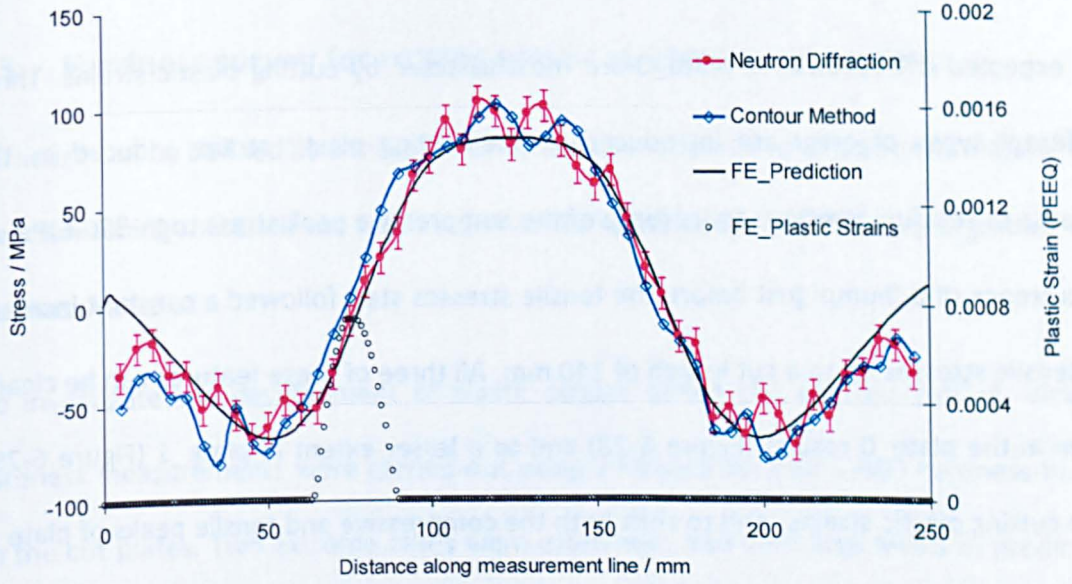

Figure 6-30: Comparison of plate_2 transverse component of residual stress determined by neutron diffraction, the contour method and finite element analysis. The predicted cutting plastic strains from the contour method simulation are also shown.

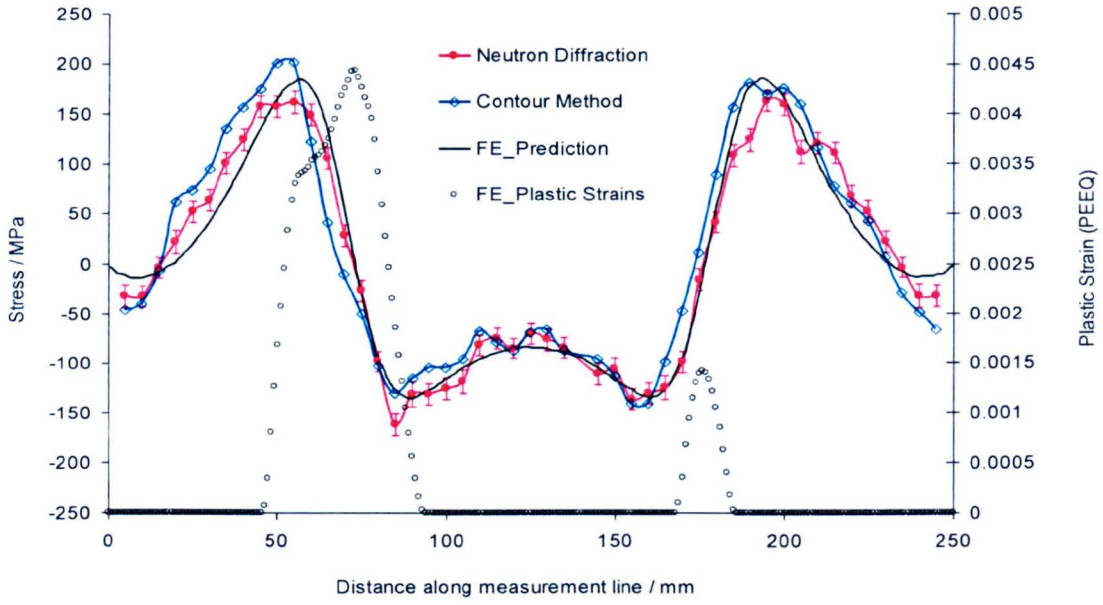

Figure 6-31: Comparison of plate_3 transverse component of residual stress determined by neutron diffraction, the contour method and finite element analysis. The predicted cutting plastic strains from the contour method simulation are also shown.

As expected the results for plate_0 are most affected by cutting plastic strains. Three different types of error are introduced by the cutting plastic strains induced by the release of residual stresses: an increase of the compressive peak stress to ~ -350 MPa, an occurrence of a 'hump' just before the tensile stresses start followed a constant increase of tensile stresses up to a cut length of 140 mm. All three of these features can be clearly seen in the plate_0 results (Figure 6-28) and to a lesser extent in plate_1 (Figure 6-29). The cutting plastic strains tend to shift both the compressive and tensile peaks of plate_0 in the direction opposite to that of the cut.

Similar stress profiles to the one measured in plate_0 have been observed in previous residual stress measurement by contour method and were suspected to be caused by stress redistribution and cutting plastic strains [27,33].

The errors induced in the contour measurements of plate_1 (see Figure 6-29) are less severe than for plate_0, although they are still present. This can be explained by the fact that more moderate cutting plastic strains were predicted owing to the reduced magnitude residual stress field.

The residual stresses measured by the contour method in plate_2 (see Figure 6-30) are in a very good agreement with the neutron diffraction and the FE results. This was expected, as negligible cutting plastic strains were predicted. The slight difference observed in the compressive stresses at a cut depth of 35 mm, might be caused by the cutting artefacts already mentioned.

Overall, the residual stresses measured by the contour method in plate_3 are in very good agreement with neutron diffraction and FE predictions (Figure 6-31). This can be explained by the fact that low plastic strains were predicted by FE for plate_3.

6.3. Hardness survey for cutting plastic strains measurement

Hardness can be defined as a measure of materials resistance to plastic deformation. For work hardening material, the more the material is plastically deformed, the greater the hardness value is.

To investigate the development of plastic strains during the contour cutting, Vickers hardness measurements were carried out using a Struers Duramin-A300 hardness tester on the cut plates. Two extreme cases were examined: that with high levels of predicted cutting plastic strains (plate_0) and the other with no predicted cutting plastic strains (plate_2). Because of the limitations of positioning the sample during hardness testing, (width of the cut sample (100 mm) greater than the available space where the cut sample

needed to be placed for the hardness test) the measurements were conducted on the side face of each plate along a line located at 1.5 mm below the cut plane.

The distance between the measurement line and the plate edge and the spacing between the different points (1 mm) were chosen according to the ASTM_E384-11 standard [35]. The first and last measurement points were located at 5 mm from the ends of half-cut plate giving a total of 240 measurement points. Figure 6-32 shows a schematic sketch of the cut plate with the measurement points' locations.

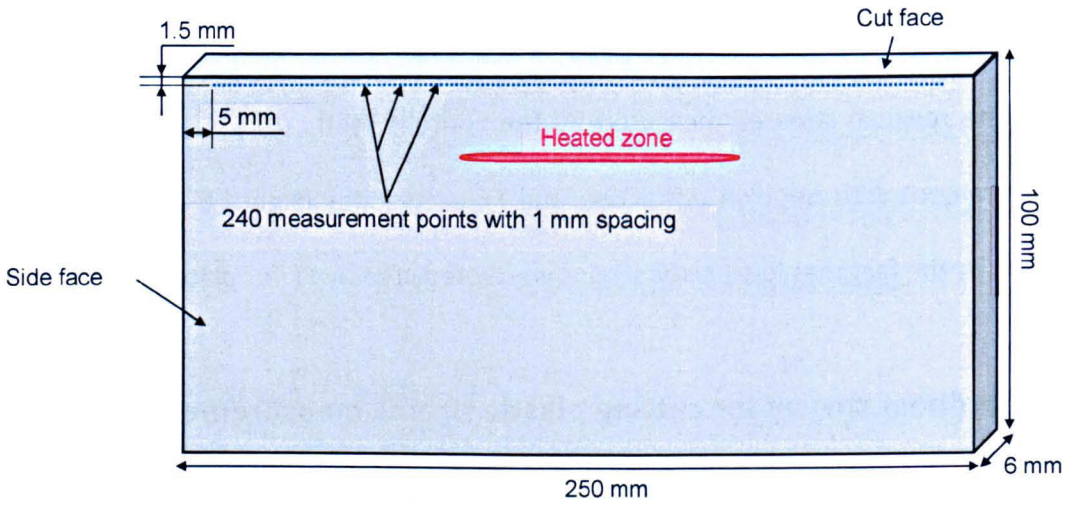

Figure 6-32: Schematic of a cut plate showing the hardness measurement points on the side face.

Before hardness testing, the surfaces of the two cut plates were carefully prepared. Each plate was hand-ground using a Struers Transpol-2 machine with different grades of silicon carbide paper (60, 240, 500, 800, 1200 and 2500 grit). Following grinding, the surfaces were hand-polished with 6 micron diamond abrasive and Struers red lubricants until visible grinding marks were removed. On completion of surface preparation, hardness measurements were conducted using a 5 Kgf indentation load.

Figure 6-33 and Figure 6-34 show the variation in measured Vickers hardness along the measurement line for plate_0 and plate_2, respectively. A moving average approach with 10 points averaged was used to fit a trend curve to the hardness data. The Figures also show the corresponding distributions of predicted cutting plastic strains along the measurement line.

Although there is high level of scatter in hardness results, they do correlate fairly well with the FE prediction of plastic strain (see Figure 6-33). It is important to note that the range of the hardness values across the measurement line is only 15 HV5. This made it difficult to observe significant changes in hardness across the measurement line. However, despite these challenges, a moving average of the hardness measurements (blue line in Figure 6-33) does reveal two fairly distinct peaks broadly centred on the peaks in predicted cutting plastic strain. Therefore, although this data is clearly not ideal it does suggest that the predicted cutting plastic strains are reasonable.

From Figure 6-34 it can be seen that the measured hardness results along the line of interest are fairly constant (~ 195 HV5) for plate_2. Since no cutting plastic strains were predicted in this plate, the hardness results can be considered to be in good agreement with the FE predictions.

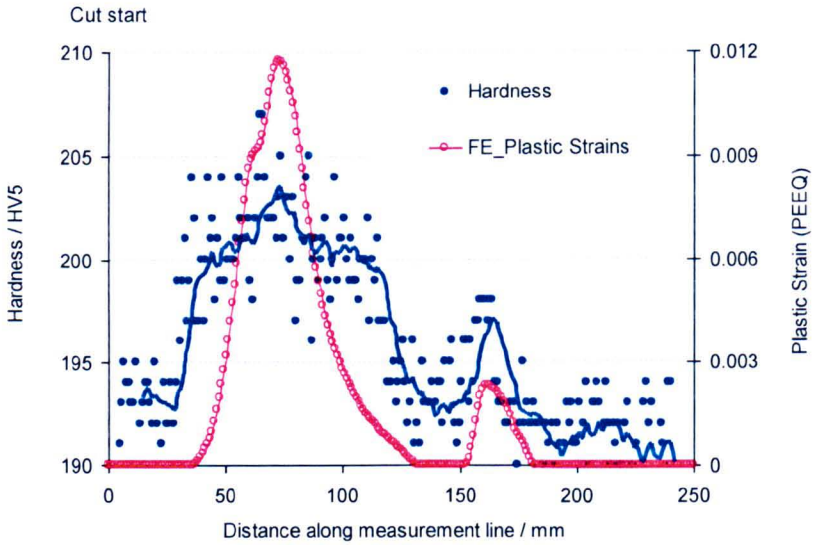

Figure 6-33: Comparison of predicted cutting plastic strains and the distribution of measured hardness along the measurement line at 1.5 mm from the cut face of plate_0.

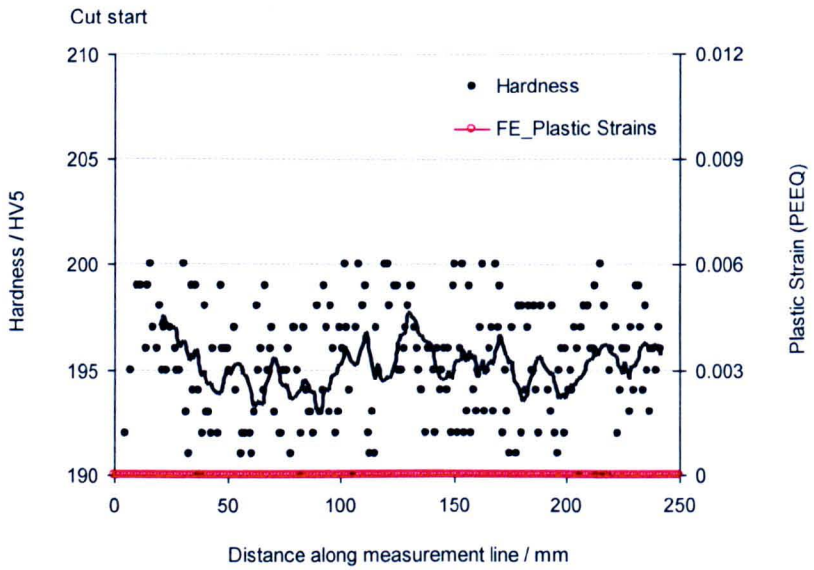

Figure 6-34: Comparison of predicted cutting plastic strains and the distribution of measured hardness along the measurement line at 1.5 mm from the cut face of plate_2.

6.4. Validation of the correlations

The correlations for plasticity-induced errors estimation were validated using two independent approaches. First, the transverse residual stresses measured by neutron diffraction for each of the four plates was used as the initial stress state to determine the normalised average PZS and then this was used to estimate the plasticity-induced errors from the FE-based correlations. Second, the neutron diffraction results are compared to contour measurements to determine the average stress error for each plate. Finally, the average errors obtained from the two approaches are compared for validation.

6.4.1. Estimated average stress error

The average stress error for each plate was estimated using the correlations developed in Chapter 5. Residual stress intensity factors were calculated using 2D linear finite element analysis within ABAQUS. The distributions of the transverse component of residual stress measured by neutron diffraction in the different plates were assumed as initial loading conditions for this purpose.

As described previously in section 6-1-3, symmetry boundary conditions were defined along the measurement line allowing one half of each plate to be modelled. The plates were meshed with first order plane stress elements. A fine mesh was chosen in the vicinity of the measurement line (0.25 mm) and a coarse mesh was used for the rest of the model giving a total of 66000 elements. The 'finger' clamping (used during the plates cutting) was modelled in FE by a free restraint.

As in the previous simulations for determining the stress intensity factor distributions (section 4-3-2), the wire EDM cut was treated as an incremental sharp crack. For each cut

portion, the corresponding residual stress field was applied as an internal load and the resulting cut tip stress intensity factor extracted from the FE model. For a 5 mm cut increment, the plates cutting process was completed in 50 steps, resulting in 50 stress intensity factor data.

Figure 6-35 shows the variation in predicted stress intensity factor with cut length for the four plates. The trends of the residual SIF distributions for the plates with parallel heating zones (plate_0, plate_1 and plate_2) are very similar to each other. The maximum negative value of the residual SIF for the start end compressive stress region for each of the three plates occurs at approximately the same cut depth (70 mm). The peak residual SIF in the tensile stress region occurs at a cut depth of 170 mm for the three plates with parallel heating zones.

As expected, the residual SIF distribution with cut length for plate_3 is different from the SIF profiles for the three plates with parallel heating zones. However the peak values of residual SIF in the compressive and tensile stress regions occur approximately at the same cut depths, although of opposite sign.

In the next step, the residual SIF data for the different plates are used to investigate the predominant stress state in the four laser heated plates. Although the four plates were designed to approach plane stress conditions, the inequality (Equation 5-4) in section 5-13 indicates that plane strain conditions prevail in the plate_2 (plate with low magnitude of residual stress).

The normalised average plastic zone size for the four plates was analytically calculated by applying Equation 5-5. The equation is given below.

$$\overline{PZS}_{Norm} = \frac{1}{p\pi\sqrt{Lt}}\sum_{i}\left(\frac{K_I^i}{\sigma_0}\right)^2$$

where K_I^i is the residual stress intensity factor, σ_0 is the material yield stress (550 MPa) and $p=1$ (plane stress), L is the length of cut (250 mm), t is the side of the area over which the neutron diffraction residual stress (used to calculate the SIF) were averaged (1.4 mm).

Table 6-3 summarises the normalised average plastic zone size values for the different plates. As expected, the highest normalised average PZS (0.21) is obtained with plate_0. A moderate normalised average PZS is obtained for plate_1 (0.1), and plate_2 and plate_3 have normalised average PZS values of 0.01 and 0.05, respectively.

Following the normalised average plastic zone size determination, the RMS average errors were estimated from Figure 5-26, respectively (see Table 6-3). As expected the highest stress error of ~17% was predicted for plate_0, while negligible stress error (1 %) was predicted for plate_2.

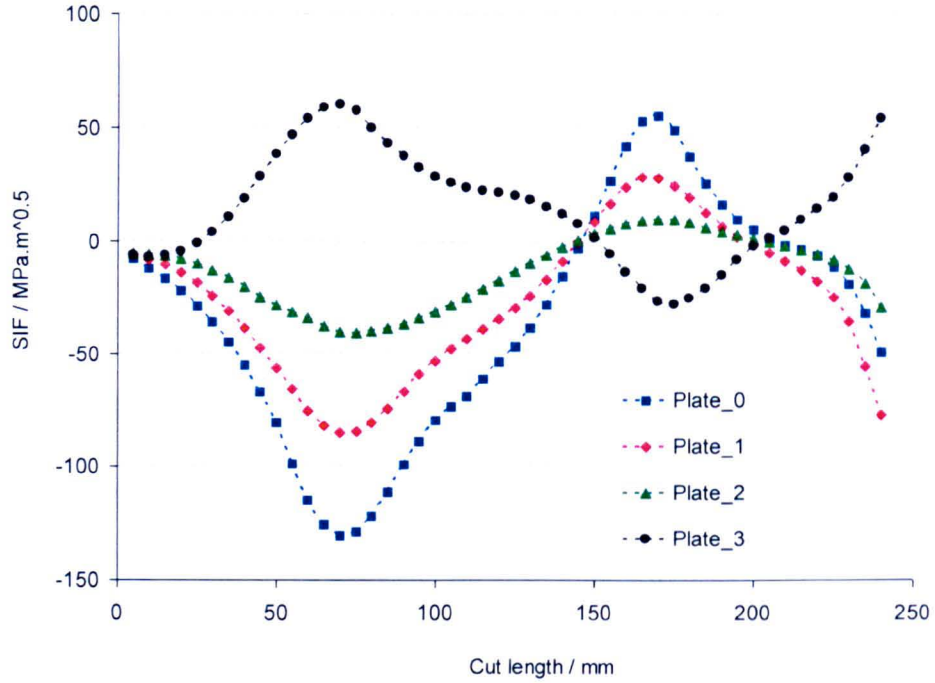

Figure 6-35: Variation of the residual stress intensity factor calculated with cut length in the four plates based on transverse residual stresses measured by neutron diffraction.

Table 6-3: Calculated normalised average plastic zone size (PZS) and corresponding RMS average error estimated from the correlations of Chapter 5.

Plate	0	1	2	3
Normalised Average PZS	0.21	0.1	0.01	0.05
RMS Average Error (%)	17	8.5	1	4.5

To take into account the effect of the cut width, first, the RMS average error values in Table 6-3 were used to determine, from Figure 5-27 and Figure 5-32, the corresponding normalised average plastic zone depth for plane stress and plane strain conditions, respectively (see Table 6-4). Then, the cut width was determined, normalised (Equation 5-6) and subtracted from the normalised average plastic zone depth in Table 6-4. Note that

'finger' clamps were used for the plates' cutting process. Therefore, $1/2W$ in Equation 5-6 is one-half of the laser heated plate's width (100 mm) (see section 5-6-2).

The cut width was approximated to be about 110 % of the wire diameter used for the contour cutting [36]. For the 150 µm wire size used, a normalised cut width of ~0.01 was obtained and subtracted from the normalised average PZD (Table 6-5). The corresponding RMS average errors were estimated using Figure 5-27 for plate_0, plate_1 and plate_3 and Figure 5-32 for plate_2. Finally Figure 5-17 of the set of correlations was used to convert the obtained RMS error value into absolute average error for each plate (see Table 6-5).

Table 6-4: Average plastic zone depth estimated from correlations of Chapter 5.

Plate	0	1	2	3
Normalised Average PZD	0.30	0.14	0.03	0.07

Table 6-5: Corrected normalised average PZD and corresponding RMS and absolute error for the different plates.

Plate	0	1	2	3
Corrected Normalised Average PZD	0.29	0.13	0.02	0.06
RMS Average Error (%)	16	7.8	0.7	3.8
Absolute Average Error (%)	11	4.9	0.4	2.2

6.4.2. Measured average stress error

Measured average stress errors were determined by comparing the contour method results with those obtained by neutron diffraction for each validation plate. The stress

errors between the two sets of results were calculated by applying the equations used in Chapter 5, Equation 5-1 for the RMS average error and Equation 5-2 for the absolute average error.

Table 6-6 shows the calculated average stress error found in the contour method measurements for the different plates assuming the neutron diffraction results represented an accurate characterisation of the real residual stress profile present. As for the previous results estimated using the correlations, the highest average stress error is induced in the plate_0, while negligible average stress error is obtained for plate_2.

Table 6-6: Measured stress error determined by comparing the contour method and neutron diffraction transverse residual stress profile for four plates.

Plate	0	1	2	3
RMS Average Error (%)	17	6	2.5	5
Absolute Average Error (%)	12	5	2	4

6.4.3. Comparison of the stress error obtained from the two approaches

Figure 6-34 compares the average stress error determined from the FE based correlations with that from comparing contour method measurement with neutron diffraction measurement for each of the four designs of laser heated plates.

The comparisons are separately made for the RMS average error (Figure 6-36–a) and absolute average error (Figure 6-36 –b).

It can be seen that, overall, the average stress errors correlate well with each other for the four plates, especially for the plates with a significant amount of plasticity-induced stress errors (plate_0 and plate_1) .

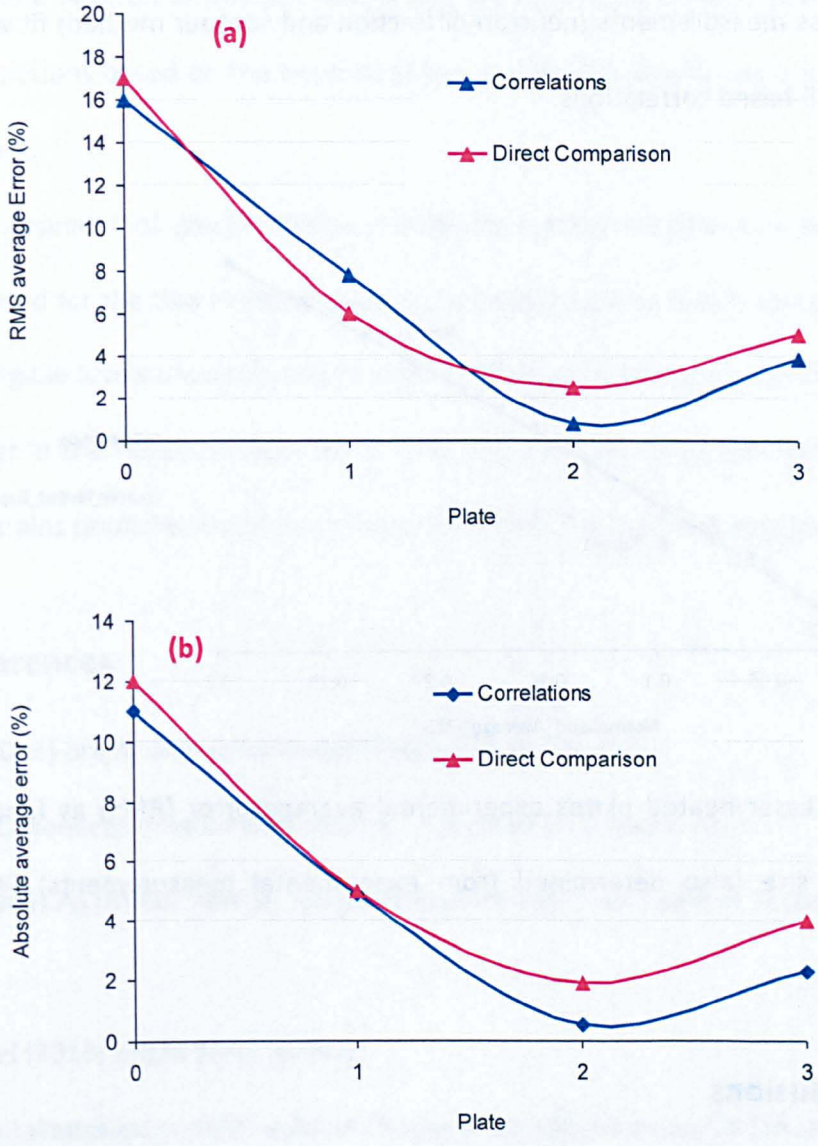

Figure 6-36: Comparison of the average stress errors determined from the two different approaches (correlations and direct comparison) for the laser heated plates.

Another approach of investigating the validity of the correlations consists of placing the pair of coordinates (normalised average plastic zone size, RMS average error) for each of the four laser heated plates in Figure 5-26. The normalised plastic zone sizes and the RMS average error were both calculated from the neutron diffraction and contour method measurements. From Figure 6-37 it can be noticed that the results obtained from the

residual stress measurements (neutron diffraction and contour method) fit well in Figure 5-26 of the FE-based correlations.

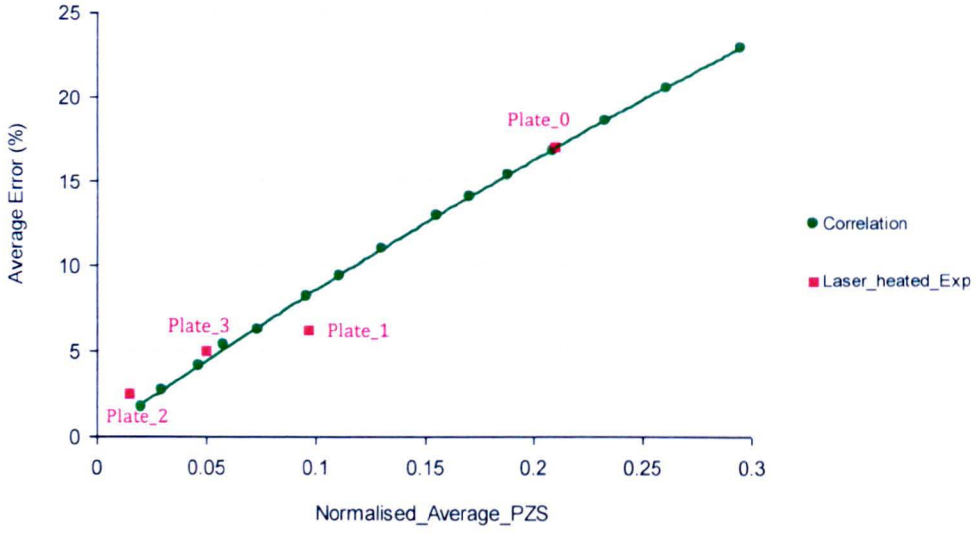

Figure 6-37: Laser heated plates experimental average error (RMS) as function of the plastic zone size (also determined from experimental measurements) fitted in the correlations.

6.5. Conclusions

1. The finite element method was used to design test specimens for validating plasticity-error estimation correlations for contour measurements. The test specimens use laser heating/welding in a unique way to introduce controlled distributions of residual stress of varying magnitude such that different levels of plasticity error (high, moderate and negligible) would be introduced in contour method measurements.
2. The residual stresses in the test specimens were measured using neutron diffraction and the contour method.
3. Validation of the plasticity induced stress error correlations' has been achieved by comparing the average stress errors determined from the differences between the

contour and neutron diffraction results and the estimated average stress error from the correlations based on the neutron stress profile. The results were in a very good agreement.

4. The development of plastic strains during the cutting process was experimentally investigated for the two extreme cases by hardness survey: that is samples with high and negligible levels of cutting plastic strains. Although there was a significant amount of scatter in the hardness data, the results did correlate fairly well with the cutting plastic strains predicted by finite element simulation for both test specimens.

6.6. References

1. Acenta (2013) Bright drawn/machined 080A15 steel [Online]. http://acentasteel.com/ms-bd-flat-080a15p. Accessed 20 January 2013

2. ASTM (2006) ASTM E8/E8M-1- Standard Test Methods for Tension Testing of Metallic Materials.

3. TATA Steel (2013) Bright Steel [Online]. http://www.tatasteelnz.com/downloads/Bright_XCQ.pdf. Accessed 19 January 2013

4. IMCE (2013) RFDA basic [Online]. http://www.imce.net/rfda-mf-basic. Accessed 19 January 2013

5. Blondeau R (2008) Metallurgy and Mechanics of Welding. Wiley, London, UK

6. W. Suder, S. Ganguly, S. Williams, A. M. Paradowska, Colegrove P (2011) Comparison of joining efficiency and residual stresses in laser and laser hybrid welding. Science and Technology of Welding & Joining 16 (3):244-248

7. Assuncao E, Ganguly S, Yapp D, Williams S, Paradowska A (2010) Characterisation of residual stress state in laser welded low carbon mild steel plates produced in keyhole and conduction mode. Science and Technology of Welding and Joining 16 (3):239-243

8. Dowden J, Kapadia P (1996) The penetration depth in keyhole welding with pseudo-continuous Nd-YAG and CO lasers investigated mathematically. Applied Surface Science 106 (0):235-239

9. Epilog Laser (2013) Technical Library: YAG vs. CO2 Lasers [Online]. http://www.epiloglaser.com/tl_yaginfo.htm. Accessed 13 April 2013

10. El-Batahgy A-M (1997) Effect of laser welding parameters on fusion zone shape and solidification structure of austenitic stainless steels. Materials Letters 32:155-163

11. Farson D, Duhamel RF (2001) Taking advantage of laser welding. Automation and Robotics. The Fabricator,

12. Assancao EG (2012) Investigation of conduction to keyhole mode transition. PhD Thesis, Cranfield University, Cranfield

13. Weberpals J, F. D (2008) Fundamental Understanding of Spatter Behavior at Laser Welding of Steel. Paper presented at the ICALEO Conference, Temecula, CA, USA,

14. Misu T, Yoshioka S, Tokunaga T, Miyazaki V, Kitamura Y (2005) Monitoring of Nd:YAG Laser Spot Welding - Detection of Porosity Defect by Weld Sound. Paper presented at the ICALEO Conference, Miami, FL, USA,

15. Zhou J, Tsai H-L, Wang PC, Menassa R (2004) Melt flow and porosity formation in pulsed laser keyhole welding. Paper presented at the ASME Heat Transfer/Fluids Engineering Summer Conference, Charlotte, NC, USA,

16. Lima MSF, Riva R, de Oliveira AC, Siqueira GR (2008) Laser beam welding aerospace aluminum using fiber lasers.713128-713128

17. ABAQUS (2010) ABAQUS/Standard Documentation Version 6.10.2. ABAQUS, Inc

18. Prager M (2001) MPC Material Property Database for ASME Div II Rewrite, 2001-2003

19. ToolBox TE (2013) Convective Heat Transfer [Online]. http://www.engineeringtoolbox.com/convective-heat-transfer-d_430.html. Accessed 10 June 2013

20. Chen J, Young B, Uy B (2006) Behavior of high strength structural steel at elevated temperatures. Journal of Structural Engineering 132:1948-1954

21. James J (2013) SScanSS [Online]. http://materials.open.ac.uk/research/Struct_integ/si_research_projects.htm#scan. Accessed 03 February 2013

22. Hutchings MT, Withers PJ, Holden MT, Lorentzen T (2005) Introduction to the Characterization of Residual Stress by Neutron Diffraction. Taylor & Francis Group,

23. Manns T, Scholtes B (2010) Eine Software zur Berechnung diffraktionselastischer Konstanten aus Einkristalldaten. HTM J Heat Treatm Mat 65:75-84

24. Kröner E (1958) Berechnung der elastischen Konstanten des Vielkristalls aus den Konstanten des Einkristalls. Zeitschrift für Physik 151 (4):504-518

25. Adams JJ, Agosta DS, Leisure RG (2006) Elastic constants of monocrystal iron from 3 to 500 K. JOURNAL OF APPLIED PHYSICS 100:113530

26. Rietveld HM (1969) A profile refinement method for nuclear and magnetic structures. Journal of Applied Crystallography 2 (2):65-71

27. Smith MC, Smith AC (2009) NeT bead-on-plate round robin: Comparison of residual stress predictions and measurements. International Journal of Pressure Vessels and Piping 86 (1):79-95

28. Bouchard PJ, Ledgard P, Hiller S, Hosseinzadeh F (2012) Making the Cut for the Contour Method. Paper presented at the 15th International Conference on Experimental Mechanics, Porto, Portugal,

29. Hosseinzadeh F, Ledgard P, Bouchard PJ (2012) Controlling the Cut in Contour Residual Stress Measurements of Electron Beam Welded Ti-6Al-4V Alloy Plates. Experimental Mechanics:1-11

30. Hosseinzadeh F, Bouchard PJ (2012) Mapping Multiple Components of the Residual Stress Tensor in a Large P91 Steel Pipe Girth Weld Using a Single Contour Cut. Experimental Mechanics:1-11

31. Hosseinzadeh F, Toparli MB, Bouchard PJ (2012) Slitting and Contour Method Residual Stress Measurements in an Edge Welded Beam. Journal of Pressure Vessel Technology 134 (1):011402-011406

32. Prime M, Sebring R, Edwards J, Hughes D, Webster P (2004) Laser surface-contouring and spline data-smoothing for residual stress measurement. Experimental Mechanics 44 (2):176-184

33. Bouchard PJ, Turski M, Smith MC (2009) Residual Stress Concentrations in a Stainless Steel Slot-Weld Measured by the Contour Method and Neutron Diffraction / PVP2009-77234. Paper presented at the ASME PVP Conference, Prague, Czech Republic,

34. Turski M, Edwards L (2008) Boiler Spines Residual Stress Measurements Programme Task 1.2: Residual Stress Measurements on Slot Weld Specimen by the Contour Method and Neutron Diffraction. The Open University, Milton Keynes

35. ASTM (2011) Standard test method for microindentation hardness of materials.

36. Johnson G (2008) Residual stress measurements using the contour method. PhD Thesis, University of Manchester, Manchester

Chapter 7: Guidelines for controlling plasticity-induced errors in the contour method

Plasticity induced-errors in residual stress profiles measured by the contour method have been carefully investigated using 2D finite element simulations and linear elastic fracture mechanics (Chapter 3 and Chapter 4). An innovative cutting strategy [1] has been proposed to help mitigating such errors based on controlling the cut tip plastic zone size (see Chapter 4). Furthermore, a set of correlations have been developed in order to estimate the level of plasticity-induced stress error in a contour method measurement (Chapter 5).

The present chapter provides measurement practitioners with guidelines for controlling the stress relaxation process and estimating plasticity-induced errors in residual stress profile measurements made with the contour method. The proposed guidelines are first fully explained and then applied to a case study, a three-pass slot weld specimen.

7.1. Procedure for the controlling the plasticity-induced errors

As explained earlier in Chapter 4, plasticity-induced stress measurement errors in the contour method are directly related to the high level of stresses concentrated at the cut tip during the specimen cutting process. It was demonstrated that the cutting strategy and the restraining regime can significantly affect the level of stresses at the cut tip. These two factors (*i.e.* cutting and restraining) can be carefully designed to control the stress concentration while cutting and hence to mitigate contour method plasticity-induced errors. The essential inputs to design an optimum cutting/restraining strategy for mitigating plasticity-induced errors are:

- ✓ An estimate of the initial residual stresses (either from another measurement technique, from prediction, or published data for a similar component).
- ✓ Specimen dimensions.
- ✓ Material properties: Young's modulus, Poisson's ratio and yield stress.

The procedure presented in the flowchart shown in Figure 7-1 is proposed for assessing and controlling plasticity-induced errors, and comprises the following steps:

- ✓ *Step 1:* gather the input data.
- ✓ *Step 2:* design of a cutting/restraining configuration.
- ✓ *Step 3:* determination of the residual stress intensity factor distribution based on the designed configuration.
- ✓ *Step 4:* calculation of the normalised average plastic zone size.
- ✓ *Step 5:* estimation of the average plasticity-induced errors using the correlations.
- ✓ *Step 6:* assess whether average error is acceptable.
- ✓ *Step 7:* if the errors are not acceptable, design an alternative cutting/restraining strategies.

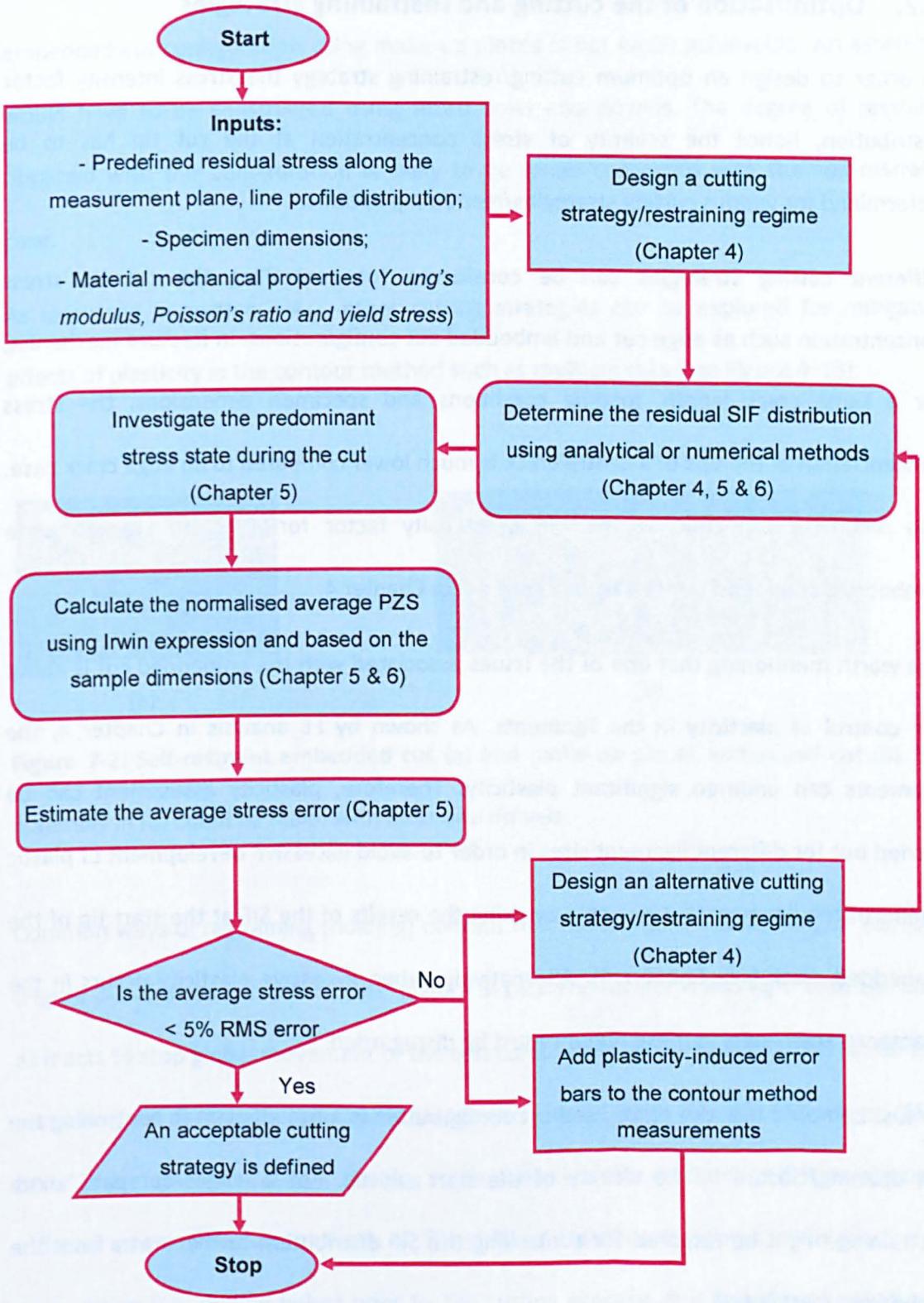

Figure 7-1: Flowchart illustrating the proposed procedure for minimising plasticity-induced stress errors in contour method measurement.

7.2. Optimisation of the cutting and restraining strategies

In order to design an optimum cutting/restraining strategy the stress intensity factor distribution, hence the severity of stress concentration at the cut tip has to be determined for various cutting strategies/restraining options.

Different cutting strategies can be considered for controlling the cut tip stress concentration such as edge cut and embedded cut configurations. In fracture mechanics, for a same crack length, loading conditions and specimen dimensions, the stress concentration at the tips of a centre crack is much lower compared to an edge crack case. The beneficial reduction in the stress intensity factor for a centre cracked plate (embedded crack) can be seen from Figure 4-3 in Chapter 4.

It is worth mentioning that one of the issues associated with the embedded cut is about the control of plasticity in the ligaments. As shown by FE analysis in Chapter 4, the ligaments can undergo significant plasticity. Therefore, plasticity assessment can be carried out for different ligament sizes in order to avoid excessive development of plastic strains in the ligament, for example by using the results of the SIF at the start tip of the embedded crack (see Chapter 4). Alternatively, when excessive plasticity occurs in the ligaments, the results in these regions must be disregarded.

It must be noted that the embedded cut configuration is more efficient in controlling the cut opening/closure in the vicinity of the start cut tip. For a longer cut path, extra restraining might be required for controlling the SIF distribution further away from the embedded start cut tip.

In practice, the embedded cut configuration can be achieved by initiating the cut within the test component (self-restraint) or by attaching make-up pieces onto the test

component and starting the cutting within one of the make-up pieces (Figure 7-2). The embedded cut configuration using make-up pieces is not easily achievable. An assembly would have to be constructed using fitted bolts and dowels. The degree of restraint obtained with this configuration is likely to be lower compared with the self-restraint case.

As discussed in section 4-4-2, other cutting strategies can be explored for mitigating effects of plasticity in the contour method such as multiple cuts (see Figure 4-13).

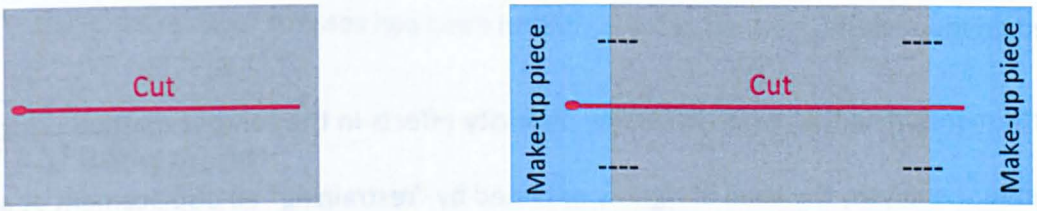

Figure 7-2: Self-restraint embedded cut (a) and make-up pieces embedded cut (b). The assembly in (b) could be made with bolts and dowels.

Common ways of restraining (holding) contour test components include 'finger' clamping (Figure 3-1-a) or use of 'fitted bolts' (Figure 3-1-b). The former is less rigid than the latter as it acts to stop global movement of the test component on the machine bed rather than restricting cut face opening/closure (which can involve large forces). The use of 'fitted bolts' is preferable because it enables some control of the mechanism driving plasticity-induced errors. However, the use of 'fitted bolts' restraint requires initial experimental preparation (*i.e.* drilling holes) prior to the cutting process. It is beneficial to clamp the test component as close as possible to the cut plane [2,3] as this increases the restraint and therefore decreases the stress intensity factor profile. Indeed several fitted bolts

along the clamp line should be used to increase the restraint conditions for long embedded cuts. However, as demonstrated in Chapter 3, the nature of the plasticity stress errors introduced depends very much on global restraint strategy adopted. The completely unrestrained case gave a different type/distribution of error to the restrained case.

The wire diameter used for the cutting process can also help to minimise the plasticity-induced errors by the removal of the plastic wake. In fact as explained in Chapter 5, when the generated plastic wake depth is less than the cut width, no effect of plasticity is observed on the results.

It is worth mentioning that when assessing plasticity effects in the contour method using finite element analysis, the level of rigidity obtained by "restraining" all displacement at a line or along a plane is not reproducible in practice. It can be approached perhaps by use of 'fitted bolts', but it is advisable to try to simulate the real level of restraint in the FE analysis (although this may be time consuming).

Having the essential inputs explained in section 7-1-1, the stress intensity factor distribution is determined for each cutting and/or restraint strategy using either numerical tools [4,5] or analytical solutions [6,7]. From the obtained SIF data, the material yield stress and the specimen dimensions; the normalised average plastic zone size is analytically calculated. Finally, the developed correlations in Chapter 5 are used to predict the plasticity-induced errors in the intended residual stress contour measurement. This routine can be repeated for a variety of cutting/restraining configurations until the plasticity-induced error threshold is met (see Chapter 5 and flowchart) or satisfactory results are obtained.

7.3. Case study: residual stress measurement in a 3-pass specimen

In the present section the proposed procedure for estimating and mitigating plasticity-induced errors in a contour residual stress measurement (see Figure 7-1) is applied to a specific weld component. The transverse component of residual stresses in a 3-pass slot weld specimen is examined here because:

- ✓ a spare sample was available for contour method measurement;
- ✓ an earlier contour method measurement on an identical test component showed evidence of plasticity-induced errors;
- ✓ the initial residual stresses had been measured using neutron diffraction [8,9].

7.3.1. Background

The test specimen studied was supplied by EDF Energy (formerly British Energy) and manufactured by Mitsui Babcock [10]. The base-plate of the test specimen, made of an AISI Type 316L austenitic stainless steel, was cut from a 50 mm thick plate down to a 310 x 200 x 30 mm^3 blank plate and stress relief heat-treated. Subsequently, the 30 mm thick plate was reduced to a thickness of 25 mm by milling a further 2. 5 mm from the blank plate's top and bottom surfaces. Finally, the weld groove was machined from the top surface of the blank plate. Figure 7-3 illustrates the schematic of the blank plate prepared for the welding process.

On completion of the machining process, a Manual Metal Arc (MMA) welding process was undertaken with Babcock type S electrodes [11], having a diameter of 5 mm and length of 350 mm. Three weld beads were deposited to fill the 10 mm deep slot shown in Figure 7-3. All three weld beads were laid in the same direction. The welded metal was 80 mm

long at its bottom and 100 mm long at the top face of the plate. Figure 7-4 illustrates a photograph of the completed 3-pass slot weld specimen.

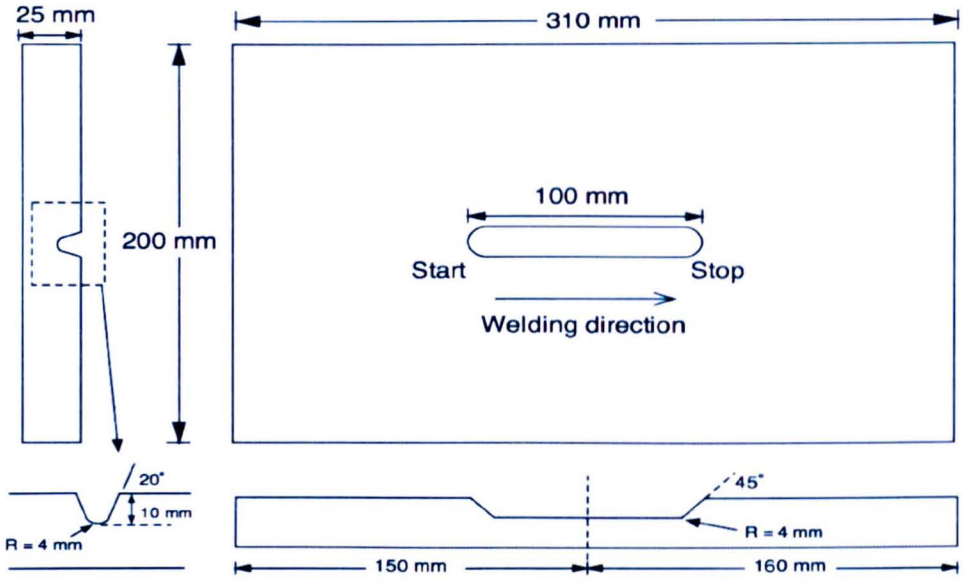

Figure 7-3: Schematic drawing showing the base plate dimensions and geometry of the slot into which the three weld beads were deposited [8].

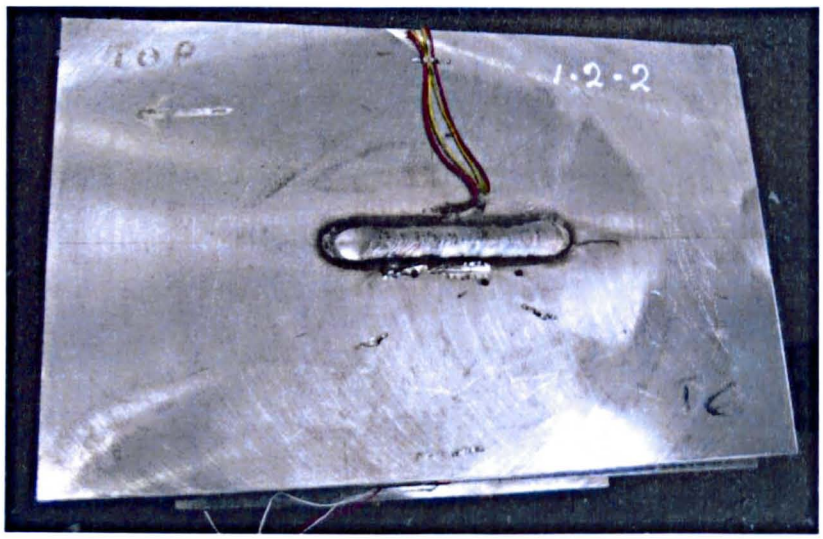

Figure 7-4: Photograph of the test specimen after the welding process [10].

The distribution of the transverse component of residual stresses was measured in a notionally identical test specimen using neutron diffraction and the contour method [8,9]. The residual stress measurements were conducted on the Engin-X instrument at the Rutherford Appleton Laboratory (UK), ISIS facility using 311 planes. Figure 7-5 compares the neutron diffraction and contour method transverse component of residual stresses along a measurement line parallel to the weld and located at 7.5 mm below the plate top surface. The contour method results were averaged over an area (2.8 x 2.8) mm^2 representative of the gauge volume used in neutron diffraction (4 x 4 x 4) mm^3.

For clarity, this contour method measurement is referred to as the "old contour cut" and the one performed in the present project is called the "new contour cut".

Although the "old" results from the two measurement techniques were in broad agreement in terms of the general shape of the profile, detailed comparisons along the measurement line revealed some local discrepancies.

In the neutron diffraction results, a drop in magnitude of tensile stresses in the weld metal is observed. This drop was explained by a possible effect of the stress free cube data [8,9], as the residual strains were calculated using a single averaged d_0 value in the weld metal instead of direction dependent d_0 values.

The contour results deviate from the neutron results in two regions which are possibly associated with cutting process plasticity: a tensile peak ('hump A') just before the weld start (70 – 100 mm from the edge) and constant increase of tensile stresses ('hump B') in the weld metal [8,9]. Similar features were also observed in the residual stresses previously measured by the contour method in the NeT single bead-on-plate benchmark test specimen [12] which could be again due to plasticity effects. These types of feature

were observed in the experimental work of Chapter 6. For example see the contour method measurement results for the laser heated plate_0 (Figure 6-28) and to a lesser extent in plate_1 (Figure 6-29). Contour cut simulation of the laser heated plates (plate_0, plate_1) demonstrated evidence of cutting compressive plastic strains at the location of tensile 'hump A' and tensile plastic strains in the region of magnified tensile stresses 'hump B'. Therefore there is strong evidence that the features in the "old contour cut" stress measurement are associated with occurrence of plasticity during the cutting process.

An idealised stress profile, self-equilibrated across the plate, was fitted to the neutron diffraction measurements, taking into account the uncertainties surrounding the stress-free reference data used for the weld measurements (See Figure 7-5). The peak at the end of the tensile stress region was chosen based on the FE predictions carried out on the 3-pass slot weld specimen [13].

From the map of the neutron diffraction measurement (Figure 7-6) it can be observed that the selected stress profile, from which the idealised stress distribution was derived, is representative of the upper region stress field on the 3-pass slot weld mid-width plane. For the lower region, the magnitude of the residual stresses is overall lower compared to the upper region results. The selected stress profile was used as the input for optimising the cutting and clamping strategy in this study.

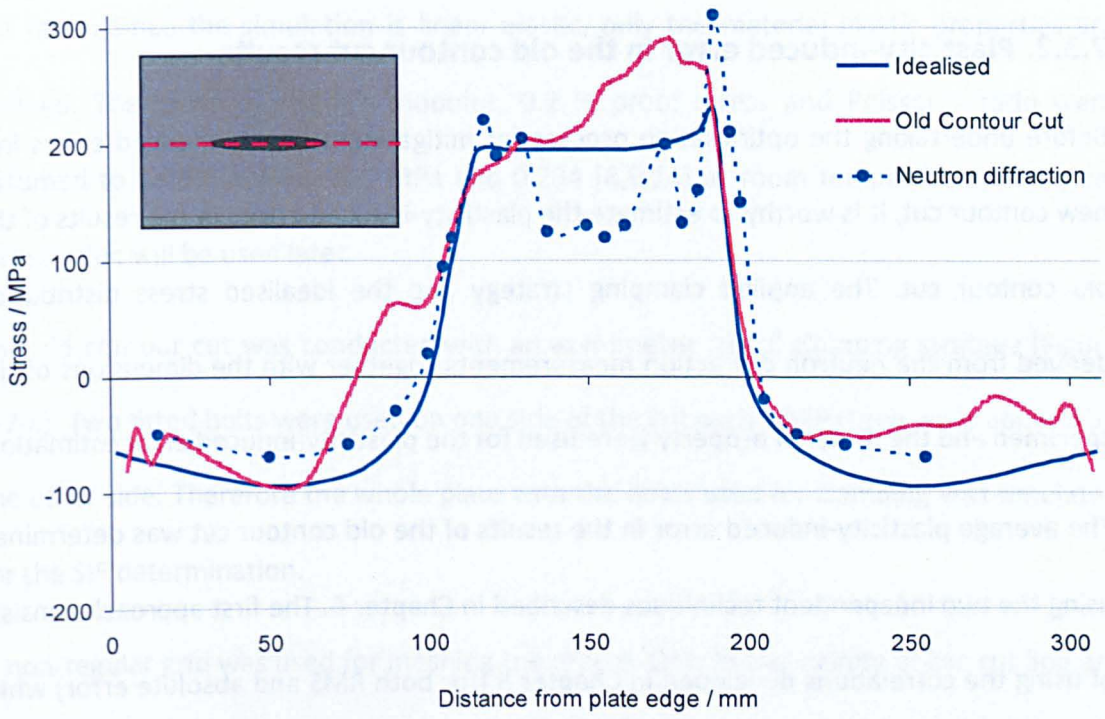

Figure 7-5: Comparison of the transverse component of residual stresses in a 3-pass slot weld specimen along a line parallel to the weld at 7.5 mm below the top surface determined by the contour method (denoted 'old contour cut results') and neutron diffraction [8].

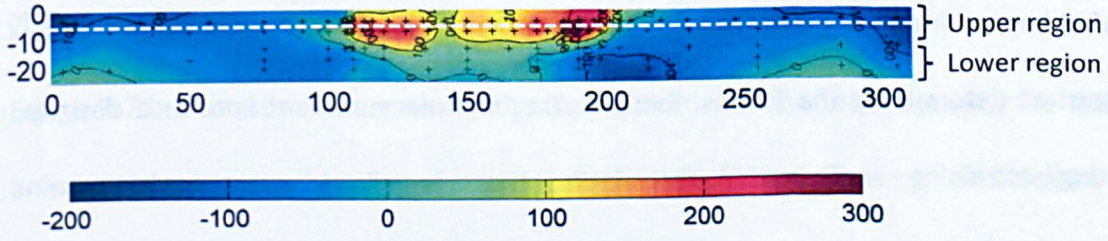

Figure 7-6: Map of the neutron diffraction transverse component of residual stresses on the mid-weld longitudinal plane of the 3-pass slot weld specimen. The measurement line across which the neutron results of Figure 7-5 are plotted is shown in white dashed line [8].

7.3.2. Plasticity-induced error in the old contour cut results

Before undertaking the optimisation process for mitigating plasticity-induced errors in a new contour cut, it is worthy to estimate the plasticity-induced errors in the results of the old contour cut. The applied clamping strategy and the idealised stress distribution derived from the neutron diffraction measurements together with the dimensions of the specimen and the material property were used for the plasticity-induced error estimation.

The average plasticity-induced error in the results of the old contour cut was determined using the two independent techniques described in Chapter 6. The first approach consists of using the correlations developed in Chapter 5 (for both RMS and absolute error) while in the second approach the contour stress profile is compared with the idealised stress profile derived from neutron diffraction. Finally, the results from the two approaches are compared.

Estimated average stress error using the correlations

The average stress error estimation using the correlations and the predefined stress profile has been described in detail in section 5-13 of Chapter 5. The three main steps consist of determining the SIF distribution along the measurement line for a designed cutting/restraining configuration, calculating the normalised average plastic zone parameters and estimating the average stress error from the correlations.

The residual stress intensity factor determination using finite element analysis was conducted using the approach explained in Chapter 6. The simulation consisted of incrementally cutting a 2D FE model (representative of the test specimen geometry) and simultaneously applying the predefined stress profile as an internal load on the internal

cut faces. Since the simulation is linear elastic, only the material elastic properties are defined. The material Young's modulus, 0.2 % proof stress and Poisson's ratio were assumed to be 195.6 GPa, 290 MPa and 0.294 [8,9,14] at room temperature. The yield stress value will be used later.

The old contour cut was conducted with an asymmetric 'rigid' clamping strategy (Figure 7-7-a). Two fitted bolts were used on one side of the cut path while three were applied on the other side. Therefore the whole plate with the holes used for clamping was simulated for the SIF determination.

A non-regular grid was used for meshing the model. Only in the vicinity of the cut line are fine elements of 0.5 mm size used (see Figure 7-8). A total of 41870 linear quadrilateral with reduced integration and 20 linear triangular elements were generated in the model. Since no symmetry boundary conditions were used, a blunt cut of 0.2 mm width was simulated by incrementally removing elements along the measurement line. This is slightly greater than a cut width generated by a wire diameter of 100 μm used in the old contour cut. However, as demonstrated in section 5-1-3, the stress intensity factor is less affected by the cut width.

Figure 7-7-b illustrates schematically the 3-pass slot weld specimen showing the drilled hole for clamping and the internal stress applied to the cut faces from which material has been removed. For each cut increment, the cut tip stress intensity factor was extracted. With a 10 mm cut increment, the plate cutting process was completed in 30 steps, resulting in 30 stress intensity factor results.

For the original clamping strategy used, the associated SIF distribution is shown in Figure 7-9. For clarity, the old contour cut results and idealised stress profile are also shown.

Two different peaks in the residual SIF distribution are observed: one introduced by the release of compressive stresses (~ -35 MPa.m^$^{0.5}$ at the cut depth of 60 mm) and the other peak is caused by the release of tensile stresses (~ 83 MPa.m^$^{0.5}$ at 190 mm). The locations of the humps in the old contour cut results correspond to the regions with high magnitude of stress intensity factor. The release of the compressive stresses from 200-307 mm also causes high stress concentration, which probably results in errors in the corresponding regions.

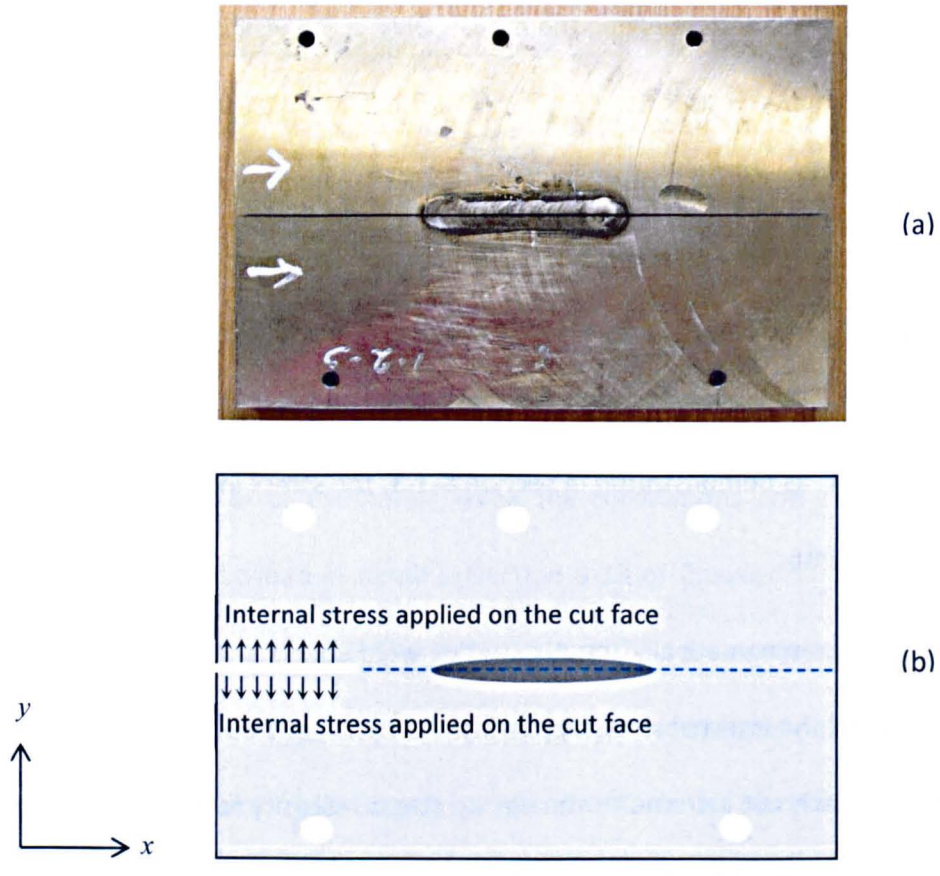

Figure 7-7: Photograph of the 3-pass slot weld specimen after the contour cut showing the clamping holes [8](a). Below, a schematic of the 3- pass slot weld showing an internal load applied on the cut faces and the clamping restrained in x and y directions (b).

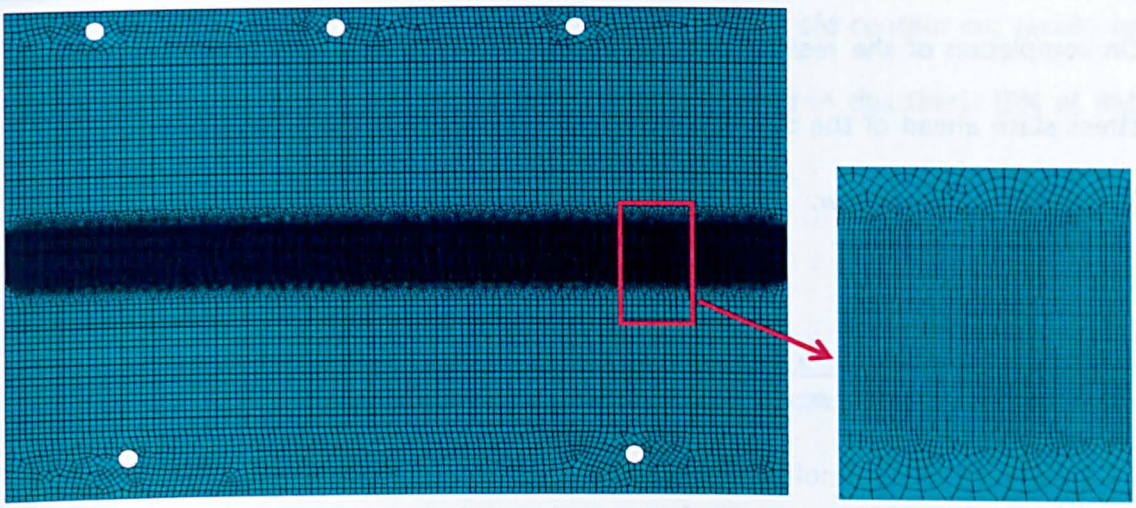

Figure 7-8: Mesh of the model used to determine the SIF distribution for the old contour cut configuration. A close-up view of the cut vicinity mesh is also shown.

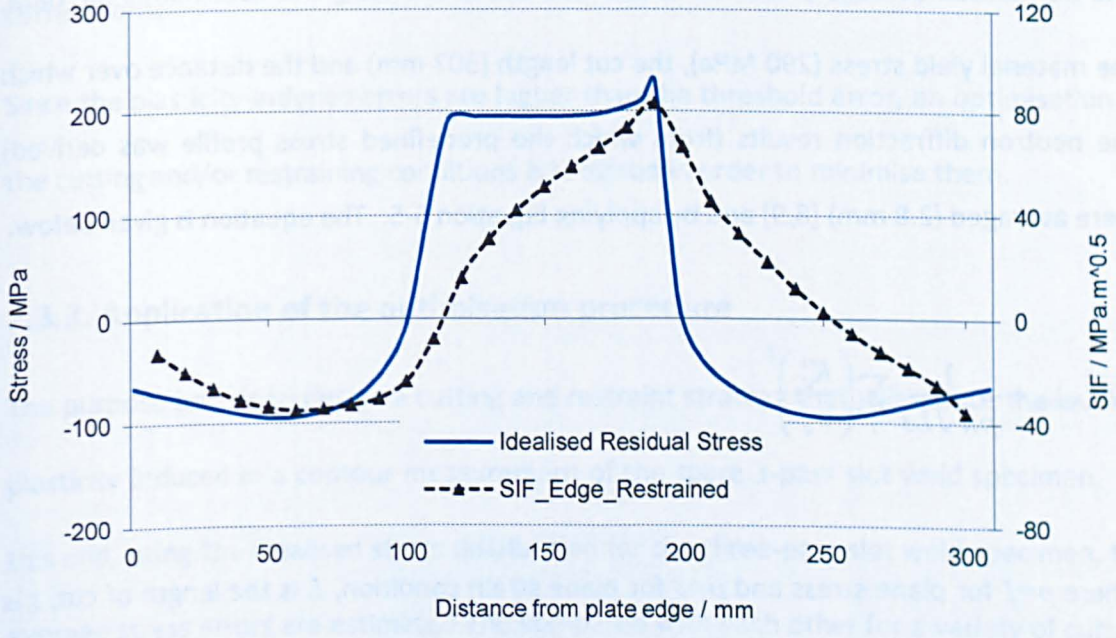

Figure 7-9: Residual stress intensity factor (SIF) distribution along the cut line for the 3-pass slot weld specimen for the old contour cut restraining conditions and assuming the idealised stress profile.

On completion of the residual stress intensity factor determination, the predominant stress state ahead of the cut was investigated by applying the inequality in Chapter 5 (Equation 5-4), see below.

$$Thickness \geq 2.5 * \left[\sum_i \left(\frac{K_I^i}{\sigma_0} \right)^2 \right]$$

where K_I^i is the stress intensity factor at the cut increment i, σ_0 is the material yield stress.

As a higher value of 44.2 mm was obtained (compared to the 3-pass slot thickness, 25 mm), a plane stress state predominantly occurred during the contour cut.

The normalised average plastic zone size was calculated using the determined SIF data, the material yield stress (290 MPa), the cut length (307 mm) and the distance over which the neutron diffraction results (from which the predefined stress profile was derived) were averaged (2.8 mm) [8,9] and by applying Equation 5-5. The equation is given below.

$$\overline{PZS}_{Norm} = \frac{1}{p\pi\sqrt{Lt}} \sum_i \left(\frac{K_I^i}{\sigma_0} \right)^2$$

where $p=1$ for plane stress and $p=3$ for plane strain condition, L is the length of cut, t is the thickness over which the residual stress data (used to calculate the SIF) are averaged.

A normalised average plastic zone of 0.19 was obtained. The corresponding RMS average error (15.5 %) and absolute average error (11 %) were estimated from Figure 5-26 and Figure 5-17, respectively.

As noticed the estimated plasticity errors introduced in the old contour cut results are higher than the threshold plasticity-induced error proposed in this thesis (5% of RMS error).

Measured average stress error

The measured RMS and absolute average stress errors were calculated by comparing the contour stress profile with the idealised stress profile. Equation 5-1 and Equation 5-2 in Chapter 5 were used for this purpose.

With the direct comparison approach, RMS and absolute average stress errors of 16.2% and 13% were found to be induced in the old contour cut results, respectively, which are close to the estimated average stress error (15.5% and 11%) using the FE based correlations.

Since the plasticity-induced errors are higher than the threshold error, an optimisation of the cutting and/or restraining conditions is required in order to minimise them.

7.3.3. Application of the optimisation procedure

The purpose here is to design a cutting and restraint strategy that will reduce the level of plasticity induced in a contour measurement of the spare 3-pass slot weld specimen. To this end, using the idealised stress distribution for the three-pass slot weld specimen, the average stress errors are estimated and compared with each other for a variety of cutting and clamping combinations. The procedure shown in flowchart (Figure 7-1) and described in section 7-1 is followed.

Step 1: Design of a cutting/restraining strategy

In the old contour cut the cutting process was initiated from one of the plate free edges and proceeded in a straight path perpendicular to the straight edge. Furthermore, the plate was firmly clamped during the cutting process using fitted bolts in order to reduce potential plasticity-induced errors [8,9]. This cutting/restraining configuration is representative of a partially restrained edge cut configuration. It can be noticed that this configuration resulted in a high level of plasticity-induced errors.

In Chapter 4, it was demonstrated that the stress intensity factor for a centre crack configuration is much lower compared to an edge cracked plate. The centre/embedded crack configuration provides a self-restraint which helps controlling the cut opening/closure. Therefore, the embedded cut configuration is explored here. As the 'rigid external restraining' regime requires additional experimental preparation prior to the cut by drilling holes, an unrestrained regime, (achieved in practice by simple 'finger' clamping) is first assessed.

Step 2: Stress intensity factor determination

The residual SIF determination using finite element analysis is conducted similarly to section 7-3-2. Unlike the simulation in section 7-3-2 for the SIF determination, only one half of the 3-pass slot weld specimen was used here. The symmetry boundary conditions were applied along the measurement line located at the plate mid-width (Figure 7-10-a). Hence, the cutting process was conducted by releasing incrementally the symmetry boundary conditions. The predefined stress profile (see Figure 7-5) was simultaneously applied as internal stress on the cut face (Figure 7-10-b).

The cut was initiated from 5 mm of the test specimen free edges perpendicular to the cut path. This results in a ligament of 5 mm between the free edge perpendicular to the cut path and the cut start. Further in this section, an investigation is carried to check whether plasticity occurred or not in the selected ligament. A nodal constraint was also applied to avoid the plate free movement during the cutting (Figure 7-10-b).

As for the previous simulations, only the cut vicinity was meshed with fine elements of 0.5 mm size (see Figure 7-11) resulting in a total 23600 first order elements with reduced integration.

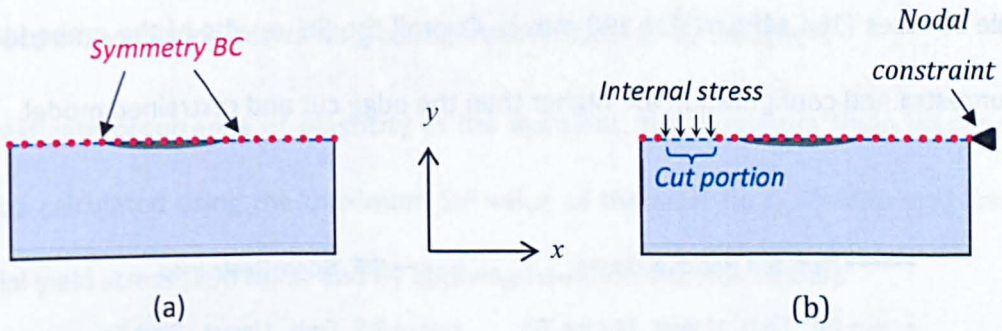

Figure 7-10: Schematic of one half of the 3- pass slot weld specimen showing the symmetry boundary conditions (BC)(a) the nodal constraint and an internal stress applied on a cut face (b).

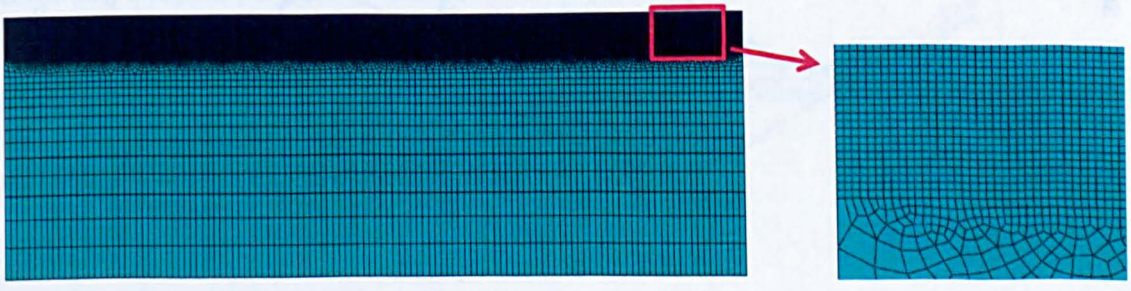

Figure 7-11: Mesh of the model used to determine the SIF distribution for the embedded cut and unrestrained configuration. A close-up view of the cut vicinity mesh is also shown.

On completion of the simulation, the stress intensity factor results for both moving and start tips were extracted for the different cut increments (see Figure 7-12). The start tip results were used to investigate occurrence of plasticity in the ligament and the moving tip results were utilised to estimate the plasticity-induced error for the designed cutting/restraining configuration. For clarity, the idealised stress distribution is plotted. The edge cut and restrained SIF distribution is also shown for comparison.

Two different peaks in the residual stress intensity factor profile are observed. The first peak (-40 MPa.m$^{0.5}$), located at ~90 mm cut depth is introduced by the release of compressive stresses while the second and most significant peak is due to the release of tensile stresses (104 MPa.m$^{0.5}$ at 190 mm). Overall the SIF results of the embedded cut and unrestrained configuration are higher than the edge cut and restrained model.

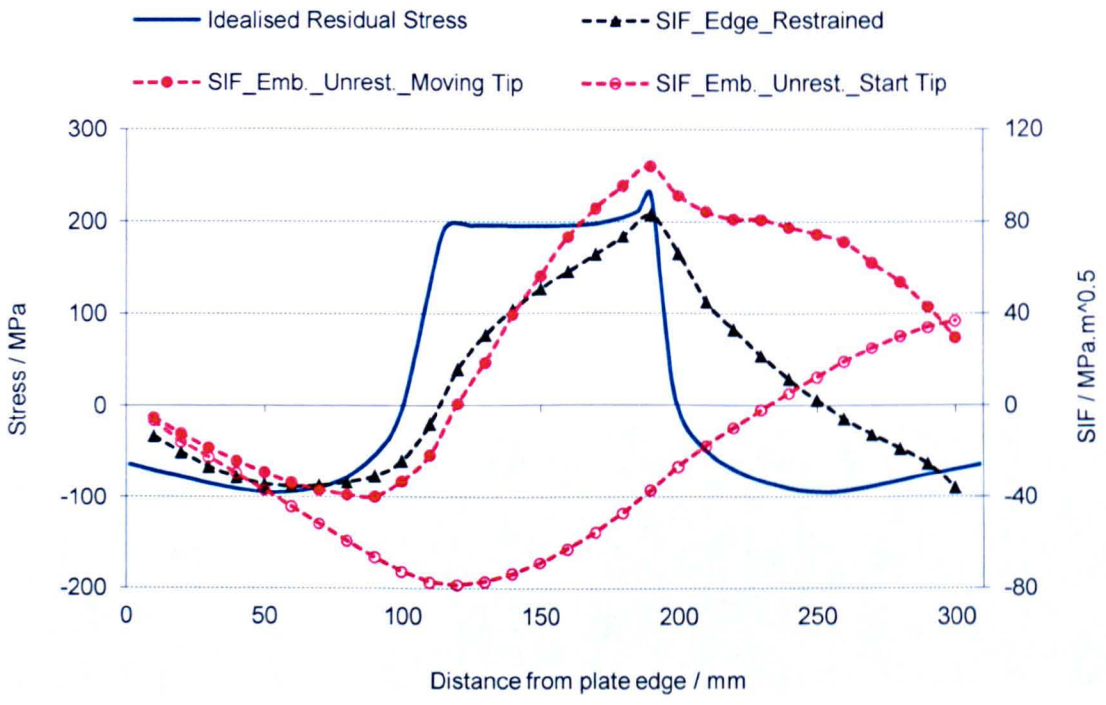

Figure 7-12: Residual stress intensity factor (SIF) distribution along the cut line for two different restraining conditions and assuming the idealised stress profile.

Step 3 & 4: Normalised average PZS calculation and error estimation

The normalised average plastic zone size was calculated following the procedure of section 7-3-2, which consists, first of investigating the predominant stress state during the cut and then calculating the normalised average plastic zone size.

As for the old contour cut case, a predominant plane stress state was found ahead of cut. Note that, here the cut length of the spare 3-pass slot weld specimen is 310 mm.

A normalised average plastic zone size of 0.43 was obtained for the embedded cut and unrestrained model, which is higher than the threshold normalised plastic zone size of 0.05 (see section 5-11) and the edge cut and restrained normalised average PZS (0.19). Therefore a new cutting/restraining configuration needs to be designed.

To investigate occurrence of plasticity in the ligament, the maximum Irwin plastic zone size was calculated using the maximum SIF value of the start tip (- 79 MPa.√m) and the material yield stress (290 MPa) and by applying Equation 4-2 (see below).

$$r_y = \frac{1}{p\pi}\left(\frac{K_I}{\sigma_0}\right)^2$$

where, K_I is the stress intensity factor, σ_0 is the material yield stress, $p=1$ for plane stress condition and $p=3$ for plane strain state.

For a maximum plastic zone size of 23.5 mm, it can be concluded that the entire ligament underwent significant plastic deformation.

Step 5: Consider alternative cutting/restraint regime

As demonstrated above, both the restrained edge cut (old contour cut) and unrestrained embedded cut configurations result in high plasticity-induced errors.

It was decided to investigate the benefits of adding external restraint. The restraint was achieved by constraining the holes for clamping in x and y directions. Four holes were used on each side of the cut face as shown in Figure 7-13.

The average stress errors were estimated following the same procedure as for the embedded/unrestrained case (Figure 7-1). Apart from the holes for restraining, the FE mesh (Figure 5-14) used here to evaluate the distribution of SIF with crack length is similar to the embedded cut and unrestrained.

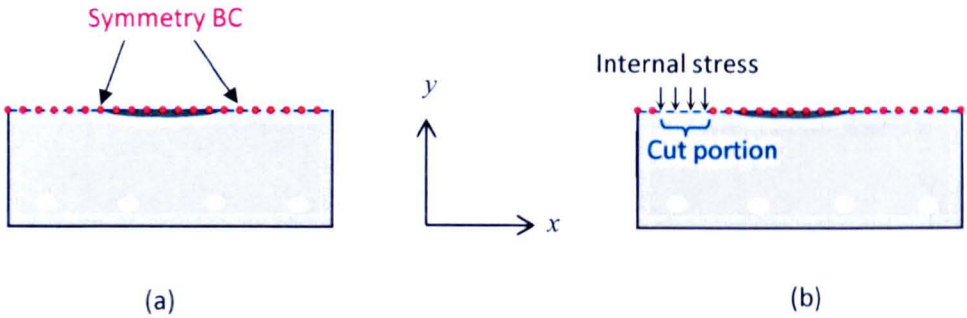

Figure 7-13: Schematic of the 3-pass slot weld specimen showing the symmetry boundary conditions (BC) (a), the internal stress applied on a cut face and the four clamping holes (b). In the FE model the holes were restrained in the x and y directions.

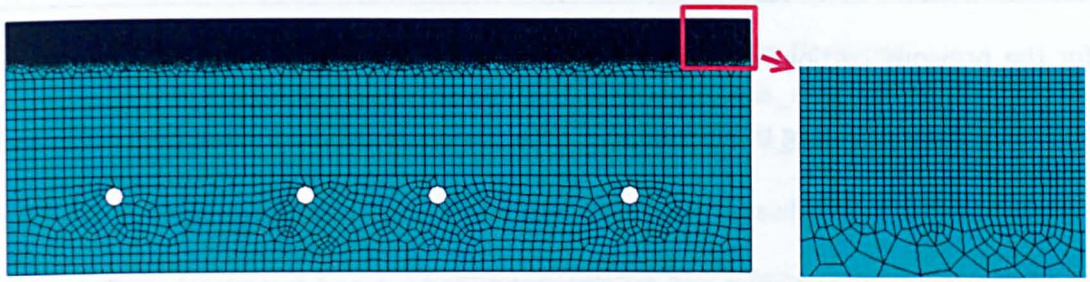

Figure 7-14: Mesh of the model used to determine the SIF distribution for the embedded cut and restrained configuration. A close-up view of the cut vicinity mesh is also shown.

Figure 7-15 compares the residual SIF distribution for the unrestrained and restrained embedded cut configurations assuming the idealised residual stress profile. The SIF results of the restrained edge cut configuration are also plotted. Overall the stress intensity factor distribution of the embedded and restrained configuration is much lower than the two other cutting/restraining cuts; although high magnitude of SIF is still observed in the tensile stress region.

Occurrence of plastic deformation in the ligament was investigated similarly as for the embedded cut and unrestrained configuration. For a maximum SIF value of -36.8 MPa√m at the cut start tip, a maximum plastic zone size of 5 mm was obtained for the ligament, which also shows that plastic deformations still occurred in the ligament. One of the solutions to this could be investigating the plastic zone size for different ligament sizes or alternatively disregarding the results of the ligament.

It must be noted that different ligament sizes result in different SIF distributions for the moving tip. This may either improve or worsen the optimised SIF results. For the present contour cut, the results of the ligament were disregarded.

As for the previous cutting/restraining conditions, predominant plane stress conditions were obtained. Substituting the residual SIF data, the material yield stress (290 MPa) and the dimensions for normalisation (L = 310 mm and t = 2.8 mm) into Equation 5-5, the normalised average plastic zone size for the embedded cut and restrained configuration was obtained as 0.12. From the developed correlations (Figure 5-26 and Figure 5-17), the associated RMS and absolute average error were estimated to be 10% and 6.5 % respectively.

As noticed, the combination of the restrained embedded cut and a more rigid restraining has considerably reduced the average stress error compared to old contour cut and the unrestrained embedded cut configuration. Therefore, it was decided to undertake the new contour cut with an embedded cut configuration and apply external restraints representing or at least approaching a rigid restraint condition.

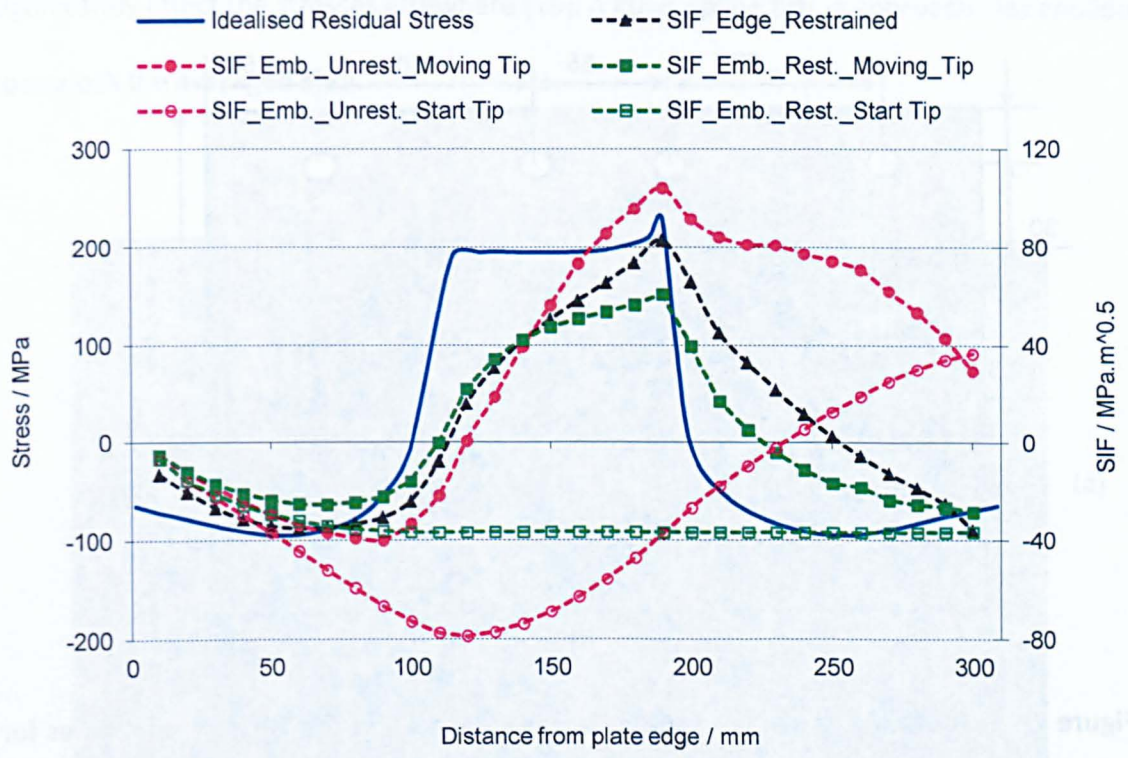

Figure 7-15: Comparison of the residual SIF distribution for different cutting configurations and clamping regimes under the idealised stress distribution for the 3-pass slot weld specimen.

7.3.4. Implementation of the new contour measurement

The contour method was applied to measure the transverse residual stresses in the spare 3-pass slot weld specimen, for the purpose of implementing the optimised cutting strategy developed above.

An embedded cut configuration was achieved by creating two holes close to the free edges and starting the cut from one of them. Note that creation of the second hole was not necessary. The 3-pass slot weld specimen was restrained by using eight fitted bolts as shown in Figure 7-16 and Figure 7-17-a in order to provide cut opening restraint in the *y-x* plane approaching theoretical rigid conditions.

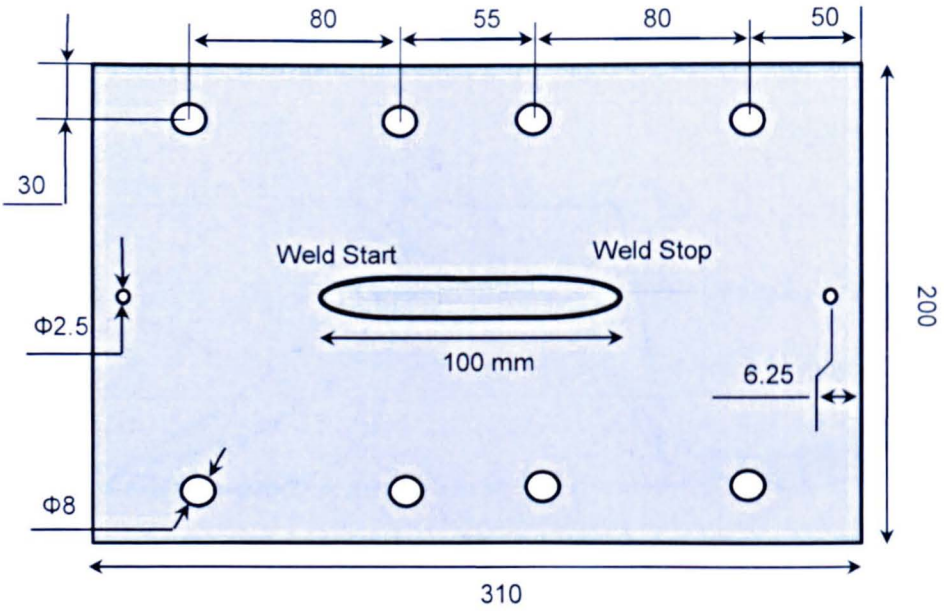

Figure 7-16: Schematic drawing of the 3-pass weld specimen showing the pilot holes for the embedded cut configuration and the clamping holes. All the dimensions are in mm.

The cutting process was conducted with a FANUC ROBOCUT wire EDM under "skim" cut settings and using a 0.25 mm wire diameter. The choice of a large wire diameter helped to reduce the plastic wake (hence, potential plasticity-induced error, see Chapter 5) and the risk of wire breakage.

Once the cutting process was completed, the distorted cut faces were measured using a MITUTOYO CRYSTA PLUS 574 CMM equipped with a 3 mm diameter Renishaw PH10M trigger probe. The measurement spacing in x (thickness) and y (length) directions was 0.5 mm. The standard data processing as explained in Chapter 2 was applied to the surface deformations of the three-pass slot weld plate. Figure 7-18 shows the averaged deformations of the two cut parts of the three-pass slot weld specimen. Measured data from the pilot holes to the free edges were disregarded. The regions with missing data were filled in by extrapolation. As reported by Prime, this extrapolation does not

significantly affect the stresses elsewhere [15]. A cubic spline fitting approach was applied to smooth the averaged data.

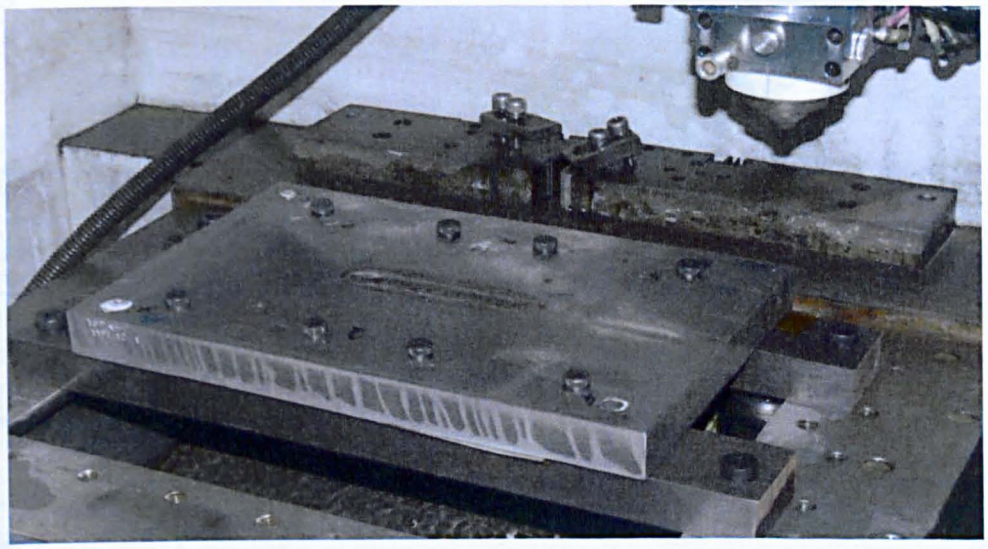

(a)

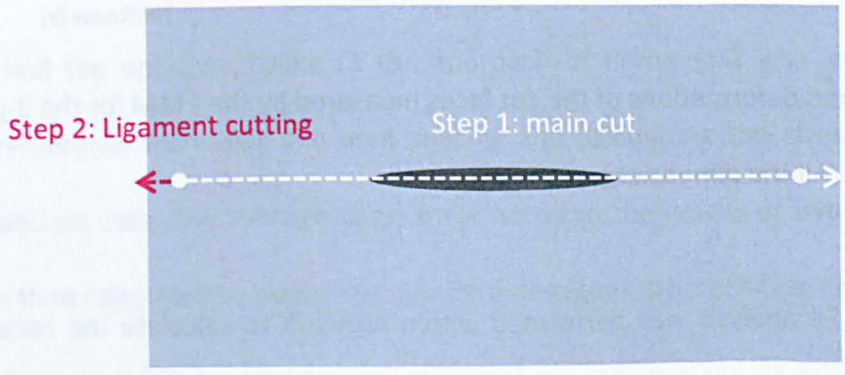

(b)

Figure 7-17: Photograph of the 3-pass slot weld specimen showing the clamping regime in the wire EDM workspace (a). The schematic shows the two cutting steps (b).

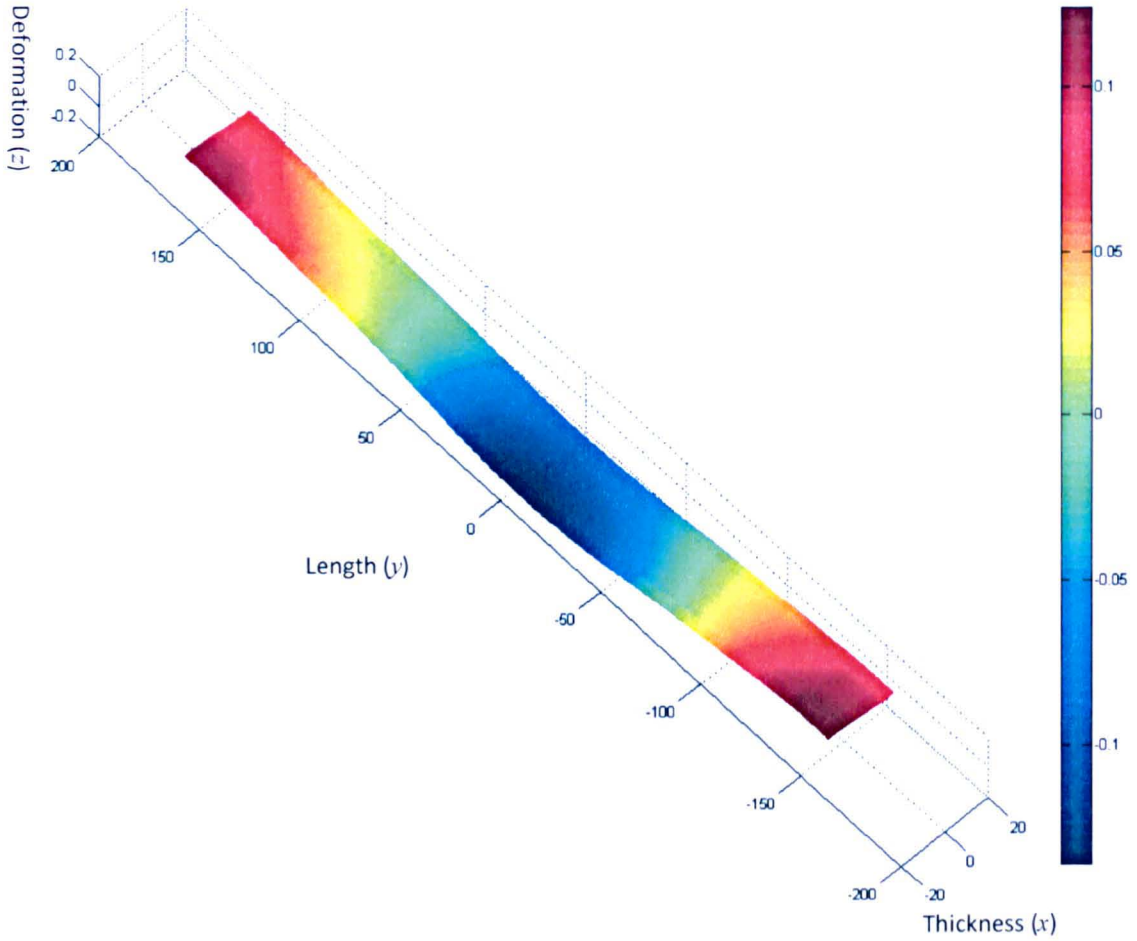

Figure 7-18: Averaged deformations of the cut faces measured by the CMM for the 3-pass slot weld specimen. All the dimensions are in mm.

A 3D linear elastic FE analysis was performed within ABAQUS to calculate the residual stresses from the applied deformation at the cut surface. The 3D FE model of the 3-pass slot weld was generated based on the cut face perimeter measured by the CMM. A non-regular mesh grid of 38000 linear hexahedral mesh elements with reduced integration (C3D8R) was used (see Figure 7-19). To avoid rigid body motions, nodal constraints were applied on two corners of the cut face. The elastic properties (Young's modulus of 195.6 and Poisson's ratio of 0.294) of the 3-pass slot weld specimen were defined. The residual

stresses were calculated back by applying as boundary conditions the smoothed deformation contour (with reverse sign) to the cut plane in the z-direction.

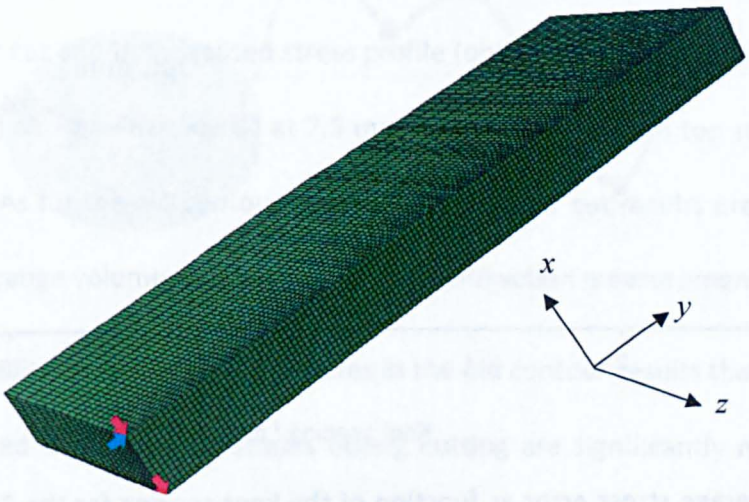

Figure 7-19: 3D FE model of the half-cut plate showing the mesh grid and the nodal constraints on the two corners for avoiding the rigid body motions.

To find the optimum spline fit the approach of Prime [15] was implemented; that is incrementally increasing the knot spacing and calculating the stresses for each set of smoothed data. The average stress error between the results of two consecutive splines was then calculated by applying a standard deviation approach (see Equation 6-1).

Figure 7-20 shows the average stress error for the different splines analysed. It can be observed that the minimum average stress error occurs for the 2×2 mm knot spacing. However as shown in Figure 6-25 for the laser weld plates, lower knot spacing can result in over-fitting. Likewise, a coarse knot spacing can under-fit the raw measurements. Therefore, the optimum fitting region corresponds to 7×7, 8×8 and 9×9 knot spacing (see Figure 7-20). Since 7×7 knot spacing was used to fit the data of the old contour cut, the same knot spacing is used here.

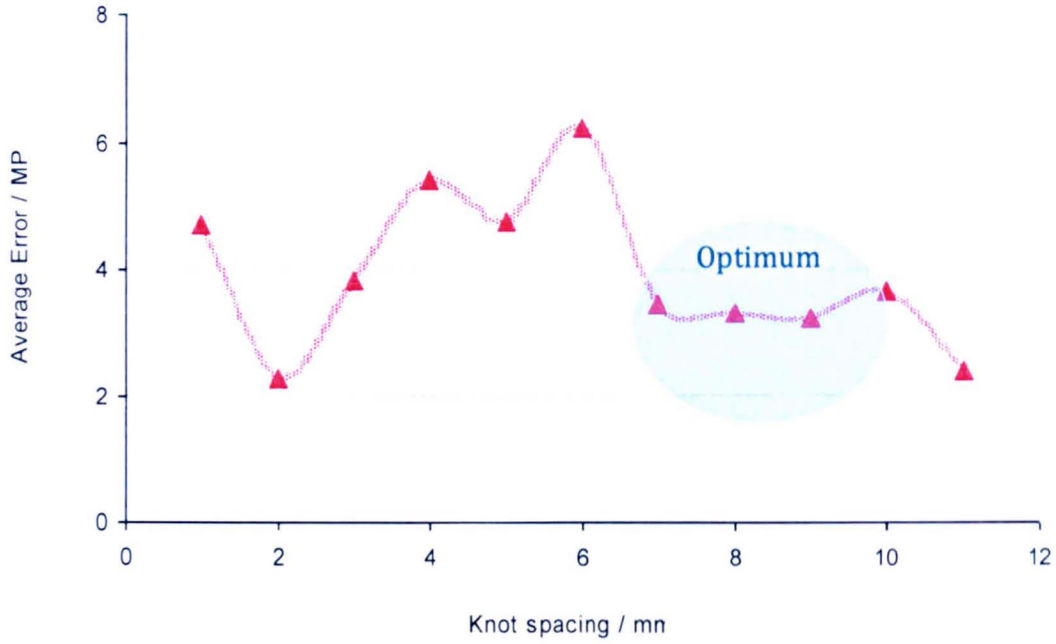

Figure 7-20: Average stress error as function of the knot spacing for the 3-pass slot weld specimen.

7.3.5. Results and Discussion

The map of the measured transverse residual stress from the new cut specimen over the longitudinal plane at mid-width of the plate is illustrated in Figure 7-21-a. The old contour cut results based on a 7×7 mm knot spacing are also shown (Figure 7-21-b). Overall the stress distribution measured using the old and new contour cut are in agreement in that:

- ✓ Tensile stress was measured in the weld region is balanced by compressive stresses in the parent material.
- ✓ Thin bands of high compressive stresses towards the specimen top surface in the parent material are observed which might be caused by cutting artefacts or machining effects.

However, there are some detailed differences between the two maps. For example the tensile region in the new contour cut is more uniformly distributed over the weld region.

Furthermore, the magnitude and extent of the thin bands of compressive stresses towards the specimen top surface is lower for the new contour cut results.

A comparison of the transverse component of residual stresses of the new contour cut, the old contour cut and the idealised stress profile (obtained from the neutron diffraction measurements) along a line located at 7.5 mm below the specimen top surface is shown in Figure 7-22. As for the old contour cut, the new contour cut results are averaged over an area of the gauge volume used for the neutron diffraction measurements.

As can be appreciated the identified features in the old contour results that were believed to have occurred due to plastic strains during cutting are significantly mitigated in the new contour cut results.

Comparing the old and new residual stress profiles in Figure 7-22 demonstrates that the errors in stress due to compressive yielding ('hump A') is reduced in the new contour cut results. The second feature due to tensile yielding (increasing trend of tensile stresses in the weld region) is moderated in the new contour cut results in that the tensile region is more uniformly distributed.

As demonstrated earlier, the average plasticity-induced stress error predicted for the new contour cut based on the idealised stress profile was 10% for the RMS error and 6.5 % for the absolute error. The actual error based on the differences between the 'new contour' measured profile and the idealised are calculated to be 11% for the RMS average error and 8.8 % for the absolute average error, which are very similar to those predicted.

As demonstrated through the case studied, the developed measures to control the stress intensity factor, hence the cut tip stress concentration during the cutting, have had an influence in moderating the plasticity-induced error. Furthermore, the developed

correlations for plasticity-induced errors estimation have been confirmed by this application example.

It is worth mentioning that although the adopted cutting/restraining strategy reduced the plasticity-induced errors in the new contour cut results, the contour results are not entirely satisfactory. The humps observed at 70-100 mm from the start cut and the higher tensile region in the weld area are features suggesting that some plasticity has occurred during cutting despite the specific measures taken to minimise this effect.

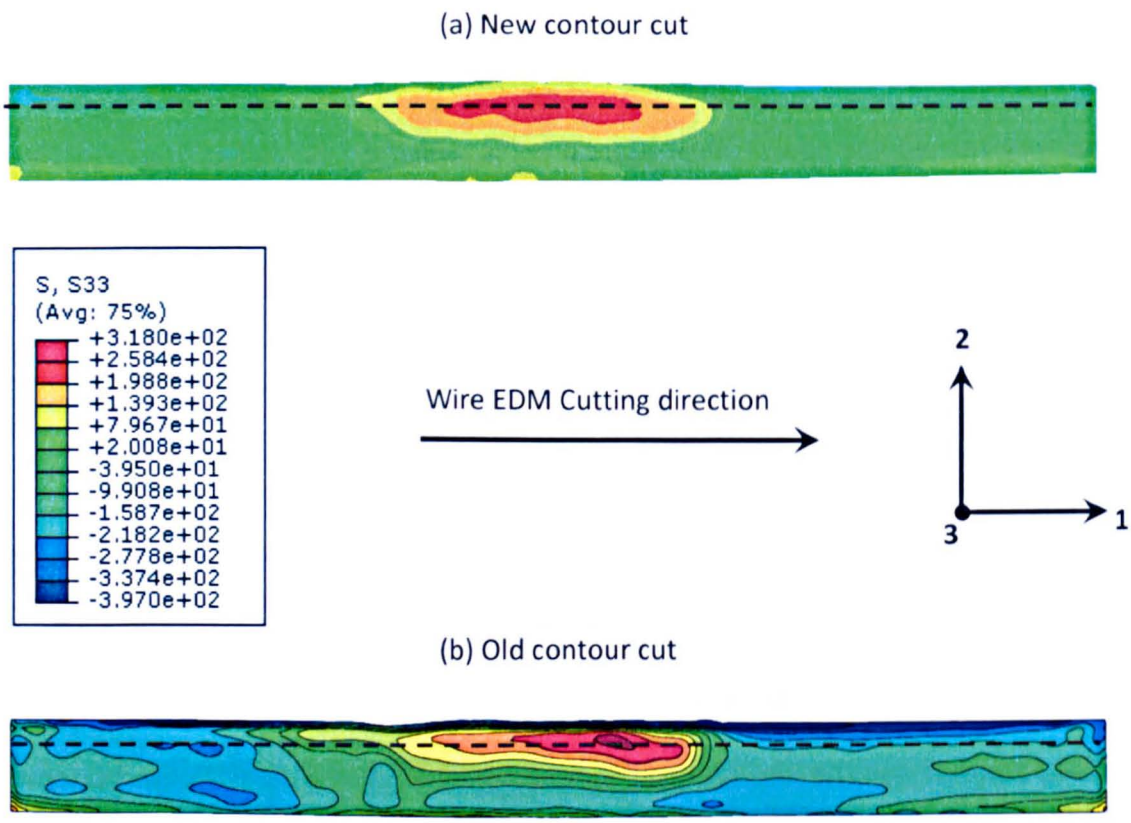

Figure 7-21: Map of the transverse residual stress over the longitudinal plane at the mid-width of the 3-pass slot weld specimen for the new (a) and old contour cut (b) [8]. The dashed line is measurement line located at 7.5 mm below the plate top surface. Stress units are in MPa.

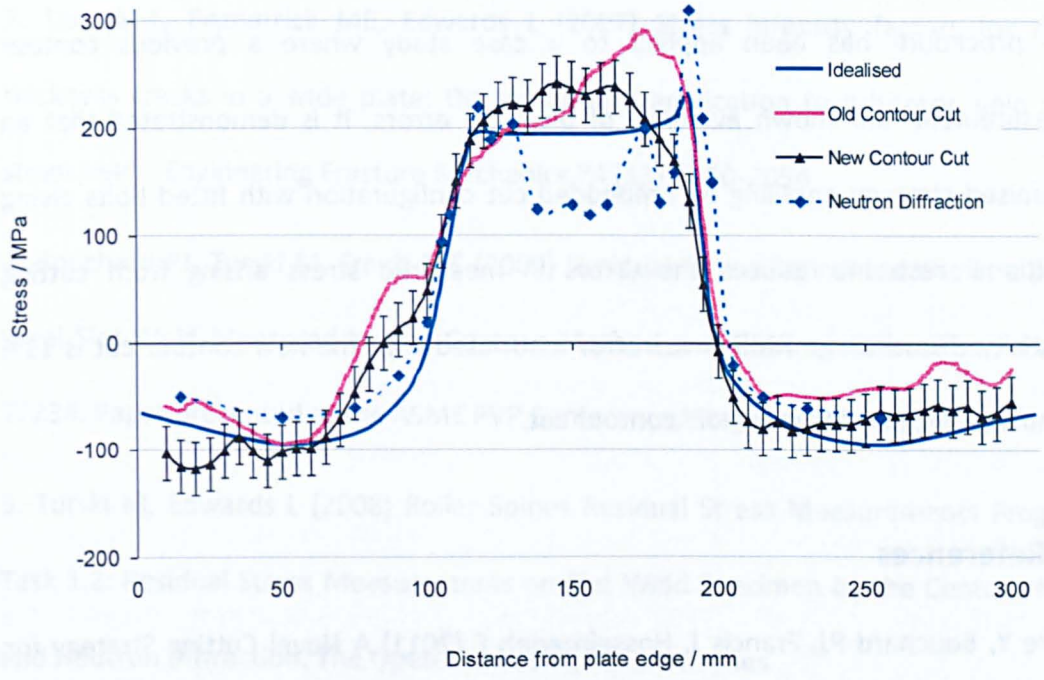

Figure 7-22: Comparison of transverse residual stress measurements for the 3-pass slot weld specimen along a line parallel to the weld at 7.5 mm below the top surface determined by the new and old contour cut. The average plasticity-induced stress error bars are added to the 'new contour' measurements.

7.4. Conclusions

1. A procedure for mitigating plasticity-induced stress errors in contour method residual stress measurements has been defined and applied to a case study.
2. The three main steps of the minimisation procedure consist of determining the residual stress intensity factor for a cutting and clamping strategy, calculating the normalised average plastic zone size and estimating the average stress error. The process can be repeated for a variety of cutting/restraining strategies to help select the approach that minimises plasticity-induced error, ideally below the threshold of 5% of RMS error proposed in this thesis.

3. The procedure has been applied to a case study where a previous contour measurement had shown evidence of plasticity errors. It is demonstrated that an optimised strategy entailing an embedded cut configuration with fitted bolts giving additional restraint reduces the errors in measured stress arising from cutting plasticity. The average RMS stress error associated with the new contour cut is 11% compared with 16.2 % in the old contour cut.

7.5. References

1. Traore Y, Bouchard PJ, Francis J, Hosseinzadeh F (2011) A Novel Cutting Strategy for Reducing Plasticity Induced Errors in Residual Stress Measurements Made With the Contour Method. ASME Conference Proceedings 2011 (44564):1201-1212

2. Shin S (2005) FEM analysis of plasticity-induced error on measurement of welding residual stress by the contour method. Journal of Mechanical Science and Technology 19 (10):1885-1890

3. Dennis RJ, Bray DP, Leggatt NA, Turski M (2008) Assessment of the Influence of Plasticity and Constraint on Measured Residual Stresses Using the Contour Method / PVP2008-61490. Paper presented at the ASME Pressure Vessels and Piping Division Conference, Chicago, USA,

4. ABAQUS (2010) ABAQUS/Standard Documentation Version 6.10.2. ABAQUS, Inc

5. EDF Energy (2013) R-Code.V4.4. http://www.r-desk.co.uk/software. Accessed 24 February 2013

6. Janssen M, Zuidema J, Wanhill RJH (2002) Fracture Mechanics. 2nd edn. Delft University Press, Delft

7. Tan JM-L, Fitzpatrick ME, Edwards L (2007) Stress intensity factors for through-thickness cracks in a wide plate: Derivation and application to arbitrary weld residual stress fields. Engineering Fracture Mechanics 74 (13):2030-2054

8. Bouchard PJ, Turski M, Smith MC (2009) Residual Stress Concentrations in a Stainless Steel Slot-Weld Measured by the Contour Method and Neutron Diffraction / PVP2009-77234. Paper presented at the ASME PVP Conference, Prague, Czech Republic,

9. Turski M, Edwards L (2008) Boiler Spines Residual Stress Measurements Programme Task 1.2: Residual Stress Measurements on Slot Weld Specimen by the Contour Method and Neutron Diffraction. The Open University, Milton Keynes

10. Moyes N (2004) Mitsui Babcock - Manufacture and Welding of Plate Specimens. Report E-04-030.

11. Moyes N (2004) British Energy - Manufacture and Welding of Plate Specimens. Mitsui Babcock,

12. Smith MC, Smith AC (2009) NeT bead-on-plate round robin: Comparison of residual stress predictions and measurements. International Journal of Pressure Vessels and Piping 86 (1):79-95

13. Dennis R (2006) NPCT - Austenitic Weld Modelling / Analysis of Slot Weld Specimen. Frazer-Nash Consultancy,

14. AK Steel (2013) 316L Stainless Steel [Online]. http://www.aksteel.com/pdf/markets_products/stainless/austenitic/316_316L_Data_Bulletin.pdf. Accessed 23 April 2013

15. Prime M, Sebring R, Edwards J, Hughes D, Webster P (2004) Laser surface-contouring and spline data-smoothing for residual stress measurement. Experimental Mechanics 44 (2):176-184

Chapter 8: Conclusions and future work

This research is motivated to fill the gap in knowledge regarding plasticity-induced errors in residual stress measurements made with the contour method.

The contour method is a powerful destructive technique for mapping the residual stress field across a surface within components with less effort and higher spatial resolution than most destructive methods. Unlike diffraction techniques it is not affected by microstructure variations. However, the contour method is prone to plasticity-induced errors when measuring residual stresses of high magnitude. That is because its theory relies on the principle of elastic residual stress relaxation. Although a limited number of publications have addressed this issue [1-3], plasticity-induced errors in residual stress measurements made using the contour method remain a major concern.

The aims of this research were to investigate/understand, quantify and suggest strategies for mitigating plasticity-induced errors in residual stress measurements made with the contour method. These aims have been addressed using linear elastic fracture mechanics, finite element method studies and experimental work.

First, the effect of restraint conditions on plasticity-induced errors was investigated by conducting contour method measurements on a CT blank specimen where unrestrained conditions for a slitting measurement were used. The errors introduced were assessed by comparing the results from the contour method with those obtained by neutron diffraction and slitting. The errors observed in the contour method results were investigated by simulating the contour method for different restraining conditions (restrained and unrestrained) assuming a 'top hat' stress distribution.

Following the assessment of restraint conditions on the plasticity-induced errors, a stress intensity factor analysis was undertaken to develop a novel cutting strategy for mitigating plasticity-induced errors.

Furthermore, correlations for plasticity-induced errors estimation in the contour method were developed and experimentally validated by conducting neutron diffraction and contour method residual stress measurements in four test specimens containing controlled residual stress distributions created by patterns of laser welds.

Finally, good practice guidelines for controlling the plasticity-induced errors have been defined and applied to a case study.

Each aspect has been presented in detail in previous chapters. The outcomes of these studies are itemised in section 8-1 of this chapter. The final part of the chapter (section 8-2) covers ideas to take forward and broaden the project.

8.1. Conclusions

8.1.1. Effect of restraining conditions on plasticity-induced errors

- ✓ Residual stress measurement by the contour method, where the test specimen was unrestrained during cutting, was performed on a CT blank (Chapter 3) and the results compared to those obtained by neutron diffraction and slitting. The contour method results were in excellent agreement with the neutron diffraction and slitting measurements apart from a small shift in the position of the tensile stress peak towards the cut start position.
- ✓ The peak stress positional shift observed in the contour method results was investigated by simulating the contour measurement method for different restraining

conditions (restrained and unrestrained) assuming a 'top hat' residual stress distribution and elastic-perfectly plastic material properties.

✓ It was found that the shape of the tensile residual stress profile measured by the contour method can indeed be shifted towards the cut starting position when the component is left unrestrained and that the level of error in contour measurements is dependent on the ratio of the magnitude of the residual stresses present to the material yield strength.

8.1.2. Plasticity-induced errors mitigation

✓ An analogy was made between the stress relaxation process during test specimen cutting and a cracked plate subjected to an internal load on the crack surfaces. It was found that a sufficiently high magnitude crack tip stress field (compared to the material yield stress) introduces a plastic zone surrounding the crack tip. Both the crack tip stress field and the corresponding plastic zone size are directly related to the mode I stress intensity factor in linear elastic fracture mechanics.

✓ It was found that a novel cutting strategy (embedded cut) can reduce plasticity-induced errors (Chapter 4) through controlling the residual stress intensity factor distribution, and that further improvement could be achieved with additional restraint.

✓ This cutting strategy was applied to measure residual stresses in a 3-pass slot weld specimen. The measurement results demonstrate that plasticity-induced errors were moderated compared with those previously obtained using an edge cut configuration.

8.1.3. Plasticity-induced errors estimation

- ✓ Sensitivity studies were conducted on the crack/cut tip plastic zone for development of procedures (correlations) for plasticity-induced error estimation (Chapter 5).
- ✓ It was demonstrated that overall the shape, the size and the depth of the plastic zone ahead of a crack are not affected by the cut width and the cut tip shape.
- ✓ Correlations between the average error in stress measured by the contour method and the average plastic zone parameters (plastic zone size and depth) along the cutting path have been developed using the finite element method and linear elastic fracture mechanics (Chapter 5). Both plane stress and plane strain conditions were considered with elastic-perfectly plastic material.
- ✓ The normalised average PZS (rather than the normalised average PZD) was found to be the most important parameter determining the introduction of plasticity-induced stress errors.
- ✓ The effect of a finite cut width has been investigated. It was found that the cut width helps to reduce the lateral extent of the plastic wake and hence will help reduce plasticity-induced errors in contour measurements.
- ✓ A threshold normalised average plastic zone size and corresponding average stress error from which plasticity starts to become significant are proposed for the plasticity-induced errors mitigation.

8.1.4. Experimental validation of the FE-based error correlations

- ✓ The finite element method was used to design test specimens for validating plasticity-error estimation correlations for contour measurements. The test specimens used laser heating/welding in a unique way to introduce controlled distributions of residual

stress of varying magnitude such that different levels of plasticity error (high, moderate and negligible) were introduced in contour method measurements.

- ✓ Validation of the plasticity induced stress error correlations' was achieved by comparing the average stress errors determined from the differences between the contour and neutron diffraction results and the estimated average stress error from the correlations based on the neutron stress profile. The results were in a very good agreement.
- ✓ The development of plastic strains during the cutting process was experimentally investigated for two extreme cases by hardness survey: that is samples with high and negligible levels of cutting plastic strains. Although there was a significant amount of scatter in the hardness data, the results did correlate fairly well with the cutting plastic strains predicted by finite element simulation for both test specimens.

8.1.5. Guidelines for plasticity-induced error mitigation

- ✓ A procedure for estimating and mitigating plasticity-induced errors in the contour method has been presented in Chapter 7. The most important inputs for the estimation/mitigation process are: an estimate of the initial residual stress distribution, the specimen's dimensions and the material mechanical properties (Young's modulus, Poison's ratio and yield stress). The different steps of the procedure are summarised in a flowchart:

    1. *Step 1:* design a cutting/restraining configuration;
    2. *Step 2:* determine the residual stress intensity factor distribution based on the designed configuration;

3. *Step 3:* Investigate the predominant stress state at the cut/crack tip according to ASTM requirement [4,5].
4. *Step 4:* Calculate the normalised average plastic zone size.
5. *Step 5:* estimate the average plasticity-induced stress errors using the normalised average plastic zone size (PZS) and from the sets of correlations. Step 1 to Step 5 can be repeated until optimum cutting conditions are obtained.
6. *Step 6:* To take into account the effect of the cut width, determine/measure/assume a cut width and extract it from the average plastic zone depth (PZD).
7. *Step 7:* Re-estimate the average stress error using the correlations and the corrected average PZD.

✓ A contour measurement case study (plate containing 3-pass slot weld) has been presented that illustrates application of the procedure. A 30% reduction in measurement stress errors is demonstrated by applying an optimised cutting strategy and restraint configuration.

8.2. Suggestions for future work

Like any research the present work could not cover all topics of interest and further interesting thoughts and questions arose raised during the course of this study. Therefore in the following sections some suggestions for future work are given: the effect of strain hardening on the plasticity-induced errors, the assessment of plasticity-induced errors for transitional behaviour from plane stress to plane strain conditions (3D case) and finally the quantification of the cutting plastic strains.

8.2.1. Strain hardening effect

In this study elastic-perfectly plastic material (*i.e.* material with no strain hardening) has been used for developing the correlations for plasticity-induced errors estimation. Furthermore, the Irwin plastic zone expression, used throughout this work, has been derived from a cracked plate with elastic-perfectly plastic material behaviour [4]. However, most materials exhibit some degree of hardening and the idealised behaviour modelled will over-estimate plasticity effects.

In the open literature, a published work of Narasimhan *et al* [6] investigating the effect of strain hardening on a growing crack tip plastic zone shape has revealed interesting outcomes. They simulated, by finite element method, a growing crack within a plate under plane stress for different strain hardening values. They reported that the size of the plastic zone in the crack propagation direction decreases when the material strain hardening is increased while the depth of the plastic zone (*i.e.* plastic zone size in the direction perpendicular to the crack propagation direction) increases with increasing strain hardening.

Work carried out in the present research revealed that the depth of plastic zone is the most important parameter for plasticity-induced error mitigation in the residual stress measurement made with contour method.

Therefore an investigation of strain hardening effects on plasticity-induced errors in the residual stress measurement made with the contour method is important and would add to the existing work and allow it to be extended to deal with strain hardening material behaviour.

8.2.2. Plane stress-plane strain transitional behaviour analysis: 3D cases

Similar to most fracture mechanics studies, this work has focused on case studies considering idealised plane stress and plane strain conditions. Therefore, plasticity assessment and mitigation using the developed correlations in this study are only valid for plane stress and plane strain conditions. It is obvious that when dealing with contour method residual stress measurements within a sample having transitional behaviour, the cutting /restraining optimisation must be conducted assuming the worst case of stress state in terms of plasticity-induced errors (*i.e.* plane stress conditions).

Nevertheless, further work is suggested to investigate the effects of plasticity-induced errors and subsequently to develop tools and strategies for mitigating/estimating the errors associated with plasticity in the results of the contour method for 3D cases and when dealing with components with complex geometries and real world features.

8.2.3. Experimental quantification of cutting plastic strains

Further work is recommended to experimentally quantify the plastic strains induced by the release of residual stresses during the sample cutting process. Hardness testing has been applied in this work to determine the cutting plastic strains (Chapter 6). The approach provided very encouraging results, although heavy experimental preparation, including manual grinding and polishing, were required.

However, because of the low magnitudes of cutting plastic strains, the range of hardness values was very low; this resulted in significant scatter in the hardness measurements. To counter this issue, different measurement techniques such as X-ray [7], neutron [8,9] and synchrotron [10] diffraction can be applied to quantify plastic strains induced by the

release of the residual stresses during the cutting process for the contour method residual stress measurements.

Because of limited access to neutron diffraction and synchrotron facilities, laboratory X-ray diffraction is a preferable technique for characterising the cutting plastic strains. Quantification of plastic strains using laboratory x-rays consists of measuring diffraction peak broadening for a particular diffraction plane and at a specific diffraction angle [7]. The approach has already been established as a process for characterising plastic strains. Therefore, it can be applied to determine the plastic strains induced by the release of residual stresses during the contour cutting process.

8.3. References

1. Shin S (2005) FEM analysis of plasticity-induced error on measurement of welding residual stress by the contour method. Journal of Mechanical Science and Technology 19 (10):1885-1890

2. Dennis RJ, Bray DP, Leggatt NA, Turski M (2008) Assessment of the Influence of Plasticity and Constraint on Measured Residual Stresses Using the Contour Method / PVP2008-61490. Paper presented at the ASME Pressure Vessels and Piping Division Conference, Chicago, USA,

3. Dennis RJ, Leggatt NA, Kutarski EA (2009) Investigation of the Performance of the Contour Residual Stress Measurement Method When Applied to Welded Pipe Structures / PVP2009-77470. Paper presented at the ASME Pressure Vessels and Piping Division Conference, Prague, Czech Republic,

4. Janssen M, Zuidema J, Wanhill RJH (2002) Fracture Mechanics. 2nd edn. Delft University Press, Delft

5. ASTM (2006) ASTM E399 - Standard Test Method for Linear-Elastic Plane-Strain Fracture Toughness K_{IC} of Metallic Materials.

6. Narasimhan R, Rosakis AJ, Hall JF (1987) A Finite Element Study of Stable Crack Growth Under Plane Stress Conditions: Part II-Influence of Hardening. Journal of Applied Mechanics 54 (4):846-853

7. Brandstetter S, Budrović Ž, Van Petegem S, Schmitt B, Stergar E, Derlet PM, Swygenhoven HV (2005) Temperature-dependent residual broadening of x-ray diffraction spectra in nanocrystalline plasticity Applied Physics Letters 87 (23)

8. Smith DJ, Leggatt RH, Webster GA, MacGillivray HJ, Webster PJ, Mills G (1988) Neutron diffraction measurements of residual stress and plastic deformation in an aluminium alloy weld. The Journal of Strain Analysis for Engineering Design 23 (4):201-211

9. Smith DJ, Webster GA (1997) The measurement of prior plastic deformation in metallic alloys using the neutron diffraction technique. The Journal of Strain Analysis for Engineering Design:32-37

10. Budiman AS, Lee G, Burek MJ, Jang D, Han SMJ, Tamura N, Kunz M, Greer JR, Tsui TY (2012) Plasticity of indium nanostructures as revealed by synchrotron X-ray microdiffraction. Materials Science and Engineering: A 538:89-97